Shear Flow Instabilities in Viscoelastic Fluids

Joel C. Miller

Churchill College

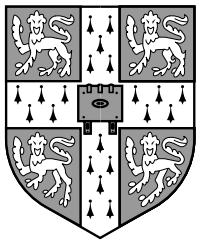

A dissertation submitted to the University of Cambridge for the degree of Doctor of Philosophy

September 2005

De sinaasappel zal zo van de tak vallen, of ligt al op de grond, aldus deze vreemde vereenvoudigers. Niemand ziet hem vallen.

Jorge Luis Borges
De Geschiedenis van de Eeuwigheid, 1936.

Transl: Barber van de Pol.
Bezige Bij, Amsterdam 1985

To my grandparents, my parents, my brother, and my wife

Preface

The first part of this dissertation studies interfacial instabilities in large Weissenberg number viscoelastic coextrusion flow. The instabilities are due to discontinuities in the elastic properties. We find new instabilities and show that the understanding of a previously known instability is incomplete.

The second part of this dissertation studies the effect of elasticity on the inertial instability of a jet. We emphasize the effect of weak elasticity on the development of cat's eyes. This is based on work begun at the Geophysical Fluid Dynamics summer school at the Woods Hole Oceanographic Institution following my second year as a PhD student.

A repeated message of the experience presented here is that serendipity is an integral and fruitful part of research, or — more pessimistically — where hard work and perseverance fail, blind luck triumphs. The better part of a year's work has been relegated to a (short) paragraph of chapter 4 while everything apart from chapter 7 was discovered by chance trying to understand something else.

All of the work described in this dissertation is believed to be original except where explicit reference is made to other sources. This dissertation is my own work and no part has been or is being submitted for any qualification other than the degree of Doctor of Philosophy at the University of Cambridge.

Acknowledgments

This thesis has been markedly improved by the assistance of many people and organizations. I would like to extend my heart-felt gratitude to John Rallison for many valuable and thought-provoking conversations as well as many hours of careful proof-reading. I am greatly indebted to him. Much of this dissertation extends Helen Wilson's thesis of the same title, and discussions with her have been helpful. Jon Dawes assisted me with nonlinear analysis, though a computational error on my own part has consigned this to "future work". Henk Slim and Lydia Heck have helped solve computational issues innumerable times. Rob, Rob, and Dominic have shown great patience enduring my intrusions, and Steve has been a partner in commiseration.

The Geophysical Fluid Dynamics summer school I attended at the Woods Hole Oceanographic Institution proved greatly beneficial, along with the supervision I received there from Neil Balmforth. I have received some funding from an Overseas Research Student grant as well as travel funding from the Department of Applied Mathematics and Theoretical Physics, the Cambridge Philosophical Society, and Churchill College. I thank the National Science Foundation of the United States of America for providing three years of funding and the Institute of Theoretical Geophysics for use of its space.

Most of all, I want to thank Anja Slim for help with numerics, vigilant proof-reading, and partially funding my fourth year.

Finally, it should go without question that I thank Mike Proctor for being my supervisor.

Summary

This dissertation is concerned with the theoretical study of the stability of viscoelastic shear flows. It is divided into two parts: part I studies inertialess coextrusion flows at large Weissenberg number where the instabilities are due to discontinuities in the elastic properties, and part II studies the effect of elasticity on the well-known inertial instabilities of inviscid flows with inflection points.

We begin part I with a previously known short-wave instability of Upper Convected Maxwell and Oldroyd–B fluids at zero Reynolds number in Couette flow. We show that if the Weissenberg number is large, the instability persists with the same growth rate when the wavelength is longer than the channel width. Intriguingly, surface tension does not modify the growth rate. Previous explanations of elastic interfacial instabilities based on the jump in normal stress at the interface cannot apply to this instability. These results are confirmed both numerically and with asymptotic methods.

We then consider Poiseuille flow and show that a new class of instability exists if the interface is close to the center-line. We analyse the scalings and show that it results from a change in the boundary layer structure of the Couette instability. The growth rates can be large, and the wavespeed can be faster than the base flow advection. We are unable to simplify the equations significantly, and asymptotic results are not available, so we use numerics to verify the results.

In studying these instabilities we encounter some others which we mention, but do not analyse in detail.

In part II we study the effect of elasticity on the inertial instability of flows with inflection points. We show that the elasticity modifies the development of cat's eyes. The presence of extensional flow complicates the analysis. Consequently we use the FENE–CR equations.

Contents

Chapter 1

Introduction

This dissertation contains a theoretical study of two distinct problems in the stability of elastic shear flow. The bulk of the thesis (part I, chapters 2–6) investigates the linear stability of inertialess parallel flow of multiple fluid layers where an instability is caused by discontinuities of elastic properties. The remainder (part II, chapter 7) studies the effect of elasticity on the inertial instability of a planar jet, as well as the effect of weak elasticity on the nonlinear development of cat's eyes.

Many industrial applications involve coextrusion of two or more fluids that harden into a multi-layered solid with desirable properties. For example, films used to wrap foods might have one side chosen for adhesive properties while the other is chosen for permeability to water or oxygen. Many of these flows are either very thin or very viscous (or both) so that the Reynolds number is small. Although we use the term "coextrusion", we consider flow of multiple layers within the die (the channel or pipe through which the fluid is extruded) and do not concern ourselves with the details of the entrance or exit. Instabilities at the interface lead to distortions affecting optical or mechanical properties, so a stable flow is needed. In other contexts these instabilities may be desirable: for example in microfluidics it may be necessary

to mix two fluids together. This is made difficult by the small length scales and resulting low Reynolds number. An instability which mixes the entire flow is needed. Part I of this thesis contains a discussion of such instabilities.

At the alternate limit of high Reynolds number it has been known for nearly sixty years that the addition of a small amount of polymer significantly reduces measured drag of turbulent flow through a pipe, a phenomenon known as *turbulent drag reduction*. This has applications including fire hose design, waste water disposal, and crude oil transport. The phenomenon is not well understood, in part because even the simplest effects of polymers on high Reynolds number flow are difficult to model. Some discussion of the theory and relevant papers can be found in the review articles of Lumley [62] and Lumley and Blossey [63]. Direct numerical simulation has captured drag reduction, but does not offer much physical insight [9, 93]. Recent study suggests that the mechanism behind turbulent drag reduction may be the modification of the "exact coherent states" believed to play a role in Newtonian turbulence [92]. Although the jet flow studied in part II is far from a model of full-scale turbulence, it extends some earlier linear studies [3, 10] and gives perhaps the simplest possible nonlinear model of high Reynolds number viscoelastic flow. This analysis forms the starting point of a continuing fully nonlinear computational study of elastic jets in collaboration with Dr. Neil Balmforth and Dr. Yuan-Nan Young.

We commence this introductory chapter with a discussion of basic elastic fluid properties in section 1.1. Section 1.2 briefly overviews some common constitutive models. The remainder of the introduction is related to coextrusion flow (part I of the dissertation): we discuss experimentally observed inertialess instabilities in section 1.3 and theoretical investigations of instabilities in section 1.4. Section 1.5 classifies the various types of instabilities we study. Finally section 1.6 outlines the remainder of the dissertation. An introduction to the inertial instability is postponed until part II.

1.1 Rheology of non-Newtonian fluids

We consider only *simple fluids*. That is: the stress Σ at a material point depends only on the past history of the local flow at that point (in the Lagrangian sense); if the velocity is held to zero, the stress relaxes to an isotropic state; and finally the fluid is material frame indifferent (*i.e.*, the stress-strain relationship is unaffected by a rigid body motion of the entire system).

The Navier–Stokes equations governing the flow of Newtonian fluids (discussed later) are derived under additional assumptions, most notably that the fluid is everywhere "in equilibrium" such that the fluid elements only know the local instantaneous velocity, velocity gradients, pressure, and forces. The flow is weak enough that information about previous orientations has been lost.

Generally the distinction between a Newtonian fluid and a non-Newtonian fluid is a distinction between flow conditions. We encounter non-Newtonian effects if the shear rate is large enough to deform the molecules from their equilibrium configuration, so a "non-Newtonian" fluid is a fluid that has non-Newtonian effects on laboratory scales. Examples of typical non-Newtonian fluids include a solvent with dissolved polymer chains or a polymer melt.

1.1.1 Shear rheology

In steady simple shear with velocity $\boldsymbol{U} = (\dot{\gamma}y, 0, 0)$, in Cartesian coordinates, any incompressible simple fluid will have a stress tensor Σ with four independent components of the form

$$\Sigma = \begin{pmatrix} \Sigma_{11} & \Sigma_{12} & 0 \\ \Sigma_{12} & \Sigma_{22} & 0 \\ 0 & 0 & \Sigma_{33} \end{pmatrix} . \tag{1.1}$$

The stress is unique up to an arbitrary constant isotropic pressure. The *shear viscosity* is defined to be

$$\mu \equiv \Sigma_{12}/\dot{\gamma}\,. \tag{1.2}$$

The first and second *normal stress differences* are defined to be

$$N_1 \equiv \Sigma_{11} - \Sigma_{22}\,, \tag{1.3}$$

$$N_2 \equiv \Sigma_{22} - \Sigma_{33}\,. \tag{1.4}$$

In the absence of a flow, the simple fluid stress is isotropic, and so $N_1(\dot{\gamma} = 0) = N_2(\dot{\gamma} = 0) = 0$. Due to symmetry considerations the stress differences cannot depend on the sign of $\dot{\gamma}$ so they are quadratic at small values of $|\dot{\gamma}|$. This motivates the definition of the *normal stress coefficients* $\Psi_1 \equiv N_1/\dot{\gamma}^2$ and $\Psi_2 \equiv N_2/\dot{\gamma}^2$.

For many fluids the values of Ψ_1, Ψ_2 and μ depend strongly on $\dot{\gamma}$ and are described as shear-thinning (*i.e.*, they decrease as $\dot{\gamma}$ increases) or shear-thickening (*i.e.*, they increase). However, for dilute viscous solutions (the "Boger fluid" discussed later), these are found to be effectively constant for a large range of $\dot{\gamma}$.

1.1.2 Extensional rheology

We consider now the uniaxial elongation of a cylinder of fluid aligned with the z axis. In Cartesian coordinates the flow is given by $\boldsymbol{U} = \dot{\epsilon}\left(-\frac{x}{2}, -\frac{y}{2}, z\right)$ where $\dot{\epsilon}$ is the extension rate, which we take to be constant. The resulting stress is of the form

$$\Sigma = \begin{pmatrix} -p - \Sigma' & 0 & 0 \\ 0 & -p - \Sigma' & 0 \\ 0 & 0 & -p + 2\Sigma' \end{pmatrix}. \tag{1.5}$$

The *extensional viscosity* is defined to be

$$\mu_e \equiv \frac{-\Sigma_{11} - \Sigma_{22} + 2\Sigma_{33}}{2\dot{\epsilon}} = \frac{\Sigma'}{\dot{\epsilon}}\,. \tag{1.6}$$

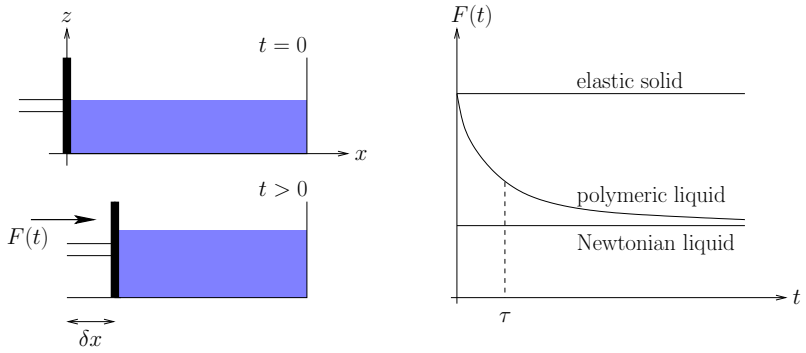

Figure 1.1: Stress relaxation.

In general polymers resist extension more than shear and so the *Trouton ratio* (the ratio of the extensional to shear viscosities) for an elastic fluid can be orders of magnitude greater than that of a Newtonian fluid, namely three.

This idealized extensional flow is difficult to realize experimentally: a constant extension rate requires exponential growth in length. A number of experimental techniques have been developed to measure the extensional viscosity. However, an attempt to test these methods on a standardized fluid (the M1 fluid) resulted in wildly differing results discussed by Sridhar [91] and references therein. Further issues related to the extensional viscosity of elastic fluids appear in the review by McKinley and Sridhar [67].

1.1.3 Stress relaxation

Consider a (highly viscous) fluid at rest in a channel $0 < x < L_x$, $-L_y < y < L_y$, and $0 < z < h$, with solid walls at $x = L_x$, $y = \pm L_y$ and $z = 0$, a free surface at $z = h$, and a movable piston at $x = 0$. The piston moves rapidly in the positive x-direction, and then stops and remains at a new location δx as shown in figure 1.1. There will be a restoring force as the molecules in the fluid attempt to return to the state they were in prior to the piston motion.

Consequently, to hold the piston in place requires a force $F(t)$, which can be measured experimentally.

For an elastic solid, the force exerted by the solid on the piston is proportional to the deformation. A Newtonian fluid immediately adjusts to its new location and the force exerted on the piston is purely hydrostatic. For an elastic fluid the force is initially like a solid, but over time the molecules relax into a new equilibrium configuration and the force becomes hydrostatic.

Although there may be multiple time scales related to this relaxation (perhaps related to different sizes of dissolved molecules or different relaxation mechanisms), we typically assume only a single relaxation time. For a polymer dissolved in a solvent, the relaxation time increases with the solvent viscosity and the polymer length.

The Weissenberg number

In a flow with typical velocity U_0 and width L for which the fluid has relaxation time τ, the *Weissenberg number* $Wi \equiv U_0\tau/L$ is frequently thought of as the ratio between the time scale of the fluid (τ) and the time scale (L/U_0) associated with the shear rate. For our purposes however, it is better to think of Wi as the ratio between the typical length scale the fluid travels while relaxing ($U_0\tau$) and the length scale over which the fluid flow rate varies (L). The Weissenberg number is therefore the ratio of two length scales.

The Deborah number

The *Deborah number* De is the ratio between the characteristic time scale of the fluid (τ) to the time scale associated with the flow. This is of particular interest in oscillating flows (*e.g.*, in a cylinder oscillating with frequency Ω) where $De = \tau\Omega$. The Deborah and Weissenberg numbers are often (incorrectly) used interchangeably. In many flows they are the same, but more

generally they can differ greatly.

Wi versus *De*

Some examples help clarify the difference between the Weissenberg and Deborah numbers.

Consider a cylinder filled with fluid undergoing high frequency but low amplitude oscillations about its axis. The time scale of the flow is the time scale associated with the oscillation frequency. This time scale is small, yielding a large Deborah number. The time scale of the shear rate depends on the amplitude of the oscillation and the depth that the oscillation penetrates into the fluid. This time scale is large, yielding a small Weissenberg number.

In contrast we can consider fast, steady shear flow through an infinite channel. The time scale of the flow is infinite, yielding a Deborah number of zero whereas the time scale of the rate of strain depends on the width of the channel and the velocity of the fluid. This time scale is small, yielding a large Weissenberg number.

1.1.4 The Boger fluid

For the purposes of analytic study, an ideal elastic fluid has constant viscosity μ and constant normal stress coefficients Ψ_1 and Ψ_2. Boger [12] developed a class of fluids which experimental measurements show to have effectively constant viscosity and normal stress coefficients over a range of shear rates.

A Boger fluid is created by dissolving a large molecular weight polymer in a viscous low molecular weight solvent. The earliest were dilute solutions of polyacrylamide dissolved in a maltose/water solvent. Aqueous solvents have a tendency to evaporate over time, and the physical properties change over time. The study has turned to organic solvents and polymers, usually using a high molecular weight polymer dissolved in a low molecular weight solvent

of the same monomer. Because the solvent is highly viscous, the polymers cannot relax quickly back to their equilibrium state. The relaxation time for a Boger fluid can be over a hundred seconds [52].

Magda *et al.* [64] studied an organic Boger fluid and found that the magnitude of the second normal stress difference is approximately 1% that of the first normal stress difference.

1.2 Constitutive equations

In this section we provide a brief overview of some constitutive models. More comprehensive references are found at the end of this section.

We assume throughout that our fluids are incompressible and so satisfy

$$\nabla \cdot \boldsymbol{U} = 0\,. \tag{1.7}$$

The momentum equation is

$$\rho \frac{D\boldsymbol{U}}{Dt} = \nabla \cdot \Sigma + \mathcal{F}\,, \tag{1.8}$$

where ρ is the density, $\boldsymbol{U}$ the velocity, $D/Dt \equiv \partial_t + \boldsymbol{U} \cdot \nabla$ the material derivative, Σ the stress tensor, and $\mathcal{F}$ can be any body force.

1.2.1 The Newtonian fluid

The Newtonian fluid is a special case of the simple fluid. The deviatoric stress (the trace-free part of the stress) is linearly related to the instantaneous local value of $\nabla \boldsymbol{U}$ and it is isotropic. We take the fluid to be incompressible and make the additional assumption that inertia is negligible, and so we arrive

at the Stokes equations

$$\begin{aligned} \nabla \cdot \Sigma &= 0\,, \\ \Sigma &= -P\mathsf{I} + 2\mu\mathsf{E}\,, \\ \mathsf{E} &= \frac{\nabla \boldsymbol{U} + (\nabla \boldsymbol{U})^T}{2}\,, \\ \nabla \cdot \boldsymbol{U} &= 0\,, \end{aligned}$$

where μ is the shear viscosity, P the pressure, and E the rate of strain tensor.

1.2.2 The upper convected derivative

The fluids we study have an elastic strain which depends on the history of rotation and stretching in the flow. The equations we use must save this information. This is accomplished by the upper convected derivative of a tensor T denoted by $\overset{\triangledown}{\mathsf{T}}$, and defined as

$$\overset{\triangledown}{\mathsf{T}} \equiv \frac{\partial \mathsf{T}}{\partial t} + (\boldsymbol{U} \cdot \nabla)\mathsf{T} - (\nabla \boldsymbol{U})^T \cdot \mathsf{T} - \mathsf{T} \cdot (\nabla \boldsymbol{U})\,. \tag{1.9}$$

This derivative contains the advection associated with the material derivative $\partial_t + \boldsymbol{U} \cdot \nabla$, but also accounts for rotation and stretching with the flow like a material element through the $\nabla \boldsymbol{U}$ terms[1], that is, it is *codeformational*. It will be useful later to note that

$$\overset{\triangledown}{\mathsf{I}} = -2\mathsf{E}\,.$$

1.2.3 The Oldroyd–B fluid

The Oldroyd–B fluid [73] is commonly used as a theoretical model of a Boger fluid. The match is not perfect, particularly at larger shear rates where other models (with more free parameters) fit the experimental data better [78].

[1]The literature is not consistent on the notation $\nabla \boldsymbol{U}$. We take $\nabla \boldsymbol{U}$ to denote the tensor whose (i, j) component is given by $\partial_{x_i} U_j$ rather than its transpose.

The stress in an Oldroyd–B fluid contains Newtonian and elastic components. We use the inertialess incompressible form

$$\nabla \cdot \mathsf{\Sigma} = \mathbf{0}\,, \tag{1.10}$$

$$\mathsf{\Sigma} = -P\mathsf{I} + \mu\left(2\beta\mathsf{E} + \frac{1-\beta}{\tau}\mathsf{A}\right)\,, \tag{1.11}$$

$$\overset{\nabla}{\mathsf{A}} = \frac{1}{\tau}(\mathsf{I} - \mathsf{A})\,, \tag{1.12}$$

$$\mathsf{E} = \frac{\nabla\boldsymbol{U} + [\nabla\boldsymbol{U}]^T}{2}\,, \tag{1.13}$$

$$\nabla \cdot \boldsymbol{U} = 0\,, \tag{1.14}$$

where β measures the relative contribution of the elastic and Newtonian contributions to the stress and the *conformation tensor* A measures the elastic strain. The Oldroyd–B fluid has a nonzero first normal stress difference N_1, but the second normal stress difference N_2 is zero.

For steady rectilinear flows such as Couette or Poiseuille flow which have a constant history, the velocity profile of an Oldroyd–B fluid is indistinguishable from that of a Newtonian fluid with viscosity μ. However, the stress will be different: energy can be stored and transported in A as elastic stress. This energy can drive an instability, even in the absence of inertia.

In extensional flow the Oldroyd–B model predicts an infinite extensional viscosity at a finite extension rate $\dot{\epsilon} = 1/2\tau$. This is unphysical and other models have been developed to correct this (discussed in sections 1.2.5 and 1.2.6).

Derivation of the Oldroyd–B equations

We follow the derivation found in Larson's book [51]. We model each polymer as a pair of beads of radius a joined by Hooke's law springs for which the restoring force $\boldsymbol{F}$ is directly proportional to the spring extension $\boldsymbol{R}$

$$\boldsymbol{F} = G\boldsymbol{R}\,, \tag{1.15}$$

where G is the spring constant. The beads move due to Brownian motion, the spring force, and the Stokes drag force. Different bead pairs do not interact. Performing an ensemble average (denoted $\langle\cdot\rangle$), the polymer stress is given by

$$\langle \boldsymbol{RF} \rangle = G\langle \boldsymbol{RR} \rangle \,, \tag{1.16}$$

which we define to be $G\mathsf{A}$.

The evolution of A can be shown to follow

$$\overset{\triangledown}{\mathsf{A}} = -\frac{1}{\tau}(\mathsf{A} - \mathsf{I}) \,.$$

The relaxation time τ is

$$\tau = 6\pi\mu_s a/G \,,$$

where μ_s is the solvent viscosity and the numerator is the Stokes drag coefficient on the bead.

This yields

$$\mathsf{\Sigma} = -P\mathsf{I} + 2\mu_s\mathsf{E} + G\mathsf{A} \,,$$

and an appropriate definition of μ and β in terms of μ_s, G and τ returns us to (1.11).

Equivalent forms of the Oldroyd–B equations

There are a number of equivalent expressions of the Oldroyd–B equations in common use. For reference, we show the equivalence between our model and several others.

- The most obviously equivalent form commonly used [103, 104, 105] involves a change in the equation for $\mathsf{\Sigma}$ only:

  $$\mathsf{\Sigma} = -P\mathsf{I} + 2\mu^*\mathsf{E} + \frac{C}{\tau}\mathsf{A} \,.$$

  This is equivalent to (1.11) under the substitution $\mu = \mu^* + C$ and $\beta = \mu^*/(\mu^* + C)$.

- A similar form [17, 84] is

$$\begin{aligned} \mathsf{\Sigma} &= -P\mathsf{I} + 2\mu\beta\mathsf{E} + (1-\beta)\mathsf{T}\,, \\ \mathsf{T} + \tau\overset{\nabla}{\mathsf{T}} &= 2\mu\mathsf{E}\,, \end{aligned}$$

  which is equivalent using $\mathsf{A} = \mathsf{I} + \tau\mathsf{T}/\mu$.

- A third alternate form [6] is

$$\begin{aligned} \mathsf{\Sigma} &= -P^*\mathsf{I} + \sigma^*\,, \\ \sigma^* + \lambda_1\overset{\nabla}{\sigma^*} &= 2\mu^*(\mathsf{E} + \lambda_2\overset{\nabla}{\mathsf{E}})\,, \end{aligned}$$

  where σ^* is the deviatoric stress and $0 \le \lambda_2 \le \lambda_1$. Setting

$$\begin{aligned} \tau &= \lambda_1\,, \\ \beta &= \frac{\lambda_2}{2\lambda_1 - \lambda_2}\,, \\ \mu &= \frac{2\mu^*}{1+\beta}\,, \\ P &= P^* + 2\mu^*/\lambda_1\,, \\ \mathsf{A} &= \frac{\lambda_1}{1-\beta}\left(\frac{\sigma^*(1+\beta)}{\mu^*} + \frac{1+\beta}{\lambda_1}\mathsf{I} - 2\beta\mathsf{E}\right) \end{aligned}$$

  returns us to the original form.

- Other variations exist, see for example [86].

The $\tau \to 0$ limit

The Oldroyd–B equations clearly describe a Newtonian fluid in the $\beta \to 1$ limit. However, it is less obvious, but frequently more useful, to note that they yield a Newtonian fluid in the $\tau \to 0$ limit, so long as $\boldsymbol{U}$ remains order 1. The physical meaning of this is that if the fluid relaxes instantaneously, it

behaves as a Newtonian fluid. To show this, we start from the constitutive equation (1.11)

$$\overset{\nabla}{\mathsf{A}} = \frac{1}{\tau}(\mathsf{I} - \mathsf{A})\,.$$

As $\tau \to 0$, we expand A in τ so that $\mathsf{A} = \mathsf{A}_1 + \tau\mathsf{A}_2 + \cdots$. At order $1/\tau$, we have $\mathsf{I} - \mathsf{A}_1 = 0$ and so $\mathsf{A}_1 = \mathsf{I}$. At next order, we get

$$\overset{\nabla}{\mathsf{I}} = -\mathsf{A}_2\,,$$

and using $\overset{\nabla}{\mathsf{I}} = -2\mathsf{E}$ we conclude $\mathsf{A}_2 = 2\mathsf{E}$.

Consequently the resulting stress is

$$\begin{aligned}\Sigma &= -P\mathsf{I} + 2\mu\beta\mathsf{E} + \mu\frac{1-\beta}{\tau}(\mathsf{I} + 2\tau\mathsf{E}) + \mathcal{O}(\tau)\,,\\ &= -\left(P - \frac{1-\beta}{\tau}\mu\right)\mathsf{I} + 2\mu\mathsf{E} + \mathcal{O}(\tau)\,.\end{aligned}$$

Thus redefining pressure by adding a constant everywhere, we arrive at the standard expression for Newtonian stress as $\tau \to 0$.

1.2.4 The Upper Convected Maxwell (UCM) fluid

The Upper Convected Maxwell (UCM) equations are the $\beta \to 0$ limit of the Oldroyd–B equations where the solvent contribution to the viscosity disappears. UCM fluids also become Newtonian as $\tau \to 0$. The governing equations neglecting inertia are

$$\begin{aligned}\nabla\cdot\Sigma &= \mathbf{0}\,,\\ \Sigma &= -P\mathsf{I} + \frac{\mu}{\tau}\mathsf{A}\,,\\ \overset{\nabla}{\mathsf{A}} &= \frac{1}{\tau}(\mathsf{I} - \mathsf{A})\,,\\ \nabla\cdot\boldsymbol{U} &= 0\,.\end{aligned}$$

1.2.5 The Finitely Extensible Nonlinear Elastic (FENE) fluid

The Oldroyd–B model is derived under the assumption that the polymers are infinitely extensible Hooke's law springs. Although this approximation is valid when the polymers are only mildly stretched from their equilibrium configuration, their behavior deviates from linear behavior as they are extended and unravelled. This leads to the Finitely Extensible Nonlinear Elastic (FENE) models.

We consider beads joined by a spring that has a nonlinear response to extension. We take

$$\boldsymbol{F} = G\boldsymbol{R}f(R)\,, \tag{1.17}$$

$$f(R) = \frac{1}{1 - R^2/l^2} = \frac{l^2}{l^2 - R^2}\,, \tag{1.18}$$

where $R^2 = \boldsymbol{R}\cdot\boldsymbol{R}$ and l represents a maximum extension. We cannot write a closed expression for the evolution of the elastic stress without a further approximation.

FENE–P

If we replace $\langle f(R)\rangle$ with $f(\langle R\rangle)$, known as the *pre-averaging* approximation, we find

$$\boldsymbol{F} = F\boldsymbol{R}f(\langle R\rangle)\,, \tag{1.19}$$

from which we arrive at the FENE–P [76] form of the elastic stress

$$\langle\boldsymbol{RF}\rangle = Gf(\langle R\rangle)\langle\boldsymbol{RR}\rangle\,. \tag{1.20}$$

The evolution of this stress can be written in closed form, and so we finally arrive at the FENE–P equations

$$\Sigma = -P\mathsf{I} + \mu\left(2\beta\mathsf{E} + \frac{1-\beta}{\tau}f(R)\mathsf{A}\right), \tag{1.21}$$

$$\overset{\triangledown}{\mathsf{A}} = -\frac{1}{\tau}[f(R)\mathsf{A} - I]. \tag{1.22}$$

This improves the extensional behavior from the Oldroyd–B model. However, it exhibits shear-thinning viscosity (*i.e.*, the shear viscosity μ decreases as $\dot{\gamma}$ increases). Consequently it is not a good model for the Boger fluid.

FENE–CR

The FENE–CR model of Chilcott and Rallison [20] uses the same form for the elastic stress, but changes its evolution. The equations are

$$\Sigma = -P\mathsf{I} + \mu\left(2\beta\mathsf{E} + \frac{1-\beta}{\tau}f(R)\mathsf{A}\right), \tag{1.23}$$

$$\overset{\triangledown}{\mathsf{A}} = -\frac{f(R)}{\tau}(\mathsf{A} - I). \tag{1.24}$$

This gives a constant shear viscosity.

1.2.6 Other models

A number of other models exist. Among the most popular are the Giesekus and Phan-Thien–Tanner fluids. These have more free parameters, allowing them to more accurately capture rheological behaviors such as shear-thinning.

The models discussed so far assume that the polymers do not interact. When instead the polymers are dense, the most successful models are based on the concept that a polymer must move parallel to its orientation, rather than transversely. This leads to different constitutive equations which more accurately model polymer melts.

More complete discussions of constitutive equations can be found in the book by Larson [51], the review by Bird and Wiest [8], or the books by Bird *et al.* [6, 7].

1.3 Observations of purely elastic instabilities

A large number of instabilities have been found in low Reynolds number elastic flows, driven by the energy stored in the elastic stress. Instabilities whose mechanism is due to elastic effects in the absence of inertia are referred to as *purely elastic*. What follows is a brief summary of a few purely elastic instabilities: more complete discussions can be found in the reviews by Larson [52] and Shaqfeh [86].

1.3.1 Flows with curved streamlines

Most known purely elastic instabilities occur in flows with curved streamlines where a *hoop stress* drives the instability. The hoop stress is caused by a tension in the streamlines which creates an inward force on a curved streamline. This acts in the opposite direction to inertia and many flows which are unstable at high Reynolds number due to centrifugal effects are unstable at low Reynolds number due to the hoop stress. This generates new instabilities which can develop into full-scale elastic turbulence at very small Reynolds number [33].

A number of elastic instabilities have been found in flows with curved streamlines. A rough criterion for instability is given by Pakdel and McKinley [74]. The best-known example is Taylor–Couette flow between two rotating concentric cylinders discussed by Larson, Shaqfeh, and Muller [71, 53, 87]. In these experiments, instabilities were seen with a Taylor number as small

as 10^{-7}.

Perhaps the most significant instability from a rheological point of view occurs in the cone-and-plate flow used to measure rheological properties. These flows can become unstable rendering the measurements invalid. This was initially mis-identified as shear-thickening behavior [45].

1.3.2 Flows with straight streamlines

Single fluid

There is little experimental evidence for a purely elastic instability in a single fluid with straight streamlines. A study by Yesilata [108] of low Reynolds number flow through a pipe found evidence of pressure fluctuations which were interpreted as the result of an instability. However, the method used to measure pressure introduces locally curved streamlines, and it is not clear that this is not causing the instabilities being measured.

Multiple fluids

It is well-known from industrial applications that even at low Reynolds number coextrusion flow of viscoelastic fluids can be unstable beyond a threshold extrusion rate. There are numerous experimental studies of these instabilities in planar flows.

Han and Shetty [34, 35] considered extrusion flows of three or five symmetric layers of polymer melts. They found conditions for instability based on wall shear stress and volume fraction. It is difficult to isolate the elastic effects from the viscous effects because their test fluids had different viscosities as well as different elasticities.

Mavridis and Shroff [66] considered three-layer symmetric flow of melts. They also found instability, but once more it is difficult to distinguish elastic from viscous effects.

Khomami and coworkers have performed a careful study of two-layer flows [49, 48, 100, 101, 102]. They observe the growth of instabilities during the flow through a transparent die. They have found that the Oldroyd–B equations predict the qualitative stability behavior observed, both in the linear and weakly-nonlinear regime.

Valette *et al.* [96, 97, 98, 99] have also performed two-layer coextrusion studies. They primarily observe instabilities by hardening the observing the interface after extrusion, but also use a transparent die to observe the flow. They find that long-wave asymptotic analysis gives a good prediction of the occurrence of instabilities, but do find some instabilities in flows predicted to be stable.

These experiments conclusively show that viscoelastic fluids can experience instability at low Reynolds number, and the elasticity ratio, the viscosity ratio and the depth ratio play an important role in determining whether the flow is stable or unstable.

It is difficult to make other general conclusions from these studies. They use a wide range of fluids which may or may not shear thin. There do not appear to be many careful studies isolating the elastic effects.

1.4 Theoretical study of extrusion flow

A number of theoretical studies have been made of inertialess coextrusion flow in a channel or a pipe. Most of these consider the UCM or Oldroyd–B equations and use a linear stability analysis (discussed further in section 2.1), although some nonlinear effects have been considered.

In studying the stability of a channel flow $\boldsymbol{U} = (U(y), 0, 0)$ in (x, y, z) coordinates with an interface at a fixed value of y, we assume a Squire's theorem [90]. Squire's theorem states that, in a two-dimensional flow of a Newtonian fluid the most unstable disturbance is always two-dimensional

and so three-dimensional perturbations may be ignored. We assume Squire's theorem applies to our flow and neglect the transverse z-direction. The jump in N_2 at the interface then disappears from the analysis. However, in core-annular pipe flow it is known to affect the growth rate [38] at least for small k.

The assumption of a Squire's theorem is tenuous. For the case of planar channel flow $\boldsymbol{U} = (U(y), 0, 0)$, Squire's theorem holds for the UCM fluid [94], even if there is an interface [84]. However, if $N_2 \neq 0$, it fails in general [60]. Indeed a jump in N_2 at an interface can create an instability in the transverse z-direction [14]. However, the value of N_2 is generally small compared to N_1 (and is zero for the Oldroyd–B fluid), and so we assume that neglecting this direction is safe.

Although it is generally assumed that linear stability follows from having all eigenvalues decaying (with growth bounded away from zero), the usual theorems do not apply to the Oldroyd–B fluid. M. Renardy [81] showed that an Oldroyd–B fluid with all eigenvalues decaying is linearly stable.

1.4.1 Single fluid

Before discussing the effect of an interface on the stability problem, we briefly discuss results for a single fluid.

The work of Ho and Denn [39] showed that channel Poiseuille flow of an inertialess UCM fluid is linearly stable to sinuous modes. This analysis was extended by Lee and Finlayson [55] who numerically considered varicose modes as well as modes of Couette flow. They also found linear stability for inertialess flows. Gorodtsov and Leonov [31] analytically studied Couette UCM flow, showing no unstable eigenvalues at zero Reynolds number, but claiming an instability at arbitrarily small Reynolds number. Renardy and Renardy [82] extended their results to larger Reynolds number, but showed

that the instability result was incorrect. Other models have also been studied, generally showing stability (see *e.g.*, [11]) but Grillet *et al.* [32] have found an instability in Couette and Poiseuille flow of a Phan-Thien–Tanner fluid and Poiseuille flow of a Giesekus fluid and Wilson and Rallison [105] found an instability due to shear-thinning effects in White–Metzner fluids.

Numerical simulations by Atalik and Keunings [2] found a finite amplitude nonlinear instability of Poiseuille and Couette channel flow for Oldroyd–B fluids at small values of β. Simultaneously, Saarloos and coworkers [68, 69, 70] have developed amplitude equations suggesting a subcritical bifurcation at infinite Wi which allows the flow to be unstable to a finite amplitude instability at finite Wi. This contrasts with a result of Ghisellini [30] who claimed a rigorous proof of stability based on energy principles. However, recent work by Doering *et al.* [22] suggests that no reasonable "energy" functional defined for the Oldroyd–B fluid can be shown to decrease monotonically in time. Indeed, Ghisellini proved only that the Couette and Poiseuille flow minimize a functional and did not show that that functional is monotonically decreasing.

A final comment should be made about Boffetta *et al.* [10] who studied Kolmogorov flow [$U(y) = \cos(y)$] for the Oldroyd–B fluid in an unbounded planar domain. They consider a nonzero Reynolds number and find an instability that is distinct from the inertial instability. This instability persists for arbitrarily small Reynolds numbers, but they do not report growth rates. It is unclear if the growth rate is bounded away from zero as $Re \to 0$.

1.4.2 Multiple fluids

It is well-known that differences in viscosity can lead to interfacial instabilities in Newtonian shear flow at arbitrarily small Reynolds number [36, 40, 109]. In the case of matched viscosities the two fluids are indistinguishable and the flow is stable. By modifying the temperatures of coextruded fluids, it is

possible to match their viscosities, eliminating the viscous instability [72].

Early theoretical work of Waters and Keeley suggested that the elasticity stratification does not affect the stability at leading order for long-waves. However, Renardy [84] showed the incongruous result that it does affect the leading order stability problem for short-waves. Shortly thereafter, Chen [15, 16] found a long-wave instability and showed that the original paper of Waters and Keeley applied an incorrect boundary condition that neglects the jump in base normal stress at the interface. Hinch *et al.* [38] explained the mechanism of the long-wave instability, showing how the jump in normal stress drives the flow when the wavelength is long compared to the channel width and the relaxation length scale. A flurry of other papers have followed [17, 18, 27, 28, 29, 54, 57, 84, 85, 103, 104, 106], and it is now generally believed that the driving force behind purely elastic interfacial instabilities is the jump in normal stress (see *e.g.*, [57]).

The available parameter space is large and has not been fully explored. As well as having multiple flow profiles or fluid models to consider, the fluids may have different viscosities, different elastic relaxation times, different values of β, or different values of any other parameter in the model. In this work, we assume that the fluids are identical except for the relaxation time. We find that even in this reduced space, the present understanding is incomplete, instabilities have been missed, and there are inaccuracies in the literature.

The previous short-wave and long-wave analysis has implicitly assumed that the wavelength is short or long compared to all length scales. In the Oldroyd–B or UCM model there is an additional length scale $U\tau$ which measures the distance travelled by the fluid in a relaxation time. This introduces the possibility of other limits, for example $U\tau \ll k^{-1} \ll L$ and $L \ll k^{-1} \ll U\tau$. In the former case the Weissenberg number $Wi = U\tau/L$ is small and elastic effects are weak. The work of Renardy [84] for two UCM fluids with matched viscosity but differing relaxation times or the work of

Wilson and Rallison [104] for Oldroyd–B fluids both still apply to this case. Instability is found whenever the relaxation times differ. In the latter case, the assumptions of previous work fail, and it is on this limit that part I of this dissertation focuses.

1.5 Instability classes

In this dissertation we extend previous work on interfacial instabilities. We find that for Couette flow it is generally most appropriate to classify the instabilities based on their longest length scale. This gives three regimes: *long-wave* for which the wavelength is the longest, *fast-flow* for which the distance travelled in a relaxation time is the longest, and *wide-channel* for which the channel width is the longest. There is a further regime in Poiseuille flow, *narrow-core* for which the relaxation length scale is the longest length scale, but the interface is close to the center-line. There are a few instabilities which we find that do not fit into any of these classes.

Under this classification, the short-wave instabilities studied previously are broken into the fast-flow and wide-channel regimes. We find that similar instabilities are observed in fast-flow or wide-channel even when the wavelength is not the shortest length scale.

In this section we describe previous results for pipe and channel coextrusion flows in the context of this classification and briefly mention some main results from later chapters.

1.5.1 Long-wave: $k^{-1} \gg U\tau, L$

The long-wave limit of core-annular pipe flow is understood from previous work by Chen [16] as well as Hinch *et al.* [38]. The flow is unstable to axisymmetric long-wave modes if the core occupies less than 32% of the pipe

volume and is more elastic or occupies more than 32% and is less elastic. The flow is unstable to cork-screw long-wave modes if the annulus is more elastic. As explained by Hinch *et al.*, the result is general and applies to fluids other than just Oldroyd–B and UCM, but the results are modified if N_2 is nonzero.

The channel flow results were found by Wilson and Rallison [103] and Ganpule and Khomami [27]. In channel Couette flow, instability occurs if the more elastic fluid (*i.e.*, the fluid with the longer relaxation time and hence the larger elastic stress) occupies less than half the channel. In contrast, for three-layer symmetric channel Poiseuille flow, varicose instability is found when the inner fluid is more elastic (has a longer relaxation time) and the fraction of the channel occupied by the inner fluid is less than $\sqrt{2}-1$ or the inner fluid is less elastic and occupies more than $\sqrt{2}-1$. Sinuous instability occurs if the outer fluid is more elastic. This is qualitatively like the pipe result.

1.5.2 Wide-channel: $L \gg k^{-1}, U\tau$

Renardy [84] studied UCM interfacial flows where the wavelength is the smallest length scale. The perturbation flow decays exponentially away from the interface and the walls can be neglected, using instead the assumption that the flow tends to zero at infinity. She found different behaviors for small and large values of $\mathcal{W}\!\!\!/$. The large $\mathcal{W}\!\!\!/$ limit corresponds to "fast-flow" and is discussed below. In the small $\mathcal{W}\!\!\!/$ limit, $L \gg U\tau \gg k^{-1}$, she found that if the two fluids had different relaxation times, there would be instability.

Wilson and Rallison [103, 104] studied Oldroyd–B interfacial flows with the wavelength the smallest length scale. They also found that the perturbation flow decays away from the interface. In the small $\mathcal{W}\!\!\!/$ limit they found instability if the fluids have different relaxation times.

We find that if $L \gg k^{-1} \gg U\tau$, the perturbation still decays exponentially away from the interface, although k^{-1} is no longer the smallest length scale. The techniques used previously can be applied and the same results are found (section 3.7).

1.5.3 Fast-flow: $U\tau \gg k^{-1}, L$

Renardy [84] showed that in UCM flows if $U\tau \gg L \gg k^{-1}$ then instability occurs if the ratio ξ of the two relaxation times satisfies $\xi_c < \xi < \xi_c^{-1}$ and $\xi \neq 1$ where $\xi_c \approx 0.27688$. Wilson and Rallison [103, 104] showed that the range of ξ leading to instability increases as β grows. Eventually all $\xi \neq 1$ give instability. Both the UCM and Oldroyd–B results were derived assuming that the perturbation flow decays away from the interface.

The assumption that the flow decays before reaching the wall does not hold if $U\tau \gg k^{-1} \gg L$. The perturbation flow is as large close to the wall as close to the interface, and so the analysis of Renardy fails. However, in chapter 3 we show that for UCM fluids the growth rates are the same as those found by Renardy. For Oldroyd–B we also find similar results to Wilson and Rallison.

We further show that the mechanism of this instability does not depend on interfacial displacement and the jump in the first normal stress, contradicting some literature assumptions. Consequently surface tension cannot stabilize the instability.

1.5.4 Narrow-core: $U\tau \gg k^{-1}, L$ and $\Delta \sim 1/\sqrt{U\tau k}$

The narrow-core regime occurs in Poiseuille flow when the interface location (relative to the center-line) ΔL is comparable to or smaller than $L/\sqrt{U\tau k}$. This scaling results from a balance between U'/U'' and $1/U'\tau k$ at ΔL. In chapters 4 and 5 we find a distinct *narrow-core* regime when $U''/\tau k U'^2 =$

$\mathcal{O}(1)$ at the interface in both channel and pipe flow.

In order to understand the scaling better, we consider why the fast-flow behavior fails. In the fast-flow regime, a boundary layer with characteristic width $1/U'\tau k$ plays an important role. This width is derived under the assumption that the shear rate is effectively constant. The boundary layer structure (and hence the stability properties) changes if the local shear rate U' is not effectively constant throughout the boundary layer.

The length scale U'/U'' is the length over which the shear rate changes by an amount comparable to the shear rate. If this length is comparable to or smaller than the boundary layer width a new regime occurs. We find a number of instabilities in this regime, some of which exist when both $k \to \infty$ and $k \to 0$ limits are stable, contradicting claims of [54, 85].

1.5.5 Other

There are instabilities which do not fit into any of these categories. We do not attempt a full analysis of these instabilities, but mention them in passing when they arise.

1.6 Scope of this dissertation

The dissertation is divided into two parts. The first studies coextrusion stability in the limit of large Weissenberg number and small Reynolds number. For a flow with length scale L, $Wi \propto L^{-1}$ while $Re \propto L$, and so this limit is most readily found for narrow flows. The second part studies the effect of elasticity on a high Reynolds number jet.

Part I is divided into five chapters. Chapter 2 derives the equations used in the remaining chapters. Chapter 3 studies the stability of a single interface in planar Couette channel flow. Chapter 4 studies the stability of

three-layer symmetric planar Poiseuille flow. Chapter 5 studies the extension of the planar results into a cylindrical core-annular pipe geometry. Chapter 6 concludes the discussion of coextrusion flow.

Part II has just one chapter, chapter 7. This chapter introduces the equations of an elastic jet and briefly discusses related work in different types of fluids, it presents results of linear stability analysis for elasticities of varying strengths and finally discusses the weakly nonlinear evolution of cat's eyes in the presence of weak elasticity.

Part I

Elastic coextrusion flows

Chapter 2

Linear perturbation equations for coextrusion flow

In this chapter we discuss and derive the linear perturbation equations needed later in the study of coextrusion flow. We first summarize the principles of linear stability analysis in section 2.1. We then introduce the governing equations in section 2.2 and derive the linearized equations for the growth of perturbations of planar Couette and three-layer symmetric planar Poiseuille flow (section 2.3) as well as the linear perturbation equations for core-annular pipe flow (section 2.4). We briefly discuss the structure of the continuous and discrete parts of the spectrum in section 2.5. Finally, in section 2.6 we discuss the numerical methods used to solve the linearized equations and the effect of the continuous spectrum on the ability of the numerics to find nearby discrete eigenvalues.

2.1 Linear stability analysis

To study the stability of a base flow, we assume that the flow looks like the base flow plus a small (order ϵ) perturbation. We then derive the equations

governing the evolution of the perturbations through expansions in ϵ. Representing the perturbed variables by the vector $\boldsymbol{\phi}$, we derive an equation of the form

$$\boldsymbol{\mathcal{L}}_1[\boldsymbol{\phi}] + \frac{\partial}{\partial t}\boldsymbol{\mathcal{L}}_2[\boldsymbol{\phi}] = \boldsymbol{\mathcal{N}}(\boldsymbol{\phi})\,,$$

where $\boldsymbol{\mathcal{L}}_1$ and $\boldsymbol{\mathcal{L}}_2$ are linear operators, and $\boldsymbol{\mathcal{N}}$ is nonlinear. All of these may depend on spatial derivatives and a control parameter (or parameters) R.

A fundamental assumption of this work is that the expansion of $\boldsymbol{\phi}$ in ϵ is well-behaved and so higher order terms $\boldsymbol{\mathcal{N}}$ can be dropped safely. This is not always the case, and plays a role in the failure of linear theory to predict the Reynolds number of the onset of turbulence in Couette or Poiseuille flow of Newtonian fluids. In this work we assume that the expansions are well-behaved.

2.1.1 Linear analysis techniques

We choose our base flow to be steady and hence translation invariant in time. We also take it to be translation invariant in one spatial direction x. Considering the invariance in these dimensions, we search for small perturbations in the form of waves that travel in the x-direction.

In order to determine the stability of a base flow to arbitrarily small disturbances, we use a linear stability analysis. If $\boldsymbol{\phi} = \epsilon\boldsymbol{\phi}_1 + \mathcal{O}(\epsilon^2)$, then $\boldsymbol{\mathcal{N}}$ is $\mathcal{O}(\epsilon^2)$ or smaller. Substituting the base flow plus $\boldsymbol{\phi}$ into the full equations, we expand them in ϵ. The $\mathcal{O}(1)$ terms cancel exactly. We neglect $\mathcal{O}(\epsilon^2)$ terms leaving just terms which are linear in the perturbation variables. This gives an equation of the form

$$\boldsymbol{\mathcal{L}}_1(R, \partial_x, \partial_y)[\boldsymbol{\phi}_1] + \frac{\partial}{\partial t}\boldsymbol{\mathcal{L}}_2(R, \partial_x, \partial_y)[\boldsymbol{\phi}_1] = 0\,.$$

This equation can be solved through separation of variables. Seeking a solu-

tion of the form $\boldsymbol{\phi}_1(x,y,t) = \boldsymbol{\psi}_1(y)\exp(ikx - i\omega t) + cc$ we find

$$\boldsymbol{\mathcal{L}}_1(R, ik, \partial_y)[\boldsymbol{\psi}_1] - i\omega\boldsymbol{\mathcal{L}}_2(R, ik, \partial_y)[\boldsymbol{\psi}_1] = 0\,.$$

For fixed k only particular values of ω, the eigenvalues, yield a nontrivial solution $\boldsymbol{\psi}_1$. The values of ω are generally found through numerical methods described later.

If the imaginary part of ω is positive, the mode experiences exponential growth in time for arbitrarily small perturbations: the flow is unstable. Perturbations grow until the nonlinear terms become important. To understand the further growth, a nonlinear analysis is required.

Even if the imaginary parts of all eigenvalues ω are negative, we do not have a guarantee of stability. Turbulence in a pipe or channel is well-known to occur in flows that are linearly stable. Given sufficiently large initial disturbances, the nonlinear terms may be large enough to prevent the solution from returning to the base state, leading to *finite amplitude instability*. Alternately, the existence of two (or more modes) with similar eigenfunctions may result in transient growth so that even a small initial disturbance is amplified until the nonlinear terms become important [95]. Finally, in systems with infinitely many eigenvalues converging to a limit point, the transient growth noted above may continue indefinitely. If the linearization does not provide an analytic semigroup (as is the case for models of elastic fluids with memory such as Oldroyd–B) then all eigenvalues having negative imaginary part does not guarantee linear stability (see example 4.2 of Pazy [75]). M. Renardy has shown that linear stability for a single Oldroyd–B fluid follows from all eigenvalues having negative imaginary part [81].

Note that this stability analysis assumes that the perturbation is uniform in space, and grows in time. That is, we perform a temporal stability analysis. We could perform a spatial stability analysis, in which time and space interchange roles. We would fix ω real and find complex values of k. If k has

negative imaginary part, then perturbations grow downstream. We consider only temporal stability.

2.2 The equations of motion

Our flows satisfy the inertialess incompressible Oldroyd–B equations (1.10)–(1.14). At walls they satisfy no-slip conditions

$$\boldsymbol{U} = \boldsymbol{U}_{\text{wall}} \,. \tag{2.1}$$

At interfaces they satisfy continuity of velocity

$$[\![\boldsymbol{U}]\!] = \boldsymbol{0} \,, \tag{2.2}$$

where $[\![\cdot]\!]$ denotes a jump in the bracketed quantity across the interface. There may be surface tension at the interface. The flows satisfy the condition that there can be no net force acting on the (massless) interface

$$[\![\Sigma]\!] \cdot \boldsymbol{N} = \gamma\kappa\boldsymbol{N} \,, \tag{2.3}$$

where $\boldsymbol{N}$ is the unit normal into the upper (or outer) fluid, γ is the coefficient of surface tension and $\kappa = \nabla \cdot \boldsymbol{N}$ is the curvature of the interface. The interface is a material surface, and so moves with the local velocity. Pipe flows satisfy an additional constraint that they be regular at the center.

2.3 Planar channel flows

The base flow profiles we study in a planar channel are two-layer Couette flow, shown in figure 2.1(a), and three-layer symmetric Poiseuille flow (the planar analogue of core-annular pipe flow), shown in figure 2.1(b). We derive our equations in a general form applicable to both flows before specializing our equations to each.

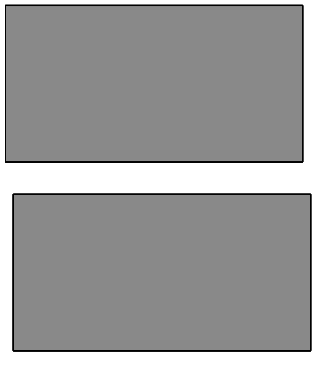

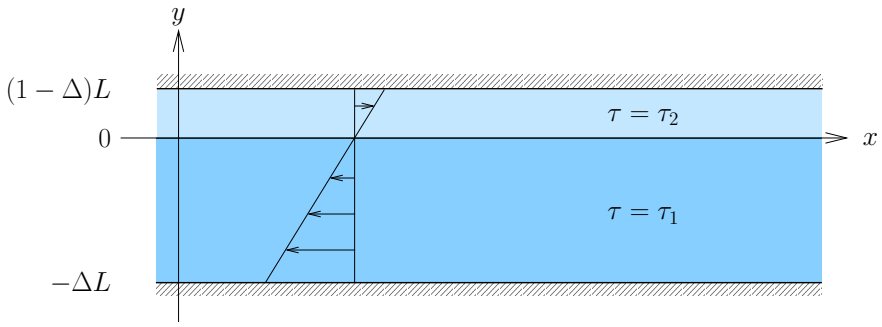

(a) Two elastic fluids in Couette flow $U = U_0 y/L$ through a channel. The fluids differ only in relaxation time τ.

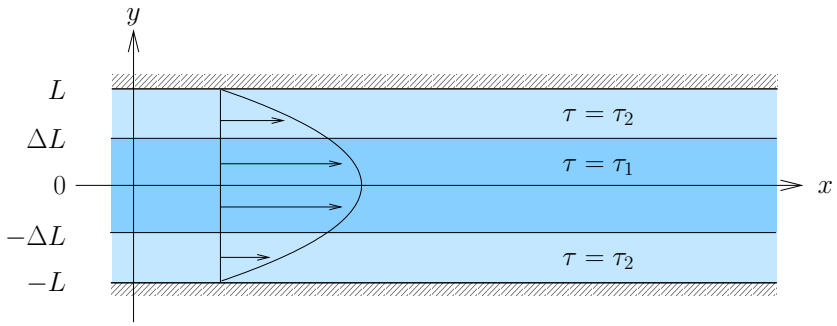

(b) Two elastic fluids in Poiseuille flow $U = U_0(1 - y^2/L^2)$ through a channel. The fluids differ only in relaxation time τ.

Figure 2.1: Two-dimensional base flows.

The velocity profile is $\boldsymbol{U} = (U(y), 0)$ with $U(y)$ given by $U(y) = U_0 y/L$ for Couette flow and $U(y) = U_0(1 - y^2/L^2)$ for Poiseuille flow, where L measures the width of the channel for Couette flow or the half-width for Poiseuille flow and y is the cross-channel coordinate. In steady rectilinear flow the history of a material particle is constant and $(\partial_t + \boldsymbol{U} \cdot \nabla)\mathsf{A} = \mathsf{0}$. Thus equation (1.12)

gives

$$\mathsf{A} = \begin{pmatrix} 1 + 2\tau^2 U'^2 & \tau U' \\ \tau U' & 1 \end{pmatrix} .$$

From this we observe that the elastic stress includes an isotropic component which behaves like pressure as well as a difference in the normal stresses, $A_{11} - A_{22} \neq 0$.

For the base flow the unit normal is $\boldsymbol{N} = (0, 1)$ and the curvature is zero. The condition $(\llbracket \Sigma \rrbracket \cdot \boldsymbol{N})_2 = 0$ implies that $-P + (1 - \beta)\mu/\tau$ is continuous at the interface, and so there is a jump in P across the interface to balance the jump in $1/\tau$. There is a discontinuity of Σ_{11} at the interface, where the value jumps by $2\mu(1 - \beta)U'^2(\tau_2 - \tau_1)$.

For Couette flow, symmetry allows us to assume $\tau_1 \geq \tau_2$ without loss of generality, but we cannot make a similar assumption for Poiseuille flow.

2.3.1 Linear equations

We consider the effect of infinitesimal disturbances to the flow. These disturbances change the velocity field $\boldsymbol{U}$, the stresses Σ and (in general) the interface location. We use lower case letters $\boldsymbol{u}$, σ, e, a, and δ to denote the complex perturbation to the velocity, stress, rate-of-strain tensor, elastic strain, and interface location respectively. We take the corresponding physical variables to be the real parts.

Because the base flow is independent of x and t, we make the standard linear assumption that the perturbation quantities are small and proportional to $\exp(ikx - i\omega t)$. We introduce a streamfunction, taking $\boldsymbol{u} = (\mathrm{D}\psi, -ik\psi)$ to satisfy incompressibility automatically, where 'D' denotes differentiation with respect to y.

The perturbed stress σ satisfies

$$\sigma = -p\mathsf{I} + \mu \left(2\beta\mathsf{e} + \frac{1 - \beta}{\tau}\mathsf{a} \right) ,$$

where p is the perturbation to the pressure, a is the perturbation to A and the perturbation to the rate of strain is

$$\mathsf{e} = \begin{pmatrix} ik\mathrm{D}\psi & (\mathrm{D}^2+k^2)\psi/2 \\ (\mathrm{D}^2+k^2)\psi/2 & -ik\mathrm{D}\psi \end{pmatrix}.$$

The perturbed momentum equation $\nabla\cdot\sigma = \mathbf{0}$ gives

$$ik\sigma_{11} + \mathrm{D}\sigma_{12} = 0\,, \tag{2.4}$$

$$ik\sigma_{12} + \mathrm{D}\sigma_{22} = 0. \tag{2.5}$$

Taking the curl of the momentum equation and substituting for σ we find the vorticity equation

$$\beta(\mathrm{D}^2-k^2)^2\psi + \frac{1-\beta}{\tau}[ik\mathrm{D}(a_{11}-a_{22}) + (\mathrm{D}^2+k^2)a_{12}] = 0\,. \tag{2.6}$$

The perturbation to the constitutive equation (1.12) gives

$$\alpha a_{11} = 2U'a_{12} + 2(1+2\tau^2U'^2)ik\mathrm{D}\psi + 2\tau U'\mathrm{D}^2\psi + 4\tau^2U'U''ik\psi\,, \tag{2.7}$$

$$\alpha a_{12} = U'a_{22} + \mathrm{D}^2\psi + (1+2\tau^2U'^2)k^2\psi + ik\tau U''\psi\,, \tag{2.8}$$

$$\alpha a_{22} = 2k^2\tau U'\psi - 2ik\mathrm{D}\psi\,, \tag{2.9}$$

where $\alpha = -i\omega + ikU + 1/\tau$. At first glance the $\beta\to 0$ limit of (2.6) appears to lose its leading derivative of ψ. However, the D^2a_{12} term contains $(\mathrm{D}^4\psi)/\alpha$ and so the limit is not singular.

The no-slip boundary conditions (2.1) give

$$\psi = \mathrm{D}\psi = 0 \tag{2.10}$$

at the walls.

The interface is a material element, so δ satisfies

$$[-i\omega + ikU]\delta = -ik\psi\,, \tag{2.11}$$

where U and ψ are evaluated at the location of the unperturbed interface. Finally, the conditions at the interface (2.2), (2.3) give

$$[\![\psi]\!] = 0\,, \tag{2.12}$$

$$[\![\mathrm{D}\psi]\!] = 0\,, \tag{2.13}$$

$$\left[\!\!\left[\beta \mathrm{D}^2\psi - 2ikU'^2\tau(1-\beta)\delta + \frac{1-\beta}{\tau}a_{12}\right]\!\!\right] = 0\,, \tag{2.14}$$

$$\left[\!\!\left[\beta\frac{i}{k}\mathrm{D}^3\psi + \frac{1-\beta}{\tau}\left(\frac{i}{k}\mathrm{D}a_{12} - a_{11} + a_{22}\right)\right]\!\!\right] = \frac{\gamma k^2}{\mu}\delta\,, \tag{2.15}$$

where we have used that fact that the perturbation to the normal to the interface is $\boldsymbol{n} = (-ik\delta, 0)$. These equations are equivalent to those of [104].

2.3.2 Two-layer Couette flow

The geometry of our Couette flow is shown in figure 2.1(a). For the base flow, $U' = U_0/L$ and $U'' = 0$.

Non-dimensionalization

We use asterisks to denote non-dimensional variables and choose a rescaling appropriate for $Wi = U_0\tau_1/L \gg 1$.

We non-dimensionalize each direction by a different length scale. In the $Wi \gg 1$ limit, the most appropriate measure of distance in the x-direction proves to be $U_0\tau_1$, the distance travelled in a relaxation time (of the lower fluid). This gives the non-dimensional wavenumber

$$k^* = U_0\tau_1 k\,.$$

For the cross-stream y-direction, we observe that fluid particles separated by $1/kWi$ in the vertical will be separated by a wavelength $2\pi k^{-1}$ in the horizontal after time $2\pi\tau_1$. We use this length scale to non-dimensionalize

the cross-stream direction, so

$$y^* = Wi\, ky\,.$$

A side-effect of the y rescaling is that the wall position scales with k. This choice of length scales differs from that used in previous work [17, 84, 104].

We rescale time with τ_1 and so

$$\tau_1^* = 1\,, \qquad \tau_2^* = \xi \equiv \tau_2/\tau_1\,.$$

Without loss of generality $0 \leq \xi \leq 1$. The values of ω and α become

$$\begin{aligned}\omega^* &= \tau_1\omega\,,\\ \alpha_{1,2}^* &= \tau_1\alpha_{1,2} = -i\omega^* + iy^* + 1/\tau_{1,2}^*\,.\end{aligned}$$

It is convenient to non-dimensionalize ψ to be

$$\psi^* = \psi k^2\tau_1 = k^{*2}\frac{\psi}{U_0^2\tau_1}\,,$$

in which case

$$\delta^* = k\delta\,.$$

Note that δ is non-dimensionalized with respect to a different length scale from either x or y.

The corresponding pressure is

$$p^* = Wi^{-3}p\tau_1/\mu\,.$$

The a_{ij} are already dimensionless, but they are not $\mathcal{O}(1)$ as Wi grows. To ensure they appear at the correct order in the equations we set

$$\begin{aligned}a_{11}^* &= Wi^{-3}a_{11}\,,\\ a_{12}^* &= Wi^{-2}a_{12}\,,\\ a_{22}^* &= Wi^{-1}a_{22}\,.\end{aligned}$$

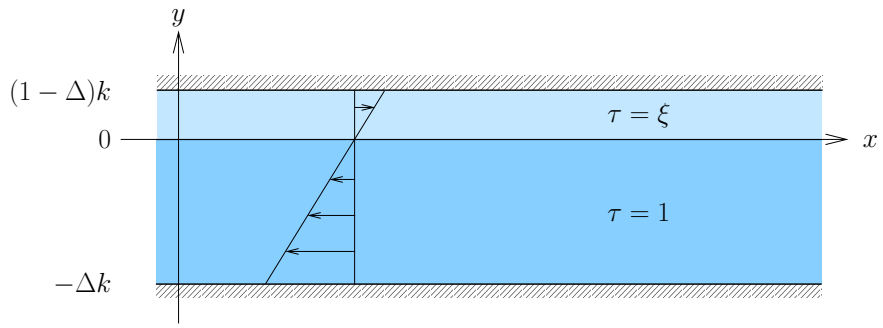

Figure 2.2: The Couette flow profile $U = y/k$ in non-dimensional variables.

The capillary number is given by $Ca \equiv U_0\mu/\gamma$. We define the dimensionless surface tension coefficient by

$$\gamma^* = Ca^{-1}Wi^{-3}\,.$$

As $Wi \to \infty$, γ^* tends to zero unless $Ca = \mathcal{O}(Wi^{-3})$.

Linear equations

We now drop the asterisks on the variables. The dimensionless flow profile is given in figure 2.2.

The dimensionless momentum equations (2.4) and (2.5) are now

$$-p + Wi^{-2}2\beta \mathrm{D}\psi + \frac{1-\beta}{\tau}a_{11} - i\mathrm{D}\left(\beta(\mathrm{D}^2 + Wi^{-2})\psi + \frac{1-\beta}{\tau}a_{12}\right) = 0\,, \tag{2.16}$$

$$\beta(\mathrm{D}^2 + Wi^{-2})\psi + \frac{1-\beta}{\tau}a_{12} - i\mathrm{D}\left(-Wi^2 p - 2i\beta\mathrm{D}\psi + \frac{1-\beta}{\tau}a_{22}\right) = 0\,. \tag{2.17}$$

The vorticity equation (2.6) becomes

$$\beta\left(\mathrm{D}^2 - \frac{1}{Wi^2}\right)^2\psi + \frac{1-\beta}{\tau}\left[i\mathrm{D}\left(a_{11} - \frac{a_{22}}{Wi^2}\right) + \left(\mathrm{D}^2 + \frac{1}{Wi^2}\right)a_{12}\right] = 0\,. \tag{2.18}$$

The constitutive equations (2.7)–(2.9) are

$$\alpha a_{11} = 2a_{12} + 2i(2\tau^2 + Wi^{-2})\mathrm{D}\psi + 2\tau\mathrm{D}^2\psi\,, \tag{2.19}$$

$$\alpha a_{12} = a_{22} + (2\tau^2 + Wi^{-2})\psi + \mathrm{D}^2\psi\,, \tag{2.20}$$

$$\alpha a_{22} = 2\tau\psi - 2i\mathrm{D}\psi\,, \tag{2.21}$$

with $\alpha = -i\omega + iy + 1/\tau$. The interfacial conditions (2.12)–(2.15) at $y = 0$ become

$$[\![\psi]\!] = 0\,, \tag{2.22}$$

$$[\![\mathrm{D}\psi]\!] = 0\,, \tag{2.23}$$

$$-2i(1-\beta)\,[\![\tau]\!]\,\delta + \beta\,[\![\mathrm{D}^2\psi]\!] + (1-\beta)\,[\![a_{12}/\tau]\!] = 0\,, \tag{2.24}$$

$$\left[\!\!\left[i\beta\mathrm{D}^3\psi + \frac{1-\beta}{\tau}\left(i\mathrm{D}a_{12} + \frac{a_{22}}{Wi^2} - a_{11}\right)\right]\!\!\right] = \gamma k\delta\,. \tag{2.25}$$

In our frame of reference, the base flow velocity is zero at the interface, so the perturbed interface location equation (2.11) becomes

$$\delta = \psi/\omega\,. \tag{2.26}$$

The no-slip boundary conditions (2.10) at the walls become

$$\psi = \mathrm{D}\psi = 0 \quad \text{at} \quad y = (1-\Delta)k,\ -\Delta k\,. \tag{2.27}$$

The wall locations explicitly depend on k. The only other appearance of the wavenumber k is in the surface tension term in (2.25).

Equations (2.18)–(2.27) define the dimensionless eigenvalue problem. The dimensionless parameters that remain are k, ξ, β, Δ, Wi and γ and so in general $\omega = \omega(k, \xi, \beta, \Delta, Wi, \gamma)$. We are primarily interested in the large Wi limit. Equation (2.18) suggests that this is a regular limit, and that the neglected terms are $\mathcal{O}(Wi^{-2})$. Section 3.1 shows more clearly that this limit is regular. Because $\gamma = Ca^{-1}Wi^{-3}$, the surface tension is negligibly small at large Wi unless $Ca = \mathcal{O}(kWi^{-3})$.

Linear equations for $Wi \gg 1$

At large Wi, the momentum equations become

$$i\left(-p + \frac{1-\beta}{\tau}a_{11}\right) + \mathrm{D}\left(\beta \mathrm{D}^2\psi + \frac{1-\beta}{\tau}a_{12}\right) = 0\,, \tag{2.28}$$

$$\mathrm{D}p = 0\,. \tag{2.29}$$

The vorticity equation becomes

$$\beta \mathrm{D}^4\psi + \frac{1-\beta}{\tau}\left(i\mathrm{D}a_{11} + \mathrm{D}^2 a_{12}\right) = 0\,. \tag{2.30}$$

We find that the y-momentum equation is satisfied provided that the perturbation pressure p is uniform across the channel from (2.29). This reflects the fact that the relaxation length scale is large compared to the channel width. The vorticity equation (2.30) can be integrated once, the constant of integration being the x-dependent pressure gradient along the channel, and so the flow is governed by the x-momentum equation (2.28). The constitutive equations are

$$\alpha a_{11} = 2a_{12} + 4i\tau^2 \mathrm{D}\psi + 2\tau \mathrm{D}^2\psi\,, \tag{2.31}$$

$$\alpha a_{12} = a_{22} + 2\tau^2\psi + \mathrm{D}^2\psi\,, \tag{2.32}$$

$$\alpha a_{22} = 2\tau\psi - 2i\mathrm{D}\psi\,, \tag{2.33}$$

where $\alpha = -i\omega + iy + 1/\tau$. The interfacial conditions become

$$[\![\psi]\!] = 0\,, \tag{2.34}$$

$$[\![\mathrm{D}\psi]\!] = 0\,, \tag{2.35}$$

$$-2i(1-\beta)\,[\![\tau]\!]\,\delta + \beta\,[\![\mathrm{D}^2\psi]\!] + (1-\beta)\,[\![a_{12}/\tau]\!] = 0\,, \tag{2.36}$$

$$\left[\!\!\left[i\beta \mathrm{D}^3\psi + \frac{1-\beta}{\tau}\left(i\mathrm{D}a_{12} - a_{11}\right)\right]\!\!\right] = \gamma k\delta\,. \tag{2.37}$$

We keep the surface tension term $\gamma k\delta$ for use in section 3.4 where we consider the possibility that $k\gamma = kCa^{-1}Wi^{-3}$ is not small. Elsewhere we take $\gamma = 0$.

The displacement of the perturbed interface remains

$$\delta = \psi/\omega\,, \tag{2.38}$$

and the no-slip boundary conditions at the walls remain

$$\psi = \mathrm{D}\psi = 0 \quad \text{at} \quad y = (1-\Delta)k,\ -\Delta k\,. \tag{2.39}$$

2.3.3 Three-layer symmetric Poiseuille flow

The geometry of our Poiseuille flow is shown in dimensional terms in figure 2.1(b). For the base flow, $U' = -2yU_0$ and $U'' = -2U_0$. We neglect surface tension at the interface, so $\gamma = 0$.

If the perturbation is sinuous, ψ is an even function while ψ is odd if the perturbation is varicose. If ψ is neither varicose nor sinuous, it can be expressed as a linear combination of a sinuous and a varicose mode. Therefore, we can restrict our attention to the upper half of the channel, replacing the no-slip condition at $y = -L$ by a symmetry condition at $y = 0$

$$\begin{aligned} \mathrm{D}\psi(0) = \mathrm{D}^3\psi(0) &= 0 \qquad \text{(sinuous)}, \\ \psi(0) = \mathrm{D}^2\psi(0) &= 0 \qquad \text{(varicose)}. \end{aligned}$$

Non-dimensionalization

In this section we again use asterisks to denote dimensionless quantities.

We are interested in two regimes. In one, the base flow is effectively Couette (in a sense made more precise in chapter 4), and in the other the variation in the base flow shear rate is significant. The dimensionless cross-stream lengths we use are

$$Y = \tau_1 k[U_0 - U(y)] \qquad (= \tau_1 k U_0 y^2/L^2)\,, \tag{2.40}$$

$$\eta = \frac{\sqrt{U_0\tau_1 k}}{L} y \qquad (= \sqrt{Y})\,. \tag{2.41}$$

Which variable is appropriate depends on whether the interface is close to the center-line or not. The Y equations are useful for finding analytical results when the interface is far from both the center-line and the wall so that both boundaries can be ignored. The η equations are more useful for numerical calculations and cases where the interface is close to the center-line.

We non-dimensionalize times by τ_1 so that the inner fluid has relaxation time $\tau_1^* = 1$. The outer fluid has relaxation time $\tau_2^* = \xi = \tau_2/\tau_1$. The complex frequency ω becomes $\omega^* = \tau_1\omega$, and α becomes $\alpha^* = \tau_1\alpha$.

In the x-direction, we non-dimensionalize with the length scale $U_0\tau_1$, representing the distance the fluid travels during a relaxation time. Thus

$$k^* = U_0\tau_1 k\,.$$

It is convenient to non-dimensionalize ψ so that

$$\psi^* = \psi k^2\tau_1 = k^{*2}\frac{\psi}{U_0^2\tau_1}\,.$$

The interface perturbation δ is non-dimensionalized with respect to k

$$\delta^* = k\delta\,.$$

The a_{ij} measuring elastic stress are already dimensionless, but for equations in terms of the Y variable, we rescale them as

$$b_{11} = \frac{a_{11}}{(\tau_1 U')^3}\,,$$
$$b_{12} = \frac{a_{12}}{(\tau_1 U')^2}\,,$$
$$b_{22} = \frac{a_{22}}{\tau_1 U'}\,,$$

and in terms of the η variable we use

$$c_{11} = a_{11}\left(kL^2/U_0\tau_1\right)^{3/2} \qquad (= -b_{11}8\eta^3)\,, \tag{2.42}$$
$$c_{12} = a_{12}\left(kL^2/U_0\tau_1\right) \qquad (= b_{12}4\eta^2)\,, \tag{2.43}$$
$$c_{22} = a_{22}\left(kL^2/U_0\tau_1\right)^{1/2} \qquad (= -b_{22}2\eta)\,. \tag{2.44}$$

We note that $\partial_y^2 = (\tau_1 k U')^2 \left[\partial_Y^2 - (U''/\tau_1 k U'^2)\partial_Y\right]$. This demonstrates the importance of the term $U''/\tau_1 k U'^2$ suggested in section 1.5.4. Where this term is small, ∂_y^2 behaves like a scaled version of ∂_Y^2, and the behavior is locally similar to that seen in Couette flow. If this term is not small, new effects are found. Note that regardless of the value of k, there is some region where this term is large. For Poiseuille flow, $U''/\tau_1 k U'^2 = -1/2Y$.

We now drop all asterisks and derive the equations in terms of both Y and η in a form anticipating the large Wi limit.

Equations in terms of Y

The vorticity equation (2.6) becomes

$$\begin{aligned}
&\frac{\beta}{1-\beta}\psi_{YYYY} + \frac{1}{\tau}(-ib_{11,Y} + b_{12,YY}) \\
&\qquad - \frac{1}{2Y}\left(-\frac{\beta}{1-\beta}6\psi_{YYY} + \frac{1}{\tau}(3ib_{11} - 5b_{12,Y})\right) \\
&\qquad + \left(\frac{1}{2Y}\right)^2\left(\frac{\beta}{1-\beta}3\psi_{YY} + \frac{1}{\tau}2b_{12}\right) \\
&+\frac{k}{Wi^2Y^2}\left[-\frac{2\beta}{1-\beta}\psi_{YY} + \frac{1}{\tau}(b_{12} + ib_{22,Y})\right. \\
&\qquad \left. -\frac{1}{2Y}\left(\frac{2\beta}{1-\beta}\psi_Y + \frac{1}{\tau}ib_{22}\right)\right] \\
&+\frac{k^2}{Wi^4Y^4}\frac{\beta}{1-\beta}\psi \qquad\qquad = 0\,, \qquad (2.45)
\end{aligned}$$

and the constitutive equations (2.7)–(2.9) become

$$\alpha b_{11} = 2b_{12} - 4i\tau^2\psi_Y + 2\tau\psi_{YY} - \frac{1}{2Y}(-2\tau\psi_Y + 4i\tau^2\psi) + \frac{k}{Wi^2Y^2}2i\psi_Y\,, \tag{2.46}$$

$$\alpha b_{12} = b_{22} + \psi_{YY} + 2\tau^2\psi - \frac{1}{2Y}(i\tau\psi - \psi_Y) + \frac{k}{Wi^2Y^2}\psi\,, \tag{2.47}$$

$$\alpha b_{22} = 2\tau\psi + 2i\psi_Y\,, \tag{2.48}$$

where $\alpha = -i\omega + ik - iY + 1/\tau$. The conditions (2.12)–(2.15) at the interface $Y = \Delta^2 k$ are

$$[\![\psi]\!]_{k\Delta^2} = 0\,, \tag{2.49}$$

$$[\![\psi_Y]\!]_{k\Delta^2} = 0\,, \tag{2.50}$$

$$\left[\!\!\left[\frac{\beta}{1-\beta}\psi_{YY} - 2i\tau\delta + \frac{b_{12}}{\tau}\right]\!\!\right]_{k\Delta^2} + \frac{1}{2\Delta^2 k}[\![\beta\psi_Y]\!]_{k\Delta^2} = 0\,, \tag{2.51}$$

$$\left[\!\!\left[\frac{-i\beta}{1-\beta}\psi_{YYY} - \frac{ib_{12,Y}}{\tau} - \frac{b_{11}}{\tau}\right]\!\!\right]_{k\Delta^2} - \frac{1}{2\Delta^2 k}\left[\!\!\left[\frac{3i\beta}{1-\beta}\psi_{YY} + \frac{2ib_{12}}{\tau}\right]\!\!\right]_{k\Delta^2} = -\frac{k}{Wi^2\Delta^4 k^2}\left[\!\!\left[\frac{b_{22}}{\tau}\right]\!\!\right], \tag{2.52}$$

and the kinematic condition (2.26) becomes

$$[\omega - k + \Delta^2 k]\delta = \psi\,. \tag{2.53}$$

At the wall $Y = k$ we use no-slip conditions (2.27)

$$\psi = \psi_Y = 0\,. \tag{2.54}$$

There are difficulties translating the conditions at $y = 0$ into the Y variable because $\partial_Y = -(1/\tau_1 kU')\partial_y$ and $U'(0) = 0$. This does not present an analytical difficulty because we only use Y variables when the interface is far from

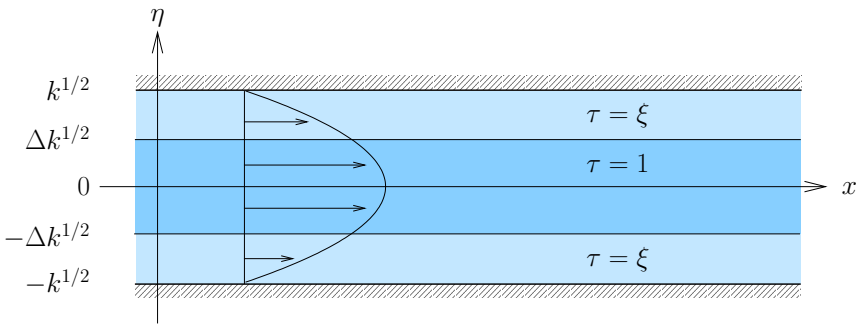

Figure 2.3: Poiseuille flow profile $U = k - \eta^2$ in dimensionless variable η.

the center-line and the boundary conditions at $y = 0$ can be neglected. For this reason we do not use the Y form of the equations in numerics.

If we neglect $\mathcal{O}(k\mathit{Wi}^{-2})$ and $\mathcal{O}(Y^{-1})$ terms in (2.45)–(2.54) we arrive at equations identical to those derived above for Couette flow (2.30)–(2.39) except for some sign changes reflecting a different sign of the shear rate. However, at large Wi our solution involves algebraic terms. For these terms ∂_Y scales like $1/Y$ and so we cannot neglect the $\mathcal{O}(Y^{-1})$ terms without changing the algebraic terms in the solution. If Y is large at the interface, we will find that the value of ω is the same as in Couette flow. However, there are qualitative differences in the structure of the eigenmode.

The complex frequency ω appears only in α and the kinematic boundary condition (2.53) in the combination $\omega - k$. If $\omega = k + \mathcal{O}(1)$ as $k \to \infty$, then k disappears from α and the kinematic boundary condition. Further, as $k \to \infty$, the wall is far from the interface and is expected to have little influence. Finally, if we further assume that $k \ll \mathit{Wi}^2$, then the only remaining parameters are $\Delta k^{1/2}$, ξ, and β.

Equations in terms of η

We show the dimensionless flow profile in terms of η in figure 2.3. The η variable is appropriate if the interface is close to the center-line so that $\eta = \Delta k^{1/2} = \mathcal{O}(1)$ at the interface. The resulting equations are not significantly simplified from the full equations. We are not able to make much analytic progress with them, but they are useful for numerical purposes. The vorticity equation (2.6) becomes

$$\begin{aligned} &\frac{\beta}{1-\beta}\psi_{\eta\eta\eta\eta} + \frac{1}{\tau}(c_{12,\eta\eta} + ic_{11,\eta}) \\ &+\frac{k}{Wi^2}\left(\frac{\beta}{1-\beta}(-2\psi_{\eta\eta}) + \frac{1}{\tau}(c_{12} - ic_{22,\eta})\right) \\ &+\frac{k^2}{Wi^4}\frac{\beta}{1-\beta}\psi \qquad\qquad = 0\,, \end{aligned} \tag{2.55}$$

while the constitutive equations (2.7)–(2.9) become

$$\alpha c_{11} = -4\eta c_{12} + 16i\tau^2\eta^2\psi_\eta - 4\tau\eta\psi_{\eta\eta} + 16i\tau^2\eta\psi + \frac{k}{Wi^2}2i\psi_\eta\,, \tag{2.56}$$

$$\alpha c_{12} = -2\eta c_{22} + \psi_{\eta\eta} + 8\tau^2\eta^2\psi - 2i\tau\psi + \frac{k}{Wi^2}\psi\,, \tag{2.57}$$

$$\alpha c_{22} = -4\tau\eta\psi - 2i\psi_\eta\,, \tag{2.58}$$

where $\alpha = -i\omega + ik - i\eta^2 + 1/\tau$. At the interface $\eta = \Delta k^{1/2}$

$$[\![\psi]\!]_{\Delta k^{1/2}} = 0\,, \tag{2.59}$$

$$[\![\psi_\eta]\!]_{\Delta k^{1/2}} = 0\,, \tag{2.60}$$

$$\left[\!\!\left[\frac{\beta}{1-\beta}\psi_{\eta\eta} - 8i\Delta^2 k\tau\delta + \frac{c_{12}}{\tau}\right]\!\!\right]_{\Delta k^{1/2}} = 0\,, \tag{2.61}$$

$$\left[\!\!\left[\frac{\beta}{1-\beta}i\psi_{\eta\eta\eta} + \frac{ic_{12,\eta}}{\tau} - \frac{c_{11}}{\tau}\right]\!\!\right]_{\Delta k^{1/2}} = -\frac{k}{Wi^2}\left[\!\!\left[\frac{c_{22}}{\tau}\right]\!\!\right]\,, \tag{2.62}$$

and the kinematic condition (2.26) becomes

$$[\omega - k + \Delta^2 k]\delta = \psi\,. \tag{2.63}$$

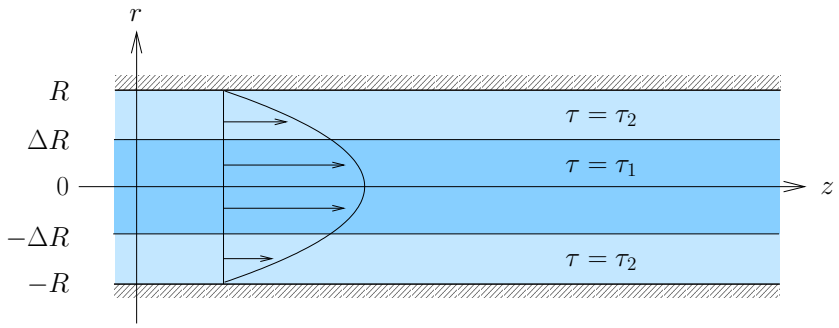

Figure 2.4: Core-annular pipe Poiseuille flow $U = U_0(1 - r^2/R^2)$.

The boundary conditions at the wall $\eta = k^{1/2}$ are

$$\psi = \psi_\eta = 0\,, \tag{2.64}$$

while the conditions at the center-line $\eta = 0$ become

$$\psi_\eta = \psi_{\eta\eta\eta} = 0 \qquad \text{(sinuous)}\,, \tag{2.65}$$

$$\psi = \psi_{\eta\eta} = 0 \qquad \text{(varicose)}\,. \tag{2.66}$$

At large $\mathcal{W}$, the wavenumber k can be eliminated from the problem except for determining the location of the interface and the walls. If η is large at the interface, we can recover the Y equations locally and find the same stability condition as in Couette flow.

2.4 Core-annular pipe flow

We consider core-annular flow through a pipe of radius R as shown in figure 2.4. We use (r, θ, z) cylindrical polar coordinates. For reference, we write out the divergence of stress and velocity in cylindrical coordinates (following

Table A.7-2 of [6]). Using the fact that Σ is symmetric, $\nabla \cdot \Sigma = \mathbf{0}$ becomes

$$\frac{1}{r}\partial_r(r\Sigma_{rr}) + \frac{1}{r}\partial_\theta \Sigma_{r\theta} + \partial_z \Sigma_{rz} - \frac{\Sigma_{\theta\theta}}{r} = 0\,, \tag{2.67}$$

$$\frac{1}{r^2}\partial_r(r^2\Sigma_{r\theta}) + \frac{1}{r}\partial_\theta \Sigma_{\theta\theta} + \partial_z \Sigma_{\theta z} = 0\,, \tag{2.68}$$

$$\frac{1}{r}\partial_r(r\Sigma_{rz}) + \frac{1}{r}\partial_\theta \Sigma_{\theta z} + \partial_z \Sigma_{zz} = 0\,. \tag{2.69}$$

For $\boldsymbol{U} = (V_r, V_\theta, V_z)$, incompressibility $\nabla \cdot \boldsymbol{U} = 0$ becomes

$$\frac{1}{r}\partial_r(rV_r) + \frac{1}{r}\partial_\theta V_\theta + \partial_z V_z = 0\,. \tag{2.70}$$

The inner fluid occupies the region $0 \le r \le \Delta R$ and the outer fluid $\Delta R < r < R$. For the base flow, $\boldsymbol{U} = (0, 0, U(r))$ where $U(r) = U_0(1 - r^2/R^2)$, and A is given by

$$\mathsf{A} = \begin{pmatrix} 1 & 0 & \tau U' \\ 0 & 1 & 0 \\ \tau U' & 0 & 1 + 2\tau^2 U'^2 \end{pmatrix}.$$

We assume that the perturbation flow is proportional to $\exp(ikz + im\theta - i\omega t)$. The value of m must be an integer, and can be assumed non-negative. The pipe analogues of varicose and sinuous modes in a channel are axisymmetric ($m = 0$) and cork-screw ($m = 1$) modes respectively. We do not consider $m > 1$. As before, we use lower-case letters to denote the perturbed quantities. In particular, v_r, v_θ and v_z denote the r, θ and z components of velocity. For axisymmetric perturbations, the azimuthal components decouple and may be neglected or considered separately (see section 5.1). We can then introduce a streamfunction. For cork-screw perturbations, all components of velocity are coupled, and there is no streamfunction.

We choose our non-dimensionalization motivated by the η equations of

channel Poiseuille flow. We take

$$t^* = \frac{t}{\tau_1}\,, \qquad z^* = \frac{z}{U_0\tau_1}\,, \qquad r^* = \frac{(U_0\tau_1 k)^{1/2}}{R} r\,,$$
$$v_r^* = v_r\tau_1 k\,, \qquad v_\theta^* = v_\theta\tau_1 k\,, \qquad v_z^* = v_z\frac{Rk^2\tau_1}{(U_0\tau_1 k)^{1/2}}\,,$$
$$\tau^* = \frac{\tau}{\tau_1}\,, \qquad \omega^* = \omega\tau_1\,, \qquad \alpha^* = \tau_1\alpha = -i\omega^* + ik^* - ir^{*2} + \frac{1}{\tau^*}\,,$$
$$\delta^* = k\delta\,, \qquad k^* = U_0\tau_1 k\,, \qquad p^* = p\frac{\tau_1}{\mu}\left(\frac{R^2k}{U_0\tau_1}\right)^{3/2}\,.$$

We scale the components of the perturbed elastic stress by

$$a_{rr}^* = a_{rr}\left(\frac{R^2k}{U_0\tau_1}\right)^{1/2}, \qquad a_{r\theta}^* = a_{r\theta}\left(\frac{R^2k}{U_0\tau_1}\right)^{1/2}, \qquad a_{\theta\theta}^* = a_{\theta\theta}\left(\frac{R^2k}{U_0\tau_1}\right)^{1/2},$$
$$a_{rz}^* = a_{rz}\frac{R^2k}{U_0\tau_1}\,, \qquad a_{\theta z}^* = a_{\theta z}\frac{R^2k}{U_0\tau_1}\,,$$
$$a_{zz}^* = a_{zz}\left(\frac{R^2k}{U_0\tau_1}\right)^{3/2}\,.$$

The Weissenberg number is $Wi = U_0\tau_1/R$ and so $R^2k/U_0\tau_1 = k^*/Wi^2$.

We drop asterisks and set $\mathrm{D} \equiv \partial_r$. The perturbation of the incompressibility condition (2.70) becomes

$$\frac{1}{r}\mathrm{D}(rv_r) + \frac{im}{r}v_\theta + iv_z = 0 \tag{2.71}$$

The components of the perturbation of the momentum equation (2.67)–(2.67) become

$$\mathrm{D}\left(-\frac{Wi^2}{k}p + \frac{a_{rr}}{\tau}\right) + \frac{1}{r}\frac{a_{rr}}{\tau} + im\frac{a_{r\theta}}{\tau} + i\frac{a_{rz}}{\tau} - \frac{1}{r}\frac{a_{\theta\theta}}{\tau} = 0\,, \tag{2.72}$$
$$\frac{1}{r^2}\mathrm{D}\left(r^2\frac{a_{r\theta}}{\tau}\right) + \frac{im}{r}\left(-\frac{Wi^2}{k}p + \frac{a_{\theta\theta}}{\tau}\right) + i\frac{a_{\theta z}}{\tau} = 0\,, \tag{2.73}$$
$$\frac{1}{r}\mathrm{D}\left(r\frac{a_{rz}}{\tau}\right) + \frac{im}{r}\frac{a_{\theta z}}{\tau} + i\left(-p + \frac{a_{zz}}{\tau}\right) = 0\,. \tag{2.74}$$

The perturbation constitutive equations become

$$\alpha a_{rr} = 2\mathrm{D}v_r - 4ir\tau v_r \,, \tag{2.75}$$

$$\alpha a_{r\theta} = \frac{im}{r}v_r + \mathrm{D}v_\theta - \frac{v_\theta}{r} - 2i\tau r v_\theta \,, \tag{2.76}$$

$$\alpha a_{\theta\theta} = \frac{2}{r}(imv_\theta + v_r) \,, \tag{2.77}$$

$$\alpha a_{rz} = -2ra_{rr} - 2\tau r\mathrm{D}v_r + 8i\tau^2 r^2 v_r + \mathrm{D}v_z - 2i\tau r v_z + 2\tau v_r + \frac{k}{Wi^2}iv_r \,, \tag{2.78}$$

$$\alpha a_{\theta z} = -2ra_{r\theta} - 2\tau r\mathrm{D}v_\theta + 8i\tau^2 r^2 v_\theta + \frac{im}{r}v_z + 2\tau v_\theta + \frac{k}{Wi^2}iv_\theta \,, \tag{2.79}$$

$$\alpha a_{zz} = -4ra_{rz} - 4\tau r\mathrm{D}v_z + 16i\tau^2 r^2 v_z - 16\tau^2 r v_r + \frac{k}{Wi^2}2iv_z \,, \tag{2.80}$$

where $\alpha = -i\omega + ik - ir^2 + 1/\tau$. At the interface we have continuity of velocity

$$[\![v_r]\!]_{\Delta k^{1/2}} = 0 \,, \tag{2.81}$$

$$[\![v_\theta]\!]_{\Delta k^{1/2}} = 0 \,, \tag{2.82}$$

$$[\![v_z]\!]_{\Delta k^{1/2}} = 0 \,, \tag{2.83}$$

as well as the condition that no net force acts on the massless interface

$$\left[\!\!\left[-p + \frac{k}{Wi^2}\frac{a_{rr}}{\tau}\right]\!\!\right]_{\Delta k^{1/2}} = 0 \,, \tag{2.84}$$

$$\left[\!\!\left[\frac{a_{r\theta}}{\tau}\right]\!\!\right]_{\Delta k^{1/2}} = 0 \,, \tag{2.85}$$

$$\left[\!\!\left[-8i\tau\delta r^2 + \frac{a_{rz}}{\tau}\right]\!\!\right]_{\Delta k^{1/2}} = 0 \,. \tag{2.86}$$

Note that this is independent of m. If the constitutive equation had a nonzero second normal stress difference N_2, then there would be m dependence. The perturbed interface location is given by the kinematic condition

$$[-i\omega + ik - ir^2]\delta = v_r \,. \tag{2.87}$$

Boundary conditions

At the walls we apply no-slip boundary conditions, and so at $r = k^{1/2}$

$$v_r = 0\,, \tag{2.88}$$

$$v_\theta = 0\,, \tag{2.89}$$

$$v_z = 0\,. \tag{2.90}$$

The boundary conditions we apply at the origin differ for $m = 0$ or $m = 1$. These conditions are discussed in more detail by Preziosi *et al.* [61]. For $m = 0$, incompressibility (2.71) implies

$$v_r(0) = 0 \qquad (m = 0)\,. \tag{2.91}$$

Assuming the streamwise perturbation velocity is smooth at $r = 0$, we find

$$\mathrm{D}v_z(0) = 0 \qquad (m = 0)\,. \tag{2.92}$$

This condition can also be derived by assuming that the solution is regular and matching powers of r as $r \to 0$. We take an additional constraint on v_θ that

$$v_\theta(0) = 0 \qquad (m = 0)\,. \tag{2.93}$$

For $m = 1$, the incompressibility condition (2.71) gives

$$\frac{\partial v_r}{\partial r} = -\frac{v_r + iv_\theta}{r} - iv_z$$

and so

$$v_r(0) = -iv_\theta(0) \qquad (m = 1)\,. \tag{2.94}$$

This condition may be derived alternately by considering uniform flow across the center-line in polar coordinates. Since both v_z and p represent physical variables which cannot depend on θ at $r = 0$, we can further conclude

$$v_z(0) = 0 \qquad (m = 1)\,, \tag{2.95}$$

$$p(0) = 0 \qquad (m = 1)\,. \tag{2.96}$$

As in Poiseuille channel flow, we can eliminate k from the problem except for determining the location of the interface and the cylinder wall. Assuming that the location of the wall is unimportant, we can use the substitution $\Omega = \omega - k$ and then k and Δ both appear only in the combination $\Delta k^{1/2}$.

2.4.1 Axisymmetric ($m = 0$) linear equations

If $m = 0$, the equations involving v_θ, $a_{r\theta}$ and $a_{\theta z}$ [equations (2.73), (2.76), (2.79), (2.82), (2.85), (2.89), and (2.93)] have no effect on the remaining equations. Consequently we can drop these from equations (2.71)–(2.92). We introduce a streamfunction to automatically satisfy incompressibility,

$$rv_z = \frac{\partial}{\partial r}\psi\,,$$
$$rv_r = -i\psi\,.$$

Taking Wi^2/k times the derivative of equation (2.74) and subtracting i times equation (2.72) eliminates the pressure and yields the vorticity equation

$$\mathrm{D}\left(\frac{1}{r}\mathrm{D}(ra_{rz})\right) + i\mathrm{D}a_{zz} - \frac{k}{Wi^2}i\left(\frac{1}{r}\mathrm{D}(ra_{rr}) + ia_{rz} - \frac{1}{r}a_{\theta\theta}\right)\,. \tag{2.97}$$

The perturbed constitutive equations (2.75)–(2.80) become

$$\alpha a_{rr} = -2i\mathrm{D}\left(\frac{\psi}{r}\right) - 4\tau\psi\,, \tag{2.98}$$
$$\alpha a_{\theta\theta} = -\frac{2i}{r^2}\psi\,, \tag{2.99}$$
$$\alpha a_{rz} = -2ra_{rr} + 2i\tau r\mathrm{D}\left(\frac{\psi}{r}\right) + 8\tau^2 r\psi + \mathrm{D}\left(\frac{1}{r}\mathrm{D}\psi\right) - 2i\tau\mathrm{D}\psi$$
$$- 2i\tau\frac{\psi}{r} + \frac{k}{Wi^2}\frac{\psi}{r}\,, \tag{2.100}$$
$$\alpha a_{zz} = -4ra_{rz} - 4\tau r\mathrm{D}\left(\frac{1}{r}\mathrm{D}\psi\right) + 16i\tau^2\mathrm{D}(r\psi) + \frac{k}{Wi^2}\frac{2i}{r}\mathrm{D}\psi\,. \tag{2.101}$$

Boundary conditions

At the interface $r = \Delta k^{1/2}$ the equations of continuity of velocity (2.81) and (2.83) become

$$[\![\psi]\!] = [\![\mathrm{D}\psi]\!] = 0\,. \tag{2.102}$$

The force balances (2.84) and (2.86) become

$$\left[\!\!\left[-\frac{a_{zz}}{\tau} + \frac{i}{\tau}\left(\mathrm{D}a_{rz} + \frac{a_{rz}}{\Delta k^{1/2}}\right) + \frac{k}{\mathit{Wi}^2}\frac{a_{rr}}{\tau}\right]\!\!\right]_{\Delta k^{1/2}} = 0\,, \tag{2.103}$$

$$\left[\!\!\left[-8i\tau\delta\Delta^2 k + \frac{a_{rz}}{\tau}\right]\!\!\right]_{\Delta k^{1/2}} = 0\,. \tag{2.104}$$

and the kinematic condition (2.87) gives

$$[\omega - k + \Delta^2 k]\delta = \frac{\psi}{\Delta k^{1/2}}\,. \tag{2.105}$$

At the walls we have no-slip conditions (2.88) and (2.90)

$$\psi = 0\,, \tag{2.106}$$

$$\mathrm{D}\psi = 0\,. \tag{2.107}$$

The conditions at the center-line (2.91) and (2.92) are more intricate. We need two boundary conditions, and it is easily shown (by considering v_z) that both ψ and ψ' are zero. This is not sufficient to uniquely determine the solution for either a Newtonian or an elastic fluid, though it has been used (incorrectly) in the literature [23, 69] without significantly affecting results. There is a singular solution which has $\mathrm{D}\psi \sim r\ln r$ as $r \to 0$, and so the correct conditions at the origin are frequently given as: ψ/r and $(\mathrm{D}\psi)/r$ remain finite as $r \to 0$ [25]. We find it simpler to apply the equivalent condition that

$$\psi = a_2 r^2 + a_4 r^4 + \cdots \tag{2.108}$$

at small r. This is discussed further in appendix A.2.5.

2.4.2 Cork-screw ($m = 1$) linear equations

When m is nonzero, we do not have a simplification analogous to a stream-function. Consequently, we must solve the full set of equations (2.71)–(2.90) with $m = 1$ and the conditions at the origin (2.94)–(2.96).

2.5 The spectrum

The spectrum is defined (for our purposes) to be the set of eigenvalues ω. The structure of the spectrum for inertialess UCM and Oldroyd–B fluids in one and two-layer flow at finite $\mathcal{W}i$ has been discussed in detail by Wilson *et al.* [107] and Kupferman [50]. We briefly summarize their results here.

For UCM fluids there is a continuous spectrum consisting of those points at which $\alpha = 0$, along with a finite number of discrete eigenvalues. The continuous spectrum results from a singularity in the constitutive equations. It has negative growth rate, with two distinct branches satisfying $\Im[\omega] = -1$ and $\Im[\omega] = -1/\xi$ corresponding to the two different fluids. Both continuously differentiable and distribution-valued eigenfunctions have been found in the continuous spectrum. The number of discrete eigenvalues changes with k, as eigenvalues enter or leave the continuous spectrum.

For the Oldroyd–B fluid the spectrum consists of a UCM part as above, along with an additional continuous spectrum and some new discrete eigenvalues. The new part of the continuous spectrum also has two branches, but results from a singularity in the momentum equation. Its location can be found by substituting for the stresses in the momentum equation in terms of ψ and setting the coefficient of the leading derivative of ψ to zero. We find $\Im[\omega] = -1/\beta$ and $\Im[\omega] = -1/\beta\xi$ for these branches.

2.6 Numerical methods

We use two methods to solve the linear eigenvalue problem: shooting and a Chebyshev spectral method. We use parameter continuation to follow modes as k, Δ, ξ, or β change. Because eigenvalues can enter (or leave) the continuous spectrum, it is therefore possible that some eigenvalues have not been considered.

The two algorithms give results consistent with asymptotic results at small and large k, with calculated results from previous work, and with each other. The details of the implementations and tests of the numerics are described in appendix A. In this section we focus on issues that affect our ability to find or follow modes.

2.6.1 The shooting algorithm

The shooting algorithm uses a variable step-size Runge–Kutta integration routine combined with Newton–Raphson iteration, both from Numerical Recipes [77]. It has several weaknesses. The code can fail by reporting a false result, by failing to converge, or by converging to a different eigenvalue. We eliminate the false eigenvalues by testing the eigenvalue with an additional calculation at higher resolution. Where the algorithm fails, we are unable to follow that eigenvalue. The results of losing the most dangerous mode (*i.e.*, the mode with most positive or least negative growth) are seen in a number of our figures (*e.g.*, figures 3.5, 4.5, and 4.9). We describe below the regions of parameter space for which shooting fails.

At large values of k, the problem has multiple length scales. Small inaccuracies affect the integration and convergence fails. For $\xi < 1$ the algorithm fails first as $k \to \infty$ when Δ is large. When k is small, the eigenvalue of the most dangerous mode tends to zero like k^2. Its basin of attraction in the Newton–Raphson algorithm shrinks and so if k is small the initial guess

must be very close to avoid converging to a different value. For $\xi < 1$ the algorithm fails first as $k \to 0$ when Δ is small.

Consequently, for some parameters we do not find the most dangerous eigenvalue, and could potentially misreport some regions of parameter space as stable when in fact they are unstable.

2.6.2 The spectral algorithm

In our spectral method we express each physical variable as a sum of approximately (see appendix A.1.2) N Chebyshev polynomials. The system of governing equations can then be written in the form $\mathsf{C}_1\boldsymbol{x} = i\omega\mathsf{C}_2\boldsymbol{x}$, where C_1 and C_2 are square matrices, C_2 is non-negative and diagonal, and $\boldsymbol{x}$ is the vector of coefficients. The eigenvalues are found using *Matlab's* `eig` and `eigs` routines which use the QZ algorithm from LAPACK and the Implicitly Restarted Arnoldi Method from ARPACK respectively. The spectral methods can generally handle larger and smaller values of k than the shooting algorithm.

The continuous spectrum appears as a balloon of eigenvalues which shrinks as the number of polynomials per variable is increased [107]. This can be seen in figure 2.5. If a discrete eigenvalue lies within the balloon, it becomes difficult to identify. We must increase the number of polynomials in order to see it. In some of our calculations we have needed C_1 and C_2 to be 2000×2000 in order to resolve the unstable modes. Some parameter values require higher resolution, but we are limited by computer memory.

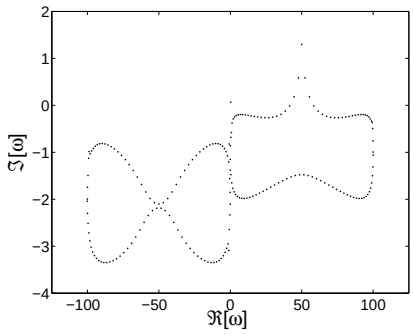

(a) $N = 50$.

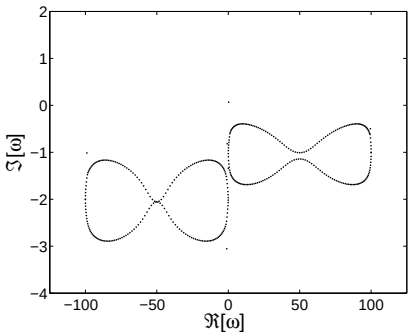

(b) $N = 100$.

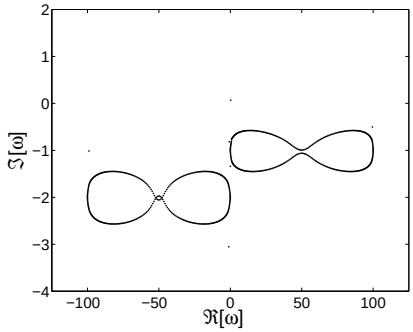

(c) $N = 200$.

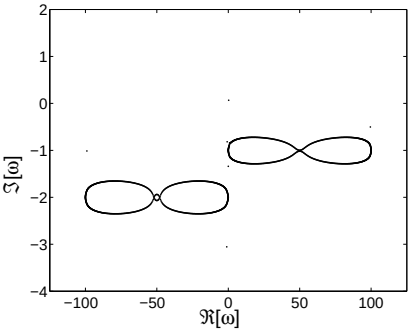

(d) $N = 400$.

Figure 2.5: The spectrum for UCM Couette flow with $\xi = 0.5$, $k = 200$ and $\Delta = 0.5$ at infinite Wi. The continuous spectrum is composed of the line segments between $-100 - 2i$ and $-2i$ and between $-i$ and $100 - i$. Each branch is surrounded by a balloon whose width decreases as N increases. The discrete eigenvalues do not move significantly, but may be obscured by the balloon until N is large.

Chapter 3

Stability of Couette flow

In this chapter we study instabilities of inertialess Couette flow with a single interface. The dimensionless flow profile is given in figure 3.1. This problem has received considerable attention, particularly in the short-wave limit [104, 84] in which the wavelength is short compared to the channel width, and also in the long-wave limit [103, 27] in which the wavelength is long compared to the channel width. These studies implicitly assume that the wavelength is also short or long compared to the relaxation length scale $U\tau$. In this chapter we investigate alternate scalings in which the wavelength is intermediate between the channel width and the relaxation length scale.

The chapter is organised as follows. In section 3.1 we give the analytic solution for the streamfunction for an Oldroyd–B fluid at arbitrary Wi, as well as the limiting cases of $Wi \to \infty$ and/or $\beta \to 0$ (a UCM fluid). In section 3.2 we asymptotically solve the stability problem for two UCM fluids in the fast flow regime $Wi \gg k \gg 1$ for which the relaxation length scale is long compared to the wavelength which is in turn long compared to channel width, and numerically solve the problem at finite values of k. In section 3.3 we show numerically that Oldroyd–B fluids also have instability for $Wi \gg k \gg 1$. In section 3.4 we find a simple corollary of our result for large Wi UCM flow,

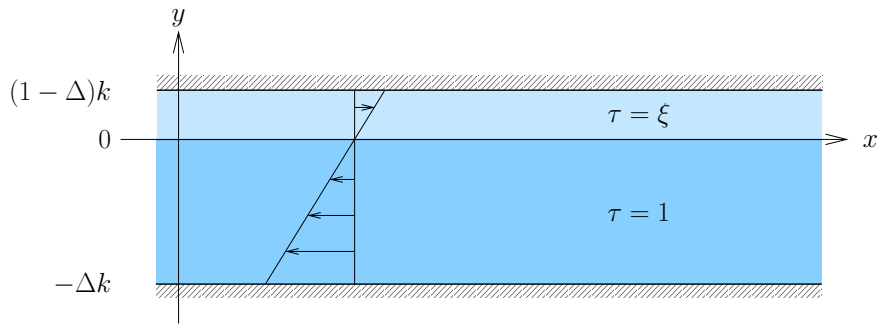

Figure 3.1: Couette flow profile $U = y/k$. Without loss of generality we take $0 \leq \xi \leq 1$.

showing that arbitrarily large surface tension does not affect the growth of the instability. We verify this numerically for UCM and Oldroyd–B fluids. We find a similar result at finite Wi. Section 3.5 gives a physical explanation of some of the unusual features of this instability. In section 3.6 we discuss a new instability found for the Oldroyd–B fluid at intermediate values of k, which does not fit cleanly into any of our classifications. Finally, in section 3.7 we briefly investigate the limit in which the channel width is long compared to the wavelength, which in turn is long compared to the relaxation length scale and show that the analysis of other authors [84, 104] may be extended to this case.

3.1 Analytic solutions

We use this section to derive the analytic form of the streamfunction in general and in various asymptotic limits which will be needed later.

For the UCM fluid ($\beta = 0$) Gorodtsov and Leonov [31] explicitly found the streamfunction ψ solving (2.18)–(2.21) by substituting for the a_{ij} into

the vorticity equation (2.18). They found that the resulting operator factors as

$$\left(\alpha^2\mathrm{D}^2 - 2i\alpha\mathrm{D} - 2 - \frac{\alpha^2}{Wi^2}\right)\left(\mathrm{D}^2 + 2i\tau\mathrm{D} - 2\tau^2 - \frac{1}{Wi^2}\right)\psi = 0\,,$$

where $\alpha = -i\omega + iy + 1/\tau$. For the Oldroyd–B fluid we have additional terms and the operator becomes

$$\begin{aligned}&\alpha^3 s\tau\left(\mathrm{D}^2 - \frac{1}{Wi^2}\right)^2\psi \\ &+\left(\alpha^2\mathrm{D}^2 - 2i\alpha\mathrm{D} - 2 - \frac{\alpha^2}{Wi^2}\right)\left(\mathrm{D}^2 + 2i\tau\mathrm{D} - 2\tau^2 - \frac{1}{Wi^2}\right)\psi = 0\,,\end{aligned} \tag{3.1}$$

where $s = \beta/(1-\beta)$.

Remarkably, the Laplacian squared which gives rise to the differential operator $(\mathrm{D}^2 - Wi^{-2})^2$ is not uniquely factorizable. It can be factored in a variety of manners, one of which allows us to re-express the Oldroyd–B operator as

$$\left(\alpha^2\mathrm{D}^2 - 2i\alpha\mathrm{D} - 2 - \frac{\alpha^2}{Wi^2}\right)\left([s\tau\alpha + 1]\mathrm{D}^2 + 2i\tau\mathrm{D} - 2\tau^2 - \frac{s\tau\alpha + 1}{Wi^2}\right)\psi = 0 \tag{3.2}$$

(recall $\mathrm{D}\alpha = i$). It is clear from this equation that the $Wi \to \infty$ limit is regular. We use this form to find the explicit solution

$$\begin{aligned}\psi(y) = {} & C_1(y-\omega)\exp(y/Wi) + C_2(y-\omega)\exp(-y/Wi) \\ & + C_3\exp(y/Wi)\mathcal{M}\left(\frac{1}{s}(1 + i\tau Wi), \frac{2}{s}, \frac{2i}{Wi}(\alpha + 1/s\tau)\right) \\ & + C_4\exp(y/Wi)\,\mathcal{U}\left(\frac{1}{s}(1 + i\tau Wi), \frac{2}{s}, \frac{2i}{Wi}(\alpha + 1/s\tau)\right)\,,\end{aligned} \tag{3.3}$$

where $\mathcal{M}$ and $\mathcal{U}$ are Kummer's functions [1]. This solution is equivalent to one found by Wilson *et al.* [107]. In practice we do not find this solution to be useful for our stability problem and turn instead to numerics to solve the equations (2.18)–(2.27).

The solution of (3.2) in the $\beta = 0$ limit found by Gorodtsov and Leonov [31],

$$\begin{aligned}\psi(y) = {} & C_1(y-\omega)\exp(y/Wi) + C_2(y-\omega)\exp(-y/Wi) \\ & + C_3 \exp\left[\tau y\left(-i - \sqrt{1+\frac{1}{\tau^2 Wi^2}}\right)\right] \\ & + C_4 \exp\left[\tau y\left(-i + \sqrt{1+\frac{1}{\tau^2 Wi^2}}\right)\right],\end{aligned} \tag{3.4}$$

is more useful for asymptotic analysis. From this solution we see that the different terms have different dependence on Wi. If Wi is large (but less than the dimensionless channel width k) there are two boundary layers at the interface, one with width of order unity and another with width of order Wi.

If Wi is large compared to k and 1, the exponentials $\exp(\pm y/Wi)$ are replaced by algebraic terms, reflecting the fact that the corresponding boundary layer has become large compared to the channel width. The solution at large Wi for the Oldroyd–B fluid is

$$\begin{aligned}\psi(y) = {} & C_1(y-\omega) + C_2 y(y-\omega) \\ & + C_3\left(\alpha + \frac{1}{s\tau}\right)^{\frac{s-2}{2s}} \mathcal{J}_{\frac{s-2}{s}}\left(2i\sqrt{2}\frac{(-1-\alpha)^{1/2}}{s}\right) \\ & + C_4\left(\alpha + \frac{1}{s\tau}\right)^{\frac{s-2}{2s}} \mathcal{Y}_{\frac{s-2}{s}}\left(2i\sqrt{2}\frac{(-1-\alpha)^{1/2}}{s}\right),\end{aligned} \tag{3.5}$$

where $\mathcal{J}$ and $\mathcal{Y}$ are Bessel functions [1]. For a UCM fluid ($\beta = 0$) at large Wi we find

$$\psi(y) = C_1(y-\omega) + C_2 y(y-\omega) + C_3 e^{(-1-i)\tau y} + C_4 e^{(1-i)\tau y}. \tag{3.6}$$

3.2 UCM fluids ($\beta = 0$) at large Weissenberg number

We first consider the UCM fluid neglecting both surface tension (*i.e.*, setting $\gamma = 0$) and $\mathcal{O}(1/Wi^2)$ terms from (2.18)–(2.27). The solution for ψ from (3.6) is

$$\psi(y) = C_1^{\pm}(y-\omega) + C_2^{\pm}y(y-\omega) + C_3^{\pm}e^{(-1-i)\tau_{1,2}y} + C_4^{\pm}e^{(1-i)\tau_{1,2}y} \qquad (3.7)$$

where $\pm$ denotes the solution on either side of the interface.

3.2.1 Asymptotic results for $Wi \gg k \gg 1$

When k is also large, we can approach the problem asymptotically.

The exponential terms in (3.7) have a length scale of order unity, but the walls are at asymptotically large distances of order k from the interface. In consequence, for the upper fluid ($y > 0$) the coefficient C_4^+ must be exponentially small otherwise the corresponding term would be exponentially large near the wall. Thus it is negligible close to the interface. Similarly, the C_3^+ term is negligible close to the wall.

We now find C_2^+ in terms of C_1^+. As $k \to \infty$, the two boundary conditions at the wall $\psi = \mathrm{D}\psi = 0$ are satisfied by

$$C_1^+(y-\omega) + C_2^+y(y-\omega) + C_4^+e^{(1-i)\xi y}$$

at $y = (1-\Delta)k \gg 1$. Some algebra shows that at leading order in k

$$C_1^+ = k(\Delta - 1)C_2^+ ,$$

and a similar argument at the bottom wall gives

$$C_1^- = k\Delta C_2^- .$$

Thus $C_2^{\pm}$ are much smaller than $C_1^{\pm}$.

Applying the interfacial conditions (2.24)–(2.26) and neglecting the exponentially small terms involving C_3^- and C_4^+, we find $\mathsf{M}\boldsymbol{v} = \mathsf{0}$ where $\boldsymbol{v} = [C_1^-, C_4^-, C_1^+, C_3^+]^T$ and

$$\mathsf{M} = \begin{pmatrix} 0 & 2\frac{\omega^2+2i\omega+\omega+i}{\omega(\omega+i)^2} & 0 & 2\xi\frac{\xi^2\omega^2+2i\xi\omega-\xi\omega-i}{\omega(\xi\omega+i)^2} \\ -\frac{2}{\Delta} & 0 & \frac{2\xi}{\Delta-1} & 0 \\ 1 & (1-i) & -1 & (1+i)\xi \\ -\omega & 1 & \omega & -1 \end{pmatrix}, \tag{3.8}$$

to leading order in k. The first and second rows arise from the x- and y-components of the force balance respectively while the third and fourth rows come from the x- and y-components of continuity of velocity respectively.

We seek ω such that $\det(\mathsf{M}) = 0$. We replace the fourth row of M with the sum of the fourth row and ω times the third row. The rows are linearly dependent if and only if the first and (new) fourth rows are linearly dependent. That is, $\det \mathsf{M} = 0$ if and only if $\det(\mathsf{N}) = 0$ where

$$\mathsf{N} = \begin{pmatrix} 2\frac{\omega^2+2i\omega+\omega+i}{\omega(\omega+i)^2} & 2\xi\frac{\xi^2\omega^2+2i\xi\omega-\xi\omega-i}{\omega(\xi\omega+i)^2} \\ 1+\omega(1-i) & -1+\omega\xi(1+i) \end{pmatrix}. \tag{3.9}$$

The combination of rows used to arrive at the second row of N represents continuity of the material derivative of the x-component of velocity at the interface, henceforth referred to as the *continuity of tangential acceleration* condition. The flow generated by $\psi = C_1^{\pm}(y-\omega)$ has the unusual property that the x-component of velocity for a material particle does not change: the Eulerian derivative at a point is balanced by the change in the base flow due to advection in the y-direction

$$\begin{aligned} \frac{D(U+u)}{Dt} &= \frac{DU}{Dt} + \frac{D\psi'}{Dt} \\ &= ik\psi U' + ik(U-c)\psi' \\ &= 0\,, \end{aligned}$$

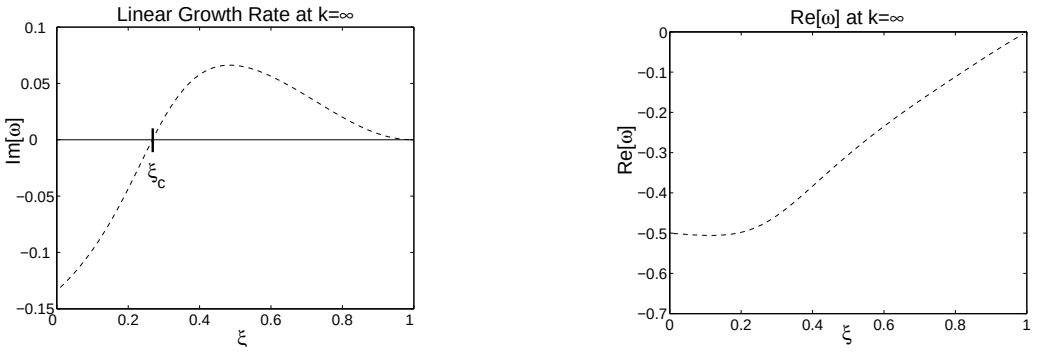

(a) Linear growth rate.

(b) Real part of ω.

Figure 3.2: Imaginary and real parts of ω solving equation (3.10) as ξ changes.

where $c = \omega/k$. Because ψ is proportional to $U - c$, we will see in chapter 4 that this result holds even in different flow profiles.

Consequently the coefficients $C_1^{\pm}$ cancel exactly and do not appear in the second row of N. They similarly drop out of the tangential force balance and thus do not affect the condition for stability. The two terms that decay exponentially away from the interface (C_4^- and C_3^+) are the only terms that can be used to satisfy the pair of tangential interfacial conditions.

We can arbitrarily set C_4^-, leaving two conditions to be satisfied by a single unknown C_3^+, which is possible when ω is an eigenvalue. The remaining coefficients are used to satisfy the other interfacial and boundary once C_4^- and C_3^+ are fixed. The $C_1^{\pm}$ algebraic terms fix the normal interfacial conditions, and the remaining algebraic ($C_2^{\pm}$) and exponential (C_3^-, C_4^+) terms are used to satisfy the conditions at the walls. Significantly, this means that the stability is entirely determined by effects within the boundary layer at the interface. Thus when k is large, ω is independent of Δ and depends only on ξ.

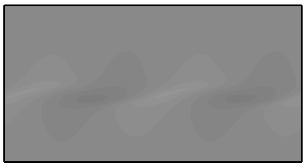

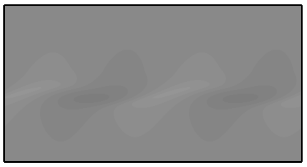

After some algebra the determinant of N yields:

$$\begin{aligned} 2\xi^3\omega^5 + (\xi^3 + 4i\xi^3 - \xi^2 + 4i\xi^2)\omega^4 + (-2\xi^3 - 8\xi^2 - 2\xi)\omega^3 \\ + (-2\xi - i\xi^3 - 3i\xi^2 - 3i\xi - i + 2\xi^2)\omega^2 \\ + (2\xi^2 - 2\xi + \xi^2 i + 2 - i)\omega - \xi + 1 \quad = \quad 0\,. \end{aligned} \tag{3.10}$$

Because this is a quintic equation there are five modes which have the same asymptotic scaling. Equation (3.10) is identical to the large $\mathcal{W}\!i$ limit of Renardy's [84] result which assumes the perturbations decay before reaching the wall. This assumption is inappropriate for the channel flow studied here. The fact that the result is unchanged is remarkable because it implies that the growth rate of the instability is unaffected by the presence of the channel walls even though the mode structure is changed.

The neutral stability boundary occurs when ω is real. The only ξ allowing real ω are $\xi = 1$ and $\xi = \xi_c \approx 0.27688$. Between these values the imaginary part of ω is positive, and below this range it is negative. The zero at $\xi = 1$ occurs because this corresponds to the two fluids having identical properties. It is a quadratic zero because there is a symmetry in the problem: $\xi > 1$ corresponds to interchanging the two fluids and so in the large k limit, the growth rate must have the same sign on either side of $\xi = 1$. The real and imaginary parts of the most dangerous root for ω are plotted in figure 3.2.

For $\xi = 0.5$, equation (3.10) gives $\omega \approx -.30544 + .06603i$. Thus at large k we expect an instability with growth rate about 0.06603 and wavespeed about $-0.30544/k$. Both limits are clear in figure 3.3 where we have solved the $\mathcal{W}\!i \to \infty$ problem (2.30)–(2.39) numerically with $\xi = 0.5$ and $\Delta = 0.7$ for a range of k. The growth rate overshoots the prediction for moderate k but decreases towards it as $k \to \infty$. Figure 3.4 shows the corresponding perturbation flow at $k = 30$. Note that it occupies the full width of the channel with boundary layers at the interface and the wall.

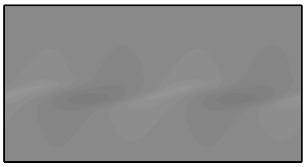

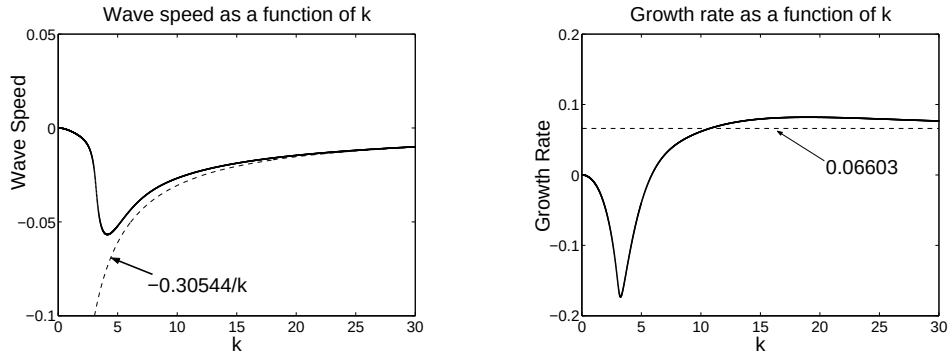

(a) Wave speed $\Re[\omega]/k$.

(b) Growth rate $\Im[\omega]$.

Figure 3.3: Growth rates and wave speeds calculated from (2.28)–(2.39) compared with the large k asymptotic predictions (dotted) for $\xi = 0.5,\ \Delta = 0.7$.

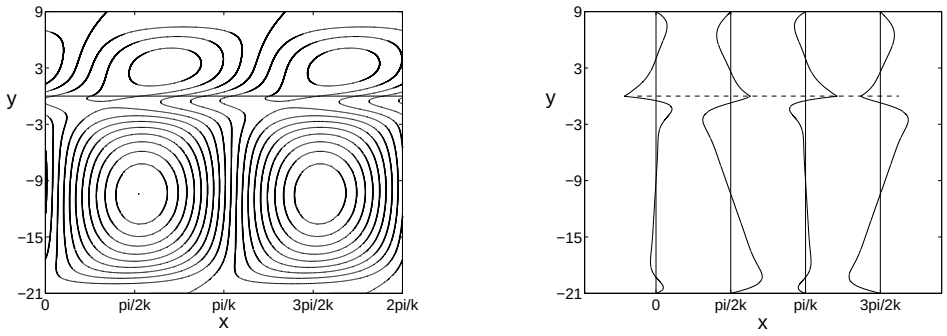

(a) Streamlines.

(b) Horizontal component of the perturbation flow. Note the boundary layers at the interface and both walls.

Figure 3.4: Unstable mode for $\xi = 0.5,\ \Delta = 0.7$, and $k = 30$. The value of ω is $-0.3000 + 0.0766i$. There are boundary layers close to the interface and the walls. The magnitude of the flow is comparable throughout the channel.

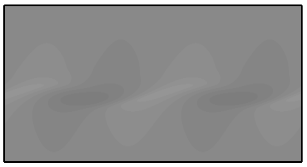

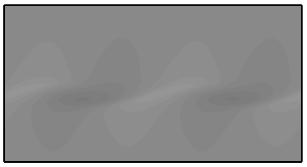

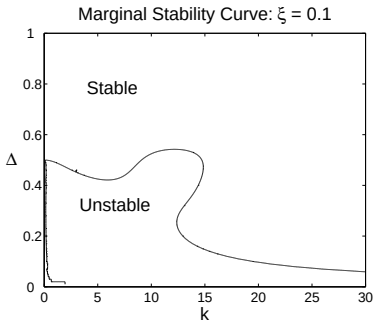

(a) $\xi = 0.1$. Well below ξ_c, short-waves are stable. There is a small unstable tongue at $10 \lesssim k \lesssim 15$.

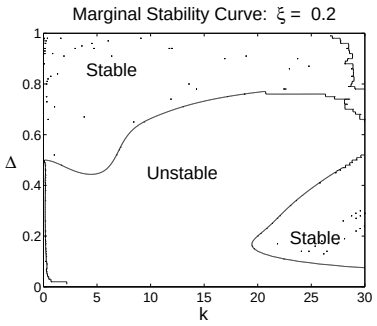

(b) $\xi = 0.2$. Just below ξ_c short-waves are stable, but the unstable tongue has grown much larger.

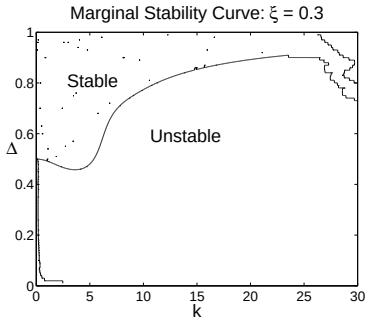

(c) $\xi = 0.3$. Just above ξ_c, short-waves are unstable and the instability persists down to $k \approx 5$.

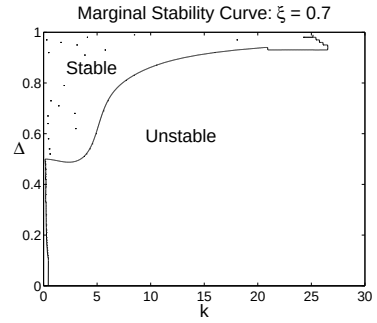

(d) $\xi = 0.7$. The picture is largely unchanged from $\xi = 0.3$.

Figure 3.5: Marginal stability curves in (Δ, k) space for $\mathcal{W}i \to \infty$ at fixed values of ξ. The noisy areas for large k or small Δ correspond to regions of numerical difficulties.

3.2.2 Stability for $\mathcal{W}i \gg 1$ and general k

To illustrate the stability boundary for general k, we fix ξ and allow Δ and k to vary. Figure 3.5 shows the marginal stability curves in (k, Δ) space. For

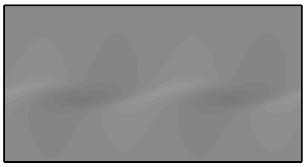

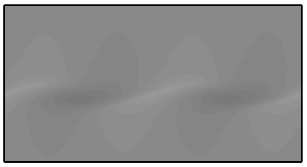

$k \to 0$ the wavelength is long compared to both the width and the relaxation length scale, so this is a special case of previous long-wave analysis [103, 27] with instability if $\Delta < 0.5$. If $\xi > \xi_c \approx 0.28$ we have shown there is an instability as $k \to \infty$. Both limits are clear in figure 3.5. For $\xi < \xi_c$, there is an unstable tongue for moderate k which grows as $\xi \to \xi_c$, filling most of the plot for $\xi = 0.2$.

The overshoot in figure 3.3 and the tongues in figures 3.5(a) and (b) both show that the growth rate overshoots the large k prediction when k is moderate. This suggests that the next correction in k as $k \to \infty$ is destabilizing.

3.3 Oldroyd–B fluids ($\beta > 0$) at high Weissenberg number

We consider here whether the $\mathcal{W}i \gg k \gg 1$ interfacial instability we have found for UCM fluids persists for Oldroyd–B fluids. In section 3.6 we discuss the existence of another instability at large $\mathcal{W}i$ for intermediate values of k.

Because $C_1(y - \omega)$ remains part of solution (3.5) even in the presence of Newtonian viscosity the remarkable coincidence that C_1 drops out of the tangential force and tangential acceleration condition at the interface remains true regardless of β. Thus if C_2 is small the algebraic terms again drop out and the stability is determined entirely by the two tangential conditions in the interfacial boundary layer.

Wilson and Rallison [104] asymptotically studied the $k \to \infty$, $\beta \to 1$ limit for Oldroyd–B fluids with moderate $\mathcal{W}i$. In this limit the perturbation flow decays away from the interface and the walls can be neglected. They showed that for β close to 1 there is instability for all ξ, with the growth rate tending to zero like $(1 - \beta)^3$ as β approaches 1. It is known from the UCM results of Renardy [84] that there are values of ξ with stability if $\beta = 0$ and

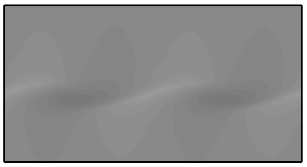

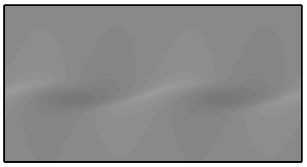

$W\!i$ is large enough. Using a shooting algorithm Wilson and Rallison found stability for β as large as 0.11, and postulated that this is the critical value of β at which stability is no longer possible.

When $W\!i$ is larger than k, their analysis breaks down because the walls lie within the boundary layer. Asymptotics become difficult, and so we have turned to numerics instead. The governing equations we use are (2.30)–(2.39).

Setting $\Delta = 0.5$ we fix $k = 30$, 60, 120 and follow the growth rate in (β, ξ) space in figure 3.6. At $k = 30$, there is stability if both ξ and β are small, shown in figure 3.6(a). As k grows, this region increases in size marginally. The stable region exists for β up to (at least) 0.2. This extends the stable region found by Wilson and Rallison [104].

If either β or ξ is sufficiently large, the flow is unstable. For fixed β and ξ, the growth rate tends to a finite limit as $k \to \infty$, but as β grows, the value of k at which the limit is seen increases.

In the limit $\beta \to 1$, the fluids become identical Newtonian fluids and so the growth rate must tend to zero. That is, for fixed k and ξ, $\lim_{\beta\to 1} \Im[\omega] = 0$. Our calculations suggest that the growth rate scales like $(1-\beta)^3$. However, figure 3.6 suggests that for fixed ξ $\lim_{\beta\to 1} \lim_{k\to\infty} \Im[\omega] \neq 0$: the limit is singular. This is different from the $W\!i \ll k$ case in [104].

To observe the structure of the unstable mode when the fluids are almost entirely Newtonian, we take $\xi = 0.5$, $\Delta = 0.7$, $\beta = 0.99$ and $k = 2000$. The perturbation flow is shown in figure 3.7. The boundary layers at the wall have effectively disappeared. There are still boundary layers close to the interface, but their structure has changed.

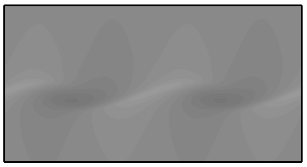

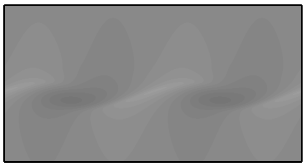

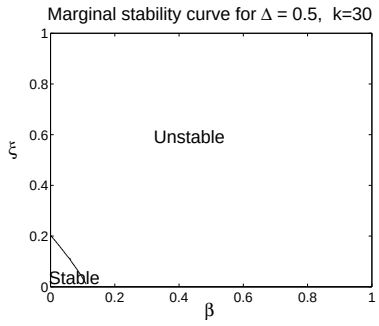

(a) The marginal stability curve at $k = 30$.

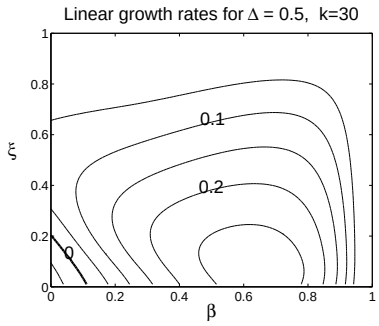

(b) The growth rate at $k = 30$.

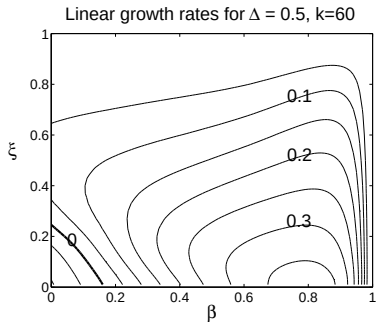

(c) The growth rate at $k = 60$.

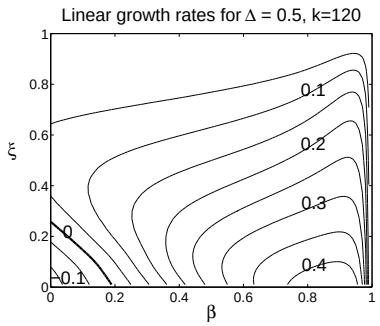

(d) The growth rate at $k = 120$.

Figure 3.6: Growth rate contours in the (β, ξ) plane for Oldroyd–B fluids with $\Delta = 0.5$, for $k = 30$, 60, and 120. The lower left corner is the only region of stability. If either $\xi = 1$ or $\beta = 1$, the two fluids are identical, and the growth rate is zero. For $\beta = 0$ (UCM) the $k \to \infty$ asymptotic results from equation (3.10) are in good agreement.

3.4 The effect of surface tension

A physical interface will have surface tension, which acts to reduce the interfacial curvature. Insofar as instability requires a displacement of the interface,

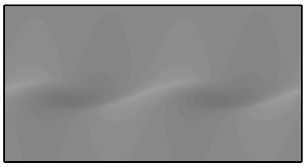

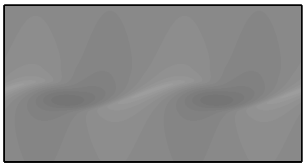

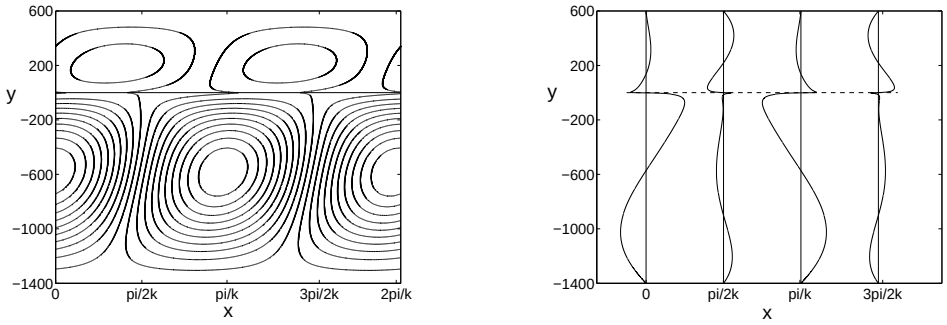

(a) Streamlines.

(b) Horizontal perturbation flow.

Figure 3.7: Unstable perturbation flow of Oldroyd–B fluid with $\beta = 0.99,\ \xi = 0.5,\ \Delta = 0.7$, and $k = 2000$. For these parameters $\omega = -0.0261 + 0.3330i$. Compare with figure 3.4 where $\beta = 0,\ \Delta = 0.7,\ k = 30$, and $\xi = 0.5$.

surface tension is expected to suppress the instability, especially for large k.

3.4.1 The effect of surface tension at high Weissenberg number

In this section we assume that $Ca \sim Wi^{-3}$ so that surface tension is still dynamically important at large Wi.

We consider equations (2.30)–(2.39), with $\gamma \neq 0$. In the limit $k\gamma \to \infty$, the normal force balance (2.37) reduces to $\delta = 0$. With $\delta = 0$, the kinematic equation for the interface (2.38) becomes $\psi(0) = 0$ and δ disappears from the problem. The only remaining terms involving time derivatives are in the evolution of a, equations (2.31)–(2.33). Thus any instability manifests itself only in the growth of the fluid velocity and elastic stresses and not in an interfacial perturbation.

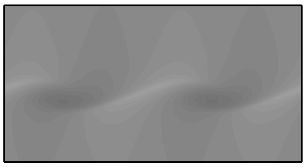

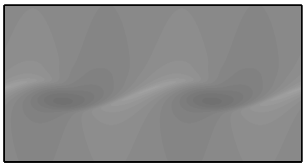

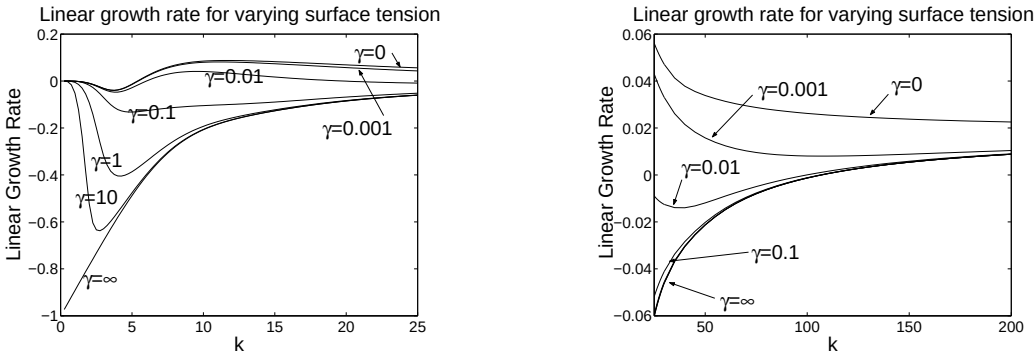

Figure 3.8: The effect of surface tension on growth rate for $\xi = 0.3$, $\Delta = 0.5$ and $\mathit{Wi} \gg 1$. As $k \to \infty$ all growth rates tend to the limit, approximately 0.019.

UCM fluids ($\beta = 0$) with nonzero surface tension

In the limit where $\mathit{Wi} \gg k \gg 1$, we have an analytic representation of the streamfunction in both fluids, and we can proceed exactly as in section 3.2.1. The addition of surface tension affects only the second row of the matrix M in equation (3.8). This row plays no role in the construction of N in equation (3.9), and so the linear stability of the system is unchanged by the addition of surface tension (although the perturbation flow is changed). The remarkable conclusion is that a perturbation with the same growth rate occurs regardless of the size of the surface tension whenever $\mathit{Wi} \gg k \gg 1$.

To see the effect of surface tension at modest k we solve the equations numerically. In figure 3.8 we plot the growth rates with $\xi = 0.3$ and $\Delta = 0.5$ for different values of the surface tension measured by γ. The infinite surface tension ($\gamma = \infty$) curve was calculated by replacing the normal force balance with the condition $\psi(0) = 0$. As expected, the growth rate of the disturbance is everywhere reduced by the addition of surface tension. For small k and γ finite, the growth rates are close to the zero surface tension limit. As k

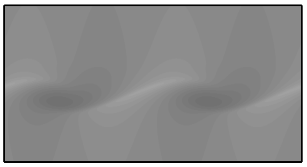
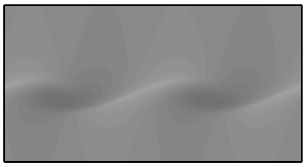

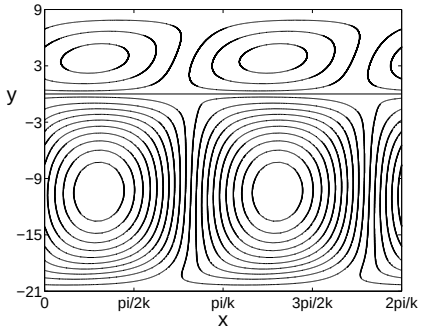

(a) Streamlines at infinite surface tension. The interface is flat.

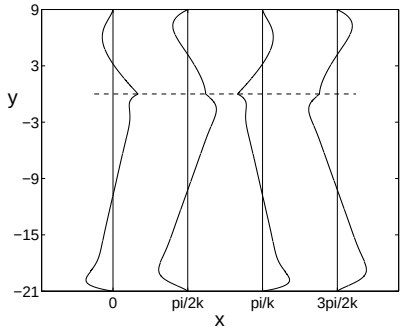

(b) Horizontal component of the perturbation flow.

Figure 3.9: Perturbation flow for the same parameters as in figure 3.4: $\xi = 0.5$, $\Delta = 0.7$, $k = 30$, and $\beta = 0$, but with $\gamma = \infty$. The value of ω is $-0.2855 - 0.0227i$. As k increases it destabilizes and tends to the same growth rate as for the zero surface tension case.

increases, they approach the infinite surface tension limit. As $k \to \infty$, both zero and infinite surface tension limits tend to the same (positive) growth rate, about 0.019.

In figure 3.9 we show the perturbation flow for the same parameters as in figure 3.4 except that the surface tension is infinite. Boundary layers exist at the interface with the same length scale as before.

The fact that surface tension does not affect the growth rate as $k \to \infty$ has significant consequences for our understanding of the physical mechanism driving this instability. It cannot depend on interfacial displacement, contradicting previous claims [29, 43], instead it must rely on effects tangential to the interface that are not directly affected by surface tension. We do not have a physical explanation for the instability mechanism, but it seems that advection of stresses by the base flow combined with relaxation plays a role.

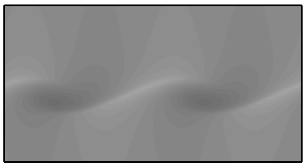

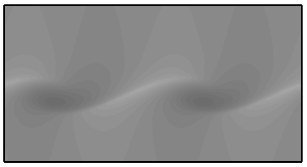

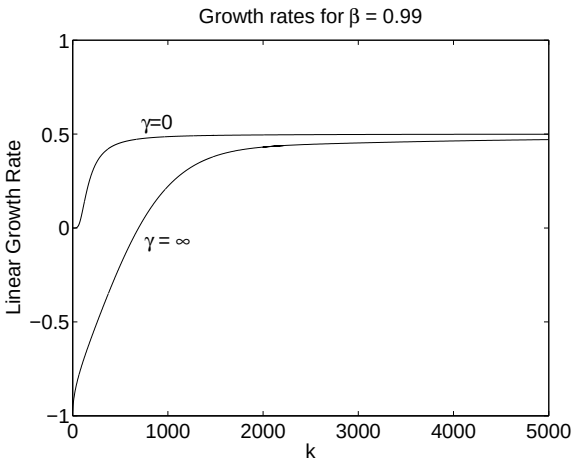

Figure 3.10: Plot of growth rate at $\beta = 0.99$ as k changes for $\xi = 0.1$ and $\Delta = 0.5$ fixed. The top curve corresponds to zero surface tension, while the bottom curve assumes it is infinite. Curves for finite values of γ lie between the two.

Oldroyd–B fluids ($\beta > 0$) with nonzero surface tension at high Weissenberg number

We have not performed a complete study of Oldroyd–B fluids with surface tension. Because of the observation in section 3.3 that tangential effects appear to determine the stability for Oldroyd–B fluids at large Wi, we expect surface tension to have no influence at large k if Wi is large.

In figure 3.10 we plot the growth rates for $\xi = 0.1,\ \Delta = 0.5$ and $\beta = 0.99$. We see that the infinite surface tension growth rate is positive as $k \to \infty$, and appears to approach the same limit as the zero surface tension growth rate.

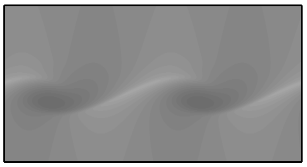

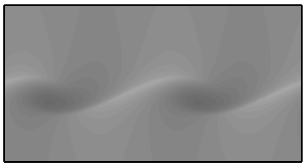

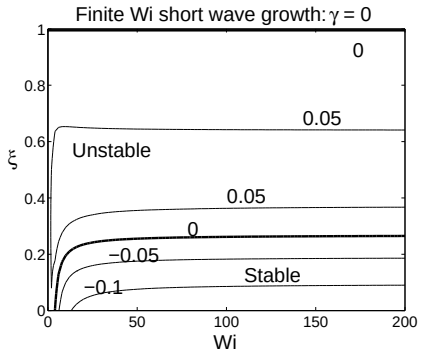

(a) Growth rate contours for UCM fluids with no surface tension. At $\xi = 1$ (identical fluids) the growth rate is zero.

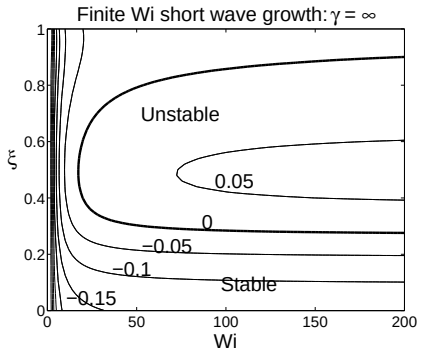

(b) Growth rate contours for UCM fluids with infinite surface tension. The growth rate tends to -1 (*i.e.*, pure relaxation) as $\mathcal{W}i \to 0$.

Figure 3.11: The effect of surface tension on the large k growth rate for finite $\mathcal{W}i$.

3.4.2 The effect of surface tension for UCM fluids at general $\mathcal{W}i$ and $k \gg 1$

Setting $\mathcal{W}i = \mathcal{O}(1)$ and $k \gg 1$ corresponds to a disturbance wavelength much shorter than the channel width as well as the relaxation length, that is, the standard short-wave limit, which has been studied in the absence of surface tension by Renardy [84] and Chen and Joseph [17].

Upon adding surface tension, Chen and Joseph [17] state that at sufficiently large k the flow is stable. This contrasts with our results at large $\mathcal{W}i$. To resolve this difference, we consider the effect of surface tension at finite $\mathcal{W}i$. We first reproduce the results of [17, 84] without surface tension and then consider the infinite surface tension limit.

As $k \to \infty$ at finite $\mathcal{W}i$, the walls become irrelevant and k disappears from the problem. The solution from (3.4) is a sum of exponentially growing and

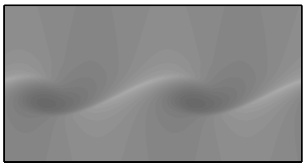

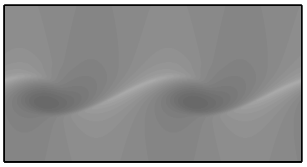

decaying terms. The growing terms must vanish, so the solutions take the form

$$\psi(y) = C_1^+(y-\omega)\exp\left(\frac{y}{Wi}\right) + C_4^+\exp\left[\xi y\left(-i+\sqrt{1+\frac{1}{\xi^2 Wi^2}}\right)\right] \quad y<0\,,$$

$$\psi(y) = C_2^-(y-\omega)\exp\left(\frac{-y}{Wi}\right) + C_3^-\exp\left[y\left(-i-\sqrt{1+\frac{1}{Wi^2}}\right)\right] \quad y>0\,.$$

Without surface tension, the four interfacial conditions define a 4×4 matrix. Setting the determinant to zero provides a quintic equation in ω found by Renardy [84] which reduces to (3.10) at large Wi. Figure 3.11(a) plots the growth rate of the most dangerous mode in (Wi,ξ) space. This figure is equivalent to figure 1 of Chen and Joseph [17] and figure 1 of Renardy [84], with different axis scalings.

In the case of infinite surface tension, we replace the normal force balance by $\psi(0)=0$. That is, we set the perturbation to the interface (and hence the cross-stream velocity) equal to zero. The same method as above gives a (significantly simpler) quintic equation for ω:

$$\begin{aligned}
&\big([R\xi^3+\xi^2Q]Wi - i\xi^2Q + iR\xi^2\big)\omega^5\\
&+\big([2i\xi^2Q+2iR\xi^3+2iR\xi^2-\xi^2+\xi^3+2i\xi Q]Wi\\
&\qquad +2i\xi^2-2R\xi^2+2\xi^2Q+2\xi Q-2R\xi\big)\omega^4\\
&+\left([-2\xi^2Q-iR\xi^2Q-4R\xi^2-2R\xi-i\xi+iRQ-4\xi Q+i\xi^3]Wi\right.\\
&\qquad \left.+2i\xi^2Q-4iR\xi-3\xi^2+4i\xi Q-3\xi-\xi^3-2iR-1+\frac{i-i\xi^2}{Wi}\right)\omega^3\\
&+\left([iQ+iR\xi^2-iR-4iR\xi-i\xi^2Q-2RQ+2R\xi Q-4i\xi Q]Wi\right.\\
&\qquad \left.-4i\xi^2-4i\xi+4R-4i-4\xi Q+\frac{2\xi-2}{Wi}\right)\omega^2\\
&+\big([-R\xi+2\xi Q-Q+i\xi^2+2R-i]Wi - iQ+4+iR+4\xi\big)\omega\\
&+[1-\xi]Wi+2i \qquad = \qquad 0\,,
\end{aligned}$$

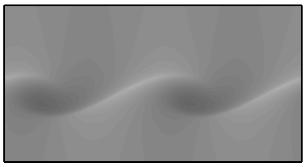

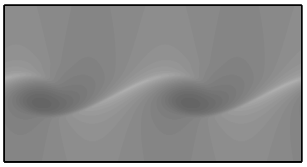

where $Q = \sqrt{\xi^2 + 1/Wi^2}$ and $R = \sqrt{1 + 1/Wi^2}$. At leading order for $Wi \to \infty$ this also reduces to equation (3.10). On solving this quintic we find a region of parameter space where the system is *unstable*, seen in figure 3.11(b). As Wi increases, figures 3.11(a) and (b) become identical.

The fact that instability persists with a growth rate of order unity even at infinite surface tension contradicts results of Chen and Joseph [17], where it is assumed that the instability is caused by displacement of the interface. This assumption leads to an inappropriate ansatz that the stabilizing effect of surface tension on the growth rate is $\mathcal{O}(k)$ as $k \to \infty$, and hence an incorrect conclusion (at large Wi) that surface tension stabilizes the flow.

3.5 Physical interpretation

Figures 3.4, 3.7 and 3.9 show that the perturbation flow in the bulk of the fluid is as large as in the boundary layer close to the interface. However, we have seen that the growth rate of the instability is independent of the position of the walls.

This implies that the instability arises at the interface and that the remainder of the flow, whether in the bulk or the wall boundary layers, has no effect. In this section we offer an explanation for how the outer region remains dynamically passive despite having a flow of comparable magnitude.

3.5.1 The UCM fluid

For clarity we focus on the infinite surface tension limit of the UCM fluids for which $\psi = 0$ at the interface and $\beta = 0$.

Because the wavelength is long compared with the channel width, the perturbation fluid velocity is parallel to the channel walls at leading order, the fluid pressure is constant across the channel, and the y-component of the

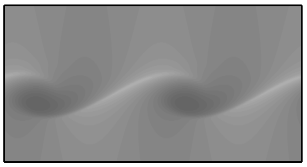

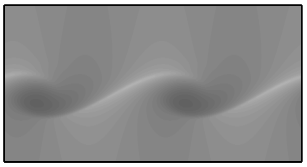

momentum equation (2.29) is automatically satisfied. The x-component of the momentum equation (2.28) becomes

$$a_{11} - i\mathrm{D}a_{12} = G\,, \tag{3.11}$$

where $G = p\tau$ is a (constant in y) rescaled perturbation pressure gradient.

The evolution of the perturbation stresses in equations (2.31)–(2.33) is controlled, through α, by the base advection y, growth ω, and relaxation τ^{-1}. In the boundary layer at the interface $y = \mathcal{O}(1)$. Outside the boundary layer $y = \mathcal{O}(k)$. It follows that $\alpha = \mathcal{O}(1)$ in the boundary layer and thus $a_{ij} \sim \psi$, but outside the boundary layer $\alpha = \mathcal{O}(k)$ and $|a_{ij}| \ll |\psi|$.

By equation (3.11), the pressure G must be at most comparable to a_{11} and a_{12} outside the interfacial boundary layer. In the interfacial boundary layer the stresses are larger and the pressure is negligible. Equation (3.11) is thus a third-order ordinary differential equation having three solutions. We find $\mathrm{D} \sim 1$. One solution grows unphysically and is discarded, leaving two solutions whose coefficients can be chosen freely. We take the y-velocity zero at the interface to satisfy the infinite surface tension assumption. The x-velocity is arbitrary, but fixed. These two conditions uniquely determine ψ throughout the interfacial boundary layer.

The solutions in the bulk are algebraic and $\mathrm{D} \sim 1/y$. At the edge of the boundary layer, the x-velocity is of comparable magnitude to its velocity in the interior. The flux of fluid in the x-direction in the boundary layer is negligible. To conserve mass, the outer region must have no net flux, but it must simultaneously satisfy an x-velocity set by the boundary layer at its edge. The pressure G is determined so as to fix the flux in the bulk.

Close to the wall the flow must satisfy the no-slip boundary condition. This forces the existence of the wall boundary layer, where $\mathrm{D} \sim 1$. There is no appreciable flux in this layer.

In this scenario there is no feedback mechanism whereby the flow in the

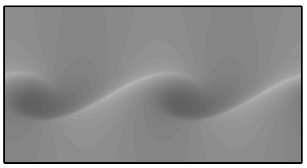

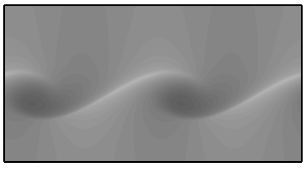

bulk can influence the flow in the interfacial boundary layer.

3.5.2 The effect of β

Including Newtonian viscosity changes the x-momentum equation to the form

$$a_{11} - i\mathrm{D}a_{12} - i\frac{\beta\tau}{(1-\beta)}\mathrm{D}^3\psi = G\,. \tag{3.12}$$

In order for the structure in each region to be affected we need: $\beta/(1-\beta) \sim 1$ in the interfacial boundary layer, $\beta/(1-\beta) \sim k$ in the bulk, and $\beta/(1-\beta) \sim 1/k$ in the wall boundary layer. Thus at large k, the wall boundary layer will be affected, the bulk region will be unaffected and the interfacial boundary layer will be affected only if β is large enough. The bulk region is unaffected and does not feed back into the interfacial layer. The stability is again determined only by effects in the interfacial boundary layer.

The structure shown in figure 3.7 ($\beta = 0.99,\ \ k = 2000$) suggests that the wall boundary layer expands and has the same length scale as the bulk region.

3.6 An additional instability of Oldroyd–B fluids

In figure 3.12 we plot the growth rates for two unstable modes for $\beta = 0.99$, $\xi = 0.5$, and $\Delta = 0.7$. As $k \to \infty$ one of the modes has fixed growth rate. This is the mode discussed earlier in section 3.3. The other mode has higher growth rate at intermediate values of k, but stabilizes as $k \to \infty$.

We do not study this mode in detail. The perturbation flow for $k = 200$ is shown in figure 3.13. The real part of ω has a different sign from the earlier fast-flow instability, and so this mode travels in the opposite direction relative to the interface.

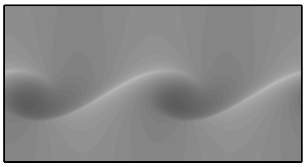

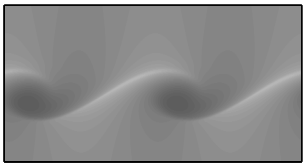

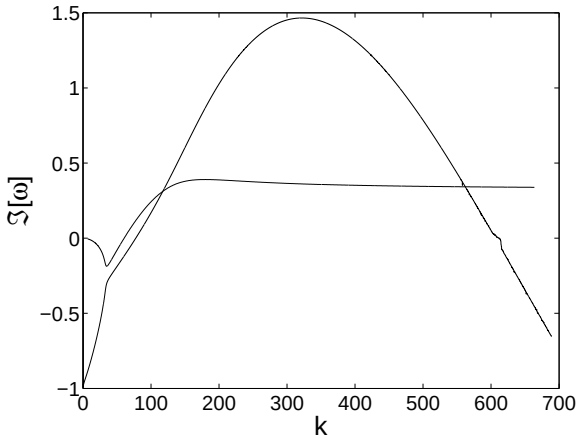

Figure 3.12: Growth rates for Oldroyd–B fluids with $\beta = 0.99$, $\xi = 0.5$ and $\Delta = 0.7$.

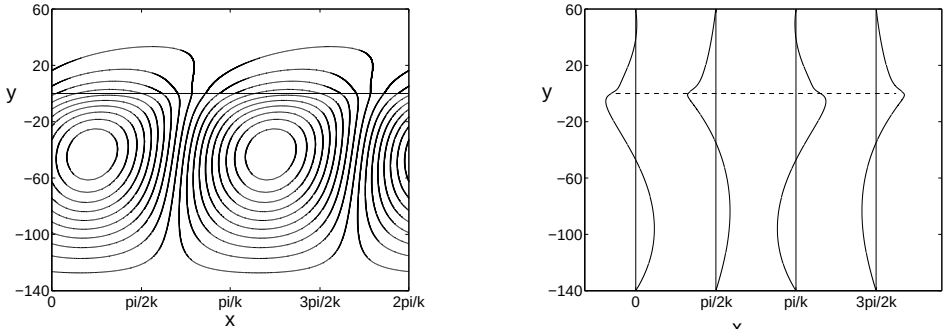

(a) Streamlines.

(b) Horizontal perturbation flow. Note the boundary layers at the interface but not at the walls.

Figure 3.13: Unstable perturbation flow of Oldroyd–B fluid with $\beta = 0.99$, $\xi = 0.5$, $\Delta = 0.7$, and $k = 200$. For these parameters $\omega = 1.6084 + 1.0262i$. Compare with figure 3.4 where $\beta = 0$, $\Delta = 0.7$, $k = 30$, and $\xi = 0.5$.

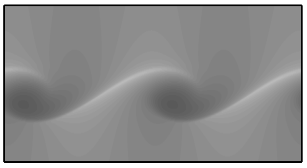

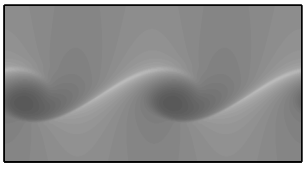

3.7 Small Wi instability

The only remaining asymptotic limit not covered by our work or previous work is $1 \gg k \gg Wi$, where the channel width is large compared to the wavelength, which in turn is large compared to the relaxation length scale.

For the UCM fluid, we use solution (3.4). The walls are at $y = \mathcal{O}(k)$ from the interface. The value of k is much larger than Wi, so two solutions grow and two solutions decay away from the interface. Requiring decay returns us to the analysis of Renardy [84] where she found instability at small Wi when $\xi \neq 1$.

In the Oldroyd–B case, we again require decaying solutions, and so we obtain the results of Wilson and Rallison [103, 104] for small Wi. They also found instability for $\xi \neq 1$ at small Wi, but with small growth rate of order Wi^6.

3.8 Discussion

There are two surprising features of the fast-flow instability: the first is that the growth rate is determined entirely within a boundary layer at the interface, but the perturbation flow fills the entire channel. The second is that the instability persists even with asymptotically large surface tension.

Section 3.2.1 shows that the growth rate depends only on continuity of tangential acceleration and the tangential force balance at the interface. Close to the interfacial boundary layer, the streamfunction of the outer flow is proportional to $ikU - i\omega$ in dimensional variables. This term drops out of the tangential conditions and so the flow in the outer region has no influence on the stability. We will see in the study of Poiseuille flow (chapter 4) that this is a more general result for large Wi flows. When the form of U changes, ψ changes accordingly, and the outer solution again drops out of the tangen-

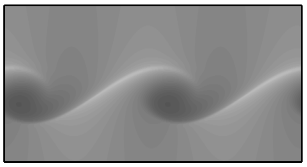

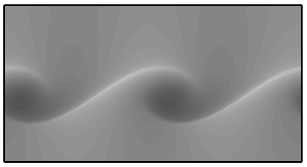

tial conditions. Consequently this instability is found in more general flows in different geometries.

The fact that the instability exists for infinite surface tension happens because the normal force balance at the interface decouples from the rest of the analysis and plays no role in the instability. This observation conflicts with a widely-held assumption about the driving force behind purely elastic interfacial instabilities namely [57]:

> *the mechanism of purely elastic interfacial instabilities has been demonstrated to be the coupling of the jump in base flow normal stresses across the interface and the perturbation velocity field.*

The jump in normal stress does not enter into our analysis, and so a distinct mechanism is involved, which we have not determined.

Throughout this analysis we have assumed that the Reynolds number is zero. However, even with non-zero Reynolds number, the boundary layer thickness can be made arbitrarily small by choosing a large enough value of k so that inertial effects are unimportant. Consequently the instability is expected to persist in the presence of inertia.

We end the chapter with a brief comment on the assumption $\xi < 1$. The symmetries of Couette flow allow us to rescale time with the largest relaxation time without loss of generality. In other flows (in particular the flows of chapters 4 and 5) we cannot assume that $\xi < 1$. For such flows, our result implies that the flow is unstable to the fast-flow instability if either $\xi_c < \xi < 1$ or $1 < \xi < \xi_c^{-1}$.

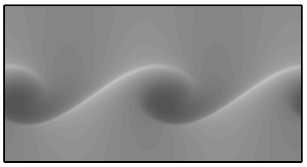

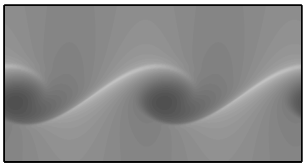

Chapter 4

Stability of three-layer symmetric channel Poiseuille flow at large Wi

In this chapter we consider three-layer symmetric channel Poiseuille flow, the two-dimensional analog of core-annular flow through a pipe. Throughout this chapter we assume the non-dimensionalization of section 2.3.3. The dimensionless base flow profile is shown in figure 4.1. The symmetries of the problem no longer allow us to assume that $\xi < 1$.

In section 2.3.3 we developed two equivalent forms of the perturbation equations in the dimensionless variables η [equations (2.55)–(2.66)] and $Y = \eta^2$ [equations (2.45)–(2.54)]. We consider the large Wi limit, using the leading order (as $Wi \to \infty$) equations. Our numerics solve the η form of the equations.

As $k \to 0$, the longest length scale is the wavelength, and the results of [103, 27] show that if both $\xi < 1$ and $\Delta < \sqrt{2} - 1$ or both $\xi > 1$ and $\Delta > \sqrt{2} - 1$, the flow is unstable to long-wave varicose modes. If $\xi > 1$ the flow is unstable to long-wave sinuous modes, regardless of Δ.

For $k \to \infty$, the fast-flow results from chapter 3 suggest stability if either

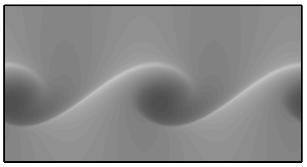

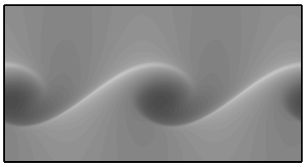

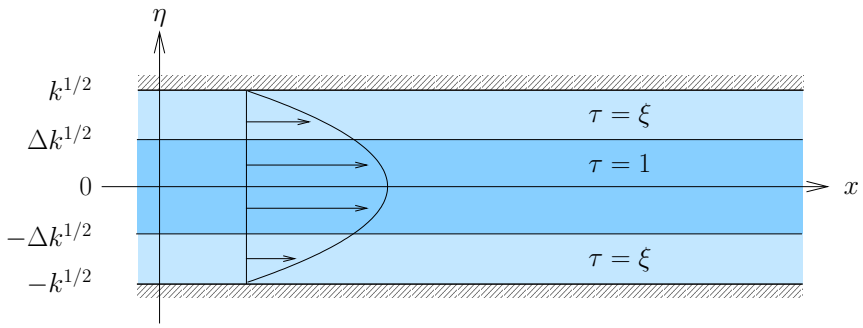

Figure 4.1: Poiseuille flow profile $U = k - \eta^2$ in the dimensionless variable η.

$\xi < \xi_c \approx 0.28$ or $\xi > \xi_c^{-1} \approx 3.6$. We postpone until later some potential complications in applying the Couette results directly to Poiseuille flow with two interfaces (*e.g.*, the perturbation flow found earlier does not decay, so the interfaces may interact). The fast-flow growth rate depends on an interfacial boundary layer much thinner than the channel width. Its width is determined by the local shear rate at the interface and is given in dimensional variables by $1/U'\tau k$. In section 4.1 we see that so long as the shear rate is effectively constant over the boundary layer thickness, the growth rates limit to the Couette values as $k \to \infty$. If, however, the dimensional value of U'/U'' at the interface is comparable to or smaller than $1/U'\tau k$, then the shear rate changes over the boundary layer length scale and the stability results change. This occurs whenever the central fluid occupies a sufficiently small fraction of the flow. The resulting *narrow-core* behavior leads to new instabilities and is the main subject of this chapter.

Using the results of chapter 3 and the long-wave analysis we can choose ξ and Δ to make the $k \to 0$ and $k \to \infty$ limits stable or unstable independently. In particular choosing $\xi < \xi_c$ and $\Delta > \sqrt{2} - 1$ stabilizes varicose and sinuous modes both as $k \to 0$ and $k \to \infty$. It is frequently assumed (and has been explicitly claimed for this flow profile [54, 85]) that stability at all wave-

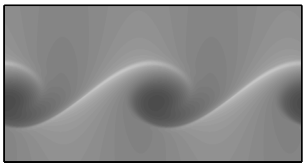

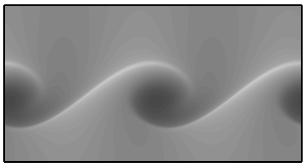

numbers follows from stability in these two limits. Consequently relatively little study has been done at intermediate wavenumbers. To motivate a more complete study, we consider some sample dispersion relations for UCM fluids with $Wi \gg 1$ that contradict this assumption due to narrow-core effects.

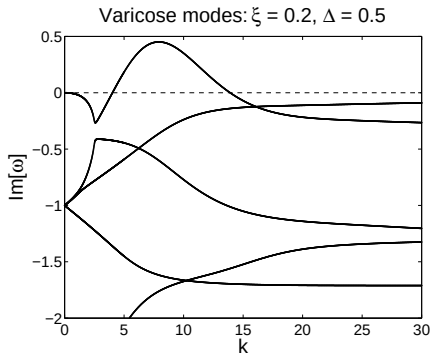

(a) Growth rates of varicose modes for $\xi = 0.2$, $\Delta = 0.5$ with $Wi \gg 1$. There is instability only for intermediate wavenumbers.

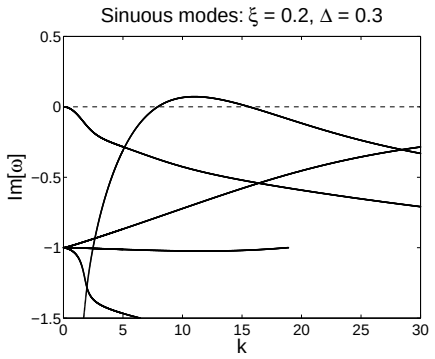

(b) Growth rates of sinuous modes for $\xi = 0.2$, $\Delta = 0.3$ with $Wi \gg 1$. A similar instability exists. (Note that a mode enters the continuous spectrum at $k \approx 20$.)

Figure 4.2: Dispersion relations for sample UCM flows.

Figure 4.2(a) shows the growth rates of varicose modes for $\xi = 0.2$ and $\Delta = 0.5$, a set of parameters for which both sinuous and varicose modes are stable as $k \to 0$ and $k \to \infty$. Figure 4.2(b) shows the growth rates of sinuous modes for $\xi = 0.2$ and $\Delta = 0.3$, for which sinuous modes are stable as $k \to 0$ and $k \to \infty$. Both cases have instability at intermediate k, showing that we must perform a more complete analysis to be assured of stability at all wavenumbers. Figure 4.3 shows that the behavior can be more complicated, with multiple unstable modes or regions appearing. These instabilities frequently (but not always) travel faster than the centerline of the base flow, so effects beyond advection of material are needed to understand how the wave travels.

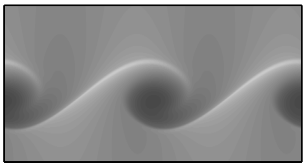

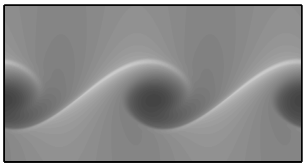

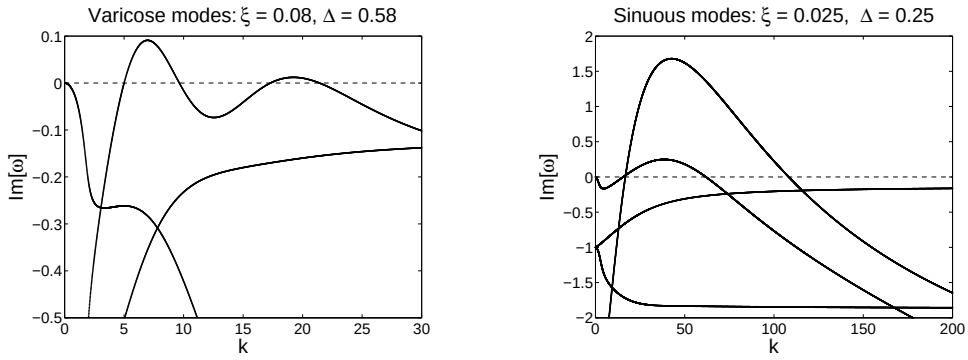

(a) Growth rates of varicose modes for $\xi = 0.08,\ \Delta = 0.58$. Two distinct ranges of k are unstable.

(b) Growth rates of sinuous modes for $\xi = 0.025,\ \Delta = 0.25$. Two distinct modes are unstable.

Figure 4.3: Dispersion relations for sample UCM flows.

To demonstrate the distinct families of instabilities, we plot contours of the growth rate in (k, Δ) space for different values of ξ in figures 4.4–4.6. We see the long-wave varicose instability ($k \to 0,\ \Delta < \sqrt{2}-1$) and the Couette-like fast-flow instabilities (Δ fixed, $k \to \infty,\ \xi > \xi_c$) as well as evidence of a $k^{-1/2}$ scaling, corresponding to the new narrow-core instability.

The chapter is organized as follows: we first consider the fast-flow regime in section 4.1. In section 4.2 we present results about the narrow-core regime. Section 4.3 briefly discusses some additional instabilities which appear, but cannot be explained by the analysis presented here.

For simplicity, we focus on the UCM fluid and consider the Oldroyd–B fluid only briefly to show that the behavior is qualitatively similar. The symmetries no longer allow us to assume that the ratio of the outer relaxation time to the inner relaxation time ξ is less than 1 without loss of generality. For the majority of the chapter we take $\xi < 1$ for which sinuous long-wave modes are stable, but when we study the narrow-core instability at large k, we also look at $\xi > 1$.

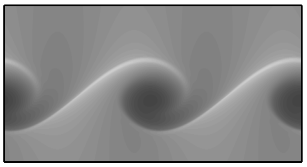

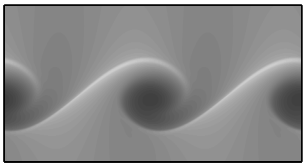

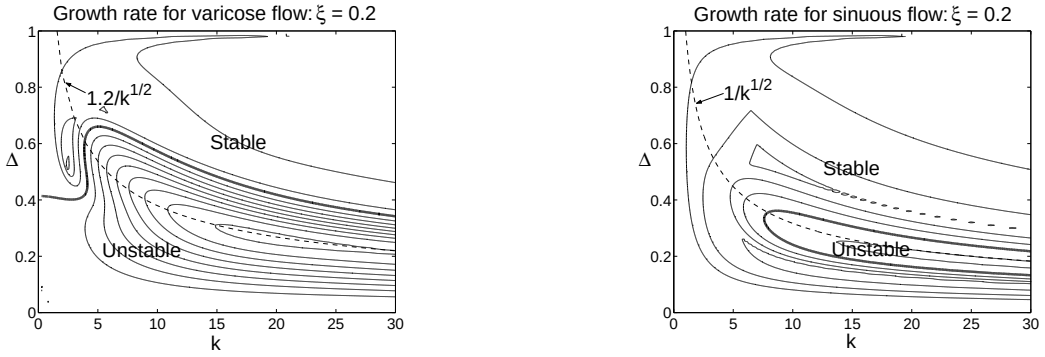

(a) Varicose: $\xi = 0.2$.

(b) Sinuous: $\xi = 0.2$.

Figure 4.4: Growth rate contour plots of the most dangerous mode in (k, Δ) space for $\xi = 0.2 < \xi_c$. For fixed Δ, the flow is stable as $k \to \infty$, with the same growth rate for sinuous and varicose modes. The narrow-core regime is observed where $\Delta \sim k^{-1/2}$.

4.1 Fast-flow instability ($k \to \infty$)

In this section we show that the fast-flow instability found for Couette flow in chapter 3 persists in Poiseuille flow with the same growth rate, although the mode structure changes qualitatively. In Couette flow the growth rate is determined by effects within a boundary layer about the interface. In Poiseuille flow with Δ fixed, at large enough k the shear rate is effectively constant over the boundary layer length scale, and so we expect similar behavior. However, the result in Couette flow depends on the algebraic terms cancelling out of the tangential interfacial conditions in the construction of the matrix N (3.9). The structure of the algebraic terms changes in Poiseuille flow, so it is not obvious *a priori* that this same cancellation occurs.

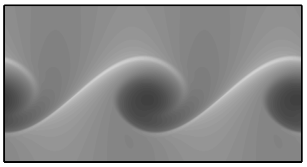

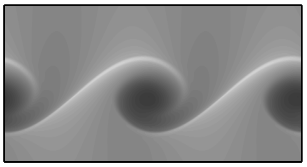

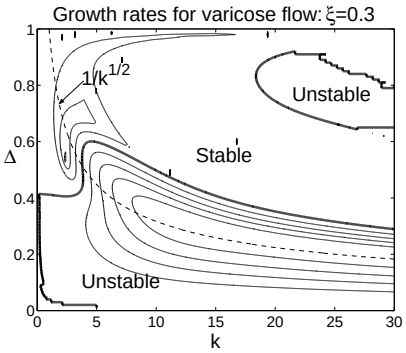

(a) Varicose: $\xi = 0.3$.

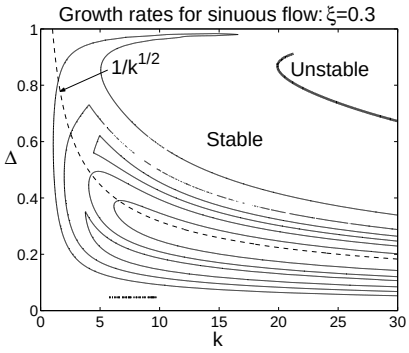

(b) Sinuous: $\xi = 0.3$.

Figure 4.5: Growth rate contour plots of the most dangerous mode in (k, Δ) space for $\xi = 0.3 > \xi_c$. For fixed Δ, the flow is unstable as $k \to \infty$, with the same growth rate for sinuous and varicose modes. We again see the narrow-core regime where $\Delta \sim k^{-1/2}$. Some numerical problems can be observed in the lower left and upper right corners where parameter continuation with the shooting method has difficulties.

4.1.1 The UCM fluid

Figure 4.7 shows the perturbation flow for sinuous and varicose modes with $\xi = 0.5$, $\Delta = 0.7$ and $k = 30$. In both cases, the flow decays exponentially in the less elastic outer fluid, but is everywhere large in the inner fluid. This mode structure differs from the Couette result where the perturbation flow is large in both fluids. After accounting for the change in frame of reference, the value of ω predicted from the results of section 3.2.1 is $\omega = (1 - \Delta^2)k + 0.30544 + 0.06603i + \mathcal{O}(1/k)$ which gives $\omega = 15.60544 + 0.06603i + \mathcal{O}(1/k)$. Our calculated results are in good agreement: for the varicose mode $\omega = 15.6203 + 0.0598i$, while $\omega = 15.6208 + 0.0590i$ for the sinuous mode.

In the velocity plots in figure 4.7 there is a hint of a boundary layer

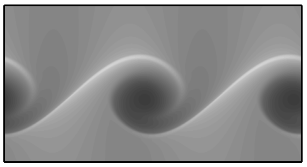

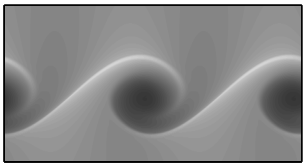

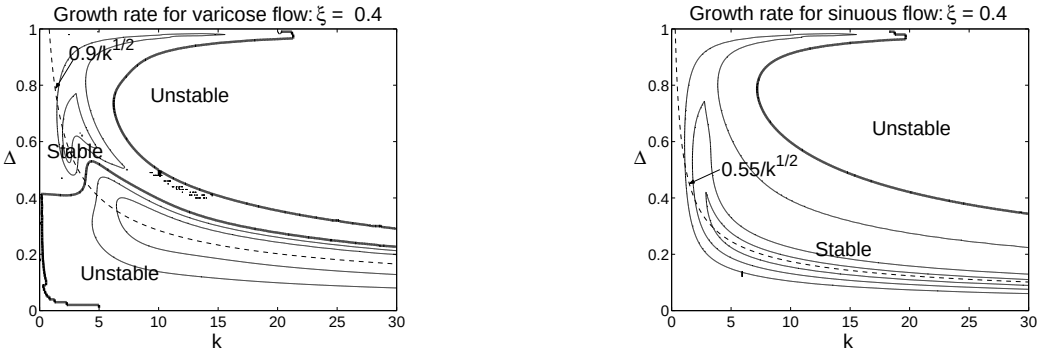

(a) Varicose: $\xi = 0.4$.

(b) Sinuous: $\xi = 0.4$.

Figure 4.6: Growth rate contour plots of the most dangerous mode in (k, Δ) space for $\xi = 0.4 > \xi_c$. For fixed Δ, the flow is unstable as $k \to \infty$, while the narrow-core regime is seen where $\Delta \sim k^{-1/2}$.

close to the center-line. This boundary layer plays a role in preventing the interfaces from interacting. We can see this by eliminating the lower interface to consider a single interface. The resulting perturbation flow is shown in figure 4.8 for $\xi = 0.5$, $\Delta = 0.7$ with $k = 30$ and $k = 500$. For $k = 30$, the value of ω is $\omega = 15.6205 + 0.0594i$, close to the prediction above, while for $k = 500$, it is $\omega = 255.3063 + 0.0657i$, which matches the predicted value of $\omega = 255.30544 + 0.06603i + \mathcal{O}(1/k)$ well. The boundary layer close to the center-line allows for a return flow which keeps the net flux zero. This permits the flux to decay in the outer fluid and the lower half of the channel. The width of this boundary layer is found by balancing U'/U'' with $1/U'\tau k$ (in dimensional variables) and is given by $y \sim L/\sqrt{U_0 \tau k}$ or $\eta \sim 1$.

In order to study the growth rate analytically, we follow the analysis of section 3.2.1, and show that the stability condition becomes identical to the condition for Couette flow. We re-express the Y form of the vorticity and

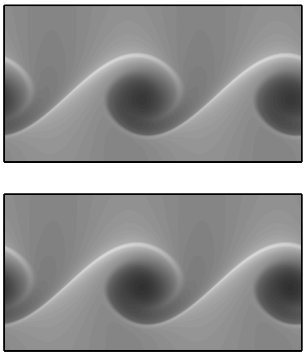

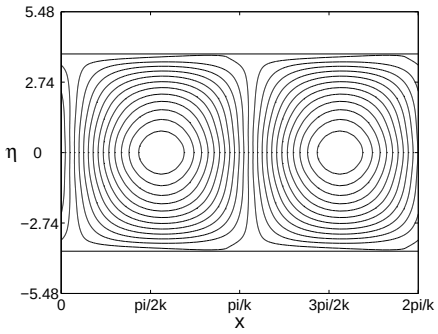

(a) Streamlines for sinuous mode.

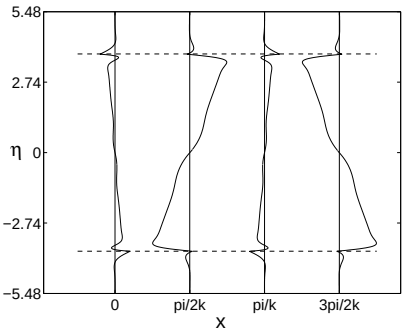

(b) Horizontal perturbation velocity.

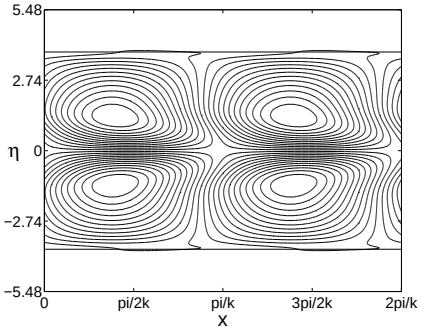

(c) Streamlines for varicose mode.

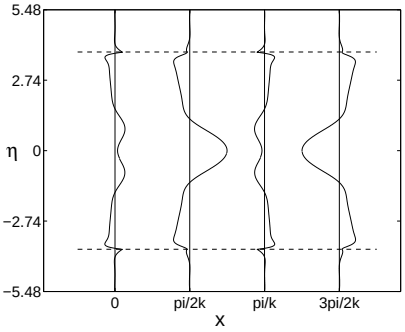

(d) Horizontal perturbation velocity.

Figure 4.7: Perturbation flows of the sinuous and varicose modes for $\xi = 0.5$, $\Delta = 0.7$ and $k = 30$.

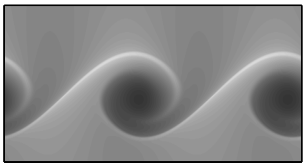

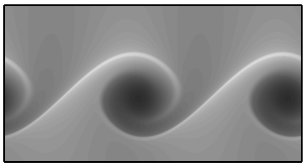

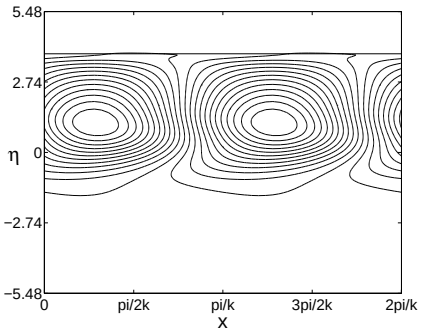

(a) Single interface streamlines with $k = 30$.

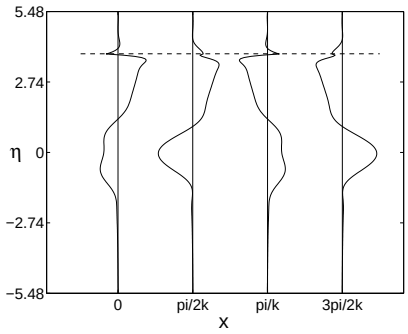

(b) Single interface perturbed x-velocity with $k = 30$.

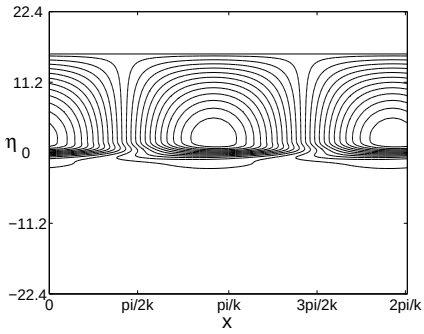

(c) Single interface streamlines with $k = 500$.

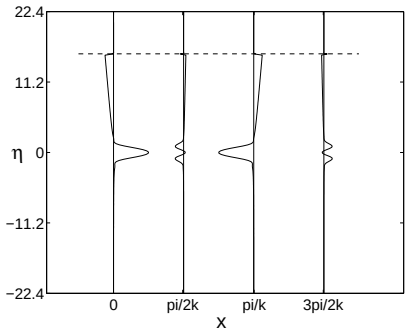

(d) Single interface perturbed x-velocity with $k = 500$.

Figure 4.8: Perturbation flows with a single interface for $\xi = 0.5,\ \Delta = 0.7$.

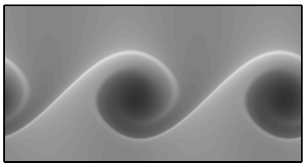

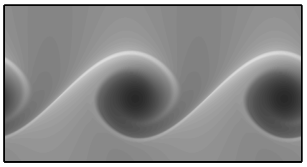

constitutive equations (2.45)–(2.54) in terms of ψ

$$\begin{aligned}
&\psi_{YYYY} + 2i(\alpha^{-1} - \tau)\psi_{YYY} - 2(\alpha^{-1} - \tau)^2\psi_{YY} + 4i\tau(\alpha^{-1} - \tau)\psi_Y + 4\frac{\tau^2}{\alpha^2}\psi \\
&\frac{3}{Y}\left(\psi_{YYY} + \frac{3}{2}(\alpha^{-1} - \tau)\psi_{YY} - (\alpha^{-1} - \tau)^2\psi_Y + \frac{i\tau}{\alpha}(\alpha^{-1} - \tau)\psi\right) \\
&+ \frac{3}{4Y^2}\left(\psi_{YY} + i(\alpha^{-1} - \tau)\psi_Y + \frac{\tau}{\alpha}\psi\right) \qquad = 0\,.
\end{aligned}$$

If the interface lies outside the boundary layer at the center-line, then $Y = \Delta^2 k$ is large at the interface. For large Y we solve the vorticity equation using an ansatz based on the correspondence with the Couette equations. The Couette solution can be expressed as the sum of two exponential terms, one proportional to $\exp[(1+i)\tau Y]$ and the other proportional to $\exp[(-1+i)\tau Y]$, together with two algebraic terms. For the Poiseuille flow, we therefore anticipate a solution in each layer of the form

$$\psi(Y) = C_1 f_1(Y) + C_2 f_2(Y) + C_3 g_1(Y) e^{(1+i)\tau Y} + C_4 g_2(Y) e^{(-1+i)\tau Y}\,, \quad (4.1)$$

and find that

$$\begin{aligned}
f_1(Y) &= Y\tau + \omega\tau\,, \\
f_2(Y) &= \frac{f_1(Y)}{\sqrt{Y\tau}}\left(1 + \frac{i}{4Y\tau} - \frac{9}{80Y^2\tau^2} - \frac{27i}{448Y^3\tau^3} + \frac{11 + 64i\omega\tau}{768Y^4\tau^4} + \cdots\right), \\
g_1(Y) &= (Y\tau)^{-3/4}\left(1 + \frac{15/32 - 3i/8}{Y\tau} + \frac{273/2048 - 237i/256}{Y^2\tau^2} + \cdots\right), \\
g_2(Y) &= (Y\tau)^{-3/4}\left(1 + \frac{-15/32 - 3i/8}{Y\tau} + \frac{273/2048 + 237i/256}{Y^2\tau^2} + \cdots\right).
\end{aligned}$$

As in Couette flow [equations (3.8) and (3.9)] the algebraic terms drop out of the interfacial conditions for tangential force balance and tangential acceleration: the coefficient C_2 is too small to affect the equations and C_1 exactly cancels from the equations. The disappearance of C_1 follows by the same argument as in section 3.2.1: f_1 is proportional to $U - c$, and so its contribution

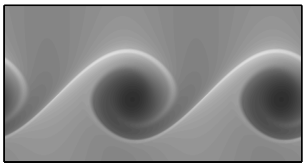

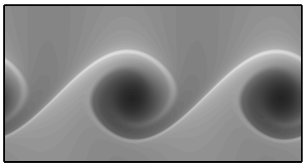

to the tangential interfacial conditions is zero. The tangential force balance and continuity of tangential acceleration conditions are therefore satisfied only by the exponential terms.

The terms which grow exponentially away from the interface must be small at the interface compared to the terms which decay away from it. So the only terms which can satisfy the two tangential conditions at the interface are the exponentially decaying solutions on either side, $g_1(Y)\exp[(1+i)\tau Y]$ for $Y < \Delta^2 k$ and $g_2(Y)\exp[(-1+i)\tau Y]$ for $Y > \Delta^2 k$. To leading order in Y, we can treat g_1 and g_2 as constant at the interface compared to the exponentially decaying terms.

We have reduced our conditions at the interface to be the same as in Couette flow. The conditions must be satisfied by ψ of the same form as in Couette flow. Consequently the growth rates found in UCM Poiseuille flow with the interface at large Y must be identical to those of Couette flow.

4.1.2 Oldroyd–B fluids

In section 3.3 we saw that for Couette flow of an Oldroyd–B fluid, the flow is unstable at large k if β is large enough. We find the same effects in Poiseuille flow. We have not found any new behavior of this instability in Oldroyd–B Poiseuille flow.

4.2 Narrow core instability ($\Delta \sim k^{-1/2},\ k \to \infty$)

Figures 4.4–4.6 show an asymptotic scaling with $\Delta \sim k^{-1/2}$ as $k \to \infty$ in the UCM fluid. This indicates the presence of a class of instabilities distinct from fast-flow. These instabilities exist for both sinuous and varicose modes. The appropriate equations are expressed in terms of η (2.55)–(2.66).

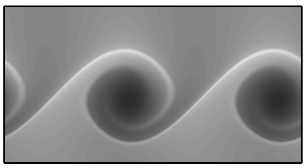

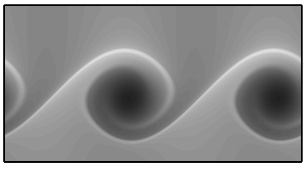

4.2.1 UCM fluids

Stability at moderate k

Although these modes are most distinct at large values of k, they are present for k as small as 5.

We look first at varicose modes. The plots of figures 4.4–4.6 have an unstable "tongue" in the marginal stability curve at $k \approx 5$. In figure 4.9 we show similar plots for smaller ξ showing multiple unstable tongues. Our results suggest that the maximum number for UCM fluids is three. As ξ increases, the tongues progressively disappear until at $\xi \approx 0.56$ they no longer exist and so there is no instability at moderate k for $\Delta > \sqrt{2} - 1$ (the $k \to 0$ stability boundary).

These tongues are of particular significance because they can give values of Δ for which both $k \to 0$ and $k \to \infty$ limits are stable, but instability exists at moderate values of k. We see this in figure 4.4(a). This contradicts claims [54, 85] that stability as $k \to 0$ and $k \to \infty$ implies stability at all wavenumbers in the absence of a destabilizing viscosity difference.

In figure 4.9 we see that as ξ increases past about 0.09 the second tongue merges with the first, while if ξ becomes small it retreats to larger values of k. The location of the local maxima of the marginal stability curve gives us information about the tongues. We plot the first two local maxima in figure 4.10(a). When $\xi = 0.069$ the first two tongues are marginally stable at $\Delta = 0.6023$. As Δ decreases past 0.6023 two instabilities with different wavenumber arise, shown in figure 4.10(b).

We turn now to sinuous modes. For moderate k, figures 4.4–4.6 show that if ξ is too large, no instability exists. However, when ξ is small, more than one unstable mode can exist. In figure 4.11 where $\xi = 0.025$, two modes are unstable, both with the $\Delta \sim k^{-1/2}$ scaling. The two modes have substantially different growth rates, shown in figure 4.12. The faster growing mode has

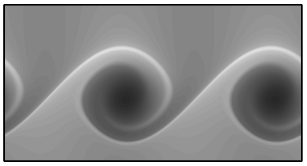

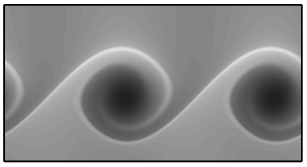

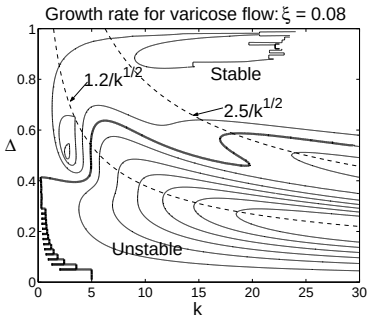

(a) At $\xi = 0.08$ a new unstable tongue appears with $k^{-1/2}$ behavior.

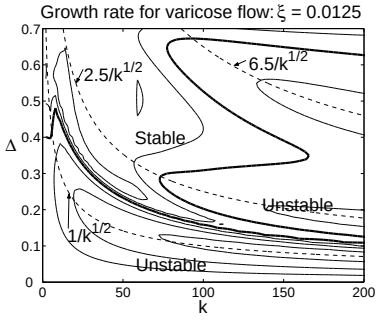

(b) At $\xi = 0.0125$ a third tongue is visible at large k (note reduced vertical and extended horizontal axes).

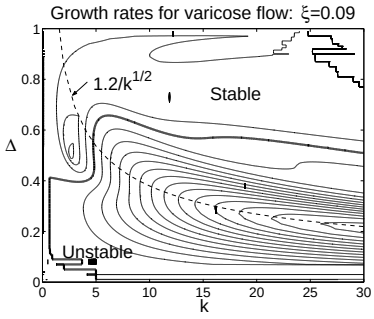

(c) At $\xi = 0.09$ the new tongue has almost merged with the primary tongue.

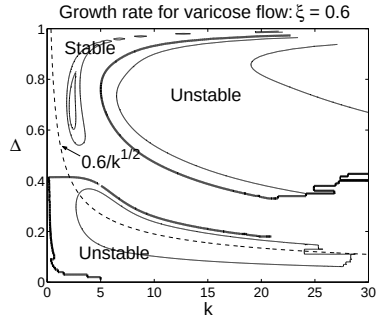

(d) At $\xi = 0.6$ the $k^{-1/2}$ mode no longer has a significant effect for $k \approx 5$.

Figure 4.9: Varicose modes. More than one unstable tongue exists at small ξ, while the tongue at $k \approx 5$ disappears for larger ξ. The shooting method used has difficulties with k and Δ both small or with large k. Figure (b) was created using the spectral method.

a wavespeed greater than 1, the base flow velocity at the center-line of the channel. Removing that mode in figure 4.11(b) we get a better picture of the less unstable mode.

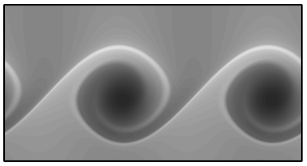

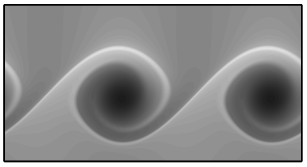

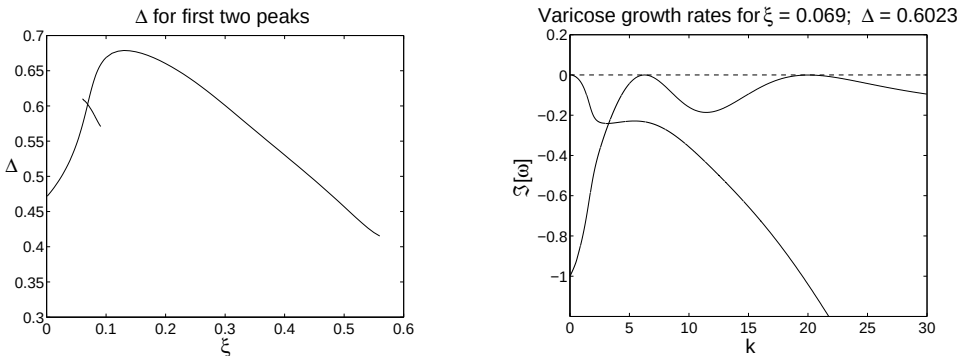

(a) Position of maxima of first two tongues.

(b) At $\xi = 0.069$, two bifurcations occur as Δ crosses 0.6023.

Figure 4.10: We followed the maxima of the first two tongues using shooting. The second tongue only has a local maximum for a short range of ξ. At $\xi = 0.069,\ \Delta = 0.6023$ both tongues are marginally stable.

Stability at large k

When k is large, the narrow-core modes are more distinct. The location of the walls ($\eta = k^{1/2}$) have no influence on the instability. The complex frequency ω scales like $k + \mathcal{O}(1)$, and so $\omega - k$ is independent of k in α and the kinematic boundary condition. The only other appearance of k (or Δ) in the problem is in the combination $\Delta k^{1/2}$. Consequently the growth rate depends only on ξ and $\Delta k^{1/2}$.

Figure 4.13 explicitly shows that $\Delta \sim k^{-1/2}$ for the fastest growing mode. Choosing $\xi = 0.2$ and letting k change, we plot the value of Δ giving the largest growth rate. Once k is larger than 10, the scaling is clear.

Because $\eta = \mathcal{O}(1)$ at the interface, the equations cannot be simplified and we cannot find an asymptotic expression for ψ close to the interface. To study the large k asymptotics, we turn to numerical methods.

In figure 4.14 we show growth rates of varicose modes at $k = 1000$ and $k =$

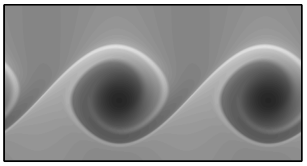

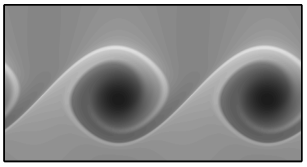

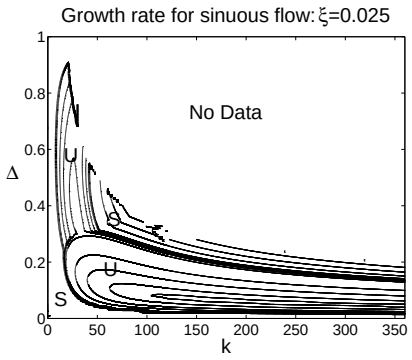

(a) Growth rate of the most dangerous mode. One unstable mode obscures another for large k.

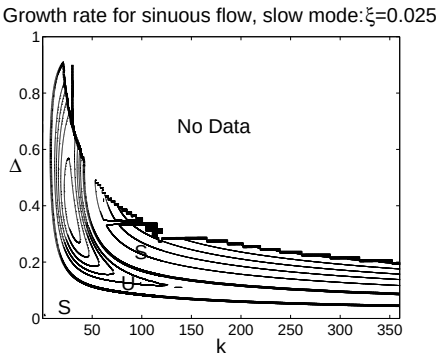

(b) Growth rate of the most dangerous mode having wavespeed less than 1.

Figure 4.11: When $\xi = 0.025$ we see more than one unstable sinuous mode at the same interface location. One mode travels faster than the center-line. The other travels slower than the center-line (and slower than the interface). The numerics could not resolve large values of $\Delta k^{1/2}$.

4000, keeping $\Delta k^{1/2}$ moderate. The figures are almost identical, suggesting that they accurately represent the $k \to \infty$ behavior.

Figures 4.15(a) and (b) show the growth rate of varicose modes at large k but moderate $\Delta k^{1/2}$ as a function of ξ. The first shows growth rates for $0 < \xi < 1$, while the second shows $1 < \xi < \infty$ with a scaled horizontal axis. Figure 4.15(c) shows the marginal stability curves for $0 < \xi < \infty$, with the same scaling of the axis for $\xi > 1$.

As $\xi \to 0$ the varicose narrow-core instability exists for any value of $\Delta k^{1/2}$. If $\Delta k^{1/2} \approx 1$, the growth rates become large. There is a small island of stability for $\xi \approx 0.06$, $\Delta k^{1/2} \approx 2$. As ξ is increased past $\xi_c \approx 0.28$ a further instability appears for sufficiently large $\Delta k^{1/2}$. This is the fast-flow instability discussed in the previous section, and is clearly distinct from the

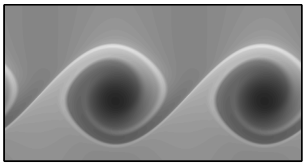

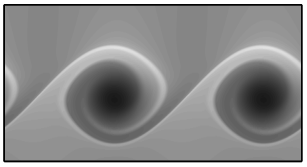

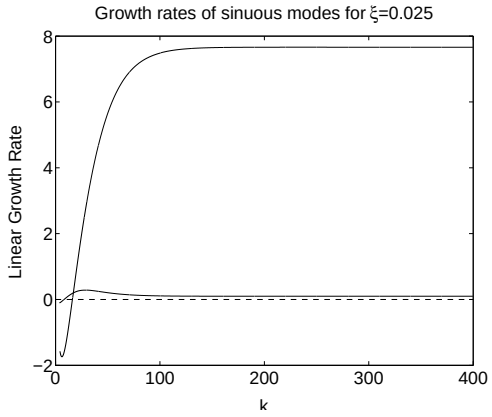

Figure 4.12: Growth rates for sinuous modes with $\xi = 0.025$ as k changes. Δ is chosen independently for each mode to maximize the growth rate. The growth rates tend to a constant at large k. Figure 4.17 shows the growth rates for fixed large k as ξ changes.

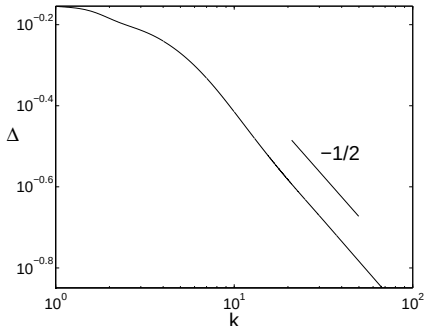

Figure 4.13: Interface location for fastest growing varicose mode at each wavenumber with $\xi = 0.2$. For large k, the fastest growing mode has $\Delta \sim k^{-1/2}$.

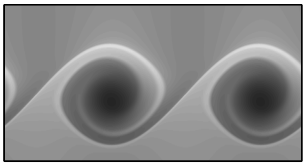

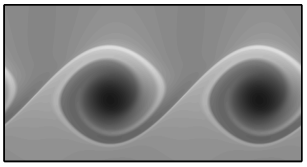

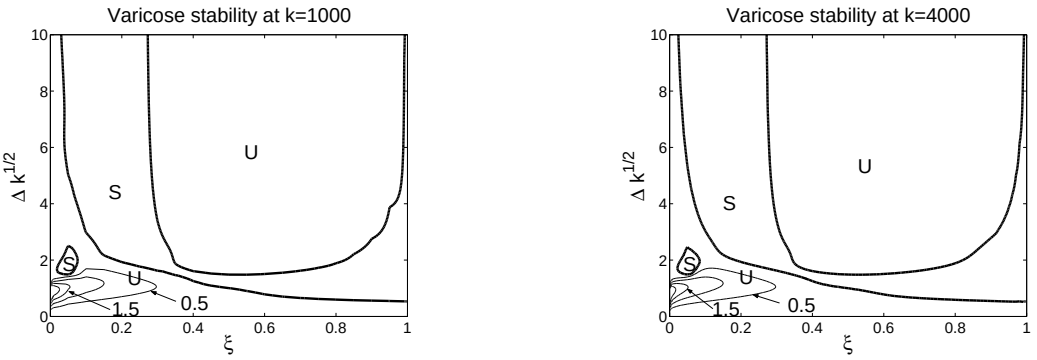

(a) Varicose: $k = 1000$.

(b) Varicose: $k = 4000$.

Figure 4.14: The difference between growth rates when $k = 1000$ and $k = 4000$ is small.

narrow-core instability. For ξ sufficiently close to 1, the fast-flow instability becomes stable. As $\xi \to 1$ (identical fluids), the growth rate approaches zero.

The growth rate generically crosses zero as ξ passes through 1, and so in figure 4.15(c) stability reverses moving from $\xi \to 1^-$ to $\xi \to 1^+$. That is, if the flow is stable [unstable] with a slightly more elastic inner fluid, then making the outer fluid slightly more elastic destabilizes [stabilizes] the flow. When $1 < \xi < \xi_c^{-1} \approx 3.6$ the fast-flow instability is present at sufficiently large $\Delta k^{1/2}$. As ξ increases past ξ_c^{-1}, the unstable region shrinks rapidly, but does not disappear as $\xi \to \infty$. The distinction between the fast-flow and narrow-core instability is less clear here. For sufficiently small $\Delta k^{1/2}$ there is stability for any $\xi > 1$.

We consider the stability to sinuous perturbations at large k in figure 4.16. We find the fast-flow instability at sufficiently large $\Delta k^{1/2}$ if $\xi_c < \xi < 1$ or $1 < \xi < \xi_c^{-1}$, but there is another instability for small ξ. This narrow-core instability is qualitatively different from the varicose narrow-core instability in that it has much higher growth rates and a maximum value of ξ of about

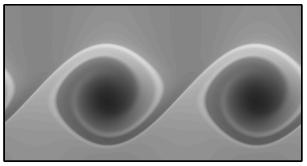

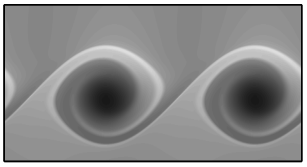

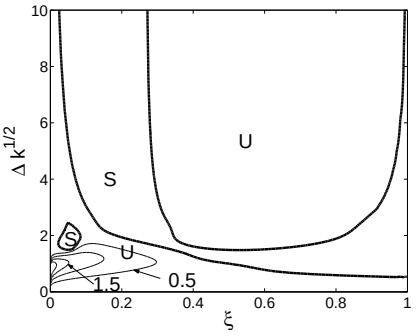

(a) Varicose: $\xi < 1,\ k = 4000$.

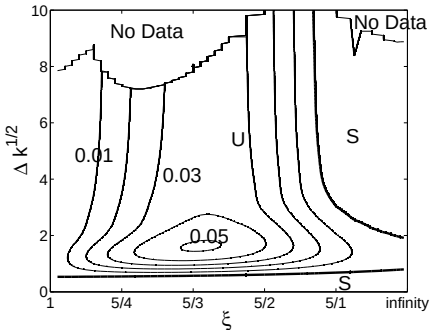

(b) Varicose: $\xi > 1,\ k = 4000$.

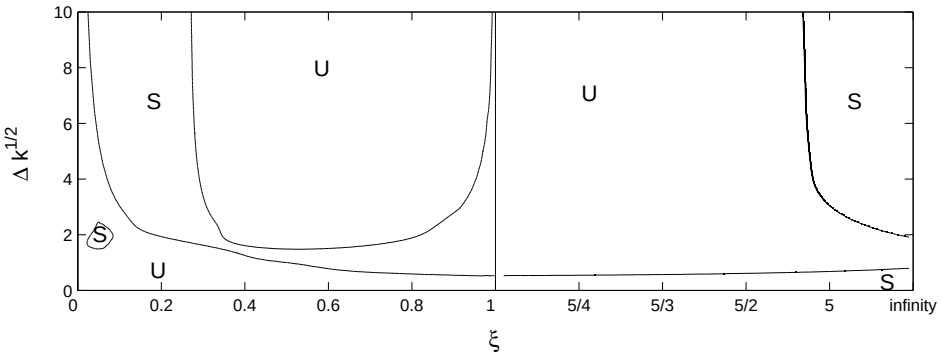

(c) Varicose marginal stability curves, $k = 4000$.

Figure 4.15: Contour plots of growth rates of varicose modes in $(\xi, \Delta k^{1/2})$ space. U and S denote unstable and stable regions respectively. For $\xi > 1$ the horizontal axis has been rescaled.

0.25. When ξ is greater than 1, a similar picture emerges to the varicose modes, except that there is no stable region at small $\Delta k^{1/2}$.

We compare the growth rates of the unstable varicose and sinuous modes in figure 4.17. At small values of ξ the varicose growth rate diverges like $\ln(\xi)$, while the sinuous growth rates diverge like $1/\xi$, with a (divergent) correction

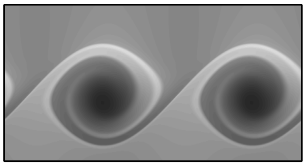

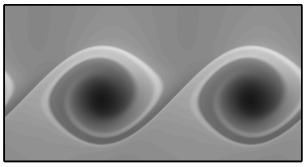

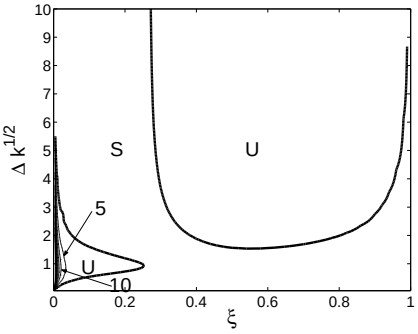

(a) Sinuous: $\xi < 1,\ k = 4000$.

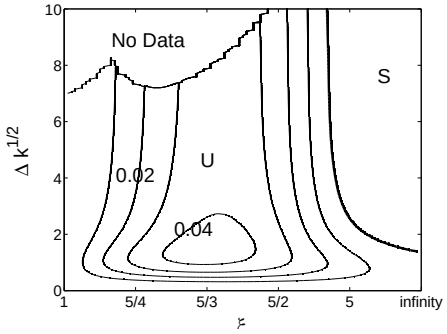

(b) Sinuous: $\xi > 1,\ k = 4000$.

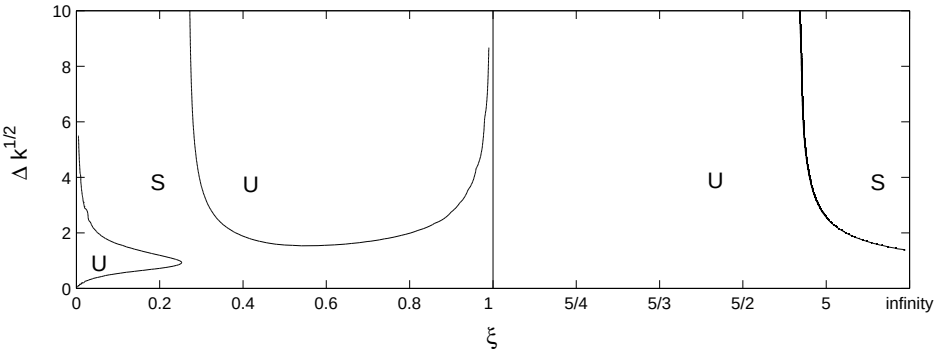

(c) Sinuous marginal stability curves, $k = 4000$.

Figure 4.16: Contour plots of growth rates of sinuous modes in $(\xi, \Delta k^{1/2})$ space. U and S denote unstable and stable regions respectively. For $\xi > 1$ the horizontal axis has been rescaled.

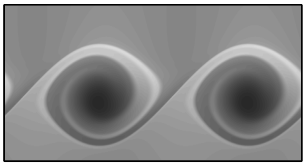

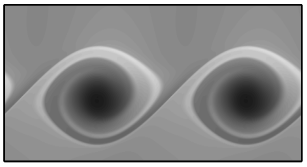

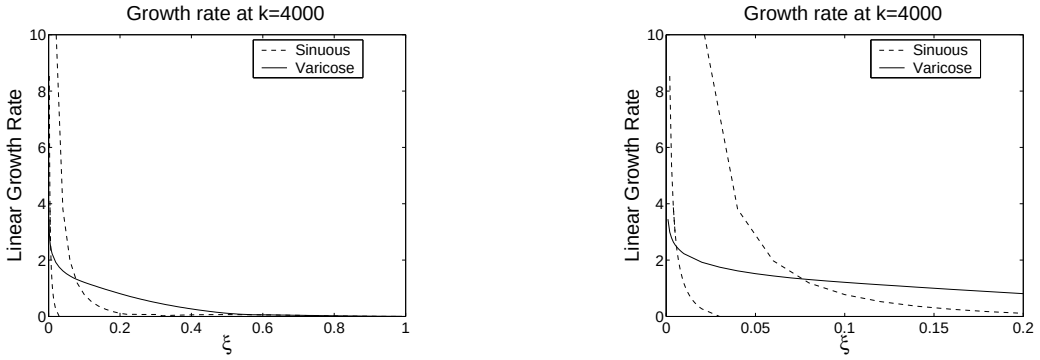

(a) $0 < \xi < 1$.

(b) $0 < \xi < 0.2$.

Figure 4.17: Growth rates of unstable modes as ξ changes with $k = 4000$. For each mode, the value of Δ is chosen to maximize the growth rate. There are two unstable sinuous modes at sufficiently small ξ. Growth rates increase sharply as $\xi \to 0$, but the sinuous growth is larger.

which appears to be logarithmic in ξ.

The apparently unphysically large growth rates indicate that when the outer relaxation time is small compared to the inner relaxation time, the instabilities grow on the shorter timescale of the outer fluid. If we rescale time by ξ such that the outer relaxation time becomes 1 and the inner relaxation time becomes ξ^{-1}, then the sinuous growth rates tend to positive constants (approximately 0.35 and 0.017) as the new inner relaxation time goes to infinity. In contrast, the growth rate of the varicose mode tends to zero. This is shown in figure 4.18.

Perturbation flow

Outside the central boundary layer, the solution ψ can be expressed in terms of the Y variables as in (4.1). There are two algebraic terms as well as a growing exponential and a decaying exponential.

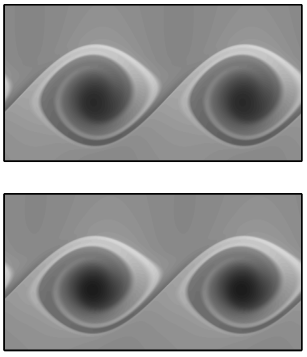

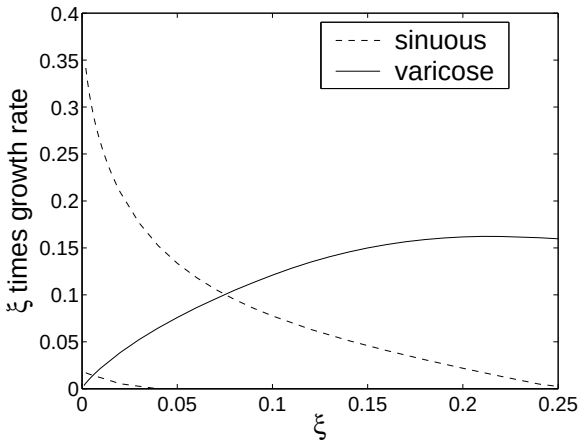

Figure 4.18: Growth rate times ξ. This corresponds to the growth rate in terms of the outer fluid's relaxation time.

In figure 4.19 we plot the perturbation flow for a varicose mode. There are boundary layers close to the walls whose widths are $\mathcal{O}(k^{-1/2})$ (in terms of η), and a boundary layer around the center-line containing both interfaces with width $\mathcal{O}(1)$. The flow does not decay between boundary layers, indicating that the algebraic terms have non-zero coefficient.

In contrast, the perturbation flow for the sinuous modes shown in figure 4.20 decays outside the central boundary layer. Because these flows decay in the outer region, the algebraic terms (which do not decay) must have zero coefficient. The exponentially growing term must also vanish to satisfy the wall boundary conditions. Thus the structure of the eigenfunction must look like the decaying exponential. Consequently, figure 4.20 shows that the perturbation flow for both sinuous modes appears similar in the outer fluid, although the growth rate and wave speeds differ substantially. This is particularly surprising because the instabilities grow on the faster time scale of the outer fluid where their perturbation flows are similar.

The distinction between the behavior of sinuous and varicose modes in

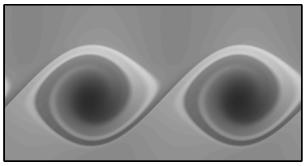

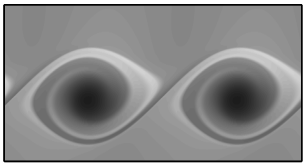

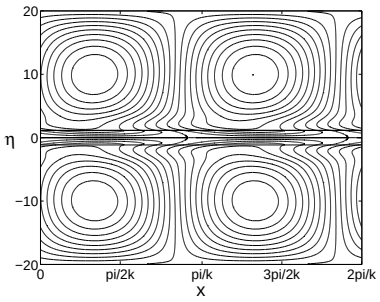

(a) Streamlines for the varicose mode.

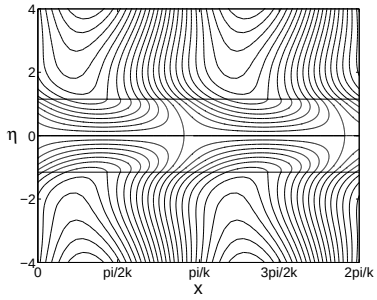

(b) Zoom in on central boundary layer.

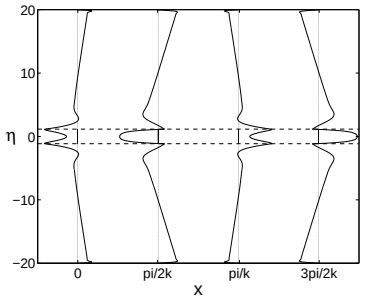

(c) Horizontal perturbation velocity. The wall boundary layers are almost too small to be seen.

Figure 4.19: The perturbation flow in a varicose mode at $k = 400$ with $\xi = 0.2$ choosing $\Delta = 0.058$ to maximise the growth rate. Note the lack of decay as $\eta \to k^{1/2} = 20$. For these parameters, $\omega = 400.16 + 0.808i$.

the outer fluid is related to the mass fluxes in the inner region. In the varicose modes, the mass flux is in the same direction on either side of the center-line, and so the central region has nonzero net flux. The outer fluid must have a comparable flux in order to satisfy mass conservation. In the sinuous modes, the mass flux within the inner fluid cancels, and no outer flow is needed to correct the fluxes.

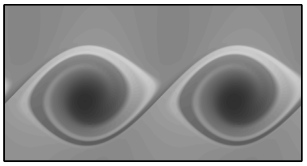

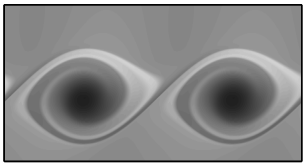

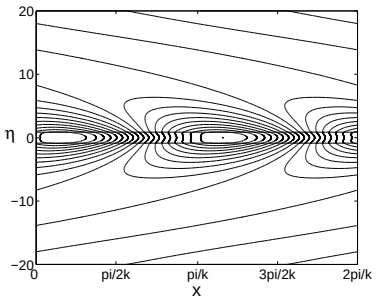

(a) Streamlines for the fast sinuous mode for $\xi = 0.025$.

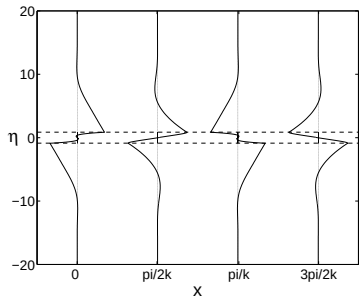

(b) Horizontal perturbation velocity.

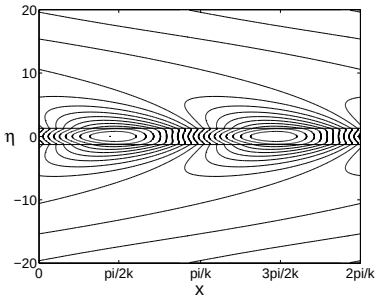

(c) Streamlines for the slow sinuous mode for $\xi = 0.025$.

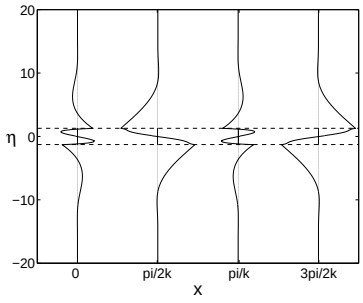

(d) Horizontal perturbation velocity.

Figure 4.20: The perturbation flow for sinuous modes with $k = 400$, $\xi = 0.025$ and $\Delta = 0.043$ and $\Delta = 0.064$ chosen to maximise the growth rate of each mode. In contrast to varicose modes, these modes decay away from the central boundary layer. For the fast mode $\omega = 418.58 + 7.66i$ and for the slow mode $\omega = 395.30 + 0.0985i$.

Wave speed

In terms of η we find $\alpha = -i\omega + ik - i\eta^2 + 1/\tau$. We expect α to remain $\mathcal{O}(1)$ in the central boundary layer, requiring that ω be k plus an $\mathcal{O}(1)$ correction.

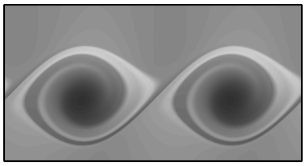

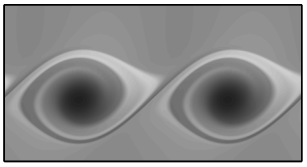

Hence, the mode travels with velocity 1 (equal to the base flow at the center) plus an $\mathcal{O}(1/k)$ correction. Remarkably this correction can be positive, so that the wave travels faster than any point in the base flow. This is shown in figure 4.21. As a consequence of this, we conclude that advection cannot account for the mechanism.

For varicose modes with $\xi = 0.2$ there is one unstable mode. In figure 4.21(a) we compare the wave-speed with the corresponding interfacial velocity and the center-line velocity. The wave travels faster than the center-line. For each value of k, we have selected Δ to maximise the growth rate.

For sinuous flow we can have multiple unstable modes. We take $\xi = 0.025$ and consider two unstable modes separately. We again select Δ to maximise each growth rate, plotting the same quantities in figure 4.21(b), (c) as in figure 4.21(a). In this case one mode moves slower than the center-line and interface, while the other moves substantially faster than both.

Finite Wi effects

The leading order corrections to the equations of section 2.3.3 are all $\mathcal{O}(kWi^{-2})$. Consequently the correction terms are small even for more moderate values of Wi, particularly if k is small. The convergence is illustrated in figure 4.22.

4.2.2 Oldroyd–B fluids

The addition of a Newtonian component of viscosity does not stabilize the flow as is shown in figure 4.23. The $\Delta \sim k^{-1/2}$ scaling is still present in (at least) two distinct tongues. As $\beta \to 1$, the fluids become identical Newtonian fluids, and so the growth rates at fixed k must approach zero. However, this limit is not approached uniformly in k. As $\beta \to 1$, one tongue moves to larger values of k, as its prefactor of $k^{-1/2}$ grows. Another tongue appears to keep the same size prefactor, but its growth rate reduces.

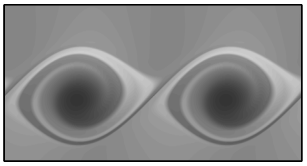

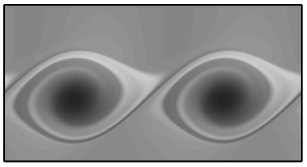

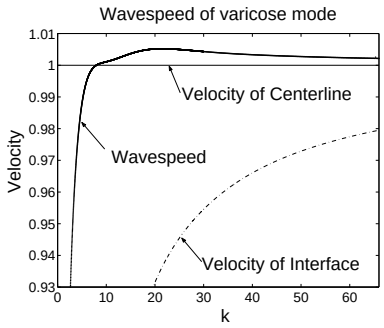

(a) Wavespeed of varicose mode with $\xi = 0.2$ for Δ giving the largest growth rate.

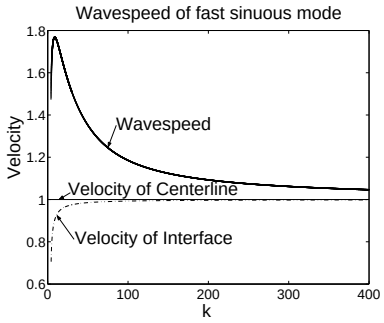

(b) Wavespeed of fast-moving sinuous mode with $\xi = 0.025$ for Δ giving the largest growth rate.

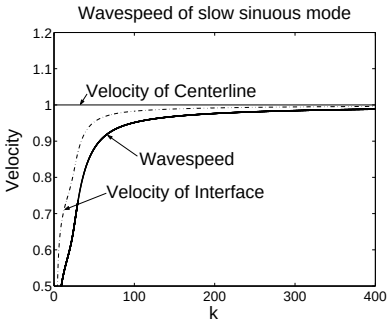

(c) Wavespeed of slow-moving sinuous mode with $\xi = 0.025$ for Δ giving the largest growth rate.

Figure 4.21: For the varicose instability and one of the sinuous instabilities the wavespeed moves considerably faster than the center-line, even when the interface is travelling considerably slower than the center-line. The other sinuous mode travels slower than the interface.

In figure 4.23(d) we see that the marginal stability curve with $\Delta \to \sqrt{2} - 1$ as $k \to 0$ has a nearly constant value of Δ until k is of order at

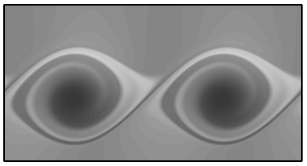

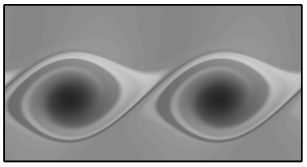

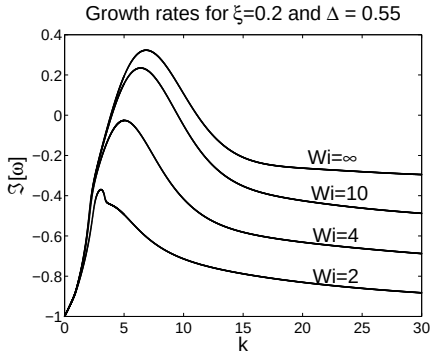

(a) Growth rate of varicose modes: $\xi = 0.2$ and $\Delta = 0.55$, with $Wi = 2$, 4, 10, and ∞.

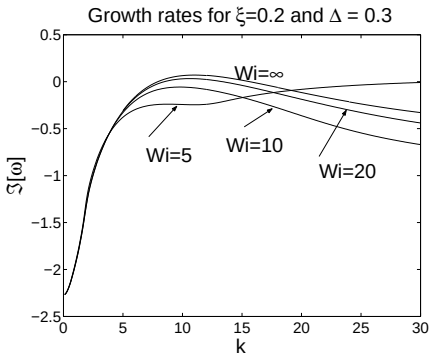

(b) Growth rate of sinuous modes: $\xi = 0.2$ and $\Delta = 0.3$ with $Wi = 5$, 10, 20, and ∞.

Figure 4.22: Convergence to the $Wi = \infty$ growth rate. As expected, convergence is quicker for smaller k. The sinuous instability for $Wi = 5$ where $k \gg Wi$ is the finite Wi instability found by Renardy [84], repeated in figure 3.11(a).

least 100. Although k is large, and the wavelength is not long compared to the relaxation length scale, this matches the predictions of the long-wave analysis [103, 27]. The long-wave analysis used the assumption that the fluids behave like Newtonian fluids on the scale of the wavelength, with the elastic stress having effect only at the interface. Because the fluids are effectively Newtonian as $\beta \to 1$, the analysis still applies even at shorter wavelengths.

4.3 Other instabilities

We have observed some instabilities for $Wi \gg 1$ that do not fall into the fast-flow, long-wave, or narrow-core regimes. Generally in these instabilities the interface is close to the wall and the wall and interfacial boundary layers

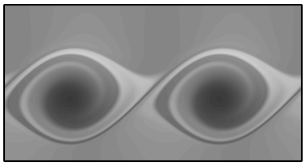

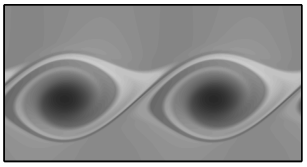

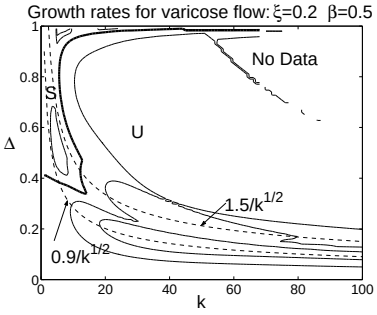

(a) $\beta = 0.5$.

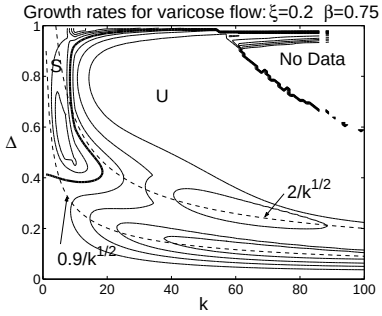

(b) $\beta = 0.75$.

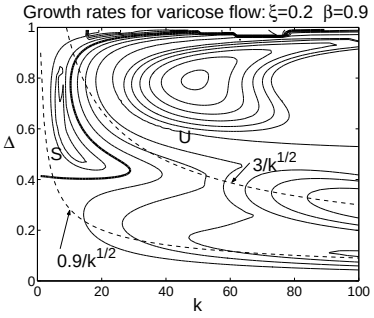

(c) $\beta = 0.9$.

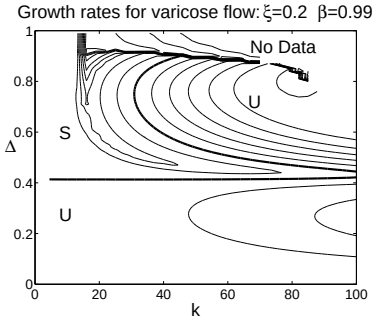

(d) $\beta = 0.99$.

Figure 4.23: The effect of changing β for varicose flow with $\xi = 0.2$.

overlap.

4.3.1 UCM fluids

Figure 4.24 shows a varicose instability for UCM fluids at a small value of ξ with Δ apparently approaching 1 as $k \to \infty$. The existence of this mode has been confirmed with both shooting and spectral methods. The shooting method could not resolve the behavior for $k > 30$, and the remaining results are from the spectral method.

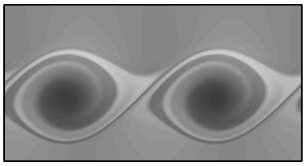

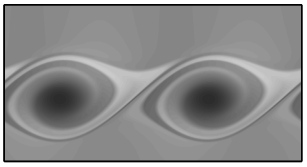

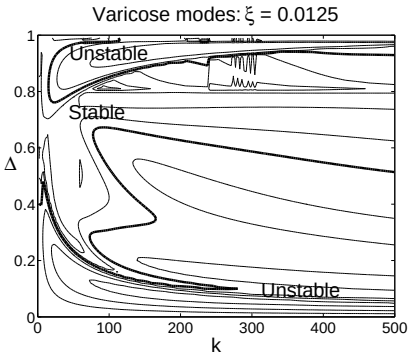

Figure 4.24: For UCM fluids with small ξ a new mode appears at large Δ. It cannot be explained by any of the previous analysis.

Because ξ is quite small, the interfacial boundary layer in the outer fluid is large and reaches the wall. The shear rate variation within the boundary layer is small (and decreases as k grows), and so the flow around the interface is effectively Couette. However, we have not found a similar instability in Couette flow with the interface close to the wall, and so it seems that the shear rate variation may play some role. We have not performed an complete search for a similar Couette flow mode, so this is not definitive.

In figure 4.24 some contour lines appear to peel off the marginal stability curve at large k and then jump back. The points where the curves jump back correspond to places where the number of Chebyshev polynomials retained per variable was increased (from 70 successively to 240). The exact stability boundary should be regarded with some suspicion.

4.3.2 Oldroyd–B fluids

In figure 4.23(c) there is a local maximum of the growth rate at $k \approx 50$, $\Delta \approx 0.8$. As k increases the value of Δ for the mode associated with this maximum appears to approach 1. It is not clear from the figure whether

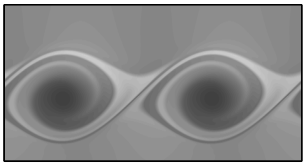

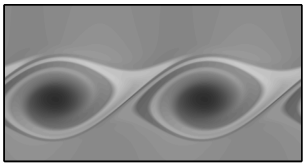

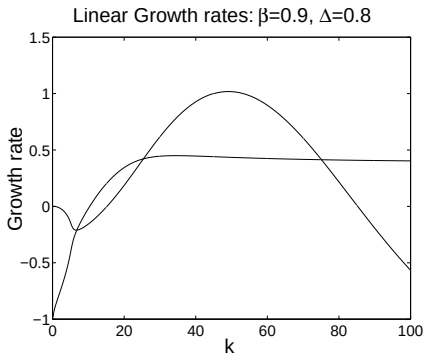

Figure 4.25: Growth rates for $\xi = 0.2$, $\beta = 0.9$ and $\Delta = 0.8$. In addition to the fast-flow mode having constant growth rate as $k \to \infty$, there is another instability which exists for moderate k.

this is distinct from the fast-flow behavior predicted in chapter 3 which approaches a constant growth rate as $k \to \infty$. However, figure 4.25 clearly shows that this instability is distinct. In fact, this is the same instability discussed in section 3.6.

4.4 Discussion

The stability of fast-flow modes for large Wi Poiseuille channel flow with an interface is similar to that of large Wi Couette channel flow. We find the same growth rates and limiting behavior as for Couette flow. However, when the interface is close to the center-line, the Couette-based analysis fails. We have found a new class of purely elastic interfacial instabilities in pressure-driven flow in a channel in this regime. These narrow-core instabilities occur if the interface is close enough to the center-line and can exist at intermediate wavenumbers when the $k \to 0$ and $k \to \infty$ limits are both stable.

The fast-flow modes depend on a boundary layer at the interface with a length scale proportional to the inverse shear rate. Close to the center-

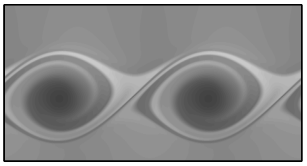

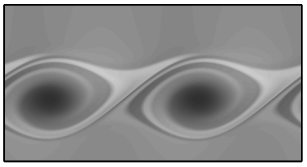

line the inverse shear rate becomes large, while simultaneously U'/U'', the distance over which the shear rate changes by an amount comparable to itself, becomes small. Hence there is a region for which the length over which the shear rate changes becomes comparable to (or shorter than) the boundary layer length, and the fast-flow regime breaks down.

It is in this regime that we find the narrow-core instabilities for three-layer channel Poiseuille flow. In fact, we can conclude the existence of narrow-core instabilities without any recourse to calculations through a simple argument. When $\xi = 1$ the growth rate of the interfacial mode must be zero because the fluids are identical. Generically the derivative of the growth rate with respect to ξ must be non-zero. Consequently there exists stability and instability on alternate sides of $\xi = 1$. This argument fails for unbounded Couette flow due to a symmetry which is absent in Poiseuille flow.

From this argument it also follows that if there are only two layers and the interface is sufficiently close to the center-line there must be narrow-core instabilities (although the name is a misnomer in this case as there is no core fluid). Further, any constitutive model which predicts a boundary layer dependent on the shear rate at the interface must have instabilities for some parameters when the interface is close to the center-line.

We observe that the narrow-core instability may persist to relatively large values of the Reynolds number, with similar properties to those found in this chapter, so long as the flow remains laminar. We find the instability for flows with the interface close to the center-line and so the local Reynolds number (based on the relative velocity and distance of the interface and center-line) will be small even if the global Reynolds number is not. Consequently inertia should be unimportant in the region that determines the growth rate.

In addition to the narrow-core instability, we have found some other purely elastic instabilities for which the interface is close to the channel walls. These instabilities are not explained by our analysis at present, but appear

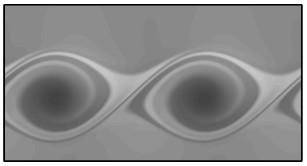

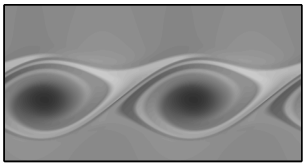

to occur for small values of ξ for which the boundary layer in the outer fluid is large and includes the interface.

The results of this chapter suggest a wealth of possible future weakly nonlinear study. The method for constructing a weakly nonlinear analysis of flows with interfaces can be found in Renardy and Renardy [83]. It is necessary to consider the moderate k instability as well as the $k = 0$ mode. Figure 4.10 shows that two separate moderate k modes are important for some parameters.

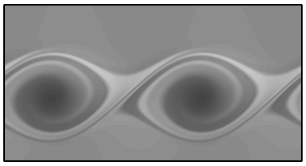

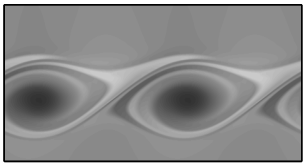

Chapter 5

Stability of pressure driven core-annular pipe flow at large Wi

In this chapter we compare the stability of core-annular Poiseuille pipe flow with the three-layer symmetric Poiseuille flow in a channel of chapter 4. We only consider UCM fluids at large Wi. As noted in the introduction, a jump in the second normal stress difference N_2 affects the growth rate for small k. It is expected to play a role at larger k as well. However, the Oldroyd–B fluid has $N_2 = 0$, and so these effects are not included in our analysis.

For either $m = 0$ or $m = 1$ we can use equations (2.71)–(2.90). The conditions at $r = 0$ are different: when $m = 0$ we take the conditions (2.91)–(2.93) while we use (2.94)–(2.96) for $m = 1$. When $m = 0$ we can eliminate the azimuthal velocity and corresponding stresses, which allows us to introduce a streamfunction. We can then use the reduced system of equations (2.97)–(2.108), but this assumes there is no mode with only azimuthal components.

For $\xi = 0.2$ and $\xi = 0.3$ we plot growth rates of axisymmetric modes in figure 5.1 as k and Δ change. The results are similar to figures 4.4–4.6 for

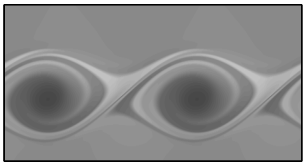

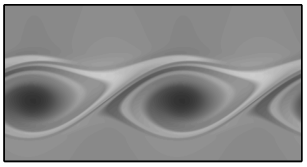

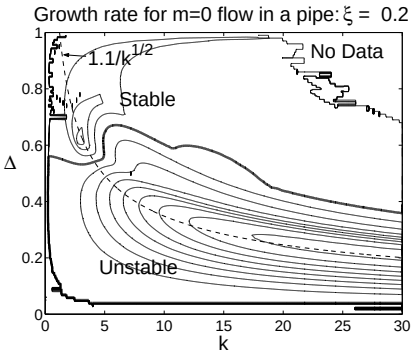

(a) Growth rate of most dangerous axisymmetric mode, $\xi = 0.2 < \xi_c$.

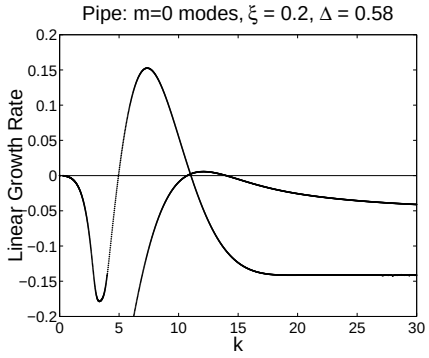

(b) Growth rates of the two unstable axisymmetric modes, $\xi = 0.2,\ \Delta = 0.58$.

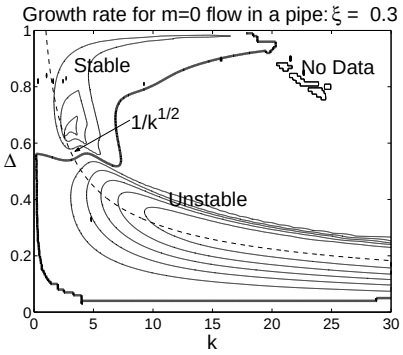

(c) Growth rate of most dangerous axisymmetric mode, $\xi = 0.3 > \xi_c$.

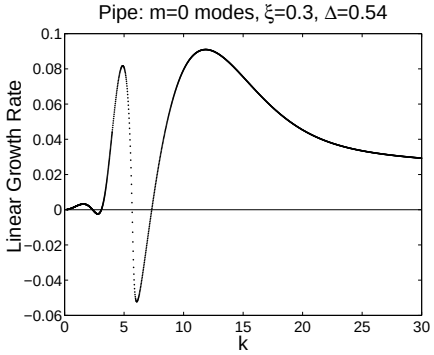

(d) Growth rate of the single unstable axisymmetric mode, $\xi = 0.3,\ \Delta = 0.54$.

Figure 5.1: Contour plots of growth rates for $m = 0$ axisymmetric mode with $\xi = 0.2$ and $\xi = 0.3$ and the dispersion relations fixing $\xi = 0.2,\ \Delta = 0.58$ and $\xi = 0.3,\ \Delta = 0.54$.

channel Poiseuille flow. When $\xi = 0.2$ we again find values of Δ for which both $k \to 0$ and $k \to \infty$ limits are stable, with an instability at moderate

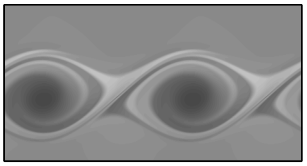

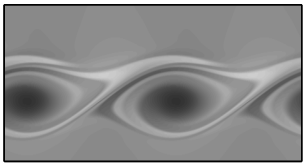

values of k, due to a narrow-core instability.

Most other results are also qualitatively similar to those found in channel flow. However, there are some notable differences, particularly in the $m = 1$ cork-screw modes.

The chapter is organized as follows: in section 5.1 we compare the fast-flow regime of pipe and channel flow. In section 5.2 we consider the long-wave cork-screw ($m = 1$)and axisymmetric ($m = 0$) limits numerically, reproducing earlier asymptotic results of Hinch *et al.* [38]. In section 5.3 we consider the narrow-core regime.

5.1 Fast-flow ($k \to \infty$)

Holding Δ fixed and increasing k corresponds to the fast-flow limit in which the relaxation length scale is large compared to the wavelength, which is in turn large compared to the pipe width. In chapter 3 we found that the growth or decay of two-dimensional modes depends on a boundary layer much thinner than the channel width. The curvature of the pipe is negligible over this length scale and so the same modes exist, regardless of the value of m.

In channel flow the quintic equation (3.10) gives the growth rates of five distinct fast-flow modes. Only one is unstable, and only for $\xi_c < \xi < 1$ or $1 < \xi < \xi_c^{-1}$. We calculate the eigenvalues ω for pipe flow with $m = 1$, $\Delta = 0.3$, $k = 100$, and ξ between 0 and 1. The results are plotted in figures 5.2(a) and (b); we find all five modes expected as well as one additional unexpected stable mode.

For $m = 0$ we do not find an additional mode using the streamfunction formulation. However, using the full equations we do find an additional mode with similar growth to the new $m = 1$ mode. This new $m = 0$ mode has $v_r = v_z = 0$ and travels with the exact velocity of the interface. It is a solution to equations (2.73), (2.76), (2.79), (2.89), and (2.93) which decouple

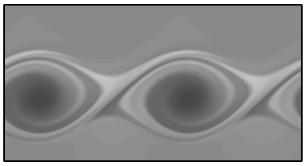

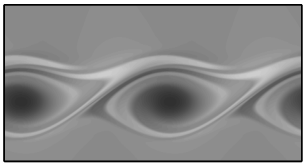

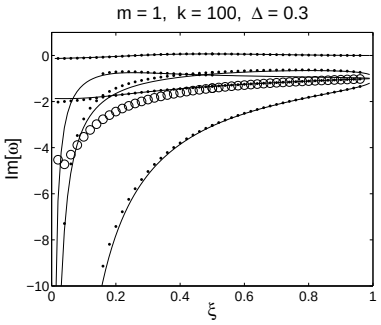

(a) Imaginary part of ω for $m = 1$ modes.

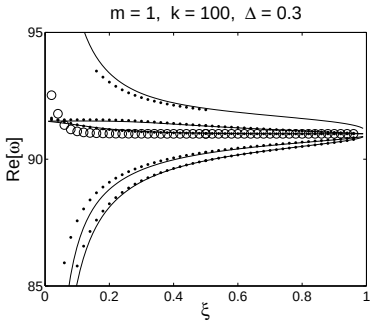

(b) Real part of ω for $m = 1$ modes.

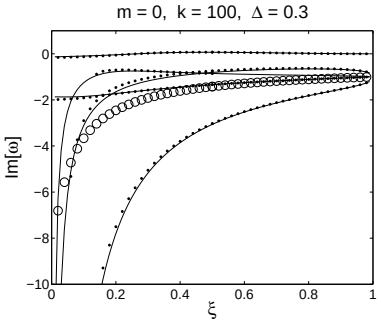

(c) Imaginary part of ω for $m = 0$ modes.

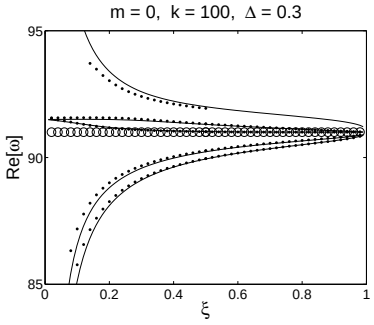

(d) Real part of ω for $m = 0$ modes.

Figure 5.2: Dots represent the modes for $k = 100$, $\Delta = 0.3$ matching the asymptotic prediction (solid). There is an additional mode depicted by circles. One mode could only be calculated for ξ in a limited range due to interference from the balloon around the continuous spectrum in the spectral method.

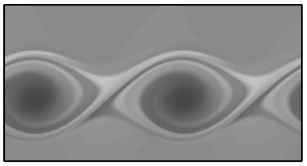

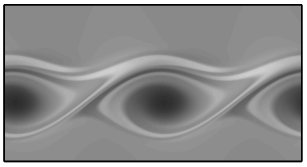

and are discarded in deriving the streamfunction formulation. The $m = 0$ growth rates are shown in figures 5.2(c) and (d).

5.2 Long-wave

The long-wave $m = 0$ asymptotic limit was initially studied numerically by Chen [16] who found instability if both $\xi < 1$ and $\Delta < 0.562$ or both $\xi < 1$ and $\Delta > 0.562$. Subsequent asymptotic work by Hinch *et al.* [38] explained the physical mechanism of the instability and predicted the growth rate.

The small k growth rates were found by Hinch *et al.* [38] to be (when specialized to the UCM fluid)

$$\Im[\omega] = 2k^2\Delta^4(-\Delta^4 + 3\Delta^2 - 2 - 2\ln\Delta)(\xi - 1) \qquad (m = 0)\,,$$
$$\Im[\omega] = k^2\Delta^4(\Delta^4 - 1 - 4\ln\Delta)(\xi - 1)/2 \qquad (m = 1)\,.$$

This result is derived with the assumption that N_2 is zero, N_1 is nonzero and the wavelength is long compared to the relaxation length scale. The growth rates depend on the jump in N_1 (which appears as $\xi - 1$), the interface location Δ, and are otherwise independent of the particular details of the model. The jump in N_1 at the interface drives a flow, but because of the long wavelength the fluid responds like a Newtonian fluid.

The difference between our calculated growth rates and those derived by Hinch *et al.* are $\mathcal{O}(k^4)$ for small k.

5.3 Narrow-core

The narrow-core regime of section 4.2 persists in pipes. However, the inner core is narrow enough that its curvature is no longer negligible. So while the behavior is different from the fast-flow and long-wave regimes, there are new

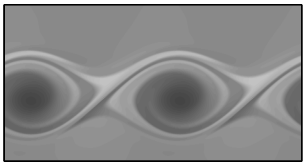

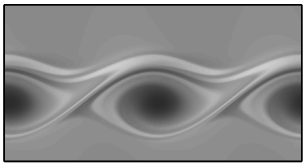

effects and so it is not clear that the behavior must be the same as in channel flow.

We follow the large k analysis of section 4.2.1 for channel Poiseuille flow, plotting the growth rates and stability in figures 5.3 and 5.4. Both of these plots show some odd bumps on the marginal stability curve for ξ just below one. This is a result of the fact that there is a quadratic minimum to the growth rate close to the marginal stability curve, and so the interpolation used to plot the contours does not fit well.

5.3.1 Axisymmetric ($m = 0$) modes

Figure 5.3 plots the growth rate at $k = 1000$ for $m = 0$ modes. The growth rates of $m = 0$ modes are qualitatively similar to varicose channel modes. Figures 5.3(b) and 4.15(b) are nearly indistinguishable and so for $\xi > 1$ the behaviors are practically identical. When $\xi < 1$ there are some small differences. In channel flow [figure 4.15(a)] there is a small band of stability between the fast-flow and narrow-core instabilities. In pipe flow the two regions of instability overlap [figure 5.3(a)]. At smaller ξ, the island of stability found in channel flow is larger. Whereas in channel flow there is varicose instability for fixed $\Delta k^{1/2}$ as $\xi \to 0$, axisymmetric modes are stable if $\Delta k^{1/2}$ is large enough. There is a thin island of instability with $\xi \to 0$ and $\Delta k^{1/2} \to \infty$.

5.3.2 Cork-screw ($m = 1$) modes

Figure 5.4 plots the growth rate at $k = 1000$ for $m = 1$ modes. The qualitative behavior for $\xi > 1$ is similar to sinuous channel modes (figure 4.16), however when ξ is small, the qualitative behavior changes. At small ξ there are two sinuous instabilities in channel flow whose growth rate scales like $1/\xi$. In $m = 1$ flow, there is no corresponding instability.

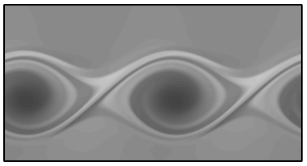

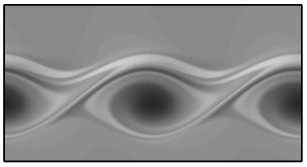

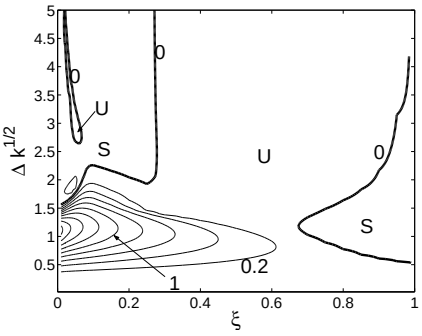

(a) $m = 0$: $k = 1000$.

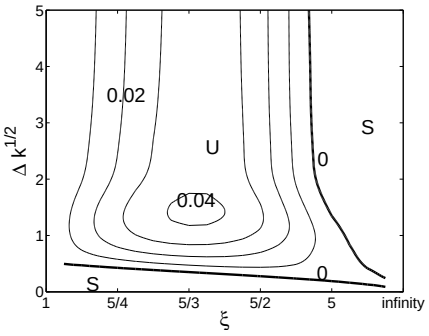

(b) $m = 0$: $\xi > 1$, $k = 1000$.

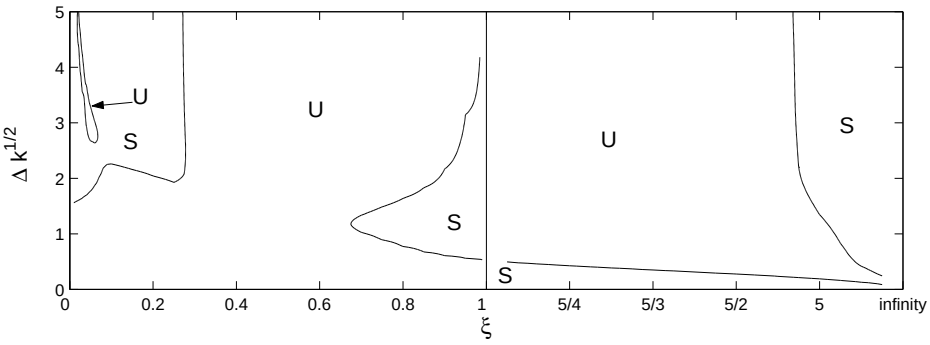

(c) Axisymmetric marginal stability curves, $k = 1000$.

Figure 5.3: Contour plots of growth rates of $m = 0$ modes in $(\xi, \Delta k^{1/2})$ space with $k = 1000$. U and S denote unstable and stable regions respectively. Compare with figure 4.15.

5.4 Discussion

Our results show that the stability of core-annular flow is generally like that of three-layer symmetric Poiseuille flow. The fast-flow instability criterion is the same. The long-wave instability criterion is similar and known from

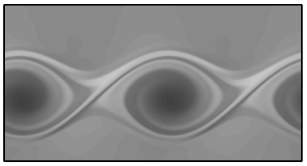

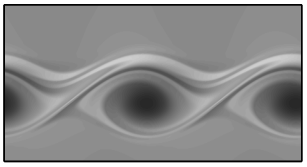

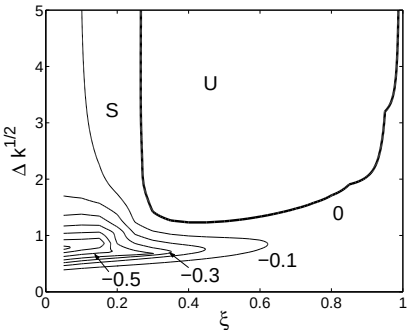

(a) $m = 1$: $k = 1000$.

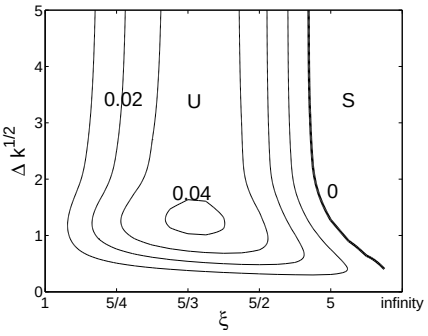

(b) $m = 1$: $\xi > 1$, $k = 1000$.

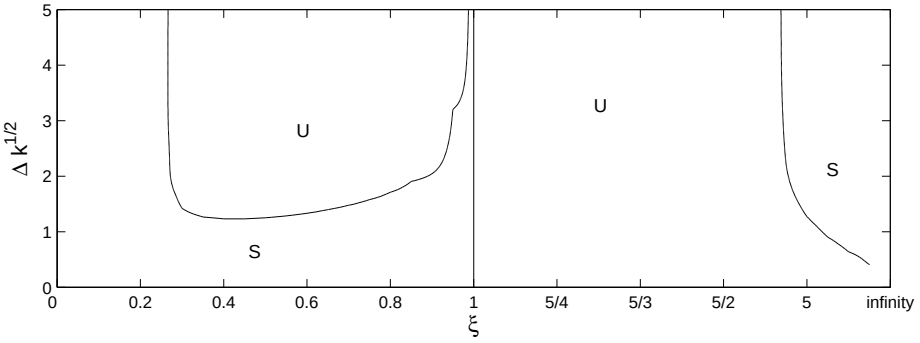

(c) $m = 1$: marginal stability curves, $k = 1000$.

Figure 5.4: Contour plots of growth rates of $m = 1$ modes in $(\xi, \Delta k^{1/2})$ space with $k = 1000$. U and S denote unstable and stable regions respectively. Compare with figure 4.16.

previous work [38]. Most of the narrow-core stability is the same.

However, there are some significant exceptions. In the fast-flow regime there is a (stable) mode which which does not exist in planar channel flow. It is possible that this mode would be found in channel flow if we had considered the transverse direction.

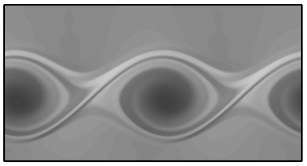

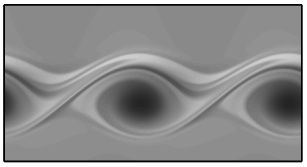

In the narrow-core regime, the axisymmetric modes are similar to the varicose channel modes. The cork-screw modes however give substantially different behavior at small ξ from sinuous channel modes. In the channel, two sinuous modes are unstable with growth rates tending to infinity as ξ tends to zero. We do not find any unstable cork-screw modes at small ξ.

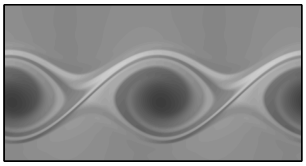

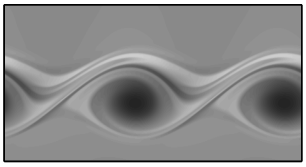

Chapter 6

Coextrusion conclusions and future work

This part of the dissertation considered the stability of coextrusion flow at large $\mathcal{W}$ both in channels and in pipes. The behavior of UCM and Oldroyd–B fluids is generally similar. We have substantially extended the understanding of an interfacial instability previously found only in short waves at large $\mathcal{W}$. We have shown that it can exist even if the wavelength is longer than the channel width and that the previously proposed mechanism cannot apply. We have discovered and systematically investigated a previously unknown instability. As a result of this mode, intermediate wavenumbers can lead to instability even when the $k \to 0$ and $k \to \infty$ limits are both stable, contradicting claims in the literature. In the course of this investigation we have found other previously unknown instabilities which appear when the interface is close to the wall.

In this chapter we return to dimensional variables. The channel width is L, the wavelength is $2\pi/k$ and the relaxation length scale is $U_0\tau_1$.

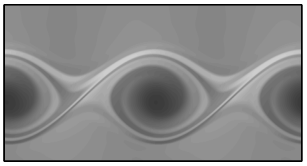

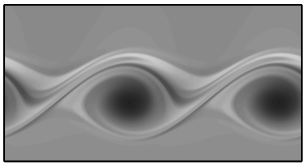

Fast-flow channel instabilities

In chapter 3 we showed that the UCM short-wave result of Renardy [84] (and similar results of Chen and Joseph [17]) contains two distinct instabilities, one at small Wi and another at large Wi. The large Wi instability persists (with the same growth rate) even if the wavelength is as large as or larger than the channel width, so long as $U_0\tau$ is large compared to both. Consequently this is more properly termed a *fast-flow* instability.

The perturbation flow of the fast-flow modes fills the channel when $k^{-1} \gg L$, but the stability is determined by a boundary layer close to the interface. The width of the boundary layer scales like $1/k\tau U'$. The instability persists for Oldroyd–B fluids even as the parameter β measuring the proportion of the viscosity due to Newtonian effects approaches one.

Intriguingly, the fast-flow instability persists even if the normal force balance is dropped and replaced with the alternate condition that the normal velocity at the interface is zero. That is, we can take the surface tension to be asymptotically large so that the normal stress jump disappears from the analysis and does not affect the growth rate. The prevailing belief that all purely elastic interfacial instabilities are caused by the normal stress jump is false for this flow: a new mechanism is needed.

Narrow-core channel instabilities

In chapter 4 we showed the existence of another class of instabilities occurring for three-layer symmetric Poiseuille channel flow. This occurs if the interface is close to the center-line, so that the boundary layer thickness associated with fast-flow $1/k\tau U'$ is comparable to or larger than U'/U''.

These *narrow-core* instabilities can appear in flows for which both the $k^{-1} \ll L, U_0\tau_1$ and $k^{-1} \gg L, U_0\tau_1$ limits are stable. This contradicts published claims [54, 85] for the three-layer symmetric geometry of chapter 4.

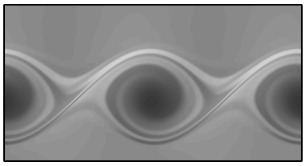

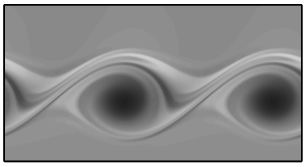

The instabilities can travel faster than the base flow, and so advection alone is not enough to explain their mechanism. When the outer fluid has much smaller relaxation time than the inner fluid, the instability grows on the shorter time scale of the outer fluid.

Instabilities of core-annular pipe flow

In chapter 5 we found that core-annular pipe flow is qualitatively similar in most respects to the corresponding three-layer symmetric channel flow. For fast-flow this follows from the fact that the length scales associated with the instability are too small to be affected by the curvature of the pipe. For long-waves, the similarity is already known from previous numeric and asymptotic studies [16, 38, 103, 27]. However, there are some significant differences in the narrow-core regime if the outer fluid has much smaller relaxation time than the inner fluid.

In channel flow there are unstable sinuous modes if the outer fluid has much smaller relaxation time. No analagous instabilities are found in pipe flow. The length scale associated with the narrow-core instabilities is large enough that the curvature of the pipe has a leading order effect on the instability.

Other instabilities

We have found some other new interfacial instabilities. These generally appear to exist when the interface is close to a wall. In this case the wall lies within the interfacial boundary layer, and so previous asymptotic analysis breaks down. We have not attempted any detailed analysis.

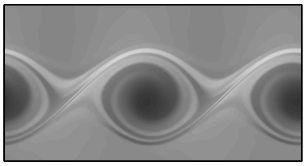

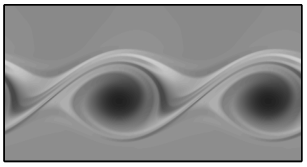

Future work

A number of unanswered questions are raised by this work and should be addressed in the future.

Both the fast-flow and narrow-core instabilities have features which suggest that the mechanisms behind them are unusual. The fast-flow instability depends only on tangential effects and the narrow-core instability travels faster than the base flow. Despite considerable effort, we have not been able to find a physical mechanism for either.

We have found some instabilities which we did not investigate closely. Figures 4.23(c) and 4.24 hint at a scaling for Δ as $k \to \infty$, and so it should be straightforward to extend the analysis.

The narrow-core instability could be extended into a weakly nonlinear analysis. This is complicated by the fact that the long-wave limit is neutrally stable and so must be considered as well. Amplitude equations for parallel flows with an interface appear in a coupled pair. Their structure is derived by Renardy and Renardy [83], though the specific coefficients are model-dependent. The analysis is complicated further by the fact that more than one mode may become unstable simultaneously, shown in figure 4.10. In such a situation, three coupled equations are needed.

Of course, having predicted a new instability, we would like to see it experimentally verified. Although our analysis assumes large $\mathcal{W}\!i$, we have found the narrow-core instability to exist for $\mathcal{W}\!i$ as small as five for a UCM fluid. The instability persists for Oldroyd–B fluids, and so it should be possible to perform an experiment with Boger fluids. Our analysis may provide an explanation for some instabilities observed experimentally by Valette *et al.* [97] in flows their long-wave analysis predicted to be stable. More work would be needed to clarify this.

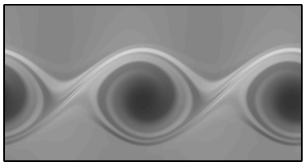

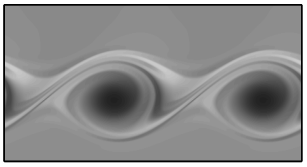

Part II

Elastic jets

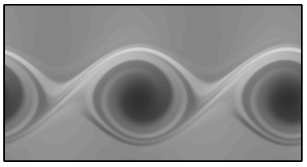

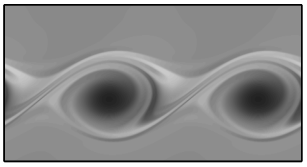

Chapter 7

Critical layers in planar viscoelastic jets

In this chapter we turn to high Reynolds number flows and consider a planar jet of elastic fluid. Much is known about the inertial instabilities that occur in the absence of elasticity. However, adding even a small amount of elasticity can qualitatively change the linear stability properties: with weak elasticity, Rallison and Hinch [38] found a new instability apparently driven by a discontinuity in the first normal stress. We want to study the effect of elasticity on the development of the inertial instability, and so we choose our base profiles to avoid the discontinuity of Rallison and Hinch.

This chapter is structured as follows: in section 7.1 we discuss related work in Newtonian, magnetohydrodynamic, and elastic fluids. In section 7.2 we describe the base flows we study and the full nonlinear UCM equations governing the flow. Section 7.3 contains the linearized perturbation equations for the large $\mathcal{W}\!i$ UCM jet and describes the numerical methods used to study the linear eigenvalue problem. Section 7.4 discusses the Rallison and Hinch linear instability caused by elastic effects and shows that the flows we study only have inertial instabilities. Section 7.5 describes how elasticity modifies

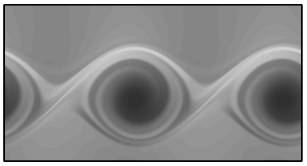

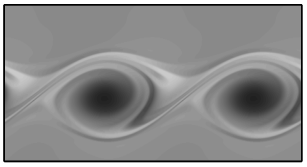

the inertial instability for our flow profiles. Section 7.6 introduces the weakly nonlinear amplitude equations (derived in appendix B) for the UCM fluid. The poor behavior of the UCM fluid in extensional flows affects the results, and so we also introduce amplitude equations based on the FENE–CR model. Section 7.7 contains the results and a discussion of numerical calculations with the amplitude equations.

Many of the results in this chapter depend on matching the wavespeed of the instability with the base velocity of the jet or with travelling waves in the jet. Hence, rather than using the complex frequency ω, we express our results in terms of the complex wavespeed $c = \omega/k$.

7.1 Related work

7.1.1 Newtonian fluids

The instabilities of inviscid parallel Newtonian flows have been studied for over a century. Much of the original work was performed by Rayleigh [80]. We give a brief discussion here.

We consider a two-dimensional shear flow $\boldsymbol{U} = (U(y), 0)$ and define $U_{\min} = \inf U(y)$ and $U_{\max} = \sup U(y)$. The governing equations are the incompressible Euler equations for inviscid Newtonian fluids

$$\rho \frac{D\boldsymbol{U}}{Dt} = -\nabla P \,,$$
$$\nabla \cdot \boldsymbol{U} = 0 \,.$$

This is a lower order system than the full Navier–Stokes equations, and so rather than applying no-slip boundary conditions, we can only apply no-penetration conditions at walls.

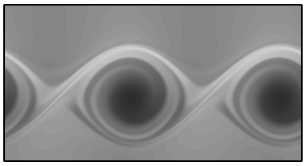

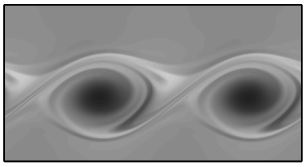

The Rayleigh equation

We consider a small perturbation to the base flow and linearize the equations assuming normal modes. Thus the streamfunction of the perturbation flow is $\psi(y)\exp[ik(x-ct)]+cc$. If the shear rate U' is continuously differentiable we arrive at the *Rayleigh equation* for the perturbation streamfunction

$$(U-c)(\psi''-k^2\psi)=U''\psi\,. \tag{7.1}$$

This can be written in the alternate (self-adjoint) form

$$[(U-c)^2\phi']'=k^2(U-c)^2\phi\,, \tag{7.2}$$

where $\phi=-\psi/(U-c)$ measures the vertical displacement of a particle in the linearized system from its position in the base flow. This is simply a generalization of δ used in the coextrusion flow as the displacement of the interface.

It is easily seen by conjugating this equation that if c and ϕ form a solution pair to the Rayleigh equation, then so do their complex conjugates c^* and ϕ^*. Consequently, finding any c with nonzero imaginary part implies instability of the system.

Rayleigh's criterion

Rayleigh [80] showed that a flow whose base velocity profile is continuous and piecewise continuously differentiable is stable, provided that the shear rate is monotonic. If U'' is continuous, then Rayleigh's criterion states that if U'' never vanishes the flow must be stable. A heuristic argument based on physical principles for why the flow is stable if U'' is of constant sign is given by Lin [58]. Summarized it is: the action of a vorticity gradient on a displaced fluid element is to move it back to its original position; however, if the gradient vanishes (*i.e.*, $U''=0$), this effect is weakened or eliminated, so other mechanisms have an opportunity to act.

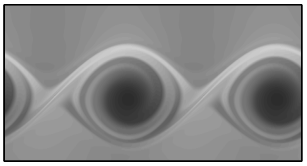

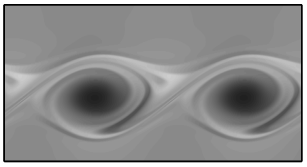

A number of improvements of Rayleigh's criterion are known [24]. However, no general necessary and sufficient stability criterion has been found.

Howard's semi-circle theorem

Howard's semi-circle theorem [41] for inviscid parallel shear flow gives a simple bound on the location of any unstable eigenvalue. Given a base flow profile U and an unstable mode with complex wavespeed $c = c_r + ic_i$, the location of c in the complex plane is within the upper half of the circle centered at $(U_{\max} + U_{\min})/2$ with radius $(U_{\max} - U_{\min})/2$. That is,

$$[c_r - (U_{\max} + U_{\min})/2]^2 + c_i^2 \leq [(U_{\max} - U_{\min})/2]^2 \,. \tag{7.3}$$

This theorem has been generalized for a number of different flows, some of which are discussed below.

The critical layer

For this discussion, we assume that the base flow profile is twice continuously differentiable.

If c is real and $U_{\min} \leq c \leq U_{\max}$, then the coefficient of the leading order derivative in (7.2) vanishes for some y. The line segment $U_{\min} \leq c \leq U_{\max}$ defines a neutrally stable continuous spectrum.

If there is an inertial instability, then in general there is instability for $0 < k < k_c$ for some k_c dependent on the flow profile. As k increases to k_c, the unstable eigenvalue c disappears by entering into the continuous spectrum. The limiting value of the wavespeed as $k \to k_c^-$ is $c = U(y_c)$ where y_c is the location of the inflection point of U. As the eigenvalue enters the continuous spectrum, $dc_i/dk \neq 0$, a fact that affects our weakly nonlinear analysis.

Modes in the continuous spectrum are generally singular where the base flow velocity matches the wavespeed. However, for the mode which is the

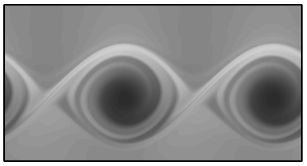

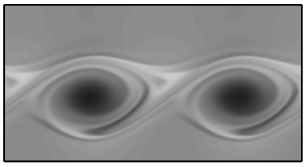

limit of the unstable mode at $k = k_c$, both $U - c$ and U'' vanish at y_c, and so $\phi'' = -2\phi'/(y - y_c)$ at leading order. Consequently $\phi \sim 1/(y - y_c)$ and there is a simple pole in ϕ at y_c. Multiplication by $U - c$ makes ψ regular.

Within an $\mathcal{O}(\epsilon)$ distance of the inflection point, both sides of (7.1) are $\mathcal{O}(\epsilon\psi)$. The nonlinear terms neglected in the derivation of this equation first become comparable to the linear terms in this *critical layer*.

If the faster growing modes at smaller k are somehow damped so that only the slowly growing modes close to $k = k_c$ exist, then there is linear growth until the nonlinear terms are large enough to affect the critical layer. At this point the flow in the critical layer rolls up into a cat's eye [4]. It is the effect of the elasticity on the development of this cat's eye that is the primary focus of this chapter.

7.1.2 Magnetohydrodynamic fluids

For the inviscid Newtonian fluid the critical layer is found where the wavespeed of the perturbation matches the base velocity. However, when the fluid can support traveling waves, the position of the critical layer changes to where the wavespeed of the perturbation matches the velocity of the travelling waves.

We consider a magnetohydrodynamic (MHD) fluid experiencing parallel shear flow in the presence of a magnetic field $\boldsymbol{B} = (B(y), 0)$ aligned with the flow. Alfvén waves travel with velocity (relative to the base flow) $c_A = |B|\mu_0/\rho$ where μ_0 is the magnetic permeability of free space and ρ is the fluid density. These waves can travel in either direction parallel to the base flow. A modified Rayleigh equation exists found by Kent [47]

$$\left[[(U - c)^2 - c_A^2]\phi'\right]' = k^2[(U - c)^2 - c_A^2]\phi\,. \tag{7.4}$$

The term $(U - c)^2$ in (7.2) has been replaced by $(U - c)^2 - c_A^2$. This is zero for y_c such that the wavespeed of the perturbation matches the local Alfvén

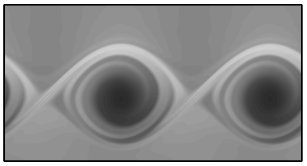

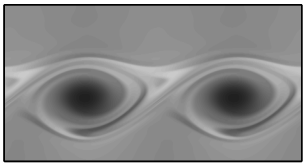

wavespeed, and so the continuous spectrum is given by the set of c such that $c_A = \pm(U - c)$ at some y.

When c_A is zero (the Newtonian case), the mode in the continuous spectrum which is the limit of the unstable mode at k_c is regular. As c_A grows, two zeros of $(U - c)^2 - c_A^2$ emerge on either side of where $U = c$, separated by a distance of order c_A. Around each of these $\phi'' = -\phi'/(y - y_c)$ at leading order. Consequently $\phi \sim \ln|y - y_c|$. This is not regularized on multiplication by $U - c$ and so ψ has a logarithmic singularity at each zero. This results in two singularities for ψ, with $\psi = 0$ somewhere between them.

The proof of Rayleigh's criterion no longer holds for this flow. Indeed, it has been shown [46] that the addition of a (continuous) magnetic field can destabilize a flow even if U'' has constant sign. Various sufficient conditions for instability have been found [46, 19]. A strengthened semi-circle theorem applies for this case [44]: any unstable eigenvalue lies in the intersection of the two distinct semi-circles

$$c_r^2 + c_i^2 \leq (U^2 - c_A^2)_{\max}\,, \tag{7.5}$$

$$[c_r - (U_{\max} + U_{\min})/2]^2 + c_i^2 \leq [(U_{\max} - U_{\min})/2]^2 - (c_A^2)_{\min}\,. \tag{7.6}$$

If these semicircles have an empty intersection, the flow is stable. In the limit $c_A \to 0$, the first semi-circle contains the second and the theorem reduces to the standard Newtonian result.

Some study of the nonlinear development of the MHD critical layer has been done by Shukhman [88, 89]. He studied two regimes. In the first, $c_A \sim \epsilon^2 U_c'$ where U_c' is the value of the shear rate at the inflection point and ϵ is a small parameter measuring the critical layer thickness. At leading order the linear problem reduces to the Newtonian Rayleigh equation. The modes are unstable for $0 < k < k_c$, and at k_c there is a regular neutrally stable mode with a single critical layer at the inflection point where the wavespeed matches the local velocity. The size of c_A is chosen such that the mode grows

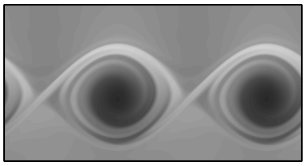

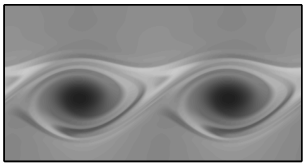

like the Newtonian mode and c_A first becomes important in the critical layer at the same time as the nonlinear terms. In the second regime $c_A \sim U_c'$ and appears in the leading order equations. The Newtonian critical layer is replaced by two separate critical layers, each centered at a singularity of the neutrally stable mode. The nonlinear terms must be considered separately in each layer. An intermediate regime exists for which the critical layers are separated by a distance comparable to the critical layer width. No significant simplification of the equations is possible here, and this regime has not been studied.

7.1.3 UCM fluids

Similarly to the MHD fluid, the UCM fluid also supports waves. The velocity of an elastic wave (relative to the base flow) is

$$c_E = \pm |U'| \sqrt{2E}\,, \tag{7.7}$$

where E (defined in section 7.2.2) measures the strength of elastic effects. The elastic Rayleigh equation is similar to the MHD Rayleigh equation (7.4). It takes the form

$$\left([(U-c)^2 - c_E^2]\phi'\right)' = k^2[(U-c)^2 - c_E^2]\phi\,. \tag{7.8}$$

This is derived under the assumption that the Reynolds number and the Weissenberg number are both large. As before, the neutrally stable modes that are the limits of the unstable modes have logarithmic singularities. The elastic Rayleigh equation was first derived by Azaiez and Homsey [3] who considered a shear flow profile $U(y) = \tanh y$. They found the effect of elasticity to be stabilizing, through a mechanism explained by Hinch [37] whereby the elasticity behaves like surface tension close to the shear layer.

Rallison and Hinch [79] considered a submerged elastic jet with parabolic

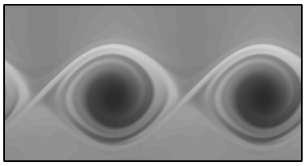

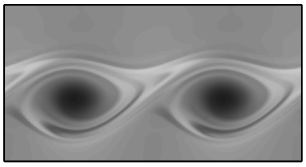

profile

$$U(y) = \begin{cases} U_0(1 - y^2/L^2) & |y| \le L \\ U(y) = 0 & |y| > L \end{cases} . \tag{7.9}$$

There is a jump in the derivative of U at $y = L$, the interface between the jet and the quiescent fluid. This jump induces a jump in the first normal stress difference which drives a new instability we refer to as the *RH mode* and discus in section 7.4.1.

It is unclear whether a flow that is stable for Newtonian fluids can be destabilized by the addition of elasticity if the normal stress differences are continuous. Although such instabilities exist for the MHD fluid, the examples of Kent [46] make use of the fact that the magnetic field is imposed independently of the base flow. Consequently the Alfvén wavespeed is independent of the base flow. In contrast, the elastic wavespeed depends on the local shear rate and is not independent of the base flow.

The proof of the strengthened MHD semi-circle theorem [equations (7.5) and (7.6)] immediately extends to UCM flow with the elastic wavespeed c_E replacing the Alfvén wavespeed c_A. However, the analogous theorem is not useful. The elastic wavespeed relative to the base flow is zero when U is a maximum [see (7.7)]. Thus the bounds we reach are those of the Newtonian version of Howard's semi-circle theorem. It is possible to slightly reduce the size of the semi-circle as noted by Rallison and Hinch [79].

7.2 Formulation of the problem

In this section we introduce the base flows. We nondimensionalize and derive the full nonlinear equations governing the evolution of perturbations.

We assume that the fluid satisfies the UCM equations, which are (in

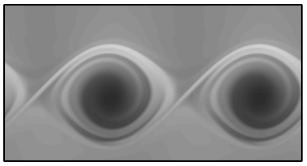

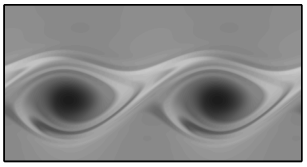

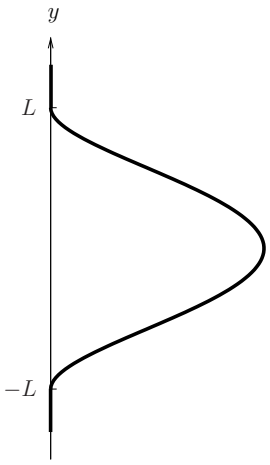

(a) The submerged jet (7.13).

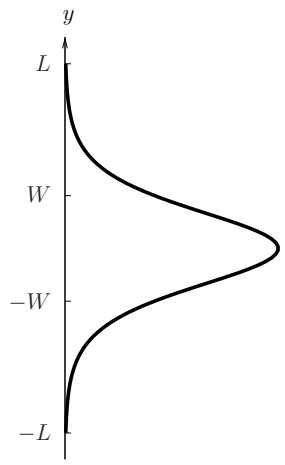

(b) The Bickley jet (7.14).

Figure 7.1: The flow profiles.

dimensional form)

$$\rho\frac{D\boldsymbol{U}}{Dt} = -\nabla P + \frac{\mu}{\tau}\nabla\cdot\mathsf{A} + \mathcal{F}\,, \tag{7.10}$$

$$\overset{\nabla}{\mathsf{A}} = \frac{1}{\tau}(\mathsf{I}-\mathsf{A})\,, \tag{7.11}$$

$$\nabla\cdot\boldsymbol{U} = 0\,. \tag{7.12}$$

The body force $\mathcal{F}$ is needed to maintain the base flows.

7.2.1 Base flow

In order to concentrate on the inertial instability we consider flows that avoid a jump in first normal stress difference. We use two flow profiles, shown in figure 7.1. The first is

$$U(y) = \begin{cases} U_0(1-y^2/L^2)^2 & |y|\le L \\ 0 & |y|\ge L \end{cases}\,, \tag{7.13}$$

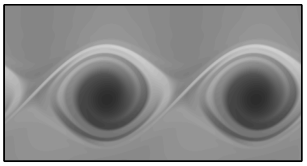

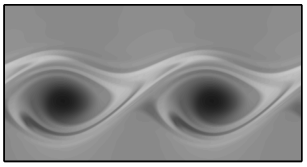

which we refer to as the *submerged jet*. It is proportional to the square of the parabolic profile (7.9) considered by Rallison and Hinch. At $y = \pm L$ both U and U' are continuous, but U'' is not. The length scale of the flow is characterized by the width $W = L$. The second profile we consider is the *Bickley jet* for which

$$U(y) = U_0 \operatorname{sech}^2(y/W)\,, \tag{7.14}$$

where W is a characteristic width of the flow. The Bickley jet was originally derived by Bickley [5] as a solution to the Prandtl boundary layer equations for an incompressible viscous jet. The flow he found travels in the x-direction with a sech^2 profile in y. The amplitude decays slowly in x while the width increases, conserving momentum. Under the assumption of constant width, this jet has become a standard profile for the study of inviscid instabilities, particularly on the β-plane. A number of linear stability results have been found [59, 42, 65, 26]. Most of these are summarized by Balmforth and Piccolo [4].

For the computations in the linear stability analysis we need a finite domain. For the submerged jet we will see that the quiescent fluid can be treated analytically and so the calculations can be restricted to the jet. For the Bickley jet we will apply periodic boundary conditions at $|y| = L \gg W$. This introduces a discontinuity for U' at $\pm L$, but $|U'|$ remains continuous.

In light of the RH mode, we must consider whether the discontinuities seen in U'' for the submerged jet and U' for the Bickley jet can generate new instabilities. In section 7.4.2 we attempt to show that they do not introduce any instability. We have not been able to give a rigorous argument, but use a parameter search with some canonical examples.

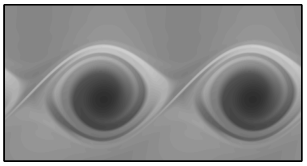

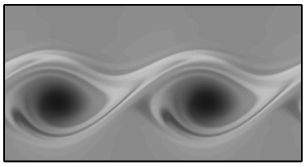

7.2.2 Nondimensionalization

We use a different nondimensionalization from that which we used for the coextrusion flow. We nondimensionalize all lengths using the typical width W and nondimensionalize time using a characteristic shear rate U_0/W. Using asterisks to denote the dimensionless variables we have $L^* = L/W$, $\boldsymbol{U}^* = \boldsymbol{U}/U_0$, $P^* = P/\rho U_0^2$ and $\nabla^* = W\nabla$. We define the Weissenberg number by

$$Wi \equiv U_0\tau/W$$

and set $\mathsf{A}^* = Wi^{-2}\mathsf{A}$. Dropping the asterisks we arrive at

$$\frac{D\boldsymbol{U}}{Dt} = -\nabla P + E\nabla\cdot\mathsf{A} + \mathcal{F}\,, \tag{7.15}$$

$$\overset{\nabla}{\mathsf{A}} = (Wi^{-3}\mathsf{I} - Wi^{-1}\mathsf{A})\,, \tag{7.16}$$

$$\nabla\cdot\boldsymbol{U} = 0\,, \tag{7.17}$$

where the elasticity $E \equiv \tau\mu/\rho W^2$ measures the ratio of elastic to inertial stresses. The Reynolds number is $Re \equiv \rho W U_0/\mu$ and so $E = Wi/Re$. Note that E is independent of the magnitude of the flow rate and depends only on fluid properties and the flow geometry.

The base flows become

$$U(y) = \begin{cases} (1-y^2)^2 & |y| \le 1 \\ 0 & |y| \ge 1 \end{cases}\,, \tag{7.18}$$

and

$$U(y) = \operatorname{sech}^2 y\,. \tag{7.19}$$

The history of every fluid element is constant, so $D\mathsf{A}/Dt = \mathsf{0}$. Using equation (7.16) we find

$$\mathsf{A} = \begin{pmatrix} 2U'^2 + Wi^{-2} & Wi^{-1}U' \\ Wi^{-1}U' & Wi^{-2} \end{pmatrix}\,.$$

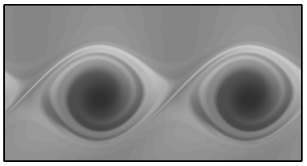

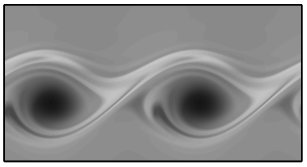

7.2.3 Perturbation equations

We take the perturbed velocity to be $\tilde{\boldsymbol{U}}(x,y,t) = \boldsymbol{U}(y) + \boldsymbol{u}(x,y,t)$ and the perturbed elastic stress to be $\tilde{\mathsf{A}}(x,y,t) = \mathsf{A}(y) + \mathsf{a}(x,y,t)$. To satisfy incompressibility automatically we introduce a streamfunction ψ such that $\boldsymbol{u} = (\psi_y, -\psi_x)$. We substitute $\tilde{\boldsymbol{U}}$ and $\tilde{\mathsf{A}}$ into equations (7.15) and (7.16). We eliminate pressure by taking the curl of the momentum equation (7.15), yielding an equation for the perturbation vorticity ζ. We reach

$$\nabla^2\psi = -\zeta\,, \tag{7.20}$$

$$\zeta_t + U\zeta_x + U''\psi_x - J(\psi,\zeta) = E[-\partial_{xy}a_{11} + (\partial_x^2 - \partial_y^2)a_{12} + \partial_{xy}a_{22}]\,, \tag{7.21}$$

$$\mathsf{a}_t + U\mathsf{a}_x - J(\psi,\mathsf{a}) - \psi_x\mathsf{A}' - U'\begin{pmatrix} 2a_{12} & a_{22} \\ a_{22} & 0 \end{pmatrix} - \mathsf{H} - \mathsf{h} = -W\!i^{-1}\mathsf{a}\,, \tag{7.22}$$

where prime denotes differentiation with respect to y and the Jacobian J satisfies $J(q,r) = q_x r_y - q_y r_x$. The tensors $\mathsf{H} = \mathsf{A}\cdot(\nabla\boldsymbol{u}) + (\nabla\boldsymbol{u})^T\cdot\mathsf{A}$ and $\mathsf{h} = \mathsf{a}\cdot(\nabla\boldsymbol{u}) + (\nabla\boldsymbol{u})^T\cdot\mathsf{a}$ are given by

$$\mathsf{H} = \begin{pmatrix} 2A_{11}\psi_{xy} + 2A_{12}\psi_{yy} & A_{22}\psi_{yy} - A_{11}\psi_{xx} \\ A_{22}\psi_{yy} - A_{11}\psi_{xx} & -2A_{12}\psi_{xx} - 2A_{22}\psi_{xy} \end{pmatrix},$$

$$\mathsf{h} = \begin{pmatrix} 2a_{11}\psi_{xy} + 2a_{12}\psi_{yy} & a_{22}\psi_{yy} - a_{11}\psi_{xx} \\ a_{22}\psi_{yy} - a_{11}\psi_{xx} & -2a_{12}\psi_{xx} - 2a_{22}\psi_{xy} \end{pmatrix}.$$

For the submerged jet (7.18) we apply decay conditions for large y. For the Bickley jet (7.19) we apply periodic boundary conditions at $y = \pm L$ where $L \gg 1$. When we study the weakly nonlinear problem later, we will use amplitude equations derived for $E \ll 1$ for which the linear problem has an analytic solution for $L \to \infty$.

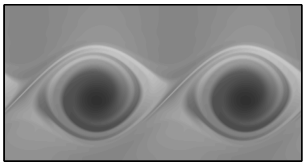

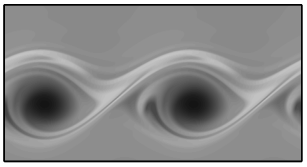

7.3 The linear problem for $Wi \gg 1$

For the linear analysis we drop the nonlinear terms $J(\psi,\zeta)$, $J(\psi,\mathsf{a})$ and h from the governing equations (7.20)–(7.22) and seek modes proportional to $\exp[ik(x-ct)]$. We derive the linearized perturbation equations at large Wi in section 7.3.1 and discuss the numerics we use to solve the equations in section 7.3.2.

7.3.1 The linearized equations

The linearized equations are

$$\begin{aligned}(-k^2+\partial_y^2)\psi &= -\zeta\,,\\ ik(U-c)\zeta + ikU''\psi &= E[-ik\partial_y a_{11} + (-k^2-\partial_y^2)a_{12}\\ &\qquad + ik\partial_y a_{22}]\,,\end{aligned}$$

$$ik(U-c)\mathsf{a} - ik\psi\mathsf{A}' - U'\begin{pmatrix}2a_{12} & a_{22}\\ a_{22} & 0\end{pmatrix} - \mathsf{H} = -Wi^{-1}\mathsf{a}\,.$$

We assume that $Wi \gg 1$ and find

$$\mathsf{H} = \begin{pmatrix}4ikU'^2\psi_y & 2k^2U'^2\psi\\ 2k^2U'^2\psi & 0\end{pmatrix} + \mathcal{O}(Wi^{-1})\,.$$

We conclude that $a_{22} = \mathcal{O}(Wi^{-1})$. Taking leading order terms in Wi, the equations simplify to

$$(-k^2+\partial_y^2)\psi = -\zeta\,, \tag{7.23}$$

$$ik(U-c)\zeta + ikU''\psi = E[-ik\partial_y a_{11} + (-k^2-\partial_y^2)a_{12}]\,, \tag{7.24}$$

$$ik(U-c)a_{11} = 4ikU'U''\psi + 2U'a_{12} + 4ikU'^2\psi_y\,, \tag{7.25}$$

$$ik(U-c)a_{12} = 2k^2U'^2\psi\,. \tag{7.26}$$

Combining these we arrive at the elastic form of Rayleigh's equation

$$[\Gamma\phi']' = k^2\Gamma\phi\,, \tag{7.27}$$

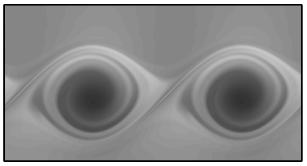

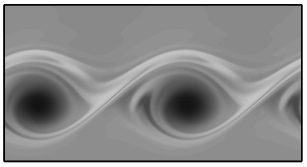

where $\Gamma = (U-c)^2 - 2EU'^2$ and $\phi = -\psi/(U-c)$. There is a neutrally stable continuous spectrum consisting of those c for which $\Gamma(y) = 0$ at some value of y.

For the submerged jet (7.13) we can explicitly find the perturbation flow for $|y| > 1$, following Rallison and Hinch [79]. In this region U and U' both vanish, and Γ is constant. The equations become

$$\phi'' = k^2\phi\,,$$

so ϕ is either a growing or decaying exponential. Enforcing decay as $y \to \pm\infty$, we find

$$\Gamma\phi' + kc^2\phi = 0 \qquad y = 1\,, \tag{7.28}$$

$$\Gamma\phi' - kc^2\phi = 0 \qquad y = -1. \tag{7.29}$$

We use these conditions to act as boundary conditions on the jet and no longer consider the quiescent fluid.

For the Bickley jet, the periodic conditions state $\phi(L) = \phi(-L)$ and $\phi'(L) = \phi'(-L)$. However varicose perturbations must satisfy $\phi(L) = -\phi(-L)$ and sinuous perturbations must satisfy $\phi'(L) = -\phi'(-L)$. Consequently for the Bickley jet we have

$$\phi(L) = 0 \qquad \text{varicose}\,, \tag{7.30}$$

$$\phi'(L) = 0 \qquad \text{sinuous}\,. \tag{7.31}$$

For both flows we have symmetry conditions at the center-line

$$\phi(0) = 0 \qquad \text{varicose}\,,$$

$$\phi'(0) = 0 \qquad \text{sinuous}\,,$$

and so we can restrict our attention to $y \geq 0$.

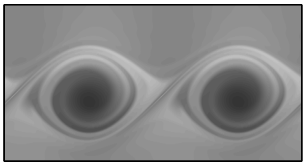

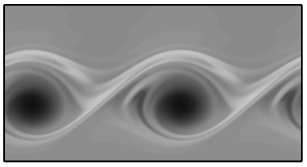

Simple observations

As in the Newtonian case, complex eigenvalues of the elastic Rayleigh equation (7.27) appear in conjugate pairs. We can further show that when c is real, it must lie in the continuous spectrum, that is, there exists a y such that $\Gamma(y) = 0$. To see this we assume c is real, multiply equation (7.27) by ϕ^* and integrate from $-L$ to L ($L = 1$ for the submerged jet and $L \gg 1$ for the Bickley jet). Using integration by parts we find

$$[\Gamma\phi'\phi^*]_{-L}^{L} - \int_{-L}^{L} \Gamma|\phi'|^2\, dy = k^2 \int_{-L}^{L} \Gamma|\phi|^2\,.$$

For the submerged jet, the first term gives a contribution of $-kc^2(|\phi(-1)|^2 + |\phi(1)|^2)$ which is at most zero. For the Bickley jet, the contribution is exactly zero because of periodic boundary conditions. Thus $\int(|\phi'|^2+k^2|\phi|^2)\Gamma\, dy \le 0$. For both flows, $U'(0) = 0$ and so $\Gamma(0) \ge 0$. However, $|\phi'|^2 + k^2|\phi|^2 > 0$ so Γ must be zero somewhere. Thus c is in the continuous spectrum.

7.3.2 Numerical method for the linear problem

As for the coextrusion flow, when we use a spectral method the modes close to the continuous spectrum are not well-resolved. For coextrusion, we simply increase the number of Chebyshev polynomials until the balloon lies in the stable half plane. Because the continuous spectrum for the inviscid elastic jet is on the real axis, the balloon always lies partly in the unstable half plane. In practice, we are unable to resolve the unstable eigenvalues spectrally.

Instead, we employ a shooting algorithm using an adaptive step-size Runge–Kutta integration routine provided by Numerical Recipes [77]. For fixed c, there is only one free condition (either ϕ or ϕ' depending on the symmetry) at $y = 0$. We fix its value and integrate from zero to L. For each c we calculate an error $\mathcal{E}$ at L [from whichever of equations (7.28)–(7.31) is appropriate]. The error is zero if and only if c is an eigenvalue. We use

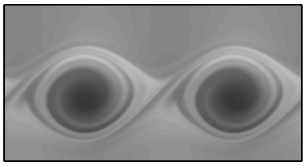

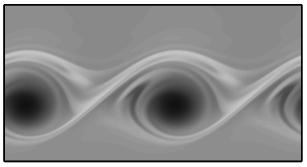

a Newton–Raphson algorithm (also from Numerical Recipes) to find c such that $\mathcal{E} = 0$. The Numerical Recipes routines have some flaws encountered in the coextrusion flow and discussed in appendix A.1.1. The same workarounds apply in this case.

It is difficult to obtain a good initial estimate of the eigenvalues for the shooting algorithm. The eigenvalues are close to the continuous spectrum and the semi-circle theorem does not give tight bounds for their position. If the initial guess is not sufficiently close, then the continuous spectrum disrupts the convergence and we do not find the eigenvalue. This is particularly problematic because there is no systematic method to determine the existence of the eigenvalue *a priori*. The failure of the shooting algorithm is insufficient to establish that the eigenvalue does not exist.

We turn to a "carpet bombing" method to find a good approximation for the eigenvalue. We systematically test possible unstable eigenvalues. The semi-circle theorem bounds the location of any unstable eigenvalue. We take a fine mesh of values of c over this region. For each value of c we integrate from $y = 0$ to L as in the shooting algorithm. We take $\|\mathcal{E}\| = |\Re[\mathcal{E}]| + |\Im[\mathcal{E}]|$. Plotting $\log_{10}(\|\mathcal{E}\|)$ against c, the eigenvalues appear as logarithmic singularities. Once we have located the eigenvalues, shooting with parameter continuation can be used to follow them as parameters change.

Testing the linear calculation

We test our calculations with the flow profile of Rallison and Hinch [79]. We reproduce their results in figure 7.2.

7.4 RH-like instabilities

The instability of Rallison and Hinch [79] is due to a discontinuity in the first normal stress difference. Its existence raises the possibility that discontinu-

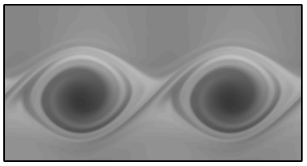

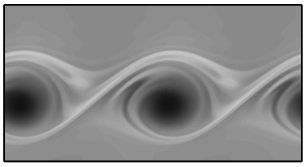

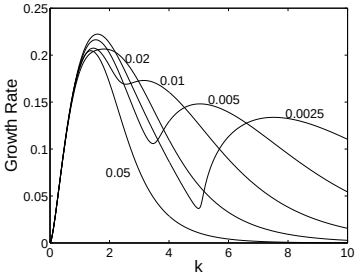

(a) Varicose growth rates for different values of E.

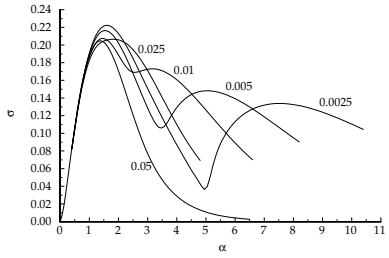

(b) Figure 9 of [79]. Their α is our k and their σ is our growth rate. Used with permission of Cambridge University Press.

Figure 7.2: Comparison between our calculations and those of Rallison and Hinch for their jet profile. The calculations are in agreement (note their curve for $E = 0.02$ is mislabelled as 0.025).

ities in some other elastic property of the base flow might result in a new instability. In particular the base flow profiles we have chosen both have a discontinuity in the derivative of the first normal stress difference.

In this section we discuss the RH instability in more detail, largely following the original analysis [79]. We show its existence in a simplified base flow. We then consider simplified base flows containing the same discontinuities as the submerged jet (7.18) and the Bickley jet (7.19).

7.4.1 The RH instability

The flow profile used by Rallison and Hinch [79] becomes

$$U(y) = \begin{cases} 1 - y^2 & |y| \leq 1 \\ 0 & |y| > 1 \end{cases}, \tag{7.32}$$

after nondimensionalization. The jump in normal stress at $y = 1$ gives rise to an instability for small values of E at large values of k, as seen in figure 7.2.

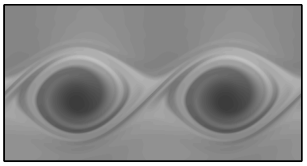

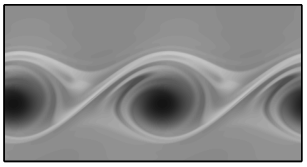

We see two distinct peaks in the growth rates in this figure, one at $k = 2$, which comes from the inertial instability and another at successively larger values of k as E decreases which is the new RH instability.

When E is small, the forward traveling elastic wave at $y = 1$ has the same velocity as the backward traveling elastic wave at $y = 1-2(2E)^{1/2}$. The shear rate in the thin layer between the two elastic waves is effectively constant. The only length scale present is the width of the layer, so we expect the most unstable wavelengths to scale like $E^{1/2}$, giving $k \sim E^{-1/2}$. Rallison and Hinch found that $\Im[c] \sim E^{1/2}$ and so the growth rate is $\mathcal{O}(1)$ as $E \to 0$, but the wavenumber tends to infinity. Figure 7.2 shows an additional qualitative difference from the inertial results: there is no k_c at which the flow stabilizes.

We demonstrate our numerical methods with this instability. In figure 7.3(b) we plot $\log_{10}(\|\mathcal{E}\|)$ for each value of c as described in section 7.3.2. The logarithmic singularity at the eigenvalue is clear in figures 7.3(c) and (d). We use this to seed the shooting algorithm and turn to shooting and parameter continuation to follow the eigenvalue. The resulting growth rates are shown in figure 7.2.

To make it clear that the RH instability is due to the jump in normal stress at $y = 1$, we consider a different flow profile

$$U(y) = \begin{cases} 2(1-y) & y < 1 \\ 0 & y > 1 \end{cases}, \tag{7.33}$$

with the perturbation flow satisfying a no-penetration boundary condition at $y = 0$, and decay as $y \to \infty$. At $y = 1$ this has the same jump in normal stresses as the RH profile, but U' is monotonic so there is no inertial instability. The results are plotted in figure 7.4. For sufficiently small values of E with $k \sim E^{-1/2}$, the growth rates are similar to figure 7.2, as expected. The instability also does not stabilize at large k.

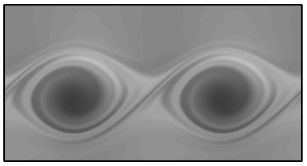

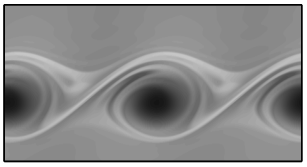

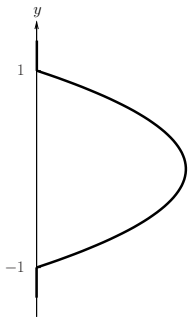

(a) Rallison and Hinch base flow (7.32).

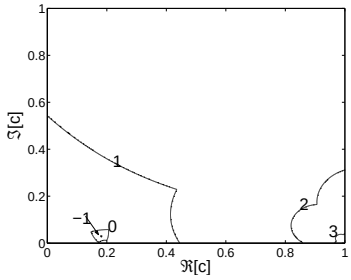

(b) Contours of $\log_{10}(\|\mathcal{E}\|)$ for $E = 0.005$ and $k = 5$.

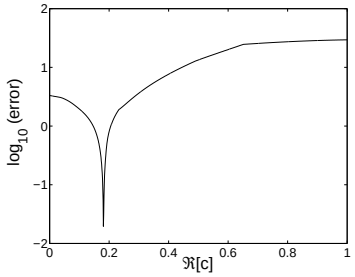

(c) Minimum $\log_{10}(\|\mathcal{E}\|)$ as a function of $\Re[c]$. The singularity is clear.

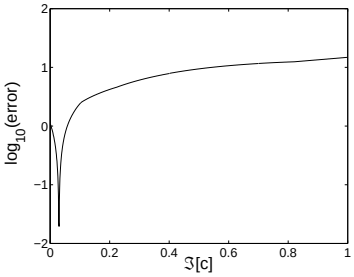

(d) Minimum $\log_{10}(\|\mathcal{E}\|)$ as a function of $\Im[c]$. The singularity is clear.

Figure 7.3: The stability behavior of (7.32). It is clear that when $E = 0.005$ and $k = 5$ there is an unstable mode with $\Re[c] \approx 0.2$ and $\Im[c] \approx 0.03$.

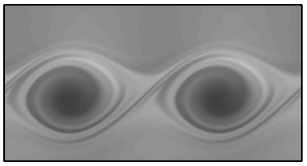

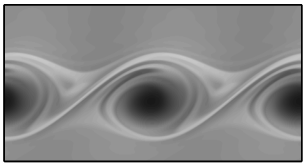

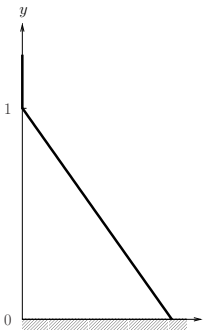

(a) Base flow (7.33).

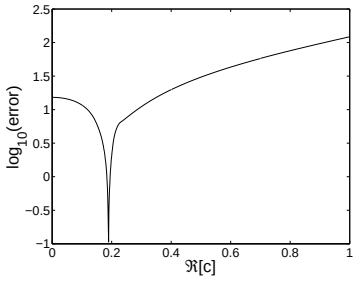

(b) Minimum $\log_{10}(\|\mathcal{E}\|)$ as a function of $\Re[c]$ for $E = 0.005$ and $k = 5$. The singularity is clear.

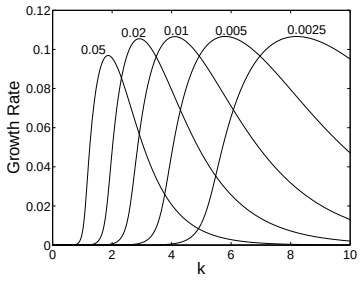

(c) Growth rates.

Figure 7.4: Results for (7.33). Given the same jump in normal stress as in the RH jet, a similar instability occurs.

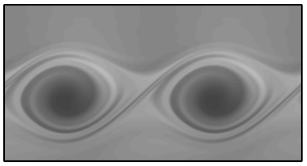

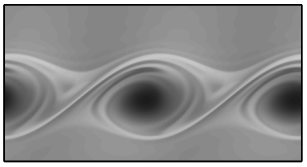

7.4.2 Eliminating the RH instability

In this section we consider simplified flow profiles that reproduce the discontinuities of the submerged jet and the Bickley jet. We seek to show that there is no instability introduced by these boundary conditions. Our argument is not rigorous, but depends on an incomplete parameter search.

At $y = 1$ the velocity profile of the submerged jet (7.18) has a quadratic zero, with a discontinuity in U''. In contrast at $y = \pm L$ the Bickley jet (7.19) has a jump in U', but not in the first normal stress difference which depends on $|U'|$.

We consider two simplified flows. The first is

$$U(y) = \begin{cases} (1-y)^2 & 0 \le y \le 1 \\ 0 & y > 1 \end{cases} , \tag{7.34}$$

with a no-penetration boundary condition at $y = 0$ and decay as $y \to \infty$. At $y = 1$ there is a discontinuity in U'', but not U'. This mimics the boundary of the submerged jet at $y = 1$. The second test flow is

$$U(y) = 1 - |y| \qquad \text{for } |y| < 1\,, \tag{7.35}$$

with no-penetration boundary conditions at $|y| = 1$. At $y = 0$, U' jumps but $|U'|$ does not, mimicking the the Bickley jet condition at $|y| = L$.

The shear rate U' is monotonic in both of these flows and so they are stable to the inertial instability. We do not find any new instabilities for the parameters searched. The results of carpet bombing for $E = 0.005$ and $k = 5$ are shown in figures 7.5 and 7.6.

7.5 Linear results

Having shown that the boundary conditions of the submerged jet and the Bickley jet are unlikely to introduce new instabilities, we now turn to the

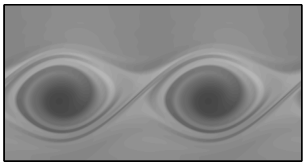

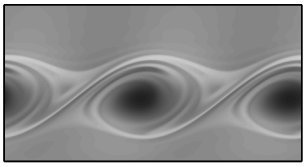

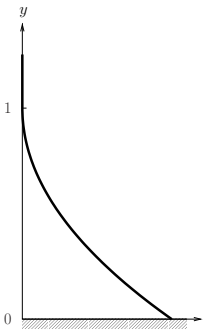

(a) Base flow (7.34).

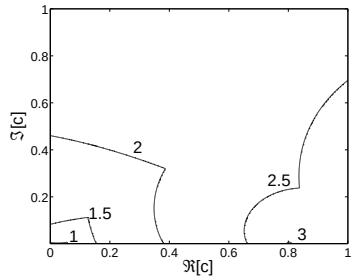

(b) Contours of $\log_{10}(\|\mathcal{E}\|)$ for $E = 0.005$ and $k = 5$.

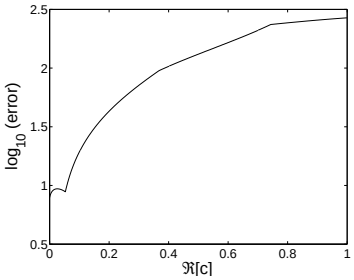

(c) Minimum $\log_{10}(\|\mathcal{E}\|)$ as a function of $\Re[c]$.

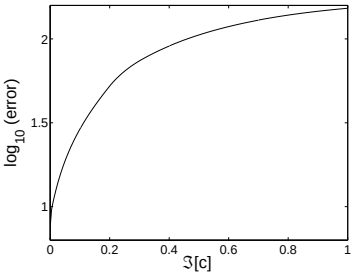

(d) Minimum $\log_{10}(\|\mathcal{E}\|)$ as a function of $\Im[c]$.

Figure 7.5: There is no singularity with $\Im[c] > 0$ for the base flow (7.34), although there appears to be a singularity as $\Im[c] \to 0$.

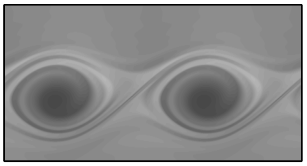

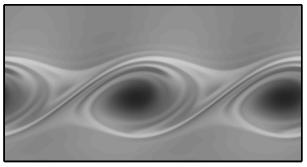

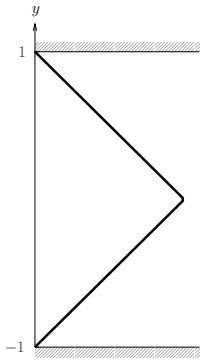

(a) Base flow (7.35).

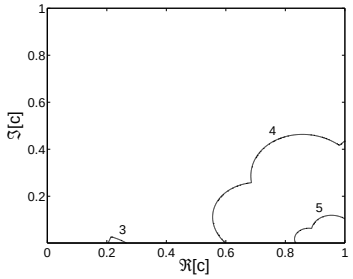

(b) Contours of $\log_{10}(\|\mathcal{E}\|)$ for $E = 0.005$ and $k = 5$.

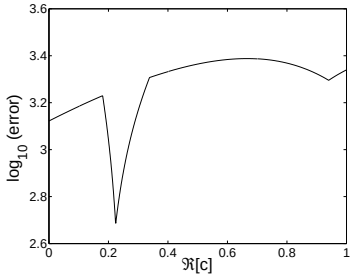

(c) Minimum $\log_{10}(\|\mathcal{E}\|)$ as a function of $\Re[c]$.

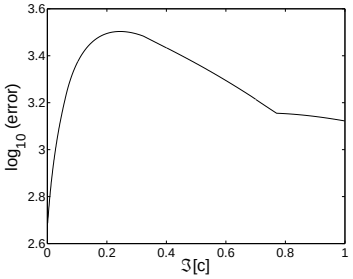

(d) Minimum $\log_{10}(\|\mathcal{E}\|)$ as a function of $\Im[c]$.

Figure 7.6: There is no singularity with $\Im[c] > 0$ for the base flow (7.35), although there appears to be a singularity as $\Im[c] \to 0$.

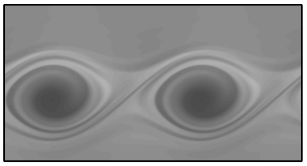

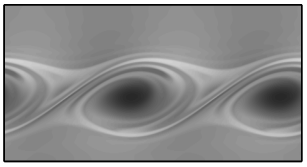

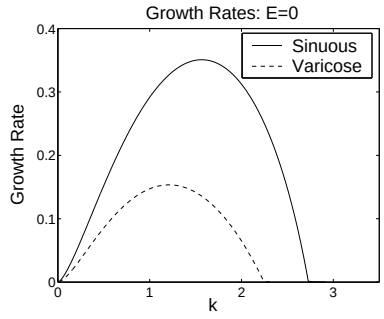

(a) Varicose and sinuous growth for the submerged jet (7.18) with $E = 0$.

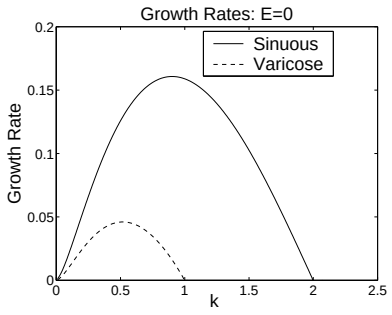

(b) Varicose and sinuous growth for the Bickley jet (7.19) with $E = 0$ and $L = 10$.

Figure 7.7: Growth rates for $E = 0$. There is simultaneously a stable mode with opposite growth rate.

effect of elasticity on the growth of the inertial mode.

We first consider the Newtonian limit $E = 0$. Growth rates for the two flows are shown in figure 7.7. For both base flows the growth rate is positive for $0 < k < k_c$, for some k_c, and the sinuous modes are more unstable than the varicose modes.

We plot the growth rates for different values of E in figure 7.8. The growth rate reduces as E increases, and the value of k_c for which it stabilizes decreases as well.

We plot the maximum growth rate as a function of E in figure 7.9. At small values of E the sinuous mode is more unstable, but as E increases, it is completely stabilized and the varicose mode is the only instability.

The submerged jet and the Bickley jet have shown qualitatively similar behavior. From here on, we focus our attention on the Bickley jet. We consider the marginally stable mode at $k = k_c$ where the flow stabilizes. At $E = 0$ the mode is continuous and smooth. For the Bickley jet Lipps [59]

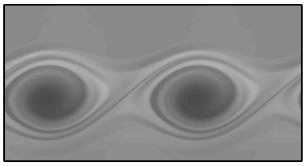

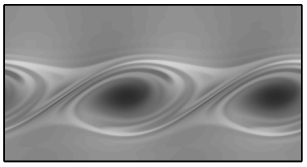

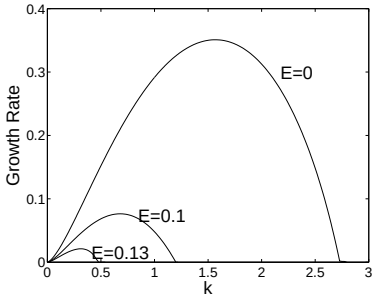

(a) Sinuous growth rates for the submerged jet (7.18).

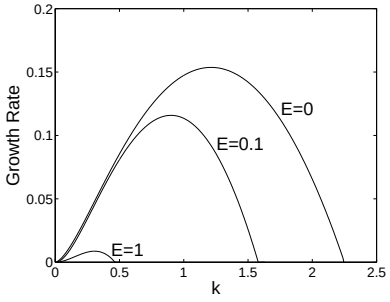

(b) Varicose growth rates for the submerged jet (7.18).

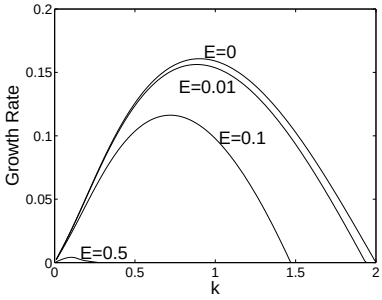

(c) Sinuous growth rates for the Bickley jet (7.19).

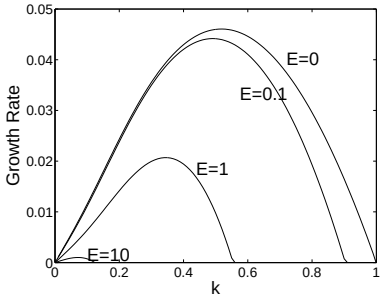

(d) Varicose growth rates for the Bickley jet (7.19).

Figure 7.8: Growth rates as E changes. The effect of E is stabilizing.

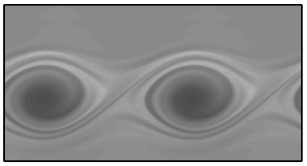

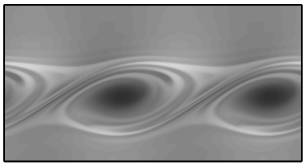

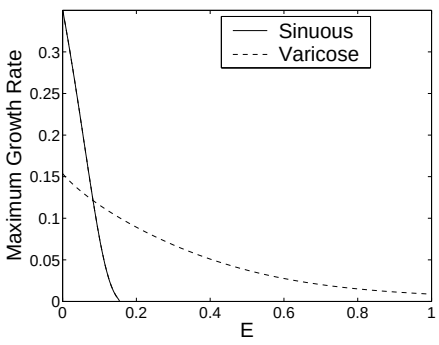

(a) Maximum growth rates of the submerged jet (7.18) as E changes.

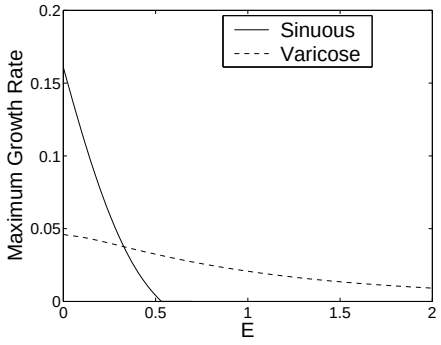

(b) Maximum growth rates of the Bickley jet (7.19) as E changes.

Figure 7.9: Maximum growth rates as E changes. Sinuous modes are completely stabilized at large enough E.

showed that $k_c = 2$ for infinite L, and the mode is given by $\psi(y) = \mathrm{sech}^2(y)$. This is clear in figure 7.10 where we take $L = 10$ and k slightly less than 2.

As E grows, two singularities emerge out of the critical location where $U'' = 0$. They are separated by a width which is $\mathcal{O}(E^{1/2})$. When this width is less than the critical layer thickness, the elasticity plays no role outside the critical layer: it only modifies the nonlinear equations for the critical layer evolution. As E increases further, the singularities must be treated separately in the nonlinear analysis.

We show the emergence and separation of the singularities for the Bickley jet in figure 7.11. It is difficult to calculate the marginally stable mode at k_c explicitly, and so instead we calculate the slowly growing mode for k slightly less than k_c.

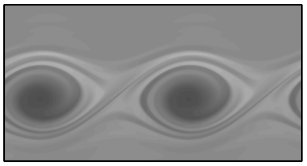

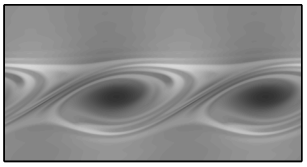

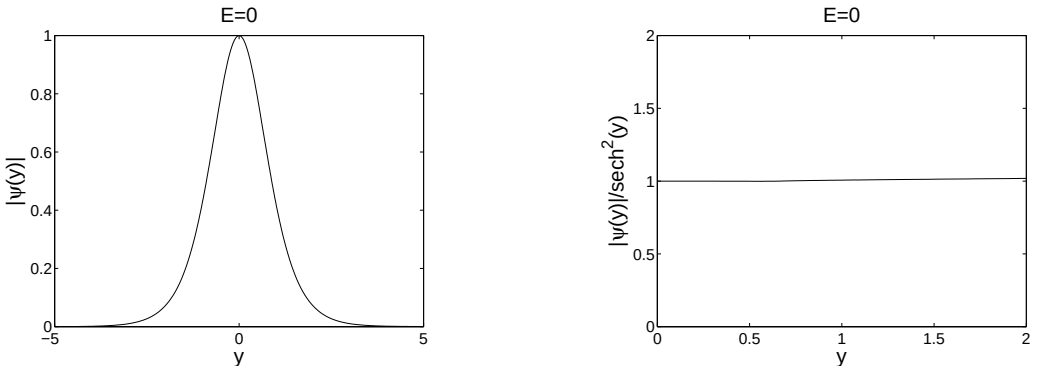

(a) The magnitude of ψ.

(b) The magnitude of ψ normalized by $\mathrm{sech}^2(y)$.

Figure 7.10: The slowly growing mode for $E = 0,\ k = 1.99$ with $L = 10$. No singularities are present

7.6 Weakly nonlinear equations for small E

The linear results for the two flow profiles are qualitatively similar, and so for the weakly nonlinear analysis we focus on just the Bickley jet. We take the $L \to \infty$ limit for which we have analytical linear results. Our analysis follows Balmforth and Piccolo [4] who considered the Newtonian problem with a Coriolis effect.

We change to a frame of reference moving with the marginally stable linear mode

$$\hat{x} = x - ct\,,$$
$$\hat{U} = U - c\,.$$

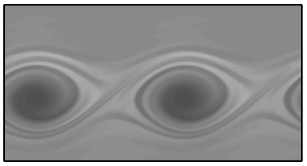

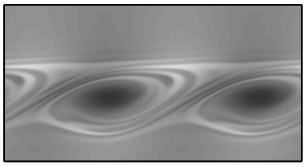

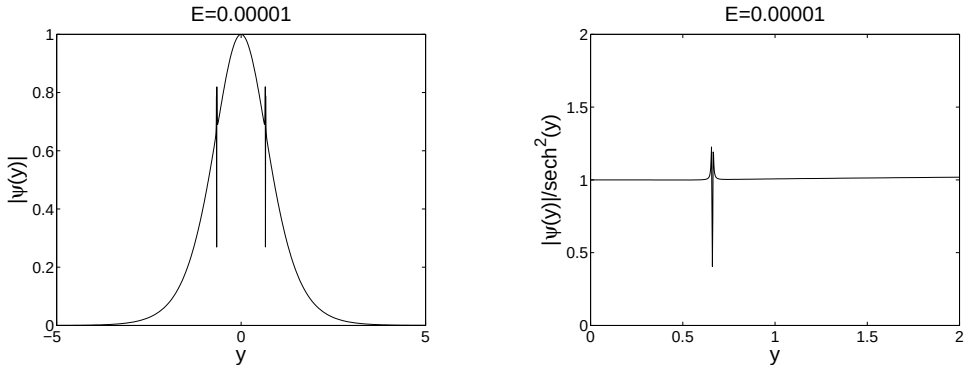

(a) Magnitude and normalized magnitude of streamfunction of slowly growing mode at $E = 0.00001,\ k = 1.99$.

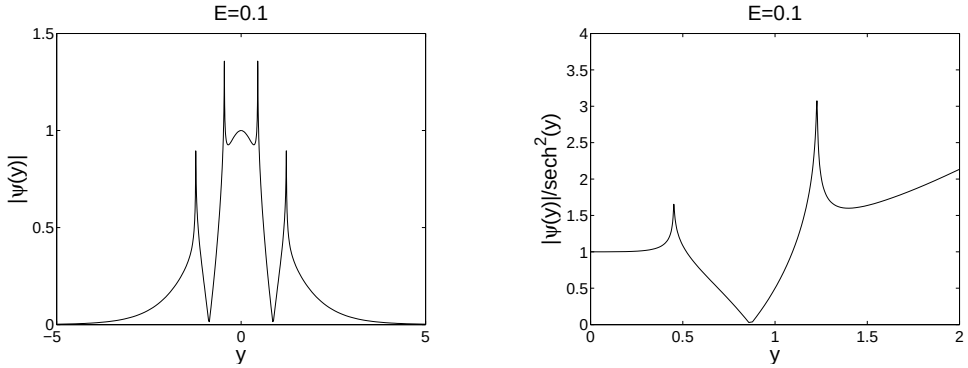

(b) Magnitude and normalized magnitude of streamfunction of slowly growing mode at $E = 0.1,\ k = 1.46$.

Figure 7.11: Plots of magnitude and magnitude normalized by the $E = 0$, $k = 2$ neutrally stable mode $\psi = \text{sech}^2(y)$ for slowly growing modes. Two singularities appear at small E and separate as E increases. At $k = k_c$, the value of ψ goes through zero between the two singularities.

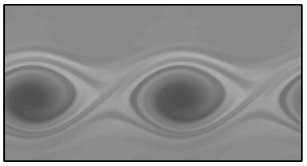

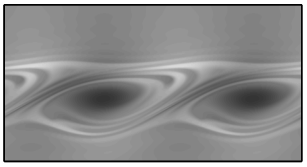

Dropping hats, (7.20)–(7.22) become

$$\nabla^2\psi = -\zeta\,, \tag{7.36}$$

$$\zeta_t + U\zeta_x + U''\psi_x - J(\psi,\zeta) = E[-\partial_{xy}a_{11} + (\partial_{xx} - \partial_{yy})a_{12} + \partial_{xy}a_{22}]\,, \tag{7.37}$$

$$\mathsf{a}_t + U\mathsf{a}_x - J(\psi,\mathsf{a}) - \psi_x\mathsf{A}' - U'\begin{pmatrix} 2a_{12} & a_{22} \\ a_{22} & 0 \end{pmatrix} - \mathsf{H} - \mathsf{h} = -Wi^{-1}\mathsf{a}\,, \tag{7.38}$$

where $U(y) = \operatorname{sech}^2 y - 2/3$, and at $y = y_c$ both U and U'' are zero.

7.6.1 The amplitude equations

We take $E = \mathcal{O}(\epsilon^4)$ and $Wi^{-1} = \mathcal{O}(\epsilon)$. We set $Wi^{-1} = \epsilon\lambda$, so λ measures the relaxation rate[1]. The elastic stresses drop out of equation (7.37) at leading order, so the linear results are the same as for an inviscid Newtonian fluid. We summarize the linear results: the flow is unstable for small values of k. Varicose modes stabilize with $k = 1$ while sinuous modes stabilize with $k = k_c = 2$. For sinuous modes at k_c, the wavespeed is $c = 0$ (in our new frame of reference) and the streamfunction of the perturbation is $\psi = \operatorname{sech}^2 y$.

We choose our domain to be periodic with length $2\pi/k$ with $k = k_0 - \epsilon k_1$ [taking $k_0 = k_c = 2$, $k_1 > 0$, $k_1 = \mathcal{O}(1)$, and $\epsilon \ll 1$]. The perturbation with wavelength equal to the domain length is unstable. As $k_1 \to 0$ the growth rate goes to zero with non-zero derivative. Consequently the most unstable wavelength that fits in the domain has $\mathcal{O}(\epsilon)$ growth rate, and the resulting long time scale is $T = \epsilon t$. It is generally found for an inviscid Newtonian jet that the amplitude of the mode grows until it is $\mathcal{O}(\epsilon^2)$, at which point the nonlinear terms stop the growth and the amplitude saturates [4].

Within the critical layer we introduce the inner variable $Y = (y - y_c)/\epsilon$. The dynamic growth of the marginally stable mode is controlled by the nonlinear terms, which are only significant in the critical layer. We need a new

[1] We use λ for the relaxation *rate*, and it should not be confused with a relaxation time.

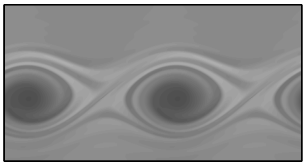

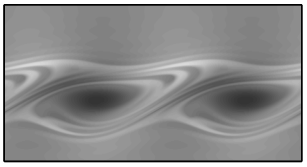

system of governing equations for the flow in the critical layer, which will be matched to the linear solution at the edge of the critical layer.

The UCM equations

For the UCM fluid we arrive at a reduced system of equations governing the critical layer, derived in appendix B.1 starting from (7.36)–(7.38). Following rescalings, we can write the equations in the canonical form

$$\mathcal{L}[\Theta] = -\Psi_x + \kappa\Psi_T + E(a_{12,YY} + a_{11,xY})\,, \tag{7.39}$$

$$\mathcal{L}[a_{11}] = 2a_{12} - \lambda a_{11}\,, \tag{7.40}$$

$$\mathcal{L}[a_{12}] = a_{22} + a_{11}\Psi + 2\Psi - \lambda a_{12}\,, \tag{7.41}$$

$$\mathcal{L}[a_{22}] = 2a_{12}\Psi + 2\lambda\Psi - \lambda a_{22}\,, \tag{7.42}$$

$$\Psi = B(T)\exp(ix) + cc\,, \tag{7.43}$$

$$iB_T = -\frac{1}{2\pi}\int_0^{2\pi}\int_{-\infty}^{\infty}\Theta\exp(-ix)\,dY\,dx\,, \tag{7.44}$$

where $\mathcal{L}[\Theta] = \Theta_T + Y\Theta_x - \Psi_x\Theta_Y$. The operator $\mathcal{L}[\Theta]$ is linear in Θ, but has the a nonlinear term $\Psi_x\Theta_Y$. The variables Θ, Ψ, a_{11}, a_{12}, and a_{22} are rescaled versions of the vorticity, streamfunction, and elastic stresses respectively, and B is the amplitude of the perturbation. The parameters E and λ are rescaled versions of the elasticity and the relaxation rate (large λ implies fast relaxation). The new parameter κ is determined by the base flow and is independent of material parameters; for the Bickley jet $\kappa = 0.470607$ (section B.1.1).

As discussed in chapter 1 the extensional viscosity of the Oldroyd–B model (and hence its UCM limit) in strong extensional flows has unphysical behavior. The limitations of the UCM model in extensional flow becomes apparent in the calculations in the critical layer. To improve the model, we turn to the FENE–CR equations.

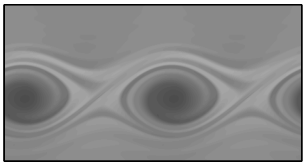

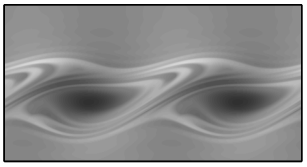

The FENE–CR equations

The dimensional form of the FENE–CR equations (in the limit of zero solvent viscosity) is

$$\rho\frac{D\boldsymbol{U}}{Dt} = -\nabla P + \frac{\mu}{\tau}\nabla\cdot[F(\mathsf{A}-\mathsf{I})] + \mathcal{F}\,, \tag{7.45}$$

$$\overset{\nabla}{\mathsf{A}} = \frac{F}{\tau}(\mathsf{I}-\mathsf{A})\,, \tag{7.46}$$

$$\nabla\cdot\boldsymbol{U} = 0\,, \tag{7.47}$$

$$F = \frac{l^2}{l^2-\mathrm{tr}(A)}\,, \tag{7.48}$$

where the parameter l measures the maximum extension of the polymers creating the elastic stress. In the limit $l\to\infty$, F tends to 1 and we recover the UCM equations. In the limit $l\to 0$, F tends to zero and we recover the Euler equations for an inviscid Newtonian fluid.

After performing the same rescalings as for the UCM fluid, we obtain the corresponding canonical form of the critical layer governing equations in

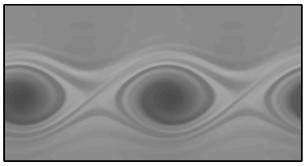

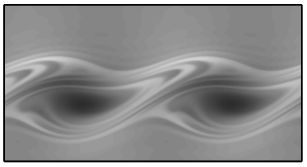

appendix B.2. The result is

$$\begin{aligned}\mathcal{L}[\Theta] &= -\Psi_x + \kappa\Psi_T + E[f_x a_{11,Y} + f_Y(a_{11,x} + 2a_{12,Y})] \\ &\quad + E[f_{xY}(a_{11} + 2/F^2) + f_{YY}(a_{12} + \lambda/F)] \\ &\quad + E[(F+f)(a_{11,xY} + a_{12,YY})]\,, \end{aligned} \tag{7.49}$$

$$\mathcal{L}[a_{11}] = 2a_{12} - \lambda[(F+f)a_{11} + 2f/F^2]\,, \tag{7.50}$$

$$\mathcal{L}[a_{12}] = a_{22} + (a_{11} + 2/F^2)\Psi - \lambda[(F+f)a_{12} + f\lambda/F]\,, \tag{7.51}$$

$$\mathcal{L}[a_{22}] = 2(a_{12} + \lambda/F)\Psi - \lambda[(F+f)a_{22} + f\lambda^2] \tag{7.52}$$

$$\Psi = B(T)\exp(ix) + cc\,, \tag{7.53}$$

$$iB_T = -\frac{1}{2\pi}\int_0^{2\pi}\int_{-\infty}^{\infty} \Theta\exp(-ix)\,dY\,dx\,, \tag{7.54}$$

$$F + f = \frac{l^2}{l^2 - 2/F^2 - a_{11}}\,, \tag{7.55}$$

$$F = (1 + \sqrt{1 + 8/l^2})/2\,, \tag{7.56}$$

where $\mathcal{L}$ is defined as for the UCM fluid. The value of κ remains 0.470607.

7.6.2 Linearization of the critical layer equations

The reduced UCM system (7.39)–(7.44) can itself be linearized and studied with normal modes. We assume a normal mode proportional to $\exp(ix+\sigma T)$. After a series of substitutions to eliminate the a_{ij} we find

$$(\sigma + iY)\Theta = B\left(-i + \kappa\sigma + \frac{4E}{(iY + \sigma + \lambda)^3}\right)\,,$$

and from (7.44)

$$\begin{aligned}\sigma &= i\int_{-\infty}^{\infty} \frac{-i + \kappa\sigma}{\sigma + iY} + \frac{4E}{(iY + \sigma + \lambda)^3(\sigma + iY)}\,dY\,, \\ &= \begin{cases} \frac{i\pi\kappa+1}{1+\pi^2\kappa^2}\pi & \Re[\sigma] > 0 \\ \frac{i\pi\kappa-1}{1+\pi^2\kappa^2}\pi - \frac{8\pi E(i+\pi\kappa)}{\lambda^3(1+\pi^2\kappa^2)} & 0 > \Re[\sigma] > -\lambda \\ \frac{i\pi\kappa-1}{1+\pi^2\kappa^2}\pi & 0 > \Re[\sigma] + \lambda \end{cases}\,, \end{aligned}$$

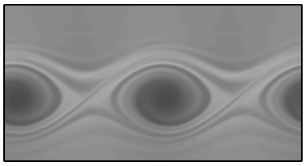

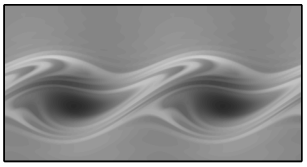

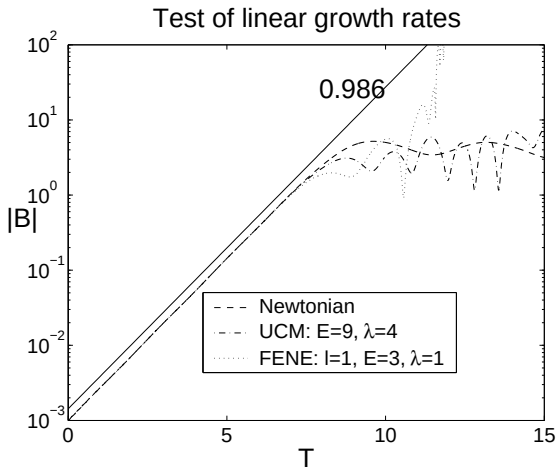

Figure 7.12: The linear growth rate is correctly found for Newtonian, UCM, and FENE–CR fluids.

using residue theory. The residue of the second term in the integrand is $4iE/\lambda^3$ at $Y = i(\sigma + \lambda)$ and $-4iE/\lambda^3$ at $Y = i\sigma$. Thus, the only appearance of E in the growth rate occurs when the poles are on opposite sides of the real axis, which can only happen if σ has negative real part. In particular, if the mode is unstable, E and λ do not affect the linear growth rate. For $\kappa = 0.470607$, we find a linear growth rate of 0.986.

A similar analysis holds for the FENE–CR equations (7.49)–(7.56), and so the growth rate of the mode at early times does not depend on the elastic parameters. We observe the linear growth rates in figure 7.12.

7.6.3 Cat's eyes

In the following sections we study the effect of elasticity on the development of cat's eyes. In order to be consistent with the calculations of Balmforth and Piccolo [4] for the Newtonian fluid we take $B(0) = -0.001$. Θ and a_{ij} are taken to be zero at $T = 0$.

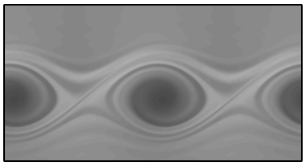

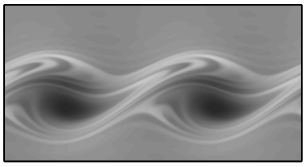

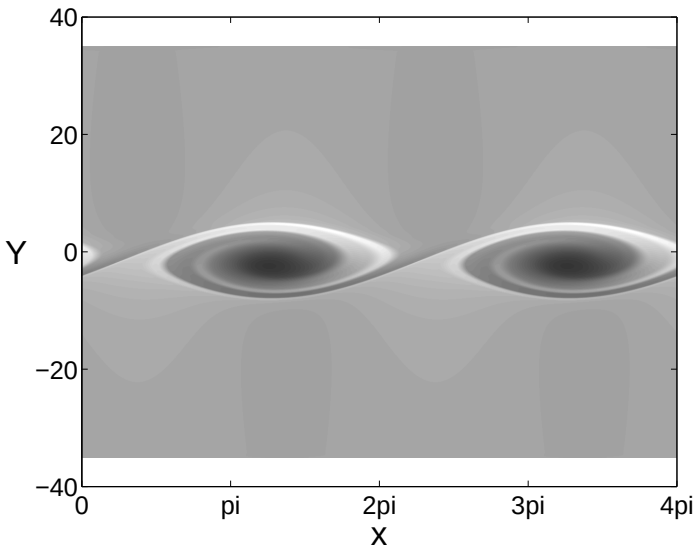

Figure 7.13: The vorticity Θ at $T = 10$, showing two periods of the Newtonian cat's eye.

Our full calculation domain [shown in figure 7.13] is much larger than the width of the cat's eyes, and is left out of the remaining figures. The calculations are performed in a box that is periodic with length 2π in the horizontal direction and use large Y asymptotics for the boundary conditions at the bottom and top boundaries $Y = -35$ and $Y = 35$. We use a 1500×1500 grid for the Newtonian and UCM calculations and an 800×800 grid for the FENE–CR calculations. The 800×800 calculations give qualitatively the same results as 1500×1500, but at later times the solution has small quantitative differences. The FENE–CR calculations are too slow to run at higher resolution. The numerical method is described in appendix B.3. The plots show two periods in the x-direction.

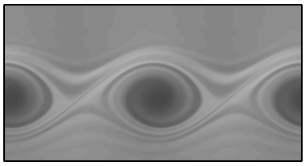

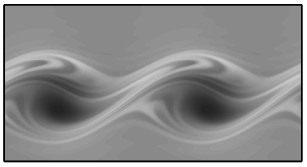

7.6.4 The Newtonian fluid

For comparison purposes, we first analyse the jet in the absence of elasticity. We study equations (7.39), (7.43), and (7.44) with $E = 0$. There are no free parameters in this system.

We plot the amplitude and maximum value of $|\Theta|$ for the Newtonian cat's eyes in figure 7.14, along with Θ for $T = 5$, 10, 15, and 20. We also plot Θ in the top picture of the flipbook at the bottom right of each page, with the time corresponding to 0.1 times the page number. At early times the mode amplitude $|B|$ grows according to the linear theory. When T is close to 10, the nonlinear terms stop the linear growth. Cat's eyes form and the amplitude begins to oscillate.

As the cat's eyes develop, they move from right to left in an apparent rolling motion. They have clearly defined top and bottom edges and are nearly symmetric under a rotation of π. The amplitude grows and begins to oscillate about $|B| \approx 4$, consistent with [4]. As time progresses, the cat's eyes keep roughly constant width. They continue to roll over and develop successively finer scales, which eventually reach the numerical grid spacing.

While the linear analysis of the critical layer applies, the growth rate is approximately 0.986. This can be seen in figure 7.12. Shortly after the nonlinear terms become important, there is a maximum in $|B|$, which we denote B_1. We use B_1 as a measure of when the nonlinear terms become important. A smaller value of B_1 indicates that the nonlinear terms become significant sooner. For the Newtonian fluid $B_1 = 5.194$, and is the first maximum of 7.14(a). Its value is reduced in the presence of elasticity.

7.6.5 The UCM fluid

Including elastic effects alters the cat's eye structure as well as the dynamic behavior from the Newtonian $E = 0$ case. There are two parameters to

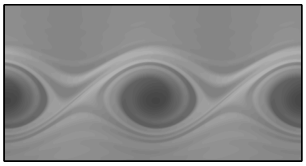

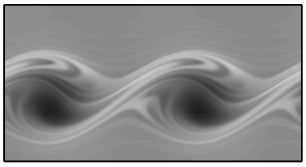

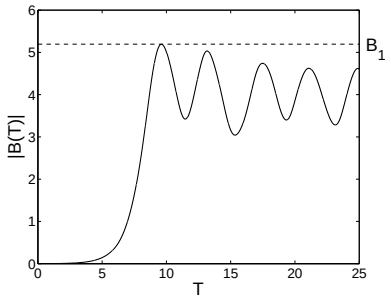

(a) Amplitude $|B|$.

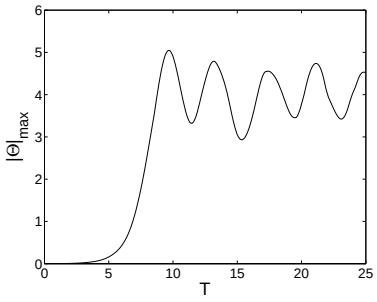

(b) Maximum value of $|\Theta|$.

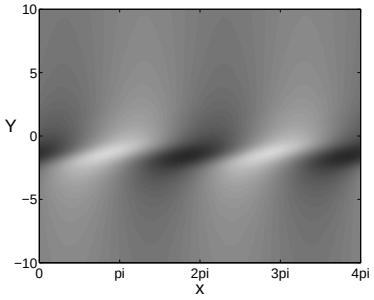

(c) Θ at $T = 5$.

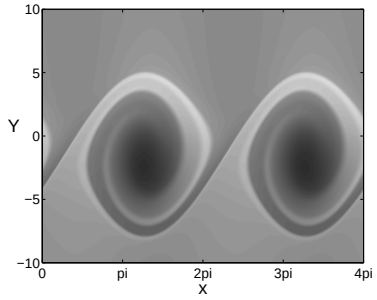

(d) Θ at $T = 10$.

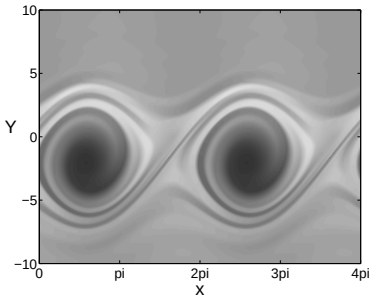

(e) Θ at $T = 15$.

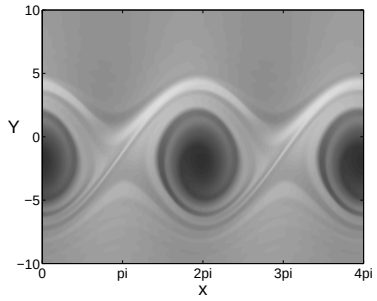

(f) Θ at $T = 20$.

Figure 7.14: Newtonian cat's eyes. The amplitude grows and saturates around $|B| = 4$ where nonlinear terms become important.

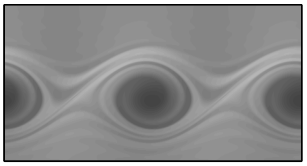

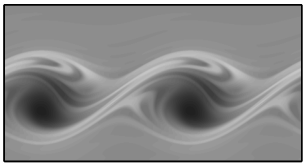

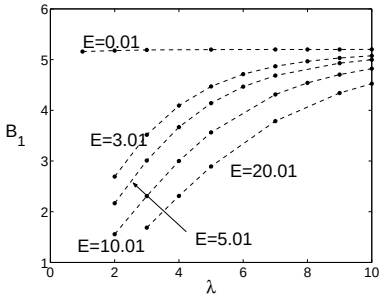

(a) B_1 for different values of E as a function of λ.

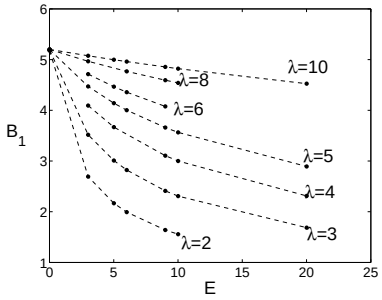

(b) B_1 for different values of λ as a function of E.

Figure 7.15: Value of B_1, the first maximum of $|B|$, for the UCM fluid.

study, E and λ.

At early times, the amplitude has the growth predicted by linear theory. The nonlinear terms affect the growth rate sooner if E is large or λ small. Figure 7.15 shows the value of B_1 as λ and E change. As either $E \to 0$, or $\lambda \to \infty$, the value asymptotes to the Newtonian limit, 5.194. As E increases or λ decreases, B_1 decreases.

Once the nonlinear terms become important, the amplitude begins to oscillate, with higher frequency than the Newtonian fluid, as seen in figure 7.16. The amplitude may diverge if λ is small. Divergence of the amplitude implies that the mode leaves the $\mathcal{O}(\epsilon^2)$ scaling assumed in the derivation of the amplitude equations. Whether the amplitude diverges depends strongly on whether the elastic stress relaxes quickly and only weakly on the strength of the elasticity, as seen in figure 7.17. In general we find that the solutions diverge if the stress is unable to relax quickly.

For large enough relaxation rates, the amplitude apparently saturates, but the dynamics are more complicated than for a Newtonian fluid. The cat's eyes form, but they are are much less symmetric, as seen in figure 7.18

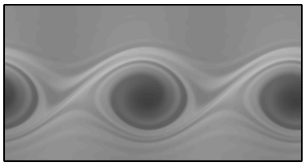

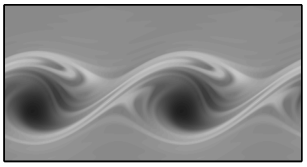

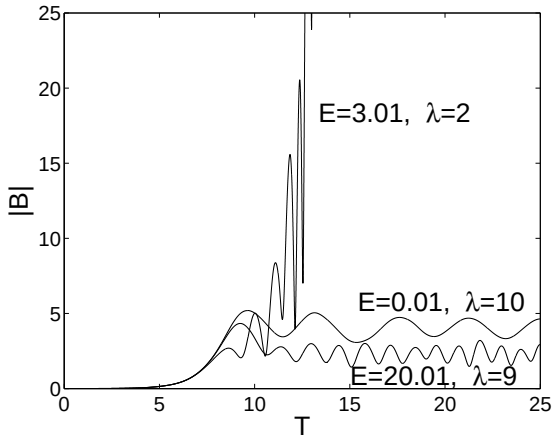

Figure 7.16: Plot of $|B|$. If E is small or λ large the behavior is roughly Newtonian. If λ is too small the amplitude diverges.

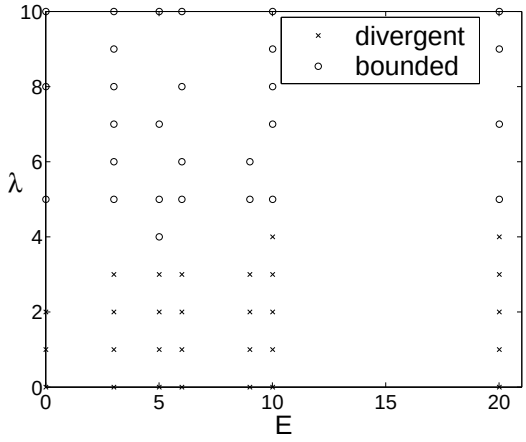

Figure 7.17: Long-term behavior of UCM solutions. If $|B|$ exceeds 500 before $T = 25$ the solution is considered *divergent*. Otherwise it is considered bounded. For small enough λ the solutions appear to diverge for any positive E. The left-most points are for $E = 0.01$.

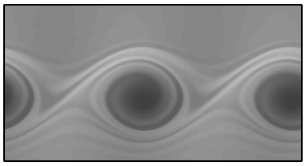

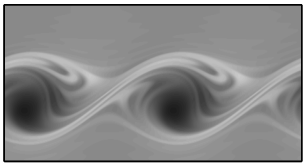

for $E = 20.01$ and $\lambda = 9$. They move from right to left faster than the Newtonian cat's eyes. As they roll, the material from the top of one eye stays in place while the next eye rolls under, and so material at the top stays approximately in place while the eyes move past. Over time, considerable material builds up above the cat's eyes and they migrate down. The center of the eyes remains largely isolated from the remainder of the flow.

The fact that some material stays in place while the eyes roll past has the additional effect of creating considerable stretching of the material. This results in large elastic stresses, particularly close to stagnation points, the '$\times$' points of the cat's eyes. Difficulties appear at these points where the extension is large and the UCM model breaks down. Although this does not affect much of the fluid, close to the stagnation points the stresses and vorticity grow unreasonably. We see this in figure 7.19(b) which shows the maximum value of $|\Theta|$ as a function of T for $E = 5.01$ and $\lambda = 5$. Although the magnitude becomes large, the effect is localized and it does not significantly affect the global integral of Θ: the amplitude B is largely unaffected.

It is clear in figure 7.19(b) that the numerics are not able to accurately determine the largest value of $|\Theta|$. To improve this we need better resolution of the stagnation points. For flows which relax quickly enough, the gradients of the stress remain small and we do not have numerical difficulties. Qualitatively the evolution of the cat's eyes remains similar.

7.6.6 The FENE–CR fluid

To resolve the difficulties caused by extensional flow, we turn to the FENE–CR equations (7.49)–(7.56). These equations require the calculation of a number of additional derivatives. This slows the code considerably, and so we have used a lower resolution for the calculations, 800×800.

The FENE–CR parameter l keeps the polymer strain from exceeding a

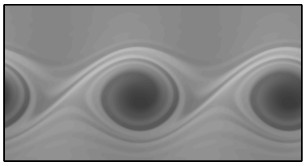

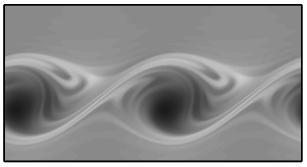

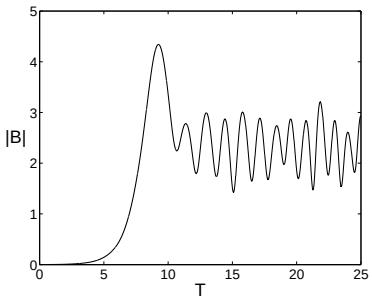

(a) Amplitude $|B|$.

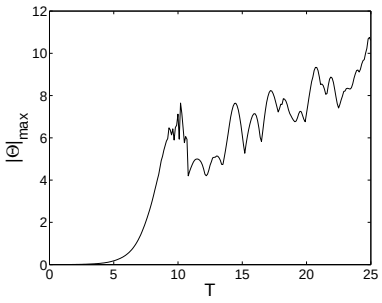

(b) Maximum value of $|\Theta|$.

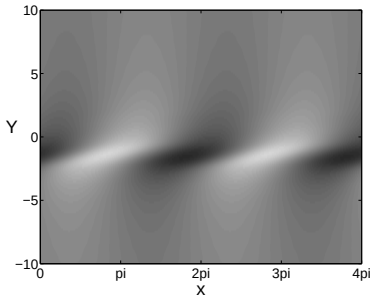

(c) Θ at $T = 5$.

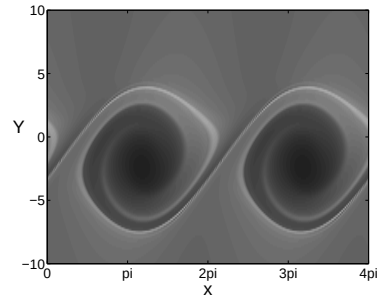

(d) Θ at $T = 10$.

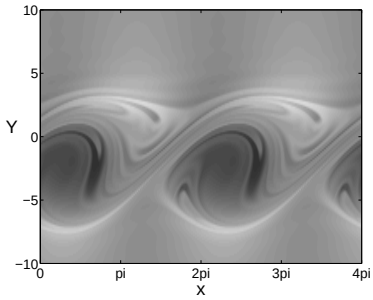

(e) Θ at $T = 15$.

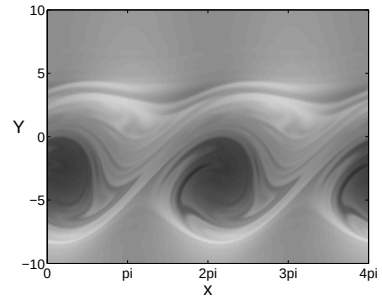

(f) Θ at $T = 20$.

Figure 7.18: Cat's eyes in a UCM fluid with $E = 20.01,\ \lambda = 9$.

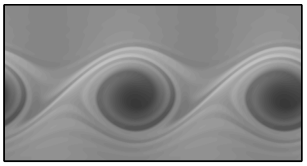

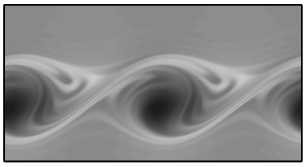

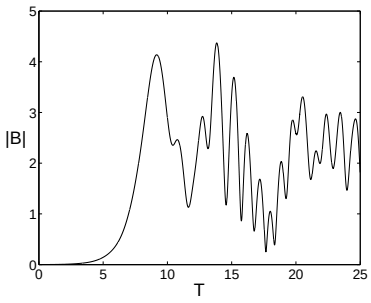

(a) Amplitude $|B|$.

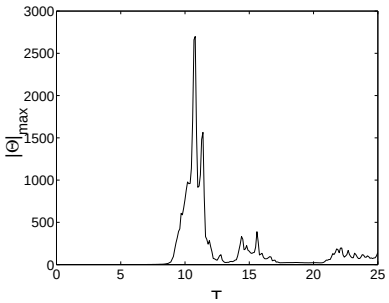

(b) Maximum value of $|\Theta|$.

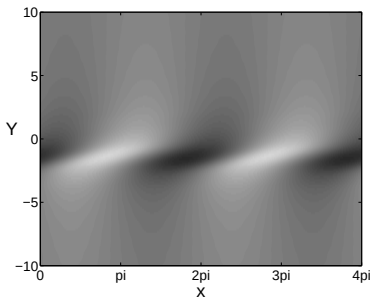

(c) Θ at $T = 5$.

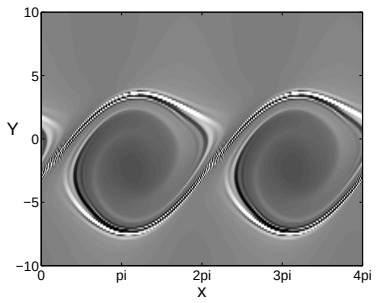

(d) Θ at $T = 10$.

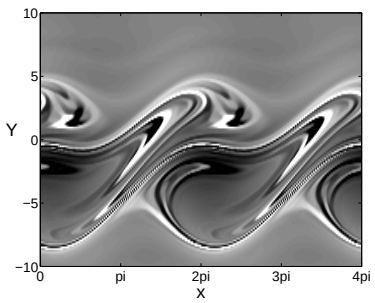

(e) Θ at $T = 15$.

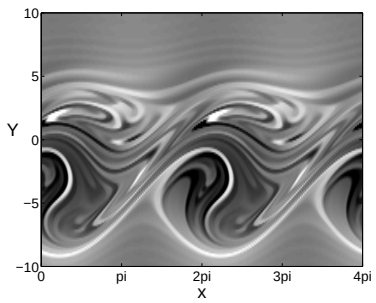

(f) Θ at $T = 20$.

Figure 7.19: Cat's eyes in a UCM fluid with $E = 5.01,\ \lambda = 5$.

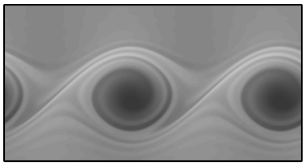

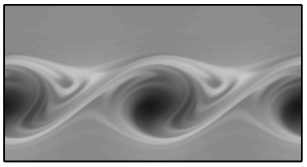

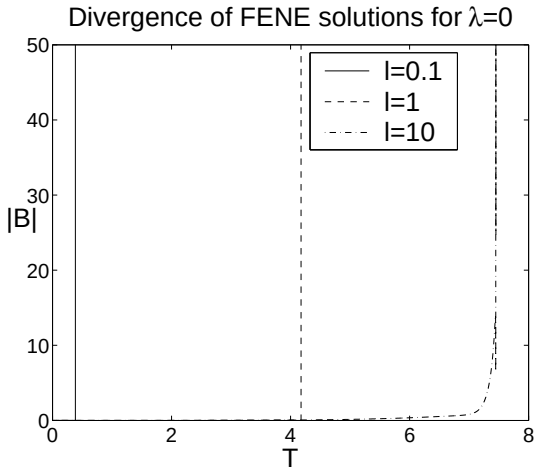

Figure 7.20: Divergence of amplitudes for $\lambda = 0$, $E = 5.01$, and different values of l.

finite limit by increasing the rate of relaxation as the maximum strain l is approached. In the limit $\lambda = 0$, there is no relaxation to increase, and so the stresses a_{ij} are not prevented from reaching (and exceeding) this maximum. Simultaneously the elastic effect in the momentum equation diverges, and so the model fails if the maximum is reached or crossed. This happens sooner for smaller values of l, as seen in figure 7.20. This can also happen for small λ if the time step is too large in the numerics and the stretching reaches or crosses its maximum, which will be addressed later.

At large values of l we still see the poor extensional behavior found in the UCM fluid. As l decreases, the extensional behavior improves. When l becomes small, the behavior becomes Newtonian.

$l = 0.1$

A small value of l models the case where the polymers do not stretch much.

In our calculations we have not taken any measures to avoid overstepping

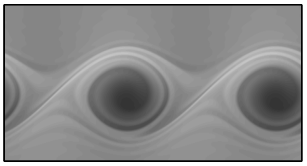

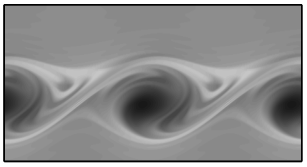

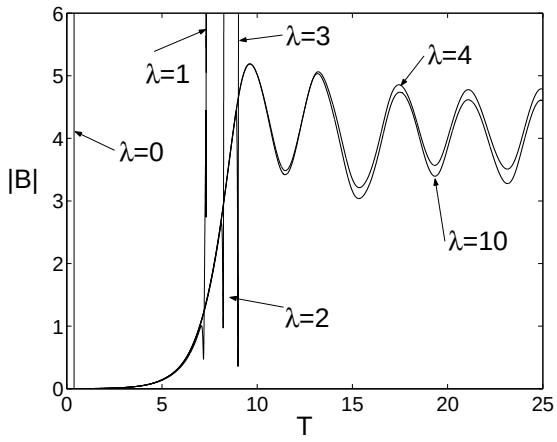

Figure 7.21: Amplitudes for $l = 0.1$, $E = 10.01$, and different values of λ. The behavior depends only weakly on E and is effectively Newtonian [compare to figure 7.14(a)]. For small values of λ, the amplitude diverges if the elastic strain grows too large

the maximum strain. In figure 7.21 we see that for $l = 0.1$ all curves have similar behavior until the elastic strain exceeds the maximum. The amplitude diverges almost immediately afterwards. If λ is large enough, the strain does not exceed this maximum, and the cat's eyes develop much as in a Newtonian fluid [see figure 7.14(a)].

Figure 7.22 shows how the cat's eyes evolve for $l = 0.1$, $E = 5.01$, and $\lambda = 5$. There is little difference between these results and those of the Newtonian fluid in figure 7.14.

$l = 1$

At a moderate value of l, the numerical difficulties causing divergence for $l = 0.1$ no longer appear except when λ is very small. In our calculations, we only observe them for $\lambda = 0$.

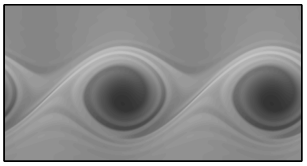

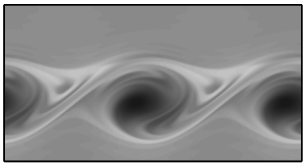

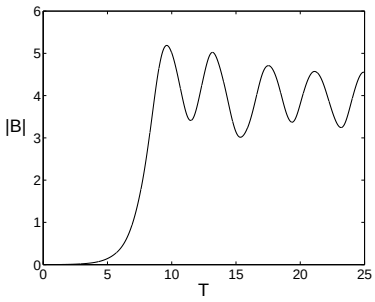

(a) Amplitude $|B|$.

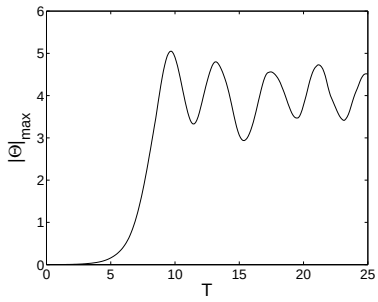

(b) Maximum value of $|\Theta|$.

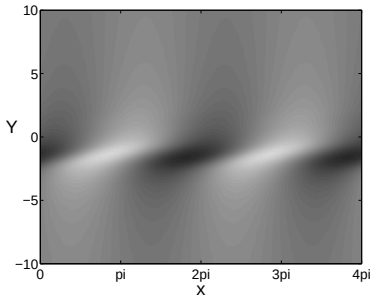

(c) Θ at $T = 5$.

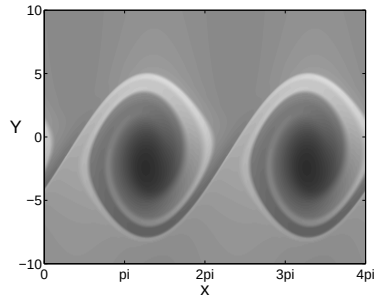

(d) Θ at $T = 10$.

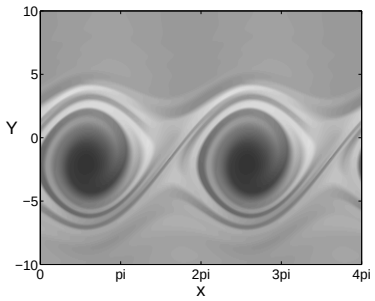

(e) Θ at $T = 15$.

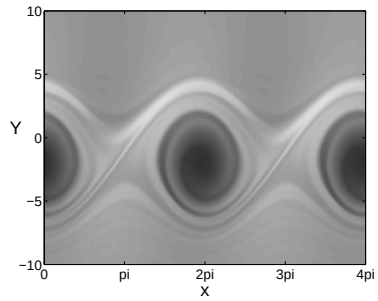

(f) Θ at $T = 20$.

Figure 7.22: Cat's eyes in a FENE–CR fluid with $l = 0.1$, $E = 5.01$, and $\lambda = 5$. Compare with figures 7.14 and 7.18.

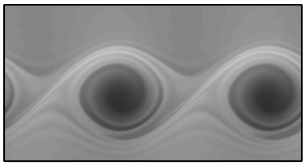

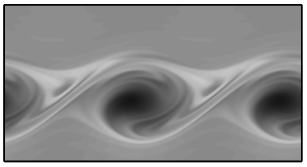

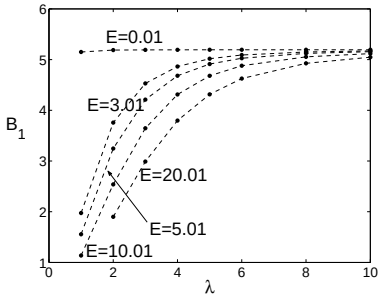

(a) curves for different values of E as a function of λ.

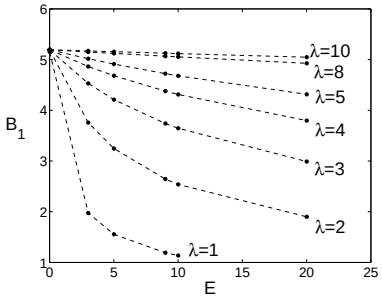

(b) curves for different values of λ as a function of E.

Figure 7.23: The value of B_1 is qualitatively similar to that of UCM fluids seen in figure 7.15.

The value of B_1 follows similar behavior to that of the UCM fluid, as shown in figure 7.23 for $l = 1$, $E = 5.01$, and $\lambda = 5$.

Our results are clearly distinct from the Newtonian fluid and do not have the same difficulties found in the UCM fluid. Figure 7.24(b) shows that the maximum of $|\Theta|$ remains small. However, the development of the cat's eyes in figures 7.24(c)–(d) remains similar to the UCM fluid: in particular they retain the feature that the top of the eyes remains in place while the bottom rolls past. These parameters are also shown in bottom picture of the flipbook in the bottom right of each page. Again the time is equal to 0.1 times the page number.

$l = 10$

When l becomes large, the behavior is very much like the UCM equations. Although the maximum value of $|\Theta|$ is smaller than for the UCM fluid, it still grows to an unreasonably large value. Figure 7.25 shows that cat's eyes develop similarly to the UCM cat's eyes in figure 7.19.

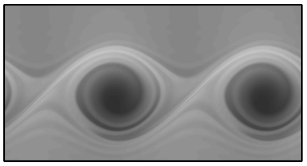

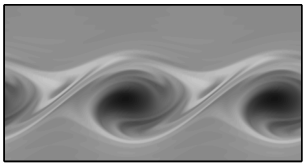

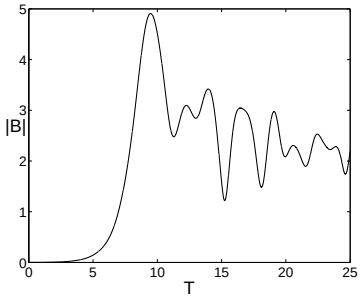

(a) Amplitude $|B|$.

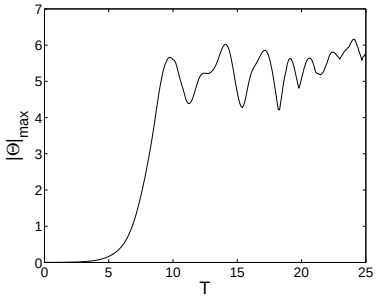

(b) Maximum value of $|\Theta|$.

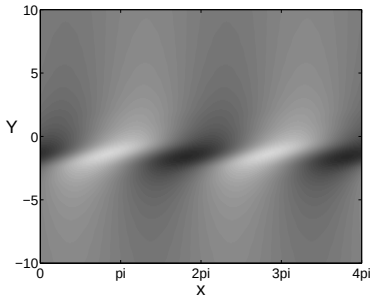

(c) Θ at $T = 5$.

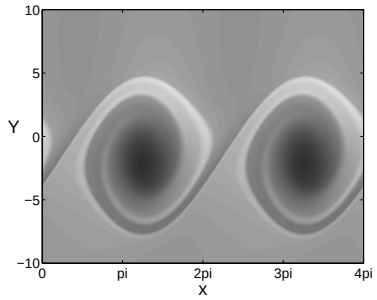

(d) Θ at $T = 10$.

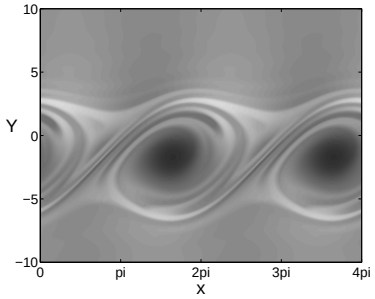

(e) Θ at $T = 15$.

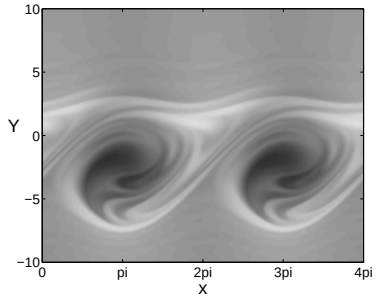

(f) Θ at $T = 20$.

Figure 7.24: Cat's eyes for $l = 1$, $E = 5.01$, and $\lambda = 5$. The cat's eyes have similar qualitative behavior to the UCM cat's eyes, but do not have the unphysical growth of Θ.

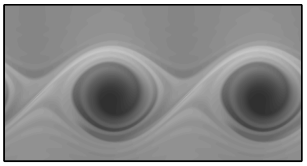

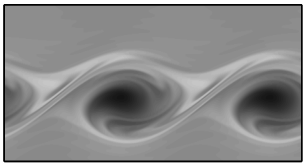

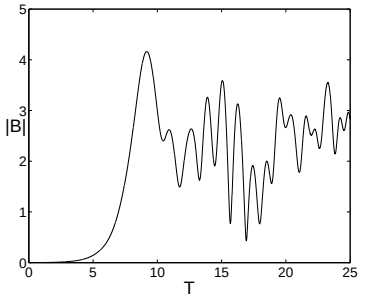

(a) Amplitude $|B|$.

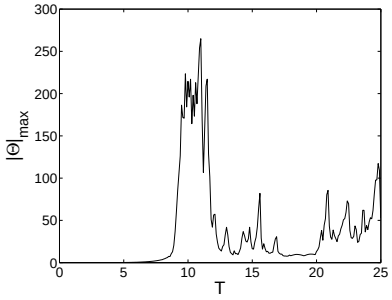

(b) Maximum value of $|\Theta|$.

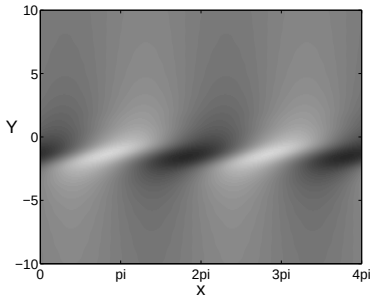

(c) Θ at $T = 5$.

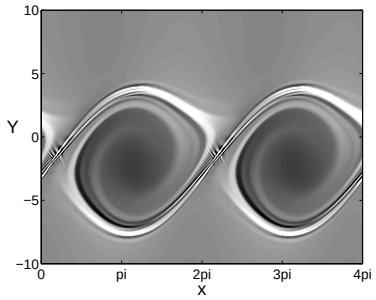

(d) Θ at $T = 10$.

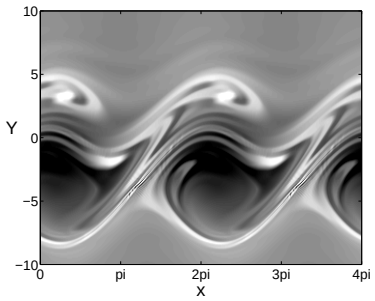

(e) Θ at $T = 15$.

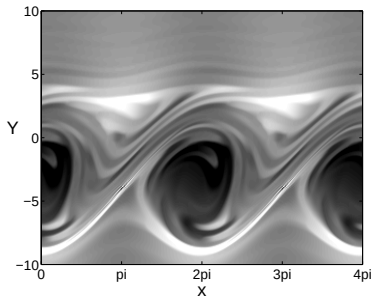

(f) Θ at $T = 20$.

Figure 7.25: Cat's eyes for $l = 10$, $E = 5.01$, and $\lambda = 5$. The development has the same failures as the UCM cat's eyes.

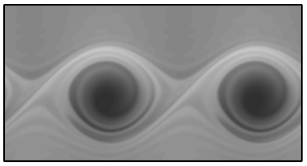

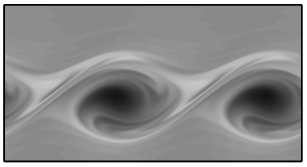

7.7 Discussion and future work

In this chapter we have studied the effect of elasticity on the inertial instability of a planar jet. We considered two test flows, both of which are symmetric and contain an inflection point, but do not have the jump in normal stress known to introduce a new elastic instability.

Our linear results show that as the elasticity grows, the growth rate of the inertial instability decreases. At large enough elasticity the sinuous mode stabilizes for all k in both of our test flows. When E is small, the neutrally stable mode has two pairs of logarithmic singularities, one pair on either side of the center-line, and so the critical layer splits into two layers. We do not attempt further analysis of the multiple critical layers.

If $E = \mathcal{O}(\epsilon^4)$ just one critical layer exists. The elasticity affects the critical layer when the mode amplitude is $\mathcal{O}(\epsilon^2)$. The nonlinear terms also appear at this time. If the relaxation is too small, the mode amplitude grows and leaves this regime. If the relaxation is large enough, the mode amplitude remains $\mathcal{O}(\epsilon^2)$. There is strong extensional flow, and this causes the UCM model to fail, so we turn to the FENE–CR equations.

The structure of the critical layer changes from the Newtonian flow. Cat's eyes develop as before, but the elasticity inhibits the roll-up, and so less material is brought into the center of the cat's eye. Over time the cat's eyes migrate across the vorticity gradient, leaving a mixed region behind them.

This analysis has a flaw in that the base stress is assumed to be in equilibrium. It takes time for the flow to establish a base stress, during which time instabilities may set in. Our base state may not accurately represent the true base flow.

This study leaves many unanswered questions. It forms the basis of a continuing fully-nonlinear simulation of elastic planar jets in collaboration with Dr. Neil Balmforth and Dr. Yuan-Nan Young which will address some

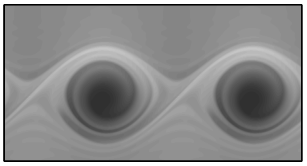

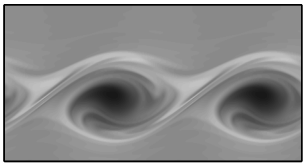

of them.

In particular we would like to address the issue raised above that the elastic stress in the base state cannot generally be considered to be in equilibrium. We also intend to investigate the existence of turbulent drag reduction in this model and the behavior of the new critical layer when the elasticity is increased.

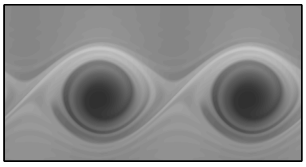

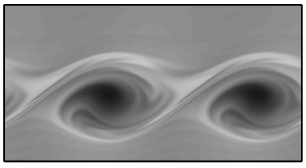

Appendix A

Numerical methods for the coextrusion flow

In this appendix we describe more details of our numerical methods as well as the tests we used to validate the code used for the coextrusion flows of part I.

A.1 Methods

We use a shooting method based on Runge–Kutta integration and a spectral method based on Chebyshev polynomials to solve the coextrusion eigenvalue problems. We did not develop both methods for all flows; the method used for each flow is summarized in figure A.1.

We outline the shooting and spectral methods for the case of Couette flow. We are solving the fourth-order system of equations (2.18)–(2.27). At each wall [$y = -\Delta k$ and $y = (1 - \Delta)k$] we have two no-slip conditions and two free conditions. At the interface ($y = 0$) there are four conditions plus an additional equation for the interfacial perturbation δ.

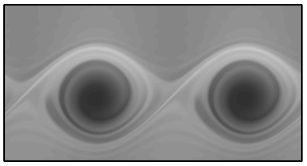

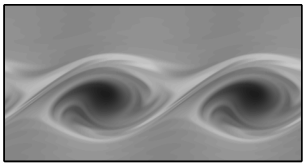

Flow	shooting	spectral
Couette	x	x
Channel Poiseuille	x	x
Pipe $m = 0$ streamfunction	x	
Pipe $m = 0$ primitive variables		x
Pipe $m = 1$		x

Figure A.1: Summary of the numerical methods developed for each flow.

A.1.1 Shooting

We eliminate a_{ij} from equations (2.18)–(2.27) and then the streamfunction ψ satisfies a fourth order differential equation (3.1). At each wall both ψ and ψ' must vanish to satisfy the no-slip conditions, but ψ'' and ψ''' are free. We take an initial guess for ω and choose $\psi_1''(-\Delta k) = 1 + i$, $\psi_1'''(-\Delta k) = 1 + i$ and $\psi_2''(-\Delta k) = 1 + i$, $\psi_2'''(-\Delta k) = -1 - i$ to serve as initial conditions for two independent solutions[1]. We integrate ψ_1 and ψ_2 from $y = -\Delta k$ to $y = 0$, apply the interfacial conditions and then integrate from $y = 0$ to $y = (1 - \Delta)k$. This gives two solutions of the ODE satisfying the no-slip boundary conditions at the wall $y = -\Delta k$: $\psi_1(y)$ and $\psi_2(y)$. Any linear combination $C_1\psi_1(y)+C_2\psi_2(y)$ is also a solution satisfying no-slip conditions at $y = -\Delta k$. In order to satisfy the boundary conditions at $(1-\Delta)k$ we seek $\mathsf{M}\boldsymbol{c} = \boldsymbol{0}$ where

$$\mathsf{M} = \begin{pmatrix} \psi_1([1-\Delta]k) & \psi_2([1-\Delta]k) \\ \psi_1'([1-\Delta]k) & \psi_2'([1-\Delta]k) \end{pmatrix},$$

and $\boldsymbol{c} = (C_1, C_2)$. The value of the determinant $\det(\mathsf{M})$ depends on ω only. We require $\det(\mathsf{M}) = 0$ for ω to be an eigenvalue of the linearized equations.

[1]We choose our two initial conditions so that they are orthogonal and so that the real and imaginary parts are nonzero. We take them both non-zero since the integration routine has an adaptive step size which becomes small if a variable is zero.

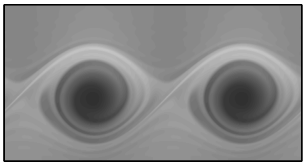

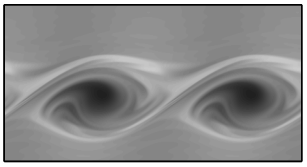

We perform the integrations using an adaptive Runge–Kutta algorithm and use a Newton–Raphson method to find the values of ω giving zeros of $\det(\mathsf{M})$. Both algorithms are from Numerical Recipes [77]. The Newton–Raphson method occasionally returns values for ω which do not yield zeros of the determinant. Consequently, we always run an additional integration at higher accuracy with the calculated value of ω to ensure that the result is correct.

Most previous studies [39, 103, 104] have used an orthogonalization step during the integration as initially suggested by Conte [21]. We have not found this to be necessary, presumably because our calculations use a higher accuracy requirement.

A.1.2 Spectral

For the spectral method, we largely follow the method presented in Dongarra *et al.* [23] (see also the book by Boyd [13]). We map the interval of the lower fluid $y \in [-\Delta k, 0]$ to $z \in [-1, 1]$ by $z = 1 + (2y/\Delta k)$. The equations can be translated into the z variable using $\partial_y = (2/\Delta k)\partial_z$. A similar transformation is used in the upper fluid. Unlike shooting, we do not eliminate the a_{ij} from the equations. This makes the coding easier, but increases the time and memory requirements. We take

$$\psi(z) = \sum_{i=0}^{N+3} p_i T_i(z)\,,$$

$$a_{11}(z) = \sum_{i=0}^{N} q_i T_i(z)\,,$$

$$a_{12}(z) = \sum_{i=0}^{N+1} r_i T_i(z)\,,$$

$$a_{22}(z) = \sum_{i=0}^{N+1} s_i T_i(z)\,,$$

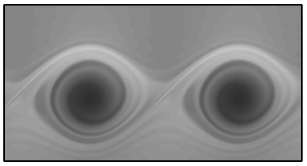

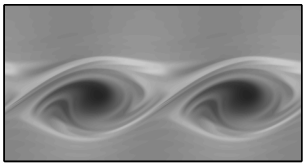

where p_i, q_i, r_i and s_i are constants and T_i is the i-th Chebyshev polynomial. Note that the sums do not have the same upper limit. This is discussed in section A.2.7. Each variable is thus defined by a vector of coefficients. We repeat this in the upper fluid and add the scalar δ to the system. This gives $8N + 19$ unknowns. We combine these into a single vector $\boldsymbol{x}$.

The streamfunction is represented by a vector of length $N+4$. Its derivative is then a vector of length $N + 3$. This vector can be found by multiplication by a suitable truncation of the infinite matrix D

$$\mathsf{D} = \begin{pmatrix} 0 & 1 & 0 & 3 & 0 & 5 & 0 & 7 & \cdots \\ 0 & 0 & 4 & 0 & 8 & 0 & 12 & 0 & \cdots \\ 0 & 0 & 0 & 6 & 0 & 10 & 0 & 14 & \cdots \\ 0 & 0 & 0 & 0 & 8 & 0 & 12 & 0 & \cdots \\ 0 & 0 & 0 & 0 & 0 & 10 & 0 & 14 & \cdots \\ \vdots & \vdots & \vdots & \vdots & \vdots & \vdots & \vdots & \vdots & \ddots \end{pmatrix}.$$

We can also represent multiplication by z as a multiplication by the matrix Z

$$\mathsf{Z} = \frac{1}{2}\begin{pmatrix} 0 & 1 & 0 & 0 & 0 & 0 & \cdots \\ 2 & 0 & 1 & 0 & 0 & 0 & \cdots \\ 0 & 1 & 0 & 1 & 0 & 0 & \cdots \\ 0 & 0 & 1 & 0 & 1 & 0 & \cdots \\ 0 & 0 & 0 & 1 & 0 & 1 & \cdots \\ 0 & 0 & 0 & 0 & 1 & 0 & \cdots \\ \vdots & \vdots & \vdots & \vdots & \vdots & \vdots & \ddots \end{pmatrix}.$$

After performing these substitutions, we match coefficients for each Chebyshev polynomial T_i in each equation, up to the maximum index for which all terms are included (for example in an equation including both ψ and ψ', we would not match coefficients of T_{N+3} because ψ' is accurate only to T_{N+2}). From equation (2.18) we get N equations, from (2.19) we get $N+1$ equations,

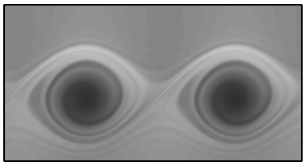

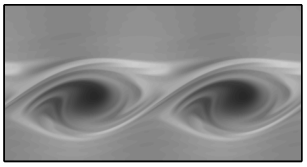

and from (2.20) and (2.21) we get $N+2$ equations each. Combined with the conditions in the upper fluid, this gives a total of $8N + 10$ equations.

To apply the conditions at the interface and at the walls we note that $T_n(\pm 1) = (\pm 1)^n$, so the values at the boundaries of each domain can be easily found from the coefficients of the vector, expressed as a dot product with $(1, -1, 1, -1, \ldots)$ at the lower boundary and $(1, 1, 1, 1, \ldots)$ at the upper boundary. This gives 8 more equations. We apply the one remaining condition on the value of δ to give a total of $8N + 19$ equations.

The full system can then be expressed in the form

$$\mathsf{C}_1 \boldsymbol{x} = i\omega \mathsf{C}_2 \boldsymbol{x}\,,$$

where C_1 and C_2 are $(8N{+}19){\times}(8N{+}19)$ matrices. By appropriately ordering the equations, we can make C_2 positive symmetric. This can be solved using the `eig` command of *Matlab* which uses the LAPACK implementation of the QZ algorithm. It finds all eigenvalues of the system. Alternatively, we use the `eigs` command which is faster, but finds only a single eigenvalue at a time and needs an initial guess. In practice we find the eigenvalues with `eig` and follow them through parameter continuation with `eigs` or the shooting algorithm.

It is known that this spectral algorithm occasionally returns spurious eigenvalues. These can be identified by the fact that they do not converge well as the number of polynomials is increased [23]. To avoid these we perform our calculations with different values of N and, whenever possible, compare with the shooting algorithm and analytic results.

A.2 Tests

To validate the algorithms, we compare with the $k \to 0$ limit [16, 38, 103] and the $k \to \infty,\ \beta \to 0$ limit of Renardy [84] and chapter 3 as well as

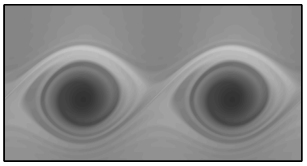

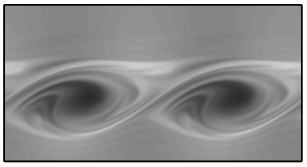

with published calculations at finite k. In all cases for which we have both a shooting and a spectral algorithm the algorithms are consistent with each other.

A.2.1 Poiseuille flow, finite $\mathcal{W}$

For Poiseuille flow with finite $\mathcal{W}$, we use equations (2.55)–(2.66). We can compare our results with those of Wilson and Rallison [103, 104, 105]. We get agreement in all cases, one of which is shown in figure A.2. We find agreement with the $k \to 0$ asymptotics [103, 27] and the $k \to \infty,\ \beta \to 0$ asymptotics of [84].

A.2.2 Poiseuille flow, infinite $\mathcal{W}$

For infinite $\mathcal{W}$ we use the leading order terms of equations (2.55)–(2.66). To test the corresponding code, we check that it matches the results of the finite $\mathcal{W}$ code as $\mathcal{W}$ increases. We also compare with the $k \to 0$ and $k \to \infty$, $\beta \to 0$ limits.

A.2.3 Couette flow, finite $\mathcal{W}$

For Couette flow, we do not have many published results to compare with. However, the spectral code requires only a few changes from the Poiseuille code. The shooting code was entirely rewritten. The two methods give consistent answers and agree with the asymptotic $k \to 0$ and $k \to \infty,\ \beta \to 0$ limits [84, 103, 104].

A.2.4 Couette flow, infinite $\mathcal{W}$

To test this code, we compare with our finite $\mathcal{W}$ code at large values of $\mathcal{W}$, and our asymptotic results in chapter 3.

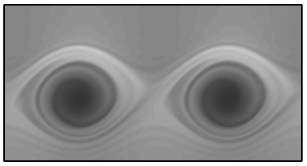

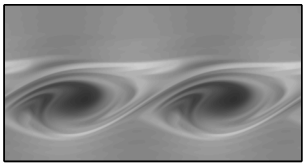

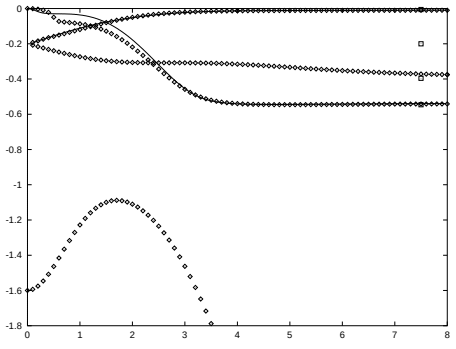

(a) Figure 3.13 of [103]. The squares represent the $k \to \infty$ asymptotic limit. There is an additional $k \to \infty$ mode with decay rate -5.9.

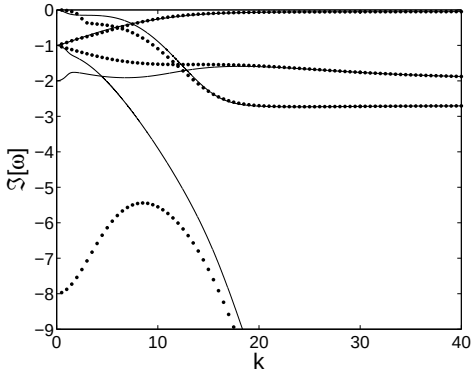

(b) Our calculations for $W\!i = 5$, $\Delta = 0.5$, and $\xi = 10^{-6}$. We show two additional sinuous modes.

Figure A.2: A comparison of our numerical calculations with those of Wilson. The outer fluid is Newtonian and the inner fluid is UCM ($\xi = 0$), with $W\!i = 5$ and $\Delta = 0.5$. Lines represent sinuous modes and points varicose modes. Our calculations use a different nondimensionalization (hence different axis scalings) and cannot solve for $\xi = 0$, so we use $\xi \ll 1$. Our asymptotic $k \to \infty$ calculations (see section 3.4.2) find a mode whose decay rate scales like $-1/\xi$ instead of the mode predicted (but not found) by Wilson with decay rate -0.2.

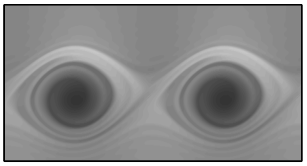

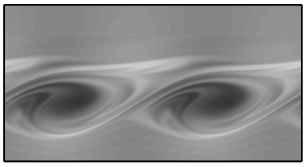

A.2.5 Pipe flow, $m = 0$, finite and infinite Wi

In pipe flow with $m = 0$ we consider only the UCM fluid, setting $\beta = 0$. Our shooting method uses the streamfunction formulation of the equations, but the spectral method does not.

Shooting

To test our shooting method, we compare with the results of Meulenbroek *et al.* [69] for a single UCM fluid. Meulenbroek *et al.* use a different shooting algorithm from ours. They do not take advantage of the linearity to reduce the problem to a determinant. Instead they set $\psi''(1) = 1$ and thus have three free parameters at the wall: $\psi'''(1)$ and the real and imaginary part of ω, which they set arbitrarily. They assume that ψ has a Taylor series expansion about $r = 0$ and integrate inwards from $r = 1$ to $r = r_c \ll 1$, attempting to match the value of ψ and its first three derivatives at $r = r_c$. This system is overdetermined, and so has solutions only when ω is an eigenvalue.

The boundary condition applied at $r = 0$ is incorrect. It may be shown by considering $v_z = \psi'/r$ that as $r \to 0$ both ψ and ψ' must vanish. So they assume that $\psi = a_2 r^2 + a_3 r^3$. Taking this condition, we are able to reproduce their results. However, by modifying the location of r_c, we find that $a_3 = \mathcal{O}(r_c)$, and so ψ does not have the assumed form. The boundary conditions $\psi(0) = 0$ and $\psi'(0) = 0$ have also been applied by Dongarra *et al.* [23] for stability of Newtonian fluid in a pipe. These conditions are not enough to specify the solution because there is a singular solution which has $\psi' \sim r \ln r$ as $r \to 0$. The correct condition is ψ'/r remains finite as $r \to 0$ [25]. We can alternately use $\psi'''(0) = 0$, that is, we attempt to match our solution to $\psi = a_2 r^2 + a_4 r^4$ and its first three derivatives at $r = r_c$. When we correct the condition, the results change slightly, but not significantly. We can reproduce the $k \to 0$ results of [16, 38] and the $k \to \infty$ results of Wilson

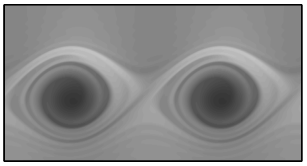

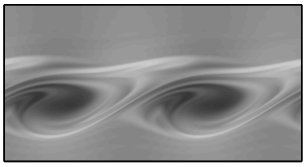

and Rallison [104].

To test the infinite Wi code, we compare with the finite Wi code at large Wi.

Spectral

Our spectral method does not use the streamfunction formulation. We solve the full equations, including the v_θ, $a_{r\theta}$, and $a_{\theta z}$ terms. We find the same results as in the shooting method, but there is an additional (stable) mode (seen for $Wi \to \infty$ in figure A.3). The mode corresponds to flow in the v_θ direction only, and so does not appear in the streamfunction form of the equations.

A.2.6 Pipe flow $m = 1$, infinite Wi

For $m = 1$ flows we again consider only UCM fluids. We have not developed a shooting algorithm for this case. Our spectral code is the same code as in the $m = 0$ case, except for changes to the boundary condition and the value of m.

We are unaware of any published calculations which solve the $m = 1$ flow of UCM fluids through a pipe. Consequently we show more details of our tests for these modes.

We compare with our asymptotic results of chapter 3 for large k based on the assumption that the flow is effectively Couette on the relevant length scales. The comparison is shown in figure A.3. We find all of the predicted eigenvalues. There is an additional mode not seen in Couette flow. This mode corresponds to the mode found for axisymmetric pipe flow whose velocity was entirely in the azimuthal direction.

Our calculations for $m = 1$ and k small are shown in figure A.4(a). They agree with the predictions of Hinch *et al.* [38]. The error between the calcu-

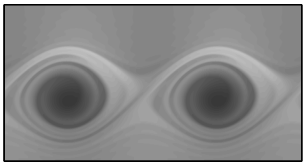

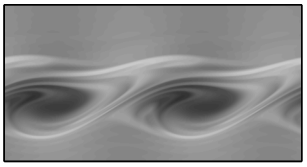

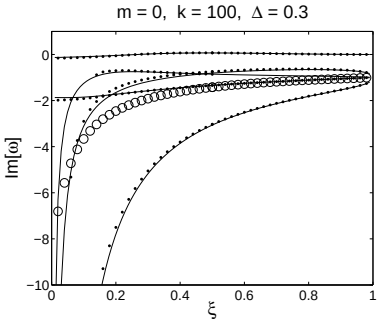

(a) Imaginary part of ω for $m = 0$ mode.

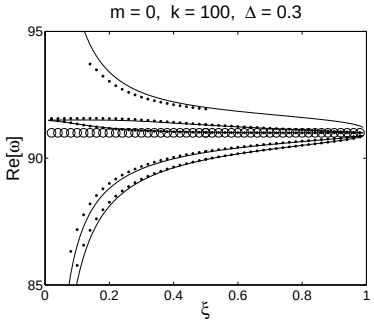

(b) Real part of ω for $m = 0$ mode.

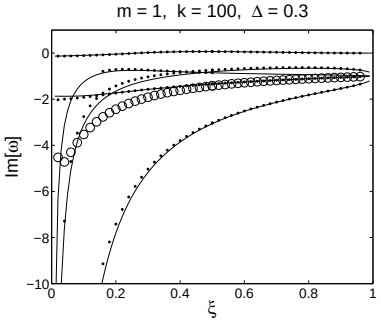

(c) Imaginary part of ω for $m = 1$ mode.

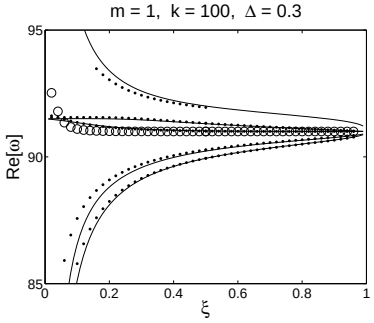

(d) Real part of ω for $m = 1$ mode.

Figure A.3: (Reproduction of figure 5.2). Dots represent the calculation at $k = 100$ and $\Delta = 0.3$. Solid lines represent the asymptotic $k \to \infty$ prediction from UCM Couette channel flow. There is an additional mode depicted by circles.

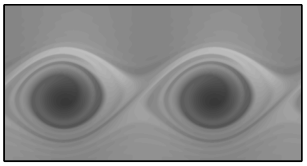

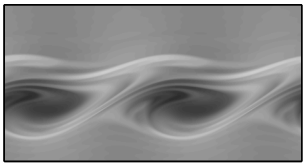

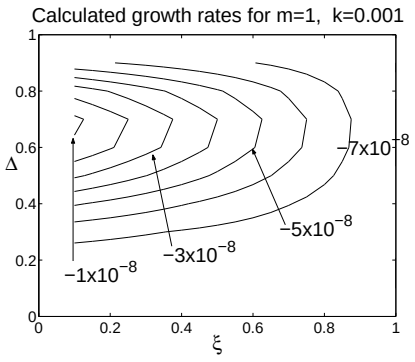

(a) Calculated growth rates.

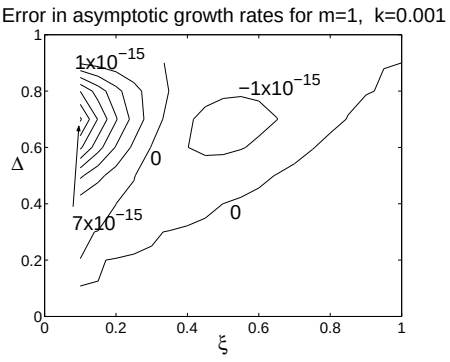

(b) Error in asymptotic approximation [38].

Figure A.4: For $\xi < 1$ the long-wave $m = 1$ growth rates are negative. The error in the prediction of [38] for $k = 0.001$ is of order 10^{-15}, while the growth rates are $\mathcal{O}(10^{-8})$. When $\xi > 1$ (not pictured) the growth rate is positive and the error also small.

lated results and the asymptotic prediction is shown in figure A.4(b).

We perform a final test that the results are identical when $m = -1$.

A.2.7 Complications with the QZ algorithm

In section A.2.5 we mention the need to use different accuracy for different physical variables. This is not a universal practice (*e.g.*, [29] keep all variables to N places), but is done by some authors (*e.g.*, [84]).

We are forced to use different accuracies due to difficulties encountered with the LAPACK implementation of the QZ algorithm as used by *Matlab*'s `eig` command. We illustrate the problems here. For definiteness we consider the varicose eigenvalue problem for UCM fluids with $\xi = 0.5$, $\Delta = 0.3$, and $k = 10$ in three-layer symmetric channel flow. We set $N = 100$ and expand all variables to N Chebyshev polynomials. For each value of the Weissenberg

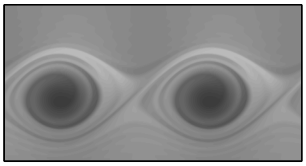

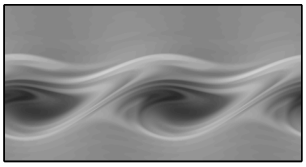

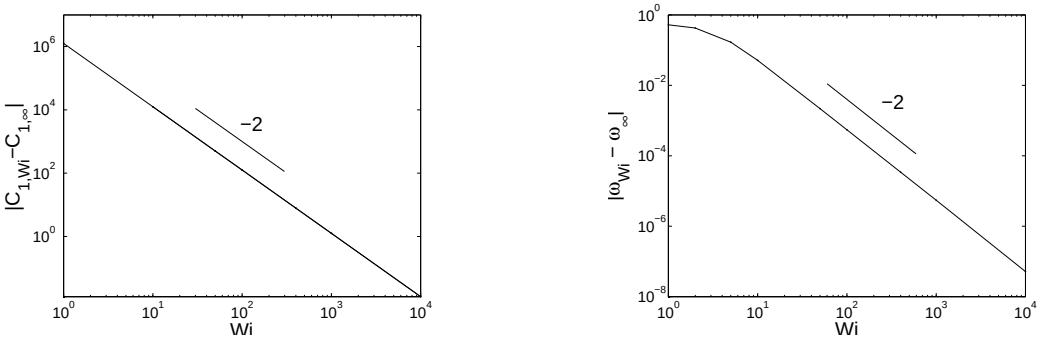

(a) Frobenius norm of difference $\mathsf{C}_{1,\infty} - \mathsf{C}_{1,Wi}$.

(b) Convergence of eigenvalues.

Figure A.5: The matrices $\mathsf{C}_{1,Wi}$ and the eigenvalues ω_{Wi} converge.

number, we calculate the matrices $\mathsf{C}_{1,Wi}$ and $\mathsf{C}_{2,Wi}$ for the eigenvalue problem

$$\mathsf{C}_{1,Wi}\boldsymbol{x} = -i\omega\mathsf{C}_{2,Wi}\boldsymbol{x}\,.$$

The matrix C_2 is independent of Wi, but the matrix C_1 changes. For finite values of Wi we get accurate results. However, in the infinite Wi case the results are wrong.

The eigenvalues ω calculated at finite Wi converge to ω_∞ as $Wi \to \infty$, and the matrices $\mathsf{C}_{1,Wi}$ converge to $\mathsf{C}_{1,\infty}$ as shown in figure A.5. The eigenvectors must have (at least) one limit point $\boldsymbol{x}_\infty$ because they come from a compact set (vectors of norm 1 in a finite dimensional Euclidian space). As the product of limits is the limit of the products, $\mathsf{C}_{1,\infty}\boldsymbol{x}_\infty = \omega_\infty\mathsf{C}_2\boldsymbol{x}_\infty$ and so the limit of ω_{Wi} is an eigenvalue of the problem at infinite Wi. However, the QZ algorithm does not find the same eigenvalues, seen in figure A.6. In the $Wi = \infty$ limit, the algorithm returns false results, without any warning.

Using the correct number of polynomials for each variable eliminates these difficulties. The algorithm again gives correct results, seen in figure A.7

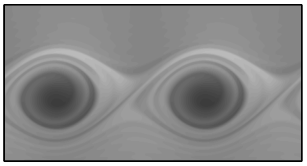

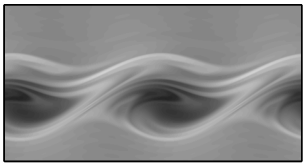

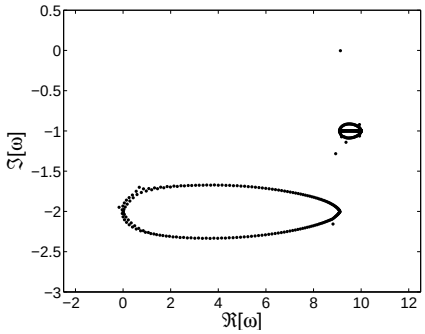

(a) $W\dot{\imath} = 1$.

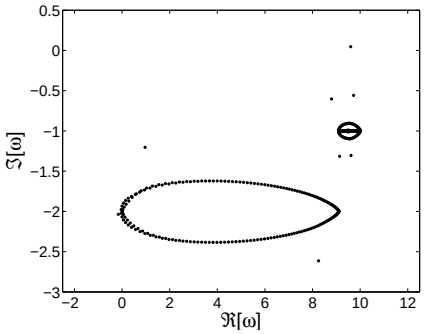

(b) $W\dot{\imath} = 10$.

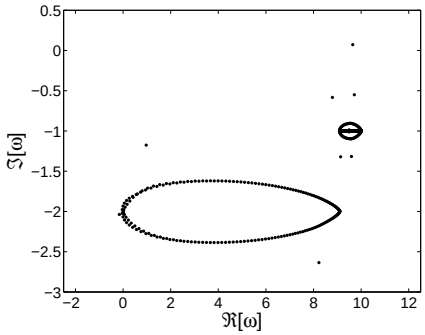

(c) $W\dot{\imath} = 10000$.

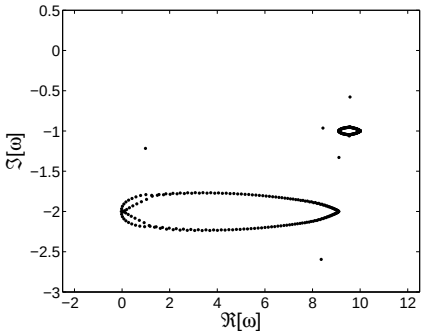

(d) $W\dot{\imath} = \infty$.

Figure A.6: Eigenvalues of UCM varicose modes with $\xi = 0.5$, $\Delta = 0.3$, and $k = 10$ calculated keeping each variable accurate to $N = 100$ Chebyshev polynomials. The $W\dot{\imath} = \infty$ calculation does not match the limit of the finite $W\dot{\imath}$ calculations. There is an error in the calculation.

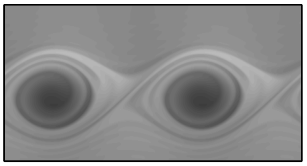

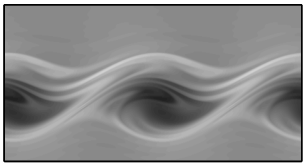

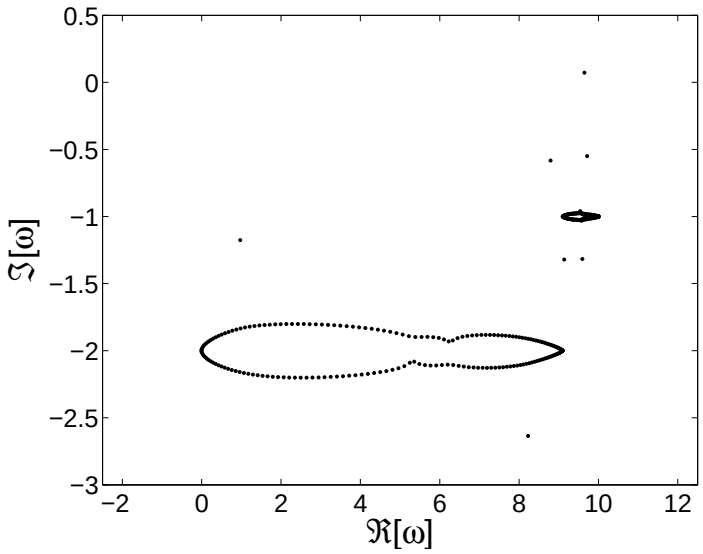

Figure A.7: The corrected calculation for $Wi = \infty$.

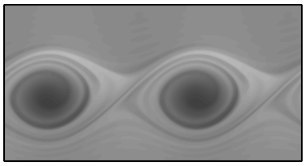

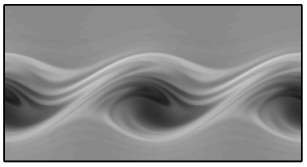

Appendix B

Amplitude equations and numerical methods for the elastic jet

In this appendix we derive the amplitude equations for the UCM [(7.39)–(7.44)] and FENE–CR [(7.49)–(7.56)] weakly-elastic planar jets of Chapter 7. We also give details of the numerical method used to solve the equations. Our derivation follows Balmforth and Piccolo [4], but our numerical method is distinct.

We consider a (symmetric) planar jet for which $E = \epsilon^4 E_4$ and is negligible at leading order. The linear problem predicts instability for $0 < k < k_0$. We take y_c to be the (positive) value at which both U and U'' are zero. The mode corresponding to $k = k_0$ is stationary in the frame of reference moving with the fluid at y_c. We assume that the mode is sinuous so that ψ is an even function. We take the flow to be periodic in the x-direction with period $2\pi/k$ for $k = k_0 - \epsilon k_1$. The mode with wavelength k is unstable with a growth rate of order ϵ. This defines the slow time scale $T = \epsilon t$.

We study two regions of the jet: an outer region where the solution looks

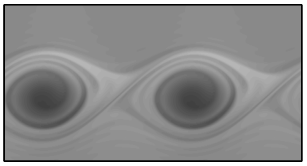

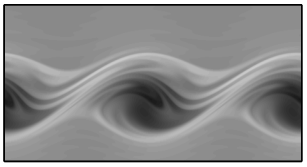

like the neutrally stable linear mode with an amplitude that varies slowly in time, and an inner region, the critical layer, centered around y_c where the nonlinear terms are important and cat's eyes develop. It is the critical layer that determines the growth rate of the amplitude of the linear mode. This appendix focuses on the derivation and solution of the critical layer equations.

B.1 Derivation of the UCM amplitude equations

Derivation of scalings

We consider the evolution of a small perturbation to the base flow. Equations (7.36)–(7.38) become

$$\nabla^2\psi = -\zeta\,, \tag{B.1}$$

$$\epsilon\zeta_T + U\zeta_x + U''\psi_x - J(\psi,\zeta) = \epsilon^4 E_4[-\partial_{xy}a_{11} + (\partial_{xx} - \partial_{yy})a_{12} + \partial_{xy}a_{22}]\,, \tag{B.2}$$

$$\epsilon\mathsf{a}_T + U\mathsf{a}_x - J(\psi,\mathsf{a}) - \psi_x\mathsf{A}' - U'\begin{pmatrix} 2a_{12} & a_{22} \\ a_{22} & 0 \end{pmatrix} - \mathsf{H} - \mathsf{h} = -\epsilon\lambda\mathsf{a}\,. \tag{B.3}$$

Far from y_c the $\mathcal{O}(\epsilon\psi)$ and nonlinear terms are neglected, and we have $\nabla^2\psi = -\zeta$, $U\zeta_x + U''\psi_x = 0$. This breaks down in the critical layer $y - y_c = \mathcal{O}(\epsilon)$ for which both U and U'' are $\mathcal{O}(\epsilon)$. This motivates the definition of an inner variable $Y = (y - y_c)/\epsilon$ for the critical layer.

In the critical layer the y-derivative in the nonlinear term $J(\psi,\zeta)$ becomes $\mathcal{O}(\epsilon^{-1})$. This term is comparable to the linear terms of (B.2) when $\epsilon\psi \sim \psi\zeta/\epsilon$, which leads to the conclusion that ψ and ζ are both $\mathcal{O}(\epsilon^2)$ when nonlinear terms become significant. We have chosen the scaling of E so that

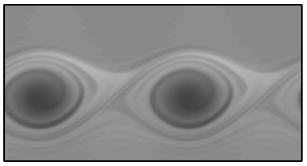

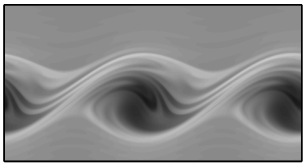

the elastic stresses affect equation (B.2) at the same time as the nonlinear terms.

Outer solution

In the outer region, away from the critical layer, ψ and ζ are expanded as

$$\psi = \psi_2\epsilon^2 + \psi_3\epsilon^3 + hot\,,$$
$$\zeta = \zeta_2\epsilon^2 + \zeta_3\epsilon^3 + hot\,.$$

We take $\psi_2 = B(T)\hat{\psi}_2(y)\exp(ikx) + cc$ and $\zeta_2 = B(T)\hat{\zeta}_2(y)\exp(ikx) + cc$, where the hat notation $\hat{\cdot}$ denotes the projection onto the Fourier mode $\exp(ikx)$ and $\hat{\psi}_2(y)$ and $\hat{\zeta}_2(y)$ solve the linear problem $\nabla^2\psi = -\zeta$, $U\zeta_x + U''\psi_x = 0$ for $k = k_0 - \epsilon k_1$.

Up to $\mathcal{O}(\epsilon^3)$ we can neglect the nonlinear terms and the elasticities. Our equations become

$$\nabla^2\psi = -\zeta\,,$$
$$\epsilon\zeta_T + U\zeta_x + U''\psi_x = 0\,.$$

Combining these, we obtain

$$-\epsilon\zeta_T + U\nabla^2\psi_x - U''\psi_x = 0\,. \tag{B.4}$$

At $\mathcal{O}(\epsilon^2)$ this equation yields

$$-U(\hat{\psi}_{2,yy} - k_0^2\hat{\psi}_2) + U''\hat{\psi}_2 = 0\,,$$

and at $\mathcal{O}(\epsilon^3)$

$$-\zeta_{2,T} = -U(2k_0k_1\psi_2 + \nabla^2\psi_3)_x + U''\psi_{3,x}\,. \tag{B.5}$$

It is from this equation that we obtain the evolution equation for B. The $k_0k_1\psi_2$ term comes from the cross term $2\epsilon k_0k_1$ in the ∂_x^2 derivative of ψ_2.

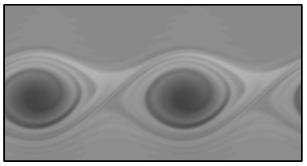

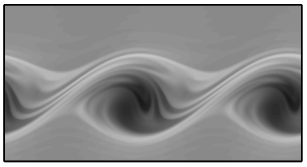

Multiplying by ψ_2^*/U and integrating in x and y we find

$$\frac{k}{2\pi}\int_{-\infty}^{\infty}\int_{0}^{2\pi/k} -\frac{\zeta_{2,T}\psi_2^*}{U} + 2k_0k_1\psi_2^*\psi_{2,x}\,dx\,dy$$
$$= \frac{k}{2\pi}\int_{-\infty}^{\infty}\int_{0}^{2\pi/k} \psi_2^*\left(-\nabla^2 + \frac{U''}{U}\right)\psi_{3,x}\,dx\,dy\,. \tag{B.6}$$

From our definition of ψ_2, it follows that $(-\nabla^2 + U''/U)\psi_2^* = 0$. Hence integrating by parts allows us to simplify the right-hand side at the expense of introducing boundary terms.

When we integrate by parts in x, the boundary terms cancel because the domain is periodic. We can only integrate by parts in y if ψ_3 is well-behaved in the integration domain. This will not hold if $U = 0$ somewhere in that domain which it does at $y = \pm y_c$. We break the y-integral on the right-hand side of (B.6) into three regions, $(-\infty, -y_c-\delta)$, $(-y_c+\delta, y_c-\delta)$ and $(y_c+\delta, \infty)$ where $\delta \to 0$. Equation B.6 becomes

$$\int_{-\infty}^{\infty} - B^*B_T\frac{\hat{\zeta}_2\hat{\psi}_2^*}{U} + 2ik|B|^2k_0k_1|\hat{\psi}_2|^2\,dy$$
$$= ikB^*\left(-\hat{\psi}_{2,c}^{*\prime}\left[\!\left[\hat{\psi}_3\right]\!\right]_{-y_c} - \hat{\psi}_{2,c}^{*\prime}\left[\!\left[\hat{\psi}_3\right]\!\right]_{y_c} + \psi_{2,c}^*\left[\!\left[\hat{\psi}_3'\right]\!\right]_{-y_c} + \psi_{2,c}^*\left[\!\left[\hat{\psi}_3'\right]\!\right]_{y_c}\right),$$

where $\hat{\psi}_3$ is the projection of ψ_3 onto the $\exp(ikx)$ Fourier mode. We use the fact that ψ_2 and its derivative are continuous to move them outside of the jump, and use the subscript c to denote its value at y_c. The jump in $\hat{\psi}_3$ can be shown to be zero. Heuristically we see this by arguing that the vertical velocity of the outer solution should be continuous across the horizontal line $y = y_c$. A rigorous argument follows from consideration of the equations within the critical layer and is postponed until the discussion of the inner solution.

We use decay conditions to eliminate the boundary terms at infinity. Dividing through by ikB^*, we find

$$2iI_0B_T + 2k_1I_1B = \left(\hat{\psi}_{2,c}^*\left[\!\left[\hat{\psi}_3'\right]\!\right]_{-y_c} + \hat{\psi}_{2,c}^*\left[\!\left[\hat{\psi}_3'\right]\!\right]_{y_c}\right)$$

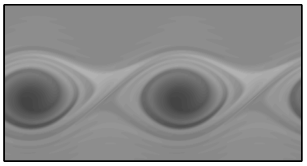

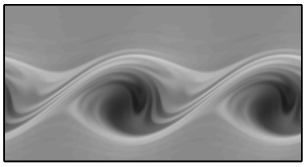

where

$$I_0 = \int_0^\infty \hat{\zeta}_2 \hat{\psi}_2^* / kU \, dy \,,$$
$$I_1 = 2k_0 \int_0^\infty |\hat{\psi}_2|^2 \, dy$$

(we can change the domain of integration to positive y by symmetry arguments). These integrals are independent of T.

To complete the amplitude equation, we need to find the jump in $\hat{\psi}_3'$. From (B.5) we have

$$U_c' \hat{\psi}_3'' = -\frac{iB_T}{k(y-y_c)} \hat{\zeta}_2 + \mathcal{O}(1) \,.$$

The solution may be written in the form

$$\hat{\psi}_3 = -(y-y_c) B_T \hat{Q} \ln|y-y_c| + \gamma |y-y_c| + R \,,$$

where $\hat{Q} = i\hat{\zeta}_{2,c}/kU_c'$ and R is a regular function of y. The $\gamma|y-y_c|$ term reflects the fact that the coefficient of the linear term need not be equal on either side of y_c. The jump in $\hat{\psi}_3'$ across y_c is 2γ, and must be found from the solution in the critical layer. The critical layers at y_c and $-y_c$ give the same value for γ.

We finally arrive at an ordinary differential equation governing the evolution of B

$$iI_0 B_T + k_1 I_1 B = 2\gamma \hat{\psi}_{2,c}^* \,, \tag{B.7}$$

with an as-yet-unknown parameter γ.

Inner solution

We use the inner variable $Y = (y-y_c)/\epsilon$ and assume that the inner solution is valid for Y in $(-\Delta, \Delta)$ where $\Delta = \delta/\epsilon \gg 1$. The inner solution must match the outer solution at $Y = \pm\Delta$, for which $y = y_c \pm \delta = y_c \pm \epsilon\Delta$.

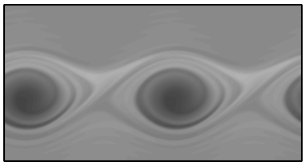

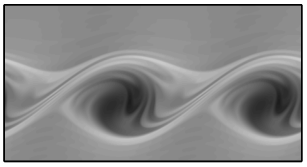

At $y = y_c + \delta$ the outer solution is

$$\begin{aligned}\hat{\psi} &= \epsilon^2\hat{\psi}_{2,c} + \epsilon^2\delta\hat{\psi}'_{2,c} + \epsilon^2\frac{\delta^2}{2}\hat{\psi}''_{2,c}(y_c) + \epsilon^3\hat{\psi}_3 + \cdots \\ &= \epsilon^2\hat{\psi}_{2,c} + \epsilon^3\Delta\hat{\psi}'_{2,c} + \epsilon^3\hat{R}_c - \epsilon^4 B_T\hat{Q}\Delta\ln\Delta \\ &\qquad - \epsilon^4\Delta B_T\hat{Q}\ln\epsilon + \epsilon^4(\Delta\gamma + \Delta^2\hat{\psi}''_{2,c}/2) + \cdots , \\ \hat{\zeta} &= \epsilon^2\hat{\zeta}_{2,c} + \cdots .\end{aligned}$$

To match this, we anticipate

$$\begin{aligned}\Psi &= \epsilon^2\Psi_2(x,T) + \epsilon^3[\Psi_3(x,T) + Y\Phi_3(x,T)] \\ &\qquad + \epsilon^4(\ln\epsilon)Y\Phi_4(x,T) + \epsilon^4\Psi_4(x,Y,T) + \cdots , \\ Z &= \epsilon^2 Z_2(x,Y,T) + \cdots .\end{aligned}$$

The relation between the vorticity and the streamfunction (B.1) in the Y variable is

$$(\epsilon^{-2}\partial_Y^2 + \partial_x^2)\Psi = -Z\,. \tag{B.8}$$

This is consistent with the assumed form of Ψ above where Ψ has at most linear dependence on Y until Ψ_4.

We now show that $\hat{\psi}_3$ cannot have a jump across the critical layer. We first note that the jump cannot depend on the value chosen for Δ. The $\mathcal{O}(\epsilon^3)$ terms of Ψ are either constant or linear in Y in order to satisfy (B.8) [as otherwise $Z = \mathcal{O}(\epsilon)$]. The change in the $\mathcal{O}(\epsilon^3)$ part of Ψ from $-\Delta$ to Δ must match with $2\Delta B\hat{\psi}'_{2,c} + \left[\!\left[\hat{\psi}_3\right]\!\right]$. However, this change is $2\Delta\hat{\Phi}_3(x,T)$. Consequently, the jump in $\hat{\psi}_3$ must be zero in order that it not depend on Δ.

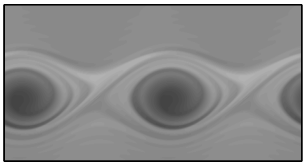

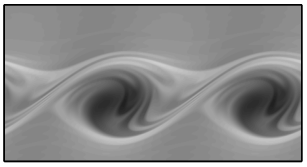

We can easily match a number of terms

$$\begin{aligned}
\hat{\Psi}_2 &= B\hat{\psi}_{2,c}\,,\\
\hat{\Psi}_3 &= \hat{R}_c\,,\\
\hat{\Phi}_3 &= B\hat{\psi}'_{2,c}\,,\\
\hat{\Phi}_4 &= -B_T\hat{Q}\,,\\
\hat{\Psi}_4(Y,T) &= \frac{\hat{\psi}''_{2,c}}{2}Y^2 + \gamma|Y| + \cdots \qquad \text{at large } |Y|.
\end{aligned}$$

We turn to the jump in $\hat{\psi}'_3$. We have

$$2\Delta B\hat{\psi}''_{2,c} + \left[\!\left[\hat{\psi}'_3\right]\!\right]_{y_c} = \left[\!\left[\hat{\Psi}_{4,Y}\right]\!\right]_{-\Delta}^{\Delta}\,,$$

From (B.8) $\Psi_{2,xx} + \Psi_{4,YY} = -Z_2$. Thus we find

$$\begin{aligned}
\left[\!\left[\hat{\psi}'_3\right]\!\right]_{y_c} &= -2\Delta(-k^2\hat{\Psi}_2 + B\hat{\psi}''_{2,c}) - \int_{-\Delta}^{\Delta}\hat{Z}_2\,dY\,,\\
&= -\int_{-\Delta}^{\Delta}\left(\hat{Z}_2 + \frac{U'''_c}{U'_c}\hat{\Psi}_2\right)dY\,,
\end{aligned}$$

where we have used the fact that $\hat{\psi}_2$ is a solution to the linear problem, the relationship between $\hat{\Psi}_2$ and $\hat{\psi}_2$, equation (B.4), and L'Hôpital's rule.

We perform the change of variables

$$\Theta = Z_2 + \frac{U'''_c}{U'_c}\Psi_2\,,$$

so that $\left[\!\left[\hat{\psi}'_3\right]\!\right]_{y_c} = -\int_{-\Delta}^{\Delta}\hat{\Theta}\,dY$. Letting $\Delta\to\infty$ we have

$$2\gamma = -\frac{k}{2\pi}\int_0^{2\pi/k}\int_{-\infty}^{\infty}\Theta\exp(-ikx)\,dY\,dx\,.$$

Thus our amplitude equation (B.7) takes the form

$$iI_0B_T + k_1I_1B = -\hat{\psi}^*_{2,c}\frac{k}{2\pi}\int_0^{2\pi/k}\int_{-\infty}^{\infty}\Theta\exp(-ikx)\,dY\,dx\,.$$

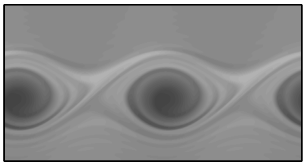

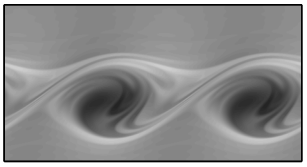

We turn now to equations (B.2) and (B.3) in the critical layer. We find that

$$\epsilon Z_T + \epsilon Y U_c' Z_x + \epsilon Y U_c''' \Psi_x - \frac{1}{\epsilon} J_Y(\Psi, Z) = \epsilon^4 E_4[-\frac{1}{\epsilon}\partial_{xY} a_{11} + (\partial_{xx} - \frac{1}{\epsilon^2}\partial_Y^2) a_{12} + \frac{1}{\epsilon}\partial_{xY} a_{22}]\,, \tag{B.9}$$

$$\epsilon \mathsf{a}_T + \epsilon Y U_c' \mathsf{a}_x - \frac{1}{\epsilon} J_Y(\Psi, \mathsf{a}) - \Psi_x \epsilon Y \begin{pmatrix} 4U_c' U_c''' & \epsilon\lambda U_c' \\ \epsilon\lambda U_c' & 0 \end{pmatrix} - U' \begin{pmatrix} 2a_{12} & a_{22} \\ a_{22} & 0 \end{pmatrix} - \mathsf{H} - \mathsf{h} = -\epsilon\lambda \mathsf{a}\,, \tag{B.10}$$

where $J_Y(a,b) = a_x b_Y - a_Y b_x$. On the left-hand side of the first equation all terms are $\mathcal{O}(\epsilon^3)$. This suggests that a_{11} is $\mathcal{O}(1)$, and we set $a_{11} = b_{11}$. From the second equation, it then follows that $a_{12} = \epsilon b_{12}$ and $a_{22} = \epsilon^2 b_{22}$. We substitute at leading order for $Z = \epsilon^2(\Theta - U_c''' \Psi_2 / U_c')$ and recall that $\Psi_{2,Y} = 0$. The vorticity equation (B.9) becomes

$$\Theta_T + Y U_c' \Theta_x - \Psi_{2,x}\Theta_Y = \frac{U_c'''}{U_c'} \psi_{2,T} + E_4[-\partial_{xY} b_{11} - \partial_Y^2 b_{12}] + \mathcal{O}(\epsilon)\,,$$

while the constitutive equation (B.10) gives

$$\mathsf{b}_T + Y U_c' \mathsf{b}_x - \Psi_{2,x}\mathsf{b}_Y - U_c' \begin{pmatrix} 2b_{12} & b_{22} \\ b_{22} & 0 \end{pmatrix} - \begin{pmatrix} 0 & -2U_c'^2 \Psi_{2,xx} \\ -2U_c'^2 \Psi_{2,xx} & -2\lambda U_c' \Psi_{2,xx} \end{pmatrix} - \begin{pmatrix} 0 & -b_{11}\Psi_{2,xx} \\ -b_{11}\Psi_{2,xx} & -2b_{12}\Psi_{2,xx} \end{pmatrix} = -\lambda \mathsf{b} + \mathcal{O}(\epsilon)\,.$$

The $\Psi_x \mathsf{A}'$ term is too small in ϵ to appear in this equation.

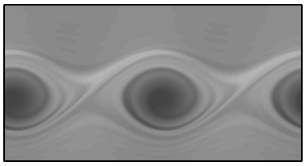

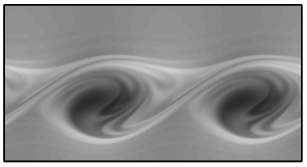

Canonical form

We introduce some rescalings to arrive at a canonical form. By appropriate shift in x, we can assume that $\hat{\psi}_{2,c}$ is real, and so $\hat{\psi}^*_{2,c} = \hat{\psi}_{2,c}$. Then

$$I = \frac{k_1 I_1}{k I_0}\,,$$

$$\tilde{x} = -k(x + IT)\,, \qquad \tilde{T} = T/T_0\,, \qquad \tilde{Y} = -(Y + I/U_c')/Y_0\,,$$

$$\tilde{B} = [B\exp(-ikIT)/B_0]^*\,, \qquad \tilde{\Psi} = \Psi_2/B_0\,, \qquad \tilde{\Theta} = -\Theta/\Theta_0\,,$$

$$\tilde{b}_{11} = b_{11}/\beta_{11}\,, \qquad \tilde{b}_{12} = b_{12}/\beta_{12}\,, \qquad \tilde{b}_{22} = b_{22}/\beta_{22}\,,$$

$$Y_0 = \frac{1}{U_c' k T_0}\,, \qquad B_0 = \frac{1}{U_c' k^2 T_0^2}\,, \qquad \Theta_0 = -\frac{U_c''' I}{U_c' k T_0}\,, \qquad T_0 = \frac{U_c'^2 I_0}{\hat{\psi}_{2,c} U_c''' I}\,,$$

$$\beta_{11} = U_c'^2\,, \qquad \beta_{12} = U_c'/T_0\,, \qquad \beta_{22} = 1/T_0^2\,, \qquad \tilde{\lambda} = T_0\lambda\,,$$

$$\tilde{E} = -\frac{T_0^3 U_c'^5 k^3}{U_c''' I} E_4\,.$$

After dropping the tildes, the vorticity and constitutive equations reduce to

$$\Theta_T + Y\Theta_x - \Psi_x\Theta_Y = -\Psi_x + \kappa\Psi_T + E(b_{12,YY} + b_{11,xY})\,, \tag{B.11}$$

$$b_{11,T} + Y b_{11,x} - \Psi_x b_{11,Y} = 2b_{12} - \lambda b_{11}\,, \tag{B.12}$$

$$b_{12,T} + Y b_{12,x} - \Psi_x b_{12,Y} = b_{22} - b_{11}\Psi_{xx} - 2\Psi_{xx} - \lambda b_{12}\,, \tag{B.13}$$

$$b_{22,T} + Y b_{22,x} - \Psi_x b_{22,Y} = -2b_{12}\Psi_{xx} - 2\lambda\Psi_{xx} - \lambda b_{22}\,, \tag{B.14}$$

$$\Psi = B\exp(ix) + cc\,, \tag{B.15}$$

where

$$\kappa = \frac{1}{k I T_0}\,.$$

The amplitude equation becomes

$$iB_T = -\frac{1}{2\pi}\int_0^{2\pi}\int_{-\infty}^{\infty}\Theta\exp(-ix)\,dY\,dx\,. \tag{B.16}$$

The parameter κ depends only on properties of the base flow profile and the marginally stable mode (which itself depends only on the base flow). In

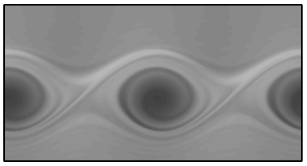

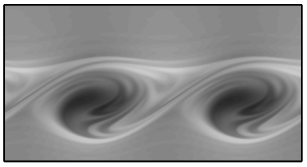

contrast, E and λ depend on material properties. Hence, once we choose the base flow, our parameter space is two-dimensional.

Noting that $\Psi_{xx} = -\Psi$, we may simplify equations (B.11)–(B.16) further, arriving at equations (7.39)–(7.44). The operators acting on the left hand side of equations (7.39)–(7.42) are identical. When $E = 0$, these equations are equivalent to (4.7) and (4.8) of Balmforth and Piccolo [4] in the inviscid limit, with their ϕ, A and γ replaced by $-\Psi$, $-B$ and -1 respectively [and on correction of a typo in their equation (4.8)].

B.1.1 Calculation of κ

The value of κ is determined by the base flow values. We have

$$\begin{aligned}\kappa &= \frac{1}{kIT_0} \\ &= \frac{\hat{\psi}_{2,c}U_c'''}{kU_c'^2 I_0}\,.\end{aligned}$$

For the Bickley jet $\hat{\psi}_2 = \operatorname{sech}^2(y)$ and $k_0 = 2$. Consequently, $U = \operatorname{sech}^2(y) - 2/3$, $\hat{\psi}_{2,c} = 2/3$, and

$$\begin{aligned}I_0 &= \int_{-\infty}^{0} \hat{\zeta}_2\hat{\psi}_2^*/k_0 U\, dy \\ &= \int_{-\infty}^{0} \frac{3\operatorname{sech}^6(y)}{\operatorname{sech}^2(y) - 2/3}\, dy \\ &= 4 - \frac{2\sqrt{3}}{3}\ln\left(\frac{\sqrt{3}-1}{\sqrt{3}+1}\right)\,,\end{aligned}$$

using the substitution $X = \operatorname{sech}^2(y)$. So

$$\kappa = \frac{3\sqrt{3}}{2I_0} \approx 0.470607\,.$$

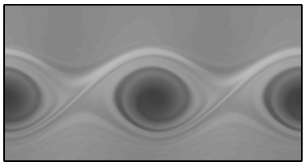

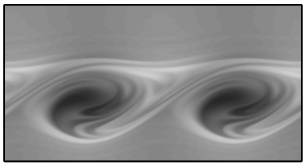

B.2 Derivation of the FENE–CR amplitude equations

The UCM model has some unphysical behavior in extensional flow which is evident in the calculations using the equations derived above. To correct this, we return to dimensional variables and consider the FENE–CR correction. The derivation is similar to that done for the UCM fluid. We assume that the elasticity is again small and so the linear problem is unchanged from the Newtonian result.

We start from equations (7.10)–(7.12) with the FENE–CR correction

$$\rho\frac{D\boldsymbol{U}}{Dt} = -\nabla P + \frac{\mu}{\tau}\nabla\cdot[F(\mathsf{A}-\mathsf{I})] + \mathcal{F}\,, \tag{B.17}$$

$$\overset{\triangledown}{\mathsf{A}} = \frac{F}{\tau}(\mathsf{I}-\mathsf{A})\,, \tag{B.18}$$

$$\nabla\cdot\boldsymbol{U} = 0\,, \tag{B.19}$$

$$F = \frac{l^2}{l^2-\mathrm{tr}(A)}\,. \tag{B.20}$$

We repeat the nondimensionalizations of section 7.2.2, with $\boldsymbol{U} = U_0\boldsymbol{U}^*$, $P = \rho U_0^2 P^*$, $t = Wt^*/U_0$, $\nabla = (1/W)\nabla^*$, $\tau = W\tau^*/U_0$, $Wi = U_0\tau/W$ and $\mathsf{A} = Wi^2\mathsf{A}^*$. We set $l = l^*Wi$. Dropping the asterisks we arrive at

$$\frac{D\boldsymbol{U}}{Dt} = -\nabla P + E\nabla\cdot[F(\mathsf{A}-Wi^{-2}\mathsf{I})]\,, \tag{B.21}$$

$$\overset{\triangledown}{\mathsf{A}} = F(Wi^{-3}\mathsf{I} - Wi^{-1}\mathsf{A})\,, \tag{B.22}$$

$$\nabla\cdot\boldsymbol{U} = 0\,, \tag{B.23}$$

$$F = l^2/[l^2-\mathrm{tr}(\mathsf{A})]\,, \tag{B.24}$$

where E is again given by $\tau\mu/\rho W^2 = Wi/Re$.

Assuming steady flow with unchanging history we find

$$\mathsf{A} = \begin{pmatrix} 2\frac{U'^2}{F^2} + Wi^{-2} & Wi^{-1}\frac{U'}{F} \\ Wi^{-1}\frac{U'}{F} & Wi^{-2} \end{pmatrix}.$$

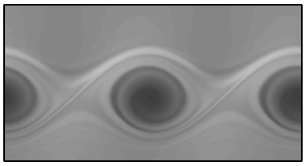

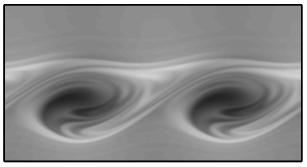

B.2.1 Perturbation equations

We substitute $\tilde{\boldsymbol{U}} = \boldsymbol{U} + \boldsymbol{u}$, $\tilde{\mathsf{A}} = \mathsf{A} + \mathsf{a}$ and $\tilde{F} = F + f$ into equations (B.21) and (B.22) and introduce a streamfunction for the perturbation flow. After taking the curl of the momentum equation, the resulting equations are

$$\nabla^2\psi = -\zeta\,, \tag{B.25}$$

$$\begin{aligned}\epsilon\zeta_T + U\zeta_x + U''\psi_x - J(\psi,\zeta) = \epsilon^4 E_4[-\partial_{xy}[(F+f)b_{11} + fC_{11}] \\ +\epsilon(\partial_{xx} - \partial_{yy})[(F+f)b_{12} + fC_{12}] \\ +\epsilon^2\partial_{xy}[(F+f)b_{22} + fC_{22}]\,,\end{aligned} \tag{B.26}$$

$$\begin{aligned}\epsilon b_{11,T} + Ub_{11,x} - J(\psi,b_{11}) - \psi_x C_{11,y} - \epsilon 2U'b_{12} - H_{11} - h_{11} = \\ \epsilon\lambda[-(F+f)b_{11} - fC_{11}]\,,\end{aligned} \tag{B.27}$$

$$\begin{aligned}\epsilon b_{12,T} + Ub_{12,x} - J(\psi,b_{12}) - \psi_x C_{12,y} - \epsilon U'b_{22} + \epsilon^{-1}(-H_{12} - h_{12}) = \\ \epsilon\lambda[-(F+f)b_{12} - fC_{12}]\,,\end{aligned} \tag{B.28}$$

$$\begin{aligned}\epsilon b_{22,T} + Ub_{22,x} - J(\psi,b_{22}) - \psi_x C_{22,y} + \epsilon^{-2}(-H_{22} - h_{22}) = \\ \epsilon\lambda[-(F+f)b_{22} - fC_{22}]\,,\end{aligned} \tag{B.29}$$

where

$$\mathsf{H} = \begin{pmatrix} 2C_{11}\psi_{xy} + 2\epsilon C_{12}\psi_{yy} & C_{22}\epsilon^2\psi_{yy} - C_{11}\psi_{xx} \\ \epsilon^2 C_{22}\psi_{yy} - C_{11}\psi_{xx} & -2\epsilon C_{12}\psi_{xx} - 2\epsilon^2 C_{22}\psi_{xy} \end{pmatrix},$$

$$\mathsf{h} = \begin{pmatrix} 2b_{11}\psi_{xy} + 2\epsilon b_{12}\psi_{yy} & \epsilon^2 b_{22}\psi_{yy} - b_{11}\psi_{xx} \\ \epsilon^2 b_{22}\psi_{yy} - b_{11}\psi_{xx} & -2\epsilon b_{12}\psi_{xx} - 2\epsilon^2 b_{22}\psi_{xy} \end{pmatrix},$$

with the same notation as in the UCM fluid and the additional variable changes $A_{11} = C_{11}$, $A_{12} = \epsilon C_{12}$, and $A_{22} = \epsilon^2 C_{22}$.

Using the same analysis and scalings as for the UCM fluid and the additional rescalings

$$\tilde{C}_{11} = C_{11}/\beta_{11}\,, \qquad \tilde{C}_{12} = C_{12}/\beta_{12}\,, \qquad \tilde{C}_{22} = C_{22}/\beta_{22}\,,$$
$$\tilde{l} = l/U_c'\,,$$

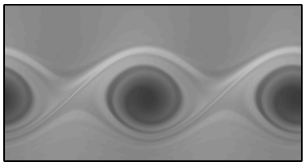

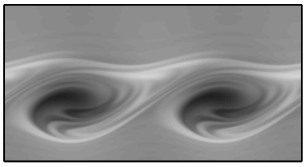

we arrive at the canonical form of the FENE–CR critical layer equations

$$\begin{aligned}
\Theta_T + Y\Theta_x - \Psi_x\Theta_Y &= -\Psi_x + \kappa\Psi_T + E[f_x b_{11,Y} + f_Y(b_{11,x} + 2b_{12,Y})] \\
&\quad + E[f_{xY}(b_{11} + 2/F^2) + f_{YY}(b_{12} + \lambda/F)] \\
&\quad + E[(F+f)(b_{11,xY} + b_{12,YY})]\,, \\
b_{11,T} + Y b_{11,x} - \Psi_x b_{11,Y} &= 2b_{12} - \lambda[(F+f)b_{11} + 2f/F^2]\,, \\
b_{12,T} + Y b_{12,x} - \Psi_x b_{12,Y} &= b_{22} - (b_{11} + 2/F^2)\Psi_{xx} - \lambda[(F+f)b_{12} + f\lambda/F]\,, \\
b_{22,T} + Y b_{22,x} - \Psi_x b_{22,Y} &= -2(b_{12} + \lambda/F)\Psi_{xx} - \lambda[(F+f)b_{22} + f\lambda^2]\,, \\
\Psi &= B\exp(ix) + cc\,, \\
iB_T &= -\frac{1}{2\pi}\int_0^{2\pi}\int_{-\infty}^{\infty}\Theta\exp(-ix)\,dY\,dx\,, \\
F + f &= \frac{l^2}{l^2 - 2/F^2 - b_{11}}\,, \\
F &= \left(1 + \sqrt{1 + 8/l^2}\right)/2\,.
\end{aligned}$$

The parameters are l, E, λ and κ. The value of κ is the same as for the UCM fluid. The value of l depends only on the material properties. E and λ come from a mixture of material properties and the base flow. The parameter space is three-dimensional.

B.3 Numerical method

To solve the nonlinear systems (7.39)–(7.44) and (7.49)–(7.56), we turn to numerical methods. We use a finite volume method. For definiteness, we describe the algorithm in terms of equations (7.39)–(7.44).

B.3.1 Algorithm

Our computational domain is (x, Y) where $x \in (0, 2\pi)$ and $y \in (-D, D)$. In each direction we use a uniform step size dx or dY.

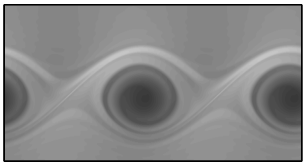

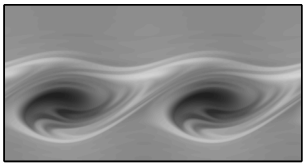

We break the calculation into four steps using Godunov splitting. We first solve the hyperbolic terms in the x-direction $[\Theta_T + Y\Theta_x]$ for the operator $\mathcal{L}$ on the left-hand side of (7.39)–(7.42). We next solve the hyperbolic terms in the Y-direction $[\Theta_T - \Psi_x\Theta_Y]$. Following that, we calculate the integral for (7.44). We finally solve the source terms on the right hand side of (7.39)–(7.42) and evolve B.

Hyperbolic terms

We use a high resolution finite volume method with a superbee limiter to solve the variable coefficient linear hyperbolic equation

$$\Theta_T + Y\Theta_x - \Psi_x\Theta_Y = 0\,,$$

following LeVeque [56].

We restrict our time step so that the CFL number $c < 1$ where

$$c = \frac{\bar{u}(dT)}{(dx)}$$

and $\bar{u} = \max(|Y|, |\Psi_x|)$. This has the practical implications that a larger domain implies a smaller time-step, and that the time step is controlled by a region far from the cat's eyes, where little of interest happens. Ideally an adaptive mesh would be useful, but we have not developed one.

We place rows of ghost cells around the domain in order to apply the boundary conditions. In the x-direction we set the ghost cells to have values based on the periodic boundary conditions. In the Y-direction we use an asymptotic approximation.

Integral

To perform the double integral

$$\int_0^{2\pi}\int_{-\infty}^{\infty} \Theta \exp(-ix)\, dY\, dx\,,$$

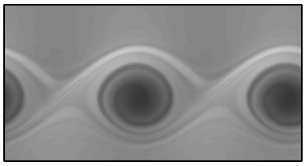

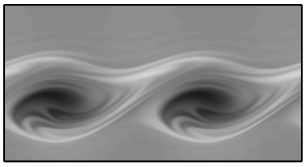

we simply sum over all cells

$$(dx)(dY)\sum_{j,k}\Theta_{j,k}\big(\cos[j(dx)]-i\sin[j(dx)]\big)\,.$$

In this summation, we truncate the Y direction at $\pm D$. This introduces an error of size $1/D$ into the calculation. We can reduce this to a $1/D^3$ error as described below.

From equations (7.40)–(7.42) we find that $a_{22}\sim 1/Y$, $a_{12}\sim 1/Y$ and $a_{11}\sim 1/Y^2$ at large Y. Thus they are too small to enter into equation (7.39). We take

$$\Theta=\frac{q_1(x,T)}{Y}+\frac{q_2(x,T)}{Y^2}+\cdots\,.$$

Substituting this into (7.39), we find that at leading order in Y

$$q_{1,x}=-\Psi_x+\kappa\Psi_T\,,$$

and hence

$$q_1=-\Psi-\kappa\Psi_{xT}\,,$$

where we have taken advantage of the fact that $\Psi_{xx}=-\Psi$. At next order,

$$q_{2,x}=-q_{1,T}\,,$$

and

$$q_2=-\Psi_{xT}+\kappa\Psi_{TT}\,.$$

When we calculate B_T, we can now approximate (7.44) as

$$\begin{aligned}2\pi iB_T&=-\int_{-D}^{D}\int_0^{2\pi}\Theta e^{-ix}\,dxdY-\left(\int_{-\infty}^{-D}+\int_D^{\infty}\right)\int_0^{2\pi}\frac{q_2}{Y^2}e^{-ix}\,dxdY\\&\quad+\mathcal{O}(D^{-3})\\&=-\int_{-D}^{D}\int_0^{2\pi}\Theta e^{-ix}\,dxdY+\frac{2}{D}2\pi(iB_T-\kappa B_{TT})+\mathcal{O}(D^{-3})\,,\end{aligned}$$

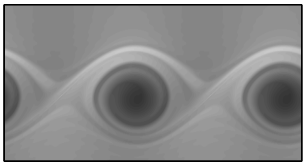

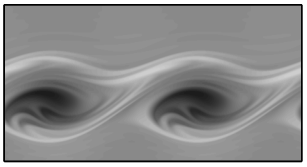

and so

$$2\pi i B_T \left(1 - \frac{2}{D}\right) \approx -\int_{-D}^{D}\int_{0}^{2\pi} \Theta e^{-ix}\, dx dY - \frac{4\pi}{D}\kappa B_{TT}\,.$$

We can approximate B_{TT} using values of B_T from the previous time step. Whether we keep this term or neglect it (as was done by Balmforth and Piccolo [4]) makes no noticeable difference in the calculations.

Source terms

To solve the source terms and evolve B we use a simple Euler forward explicit method for the Θ and B evolution and a trapezoidal implicit method for the a evolution equations.

B.3.2 Numerical tests

In this subsection, we discuss the tests we used to ensure that our numerical method gives accurate results.

Reproducing earlier work

We set E to zero and solve the Newtonian problem, attempting to match the calculations of Balmforth and Piccolo [4], who studied the Bickley jet in the $\tilde{\beta}$-plane with weak viscosity. Their value of κ depends on $\tilde{\beta}$ (the Coriolis parameter). Viscosity appears at leading order in the inner region in their problem. We do not have viscosity, so the only direct comparison we have is with their figure 4, for which they set their coefficient of viscosity to zero and additionally take $\kappa = 0$.

In their figure 4, reproduced in figure B.1, Balmforth and Piccolo plot $\Theta - Y$ at $T = 2$, 4, and 6 as well as the magnitude of the amplitude, B (which they call A), with an initial condition of $B = -0.001$. Their calculations were performed with a different set of variables, and then transformed into

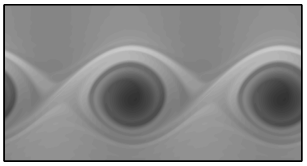

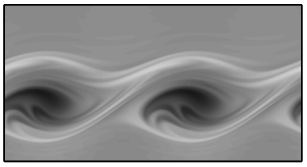

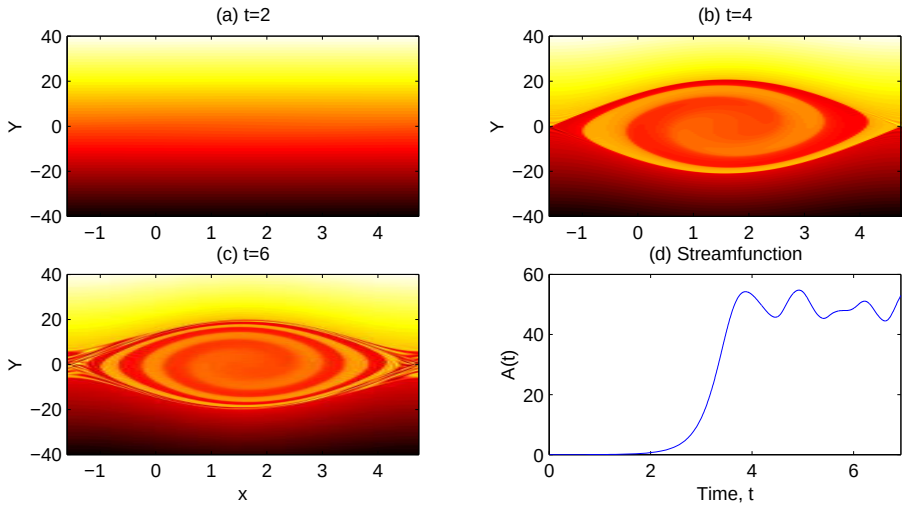

Figure B.1: Figure 4 reproduced from [4].

the plotted variables. However, there is an error in their transformation: the symmetries noted in their section 5.3 show that the figure should be symmetric under the mapping $x \mapsto -x$, $Y \mapsto -Y$ with $\Theta \mapsto -\Theta$. The only consequence of the error is that the cat's eye should be centered about zero rather than $\pi/2$. Our plot in figure B.2 shows the correct variables. The agreement for the vorticity is observed to be good, and the only discrepancy between the amplitude plots is at $T \approx 6$. We achieve a better correspondence at lower resolution.

Because κ is zero in this comparison, we want an additional comparison to test our calculations. Unfortunately all other results presented by Balmforth and Piccolo [4] include viscosity, which we neglect. However, we find good comparison for nonzero κ between their calculations with a small value of viscosity and our own with zero viscosity.

This establishes that the code works correctly in the Newtonian limit and that we accurately solve the operator $\mathcal{L}$ in (7.39)–(7.42).

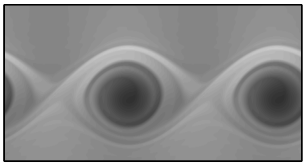

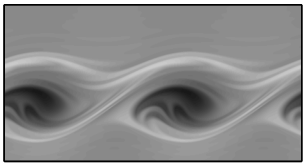

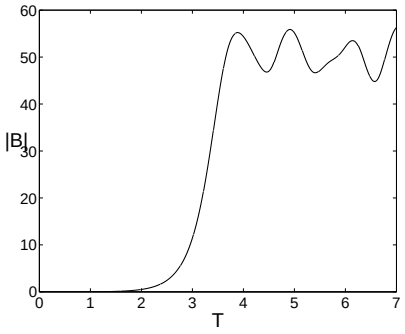

(a) Amplitude $|B|$.

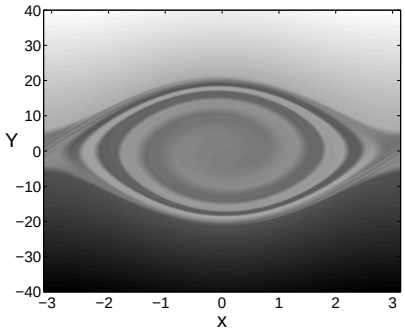

(b) $\Theta - Y$ at $T = 6$.

Figure B.2: Our calculations for the same parameters as figure 4 of [4]. The domain size is 1500×1500 grid points.

Simple tests of the elastic terms

As a test of the elastic terms in (7.39), we solve the UCM system neglecting the constitutive equations (7.40)–(7.42), setting $\Psi = 0$, $a_{11} = c_1 x Y$, and $a_{12} = c_2 Y^2$. Starting with a uniform initial condition for Θ, the solution is $\Theta = (c_1 + 2c_2)ET + \Theta(0)$. This agrees with the calculations, so we are solving (7.39) correctly.

As a test of the constitutive equations (7.40)–(7.42), we next solve the UCM system with Ψ held constant in space and time. The a_{ij} are then independent of space, so $\mathcal{L}[\boldsymbol{a}] = \boldsymbol{a}_T$ for $\boldsymbol{a} = (a_{11}, a_{12}, a_{22})^T$. The resulting system can be written as the constant-coefficient driven linear system

$$\boldsymbol{a}_T = \mathsf{M}\boldsymbol{a} + \boldsymbol{c}\,,$$

where

$$\mathsf{M} = \begin{pmatrix} -\lambda & 2 & 0 \\ \Psi & -\lambda & 1 \\ 0 & 2\Psi & -\lambda \end{pmatrix}, \qquad \boldsymbol{c} = \begin{pmatrix} 0 \\ 2\Psi \\ 2\lambda\Psi \end{pmatrix}.$$

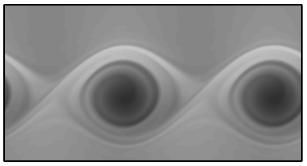

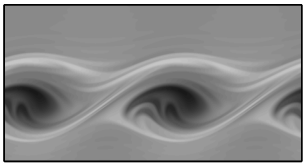

Choosing Ψ and λ such that M is invertible, the solution is

$$\boldsymbol{a} = -\mathsf{M}^{-1}\boldsymbol{c} + \exp(\mathsf{M}T)(\boldsymbol{a}_0 + \mathsf{M}^{-1}\boldsymbol{c}) \,,$$

where $\boldsymbol{a}_0$ is the initial value of $\boldsymbol{a}$. Our calculated solution agrees with this analytic result.

Thus far we have tested all terms in the UCM equations (7.39)–(7.44). Although the FENE–CR equations (7.49)–(7.56) involve a large number of additional terms, they are all equally straightforward to check.

We can make some further observations. We correctly calculate the initial linear growth rate for Newtonian, UCM, and FENE–CR fluids as shown in figure 7.12. The various limits of large λ, small E, and small l give effectively Newtonian behavior as expected. The $l \to \infty$ limit of the FENE–CR code reproduces the UCM results. Finally the FENE–CR code has the expected failures in the $\lambda = 0$ limit.

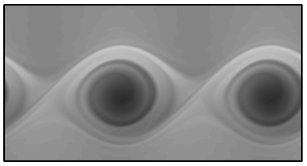

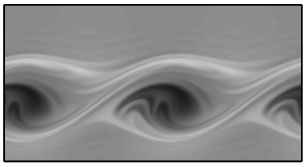

Bibliography

[1] Milton Abramowitz and Irene A. Stegun. *Handbook of Mathematical Functions with Formulas, Graphs, and Mathematical Tables*. Dover Publications, Inc., New York, 1965.

[2] Kunt Atalik and Roland Keunings. Non-linear temporal stability analysis of viscoelastic plane channel flows using a fully-spectral method. *Journal of Non-Newtonian Fluid Mechanics*, 102:299–319, 2002.

[3] J. Azaiez and G. M. Homsy. Linear stability of free shear flow of viscoelastic liquids. *Journal of Fluid Mechanics*, 268:37–69, 1994.

[4] Neil J. Balmforth and C. Piccolo. The onset of meandering in a barotropic jet. *Journal of Fluid Mechanics*, 449:85–114, 2001.

[5] W. G. Bickley. The plane jet. *The London, Edinburgh, and Dublin Philosophical Magazine and Journal of Science*, 23:727–731, 1937.

[6] R. Byron Bird, Robert C. Armstrong, and Ole Hassager. *Dynamics of Polymeric Liquids. Volume 1. Fluid Mechanics*. John Wiley & Sons, Second edition, 1987.

[7] R. Byron Bird, Charles F. Curtiss, Robert C. Armstrong, and Ole Hassager. *Dynamics of Polymeric Liquids, Volume 2, Kinetic Theory, 2nd Edition*. John Wiley & Sons, Second edition, 1987.

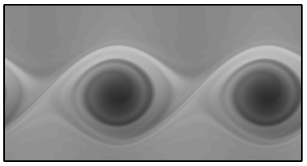

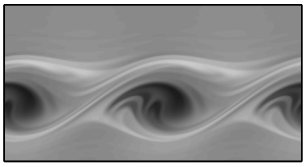

[8] R. Byron Bird and John M. Wiest. Constitutive equations for polymeric liquids. *Annual Review of Fluid Mechanics*, 27:169–193, 1995.

[9] Guido Boffetta, Antonio Celani, and Andrea Mazzino. Drag reduction in the turbulent Kolmogorov flow. *Physical Review E*, 71(3):036307/1–5, 2005.

[10] Guido Boffetta, Antonio Celani, Andrea Mazzino, A. Puliafito, and M. Vergassola. The viscoelastic Kolmogorov flow: eddy viscosity and linear stability. *Journal of Fluid Mechanics*, 523:161–170, 2005.

[11] Arjen C. B. Bogaerds, Anne M. Grillet, Gerrit W. M. Peters, and Frank P. T. Baaijens. Stability analysis of polymer shear flows using the eXtended Pom-Pom constitutive equations. *Journal of Non-Newtonian Fluid Mechanics*, 108:187–208, 2002.

[12] D. V. Boger. A highly elastic constant-viscosity fluid. *Journal of Non-Newtonian Fluid Mechanics*, 3(1):87–91, 1977.

[13] John P. Boyd. *Chebyshev and Fourier Spectral Methods*. Dover Publications, Inc., New York, Second edition, 2001.

[14] John F. Brady and Ileana C. Carpen. Second normal stress jump instability in non-Newtonian fluids. *Journal of Non-Newtonian Fluid Mechanics*, 102:219–232, 2002.

[15] KangPing Chen. Elastic instability of the interface in Couette flow of viscoelastic liquids. *Journal of Non-Newtonian Fluid Mechanics*, 40:261–267, 1991.

[16] KangPing Chen. Interfacial instability due to elastic stratification in concentric coextrusion of two viscoelastic fluids. *Journal of Non-Newtonian Fluid Mechanics*, 40:155–175, 1991.

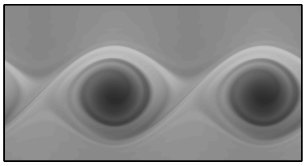

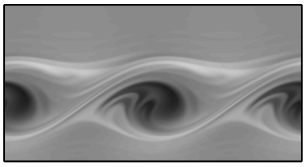

[17] KangPing Chen and Daniel D. Joseph. Elastic short wave instability in extrusion flows of viscoelastic liquids. *Journal of Non-Newtonian Fluid Mechanics*, 42:189–211, 1992.

[18] KangPing Chen and Yi Zhang. Stability of the interface in co-extrusion flow of two viscoelastic fluids through a pipe. *Journal of Fluid Mechanics*, 247:489–502, 1993.

[19] X. L. Chen and Phillip J. Morrison. A sufficient condition for the ideal instability of shear flow with parallel magnetic field. *Physics of Fluids B*, 3(4):863–885, 1991. Now *Physics of Plasmas*.

[20] M. D. Chilcott and John M. Rallison. Creeping flow of dilute polymer solutions past cylinders and spheres. *Journal of Non-Newtonian Fluid Mechanics*, 29:381–432, 1988.

[21] S. D. Conte. The numerical solution of linear boundary value problems. *SIAM Review*, 8(3):309–321, 1966.

[22] Charles R. Doering, Bruno Eckhardt, and Jörg Schumacher. Stress overshoots and the failure of energy stability in Oldroyd–B fluids at arbitrarily low Reynolds numbers. Submitted to *Journal of Non-Newtonian Fluid Mechanics*.

[23] J. J. Dongarra, B. Straughan, and D. W. Walker. Chebyshev tau-QZ algorithm methods for calculating spectra of hydrodynamic stability problems. *Applied Numerical Mathematics: Transactions of IMACS*, 22(4):399–434, 1996.

[24] Philip G. Drazin and Louis N. Howard. Hydrodynamic stability of parllel flow of inviscid fluid. *Advances in Applied Mechanics*, 9:1–89, 1966.

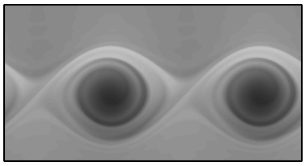

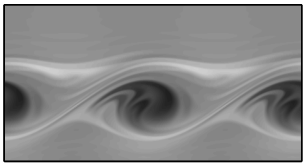

[25] Philip. G. Drazin and W. H. Reid. *Hydrodynamic Stability*. Cambridge University Press, Second edition, 2004.

[26] L. Engevik. A note on the barotropic instability of the Bickley jet. *Journal of Fluid Mechanics*, 499:315–326, 2004.

[27] Herambh K. Ganpule and Bamin Khomami. A theoretical investigation of interfacial instabilities in the three layer superposed channel flow of viscoelastic fluids. *Journal of Non-Newtonian Fluid Mechanics*, 79:315–360, 1998.

[28] Herambh K. Ganpule and Bamin Khomami. The effect of transient viscoelastic properties on interfacial instabilities in superposed pressure driven channel flows. *Journal of Non-Newtonian Fluid Mechanics*, 80:217–249, 1999.

[29] Herambh K. Ganpule and Bamin Khomami. An investigation of interfacial instabilities in the superposed channel flow of viscoelastic fluids. *Journal of Non-Newtonian Fluid Mechanics*, 81:27–69, 1999.

[30] Renato Ghisellini. Elastic free energy of an upper-convected Maxwell fluid undergoing a fully developed planar Poiseuille flow: a variational result. *Journal of Non-Newtonian Fluid Mechanics*, 46:229–241, 1993.

[31] V. A. Gorodtsov and A. I. Leonov. On a linear instability of a plane parallel Couette flow of viscoelastic fluid. *Journal of Applied Mathematics and Mechanics*, 31(2):310–319, 1967.

[32] Anne M. Grillit, Arjen C. B. Bogaerds, Gerrit W. M. Peters, and Frank P. T. Baaijens. Stability analysis of constituitve equations for polymer melts in viscometric flows. *Journal of Non-Newtonian Fluid Mechanics*, 103:221–250, 2002.

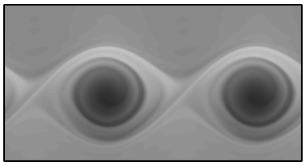

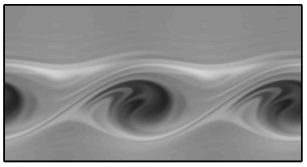

[33] A. Groisman and V. Steinberg. Elastic turbulence in a polymer solution flow. *Nature*, 405:53–55, 2000.

[34] Chang Dae Han and R. Shetty. Studies on multilayer film coextrusion I. The rheology of flat film coextrusion. *Polymer Engineering and Science*, 16(10):697–705, 1976.

[35] Chang Dae Han and R. Shetty. Studies on multilayer film coextrusion II. Interfacial instability in flat film coextrusion. *Polymer Engineering and Science*, 18(3):180–186, 1978.

[36] E. John Hinch. A note on the mechanism of the instability at the interface between two shearing fluids. *Journal of Fluid Mechanics*, 144:463–465, 1984.

[37] E. John Hinch. Appendix E. Long-wave instability of a free shear layer of an Oldroyd–B fluid. *Journal of Fluid Mechanics*, 268:64–69, 1994.

[38] E. John Hinch, O. J. Harris, and John M. Rallison. The instability mechanism for two elastic liquids being co-extruded. *Journal of Non-Newtonian Fluid Mechanics*, 43:311–324, 1992.

[39] Teh Chung Ho and Morton M. Denn. Stability of plane Poiseuille flow of a highly elastic liquid. *Journal of Non-Newtonian Fluid Mechanics*, 3:179–195, 1977.

[40] A. P. Hooper and W. G. C. Boyd. Shear-flow instability at the interface between two viscous fluids. *Journal of Fluid Mechanics*, 128:507–528, 1983.

[41] Louis N. Howard. Note on a paper of John W. Miles. *Journal of Fluid Mechanics*, 10:509–512, 1961.

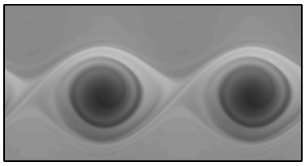

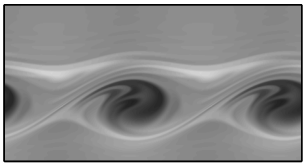

[42] Louis N. Howard and Philip G. Drazin. On instability of parallel flow of inviscid fluid in a rotating system with variable Coriolis parameter. *Journal of Mathematics and Physics*, 43:83–99, 1964.

[43] Chao-Tsai Huang and Bamin Khomami. The instability mechanism of single and multilayer Newtonian and viscoelastic flows down an inclined plane. *Rheologica Acta*, 40(5):467–484, 2001.

[44] D. W. Hughes and S. M. Tobias. On the instability of magnetohydrodynamic shear flows. *Proceedings of the Royal Society of London* A, 457(2010):1365–1384, 2001.

[45] K. P. Jackson, K. Walters, and R. W. Williams. A rheometrical study of Boger fluids. *Journal of Non-Newtonian Fluid Mechanics*, 14:173–188, 1984.

[46] Arthur Kent. Instability of laminar flow of a perfect magnetofluid. *The Physics of Fluids*, 9(7):1286–1289, 1966.

[47] Arthur Kent. Stability of laminar magnetofluid flow along a parallel magnetic field. *Journal of Plasma Physics*, 2:543–556, 1968.

[48] Bamin Khomami, Yuriko Renardy, Kuan C. Su, and M. A. Clarke. An experimental/theoretical investigation of interfacial instabilities in superposed pressure-driven channel flow of Newtonian and well characterized viscoelastic fluids. Part II: nonlinear stability. *Journal of Non-Newtonian Fluid Mechanics*, 91:85–104, 2000.

[49] Bamin Khomami and Kuan C. Su. An experimental/theoretical investigation of interfacial instabilities in superposed pressure-driven channel flow of Newtonian and well characterized viscoelastic fluids. Part I: linear stability and encapsulation effects. *Journal of Non-Newtonian Fluid Mechanics*, 91:59–84, 2000.

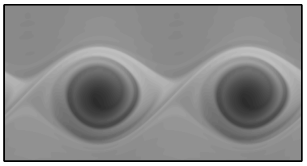

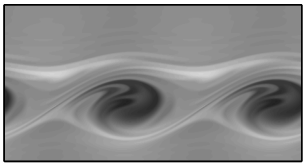

[50] Raz Kupferman. On the linear stability of plane Couette flow for an Oldroyd–B fluid and its numerical approximation. *Journal of Non-Newtonian Fluid Mechanics*, 127:169–190, 2005.

[51] Ronald G. Larson. *Constitutive Equations for Polymer Melts and Solutions*. Chemical Engineering. Butterworths, 1988.

[52] Ronald G. Larson. Instabilities in viscoelastic flows. *Rheologica Acta*, 31:213–263, 1992.

[53] Ronald G. Larson, Eric S. G. Shaqfeh, and Susan J. Muller. A purely elastic instability in Taylor-Couette flow. *Journal of Fluid Mechanics*, 218:573–600, 1990.

[54] Patrice Laure, H. Le Meur, Y. Demay, J. C. Saut, and Stéphane Scotto. Linear stability of multilayer plane Poiseuille flows of Oldroyd–B fluids. *Journal of Non-Newtonian Fluid Mechanics*, 71:1–23, 1997.

[55] Key-Chyang Lee and Bruce A. Finlayson. Stability of plane Poiseuille and Couette flow of a Maxwell fluid. *Journal of Non-Newtonian Fluid Mechanics*, 21:65–78, 1986.

[56] R. J. LeVeque. *Finite volume methods for hyperbolic problems*. Cambridge University Press, 2002.

[57] Bin Lin, Bamin Khomami, and Radhakrishna Sureshkumar. Effect of non-normal interactions on the interfacial instability of multilayer viscoelastic channel flows. *Journal of Non-Newtonian Fluid Mechanics*, 116:407–429, 2004.

[58] C. C. Lin. On the stability of two-dimensional parallel flows. Part II — stability in an inviscid fluid. *Quarterly of Applied Mathematics*, 3(3):218–234, 1945.

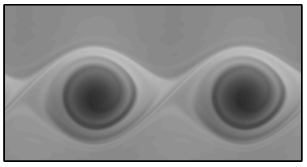

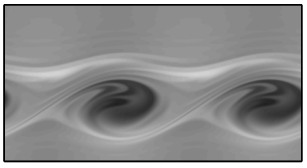

[59] Frank B. Lipps. The barotropic stability of the mean winds in the atmosphere. *Journal of Fluid Mechanics*, 12:397–407, 1962.

[60] F. J. Lockett. On Squire's theorem for viscoelastic fluids. *International Journal of Engineering Science*, 7:337–349, 1969.

[61] Preziosi Luigi, Kang-Ping Chen, and Daniel D. Joseph. Lubricated pipelining: stability of core–annular flow. *Journal of Fluid Mechanics*, 201:323–356, 1989.

[62] John L. Lumley. Drag reduction by additives. *Annual Review of Fluid Mechanics*, 1:367–384, 1969.

[63] John L. Lumley and Peter Blossey. Control of turbulence. *Annual Review of Fluid Mechanics*, 30:311–327, 1998.

[64] J. J. Magda, J. Lou, S. G. Baek, and K. L. DeVries. Second normal stress difference of a Boger fluid. *Polymer*, 32(11):2000–2009, 1991.

[65] S. A. Maslowe. Barotropic instability of the Bickley jet. *Journal of Fluid Mechanics*, 229:417–426, 1991.

[66] H. Mavridis and R. N. Shroff. Multilayer extrusion: experiments and computer simulation. *Polymer Engineering and Science*, 34(7):559–569, 1994.

[67] Gareth H. McKinley and Tamarapu Sridhar. Filament-stretching rheometry of complex fluids. *Annual Review of Fluid Mechanics*, 34:375–415, 2002.

[68] Bernard Meulenbroek, Cornelis Storm, Volfango Bertola, Christian Wagner, Daniel Bonn, and Wim van Saarloos. Intrinsic route to melt fracture in polymer extrusion: a weakly nonlinear subcritical instability

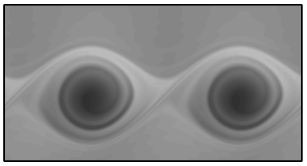

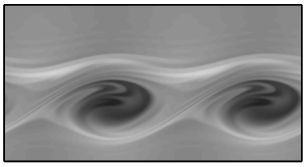

of viscoelastic Poiseuille flow. *Physical Review Letters*, 90(2):024502/1–4, 2003.

[69] Bernard Meulenbroek, Cornelis Storm, Alexander N. Morozov, and Wim van Saarloos. Weakly nonlinear subcritical instability of viscoelastic Poiseuille flow. *Journal of Non-Newtonian Fluid Mechanics*, 116:235–268, 2004.

[70] Alexander N. Morozov and Wim van Saarloos. Subcritical finite-amplitude solutions for plane Couette flow of viscoelastic fluids. *Physical Review Letters*, 95(2):024501/1–4, 2005.

[71] Susan J. Muller, Ronald G. Larson, and Eric S. G. Shaqfeh. A purely elastic transition in Taylor-Couette flow. *Rheologica Acta*, 28(6):499–503, 1989.

[72] M. E. Nordberg III and H. H. Winter. A simple model of nonisothermal coextrusion. *Polymer Engineering and Science*, 30(7):408–415, 1990.

[73] J. G. Oldroyd. On the formulation of rheological equations of state. *Proceedings of the Royal Society, A*, 200:523–541, 1950.

[74] Peyman Pakdel and Gareth H. McKinley. Elastic instability and curved streamlines. *Physical Review Letters*, 77(12):2459–2462, 1996.

[75] A. Pazy. *Semigroups of Linear Operators and Applications to Partial Differential Equations*. Number 44 in Applied Mathematical Sciences. Springer, 1983.

[76] A. Peterlin. Hydrodynamics of macromolecules in a velocity field with longitudinal gradient. *Journal of Polymer Science, Polymer Letters*, 4:287–291, 1966.

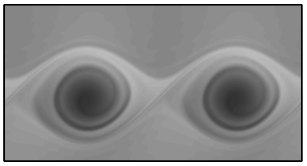

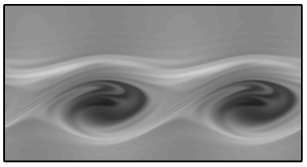

[77] William H. Press, Saul A. Teukolsky, William T. Vetterling, and Brian P. Flannery. *Numerical Recipes in* C++. *The Art of Scientific Computing*. Cambridge University Press, Second edition, 2002.

[78] L. M. Quinzani, G. H. McKinley, R. A. Brown, and R. C. Armstrong. Modeling the rheology of polyisobutylene solutions. *Journal of Rheology*, 34(5):705–748, 1990.

[79] John M. Rallison and E. John Hinch. Instability of a high-speed submerged elastic jet. *Journal of Fluid Mechanics*, 288:311–324, 1995.

[80] J. W. S. Rayleigh. *The Theory of Sound*, volume II. Dover, 1945. Reprint of 2nd ed. of 1894 by MacMillan.

[81] Michael Renardy. On the stability of parallel shear flow of an Oldroyd–B fluid. *Differential and Integral Equations*, 6(3):481–489, 1993.

[82] Michael Renardy and Yuriko Renardy. Linear stability of plane Couette flow of an upper convected Maxwell fluid. *Journal of Non-Newtonian Fluid Mechanics*, 22:23–33, 1986.

[83] Michael Renardy and Yuriko Renardy. Derivation of amplitude equations and analysis of sideband instabilities in two-layer flows. *Physics of Fluids A*, 5:2738–2762, 1993.

[84] Yuriko Renardy. Stability of the interface in two-layer Couette flow of upper convected Maxwell liquids. *Journal of Non-Newtonian Fluid Mechanics*, 28:99–115, 1988.

[85] Stéphane Scotto and Patrice Laure. Linear stability of three-layer Poiseuille flow for Oldroyd–B fluids. *Journal of Non-Newtonian Fluid Mechanics*, 83:71–92, 1999.

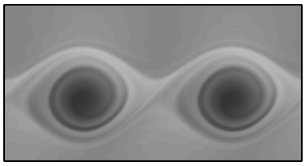

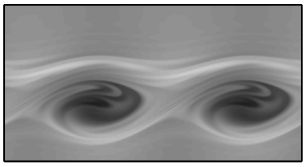

[86] Eric S. G. Shaqfeh. Purely elastic instabilities in viscometric flows. *Annual Review of Fluid Mechanics*, 28:129–185, 1996.

[87] Eric S. G. Shaqfeh, Susan J. Muller, and Ronald G. Larson. The effects of gap width and dilute solution properties on the viscoelastic Taylor-Couette instability. *Journal of Fluid Mechanics*, 235:285–317, 1992.

[88] I. G. Shukhman. Nonlinear evolution of a weakly unstable wave in a free shear flow with a weak parallel magnetic field. *Journal of Fluid Mechanics*, 369:217–252, 1998.

[89] I. G. Shukhman. A weakly nonlinear theory of the spatial evolution of disturbances in a shear flow with a parallel magnetic field. *Physics of Fluids*, 10(8):1972–1986, 1998.

[90] H. B. Squire. On the stability for three-dimensional disturbances of viscous fluid flow between parallel walls. *Proceedings of the Royal Society of London, Series A*, 142:621–628, 1933.

[91] T. Sridhar. An overview of the project M1. *Journal of Non-Newtonian Fluid Mechanics*, 35:85–92, 1990.

[92] Phillip A. Stone, Fabian Waleffe, and Michael D. Graham. Toward a structural understanding of turbulent drag reduction: nonlinear coherent states in viscoelastic shear flows. *Physical Review Letters*, 89(20):2080301/1–4, 2002.

[93] R. Sureshkumar, Antony N. Beris, and Robert A. Handler. Direct numerical simulation of the turbulent channel flow of a polymer solution. *Physics of Fluids*, 9(3):743–755, 1997.

[94] G. Tlapa and B. Bernstein. Stability of a relaxation-type viscoelastic fluid with slight elasticity. *The Physics of Fluids*, 13(3):565–568, 1970.

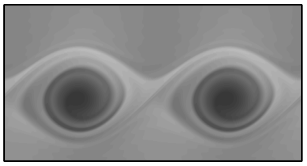

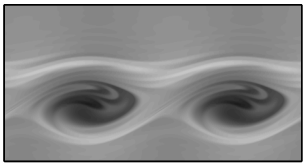

[95] Lloyd N. Trefethen, Anne E. Trefethen, Satish C. Reddy, and Tobin A. Driscoll. Hydrodynamic stability without eigenvalues. *Science*, 261(5121):578–584, 1993.

[96] Rudy Valette, Patrice Laure, Yves Demay, and Jean-Francois Agassant. Investigation of the interfacial instabilities in the coextrusion flow of PE and PS. *International Polymer Processing*, 18(2):171–178, 2003.

[97] Rudy Valette, Patrice Laure, Yves Demay, and Jean-Francois Agassant. Convective linear stability analysis of two-layer coextrusion flow for molten polymers. *Journal of Non-Newtonian Fluid Mechanics*, 121:41–53, 2004.

[98] Rudy Valette, Patrice Laure, Yves Demay, and Jean-Francois Agassant. Experimental investigation of the development of interfacial instabilities in two layer coextrusion dies. *International Polymer Processing*, 19(2):118–128, 2004.

[99] Rudy Valette, Patrice Laure, Yves Demay, Jean-Francois Agassant, and B. Vergnes. Experimental and theoretical study of the interface instability of a two-layer coextrusion flow. In *Proceedings*, volume 17. Polymer Processing Society, 2001.

[100] Gregory M. Wilson and Bamin Khomami. An experimental investigation of interfacial instabilities in multilayer flow of viscoelastic fluids. Part I. Incompatible polymer systems. *Journal of Non-Newtonian Fluid Mechanics*, 45:355–384, 1992.

[101] Gregory M. Wilson and Bamin Khomami. An experimental investigation of interfacial instabilities in multilayer flow of viscoelastic fluids. II.

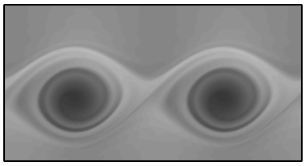

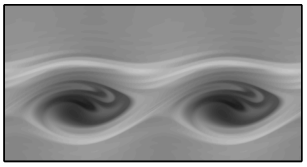

Elastic and nonlinear effects in incompatible polymer systems. *Journal of Rheology*, 37(2):315–339, 1993.

[102] Gregory M. Wilson and Bamin Khomami. An experimental investigation of interfacial instabilities in multilayer flow of viscoelastic fluids. III. Compatible polymer systems. *Journal of Rheology*, 37(2):341–354, 1993.

[103] Helen J. Wilson. *Shear Flow Instabilities in Viscoelastic Fluids*. PhD thesis, Cambridge University, Cambridge, United Kingdom, 1998.

[104] Helen J. Wilson and John M. Rallison. Short wave instability of co-extruded elastic liquids with matched viscosities. *Journal of Non-Newtonian Fluid Mechanics*, 72:237–251, 1997.

[105] Helen J. Wilson and John M. Rallison. Instability of channel flow of a shear-thinning White–Metzner fluid. *Journal of Non-Newtonian Fluid Mechanics*, 87:75–96, 1999.

[106] Helen J. Wilson and John M. Rallison. Instability of channel flows of elastic liquids having continuously stratified properties. *Journal of Non-Newtonian Fluid Mechanics*, 85:273–298, 1999.

[107] Helen J. Wilson, Michael Renardy, and Yuriko Renardy. Structure of the spectrum in zero Reynolds number shear flow of the UCM and Oldroyd–B liquids. *Journal of Non-Newtonian Fluid Mechanics*, 80:251–268, 1999.

[108] Bulent Yesilata. Nonlinear dynamics of a highly viscous and elastic fluid in pipe flow. *Fluid Dynamics Research*, 31:41–64, 2002.

[109] Chia-Shun Yih. Instability due to viscosity stratification. *Journal of Fluid Mechanics*, 27:337–352, 1967.